
# GAS SENSING WITH MODIFIED CARBON NANOTUBES, GRAPHENE AND DIAMONDOIDS

**Juan Casanova Cháfer**

DOCTORAL THESIS

# Gas Sensing with Modified Carbon Nanotubes, Graphene and Diamondoids

Ph.D Thesis

**Juan Casanova Cháfer**

Supervised by:

Prof. Eduard Llobet Valero

Department of

Electronic, Electrical and Automation Engineering

UNIVERSITAT ROVIRA i VIRGILI

Tarragona

2020

UNIVERSITAT ROVIRA I VIRGILI
GAS SENSING WITH MODIFIED CARBON NANOTUBES, GRAPHENE AND DIAMONDOIDS
Juan Casanova Cháfer

UNIVERSITAT ROVIRA i VIRGILI

FAIG CONSTAR que aquest treball, titulat “Gas Sensing with Modified Carbon Nanotubes, Graphene and Diamondoids”, que presenta Juan Casanova Cháfer per a l’obtenció del títol de Doctor, ha estat realitzat sota la meva direcció al Departament d’Enginyeria Electrònica, Elèctrica i Automàtica d’aquesta universitat.

---

HAGO CONSTAR que el presente trabajo, titulado “Gas Sensing with Modified Carbon Nanotubes, Graphene and Diamondoids” que presenta Juan Casanova Cháfer para la obtención del título de Doctor, ha sido realizado bajo mi dirección en el Departamento de Ingeniería Electrónica, Eléctrica y Automática de esta universidad.

---

I STATE that the present study, entitled “Gas Sensing with Modified Carbon Nanotubes, Graphene and Diamondoids” presented by Juan Casanova Cháfer for the award of the degree of Doctor, has been carried out under my supervision at the Department of Electronic, Electrical and Automation Engineering this university.

---

Tarragona, 20th November, 2019

El/s director/s de la tesi doctoral

El/los director/es de la tesis doctoral

Doctoral Thesis Supervisor/s

Eduard Llobet Valero

UNIVERSITAT ROVIRA I VIRGILI
GAS SENSING WITH MODIFIED CARBON NANOTUBES, GRAPHENE AND DIAMONDOIDS
Juan Casanova Cháfer

# Acknowledgements

Me gustaría dedicar este trabajo a mis padres, Juan Rafael y Mª Carmen, como agradecimiento por enseñarme todo lo necesario para la vida. Y especialmente, por grabarme a fuego que los sueños solamente se pueden alcanzar mediante el esfuerzo y el trabajo constante, ya que los atajos suelen tener un corto recorrido. Aunque no pueda compartir con ellos este momento, sé que esta tesis también realiza uno de sus mayores sueños. Por lo que estoy seguro de que estarán viéndome orgullosos desde el pedacito de cielo en el que se encuentren.

Quisiera dar mi más sincero agradecimiento a mi director de tesis, Eduard Llobet. Gracias por confiar en mí y darme la oportunidad de emprender esta aventura en tu grupo de investigación. Ha sido un auténtico placer aprender directamente de una mente tan privilegiada como la suya. Gracias por tu incalculable ayuda y motivación, así como por todo lo que me has enseñado, permitiendo que creciera a tu lado. Quisiera agradecer también a Carla todo lo que me ha enseñado, aportándome nuevos conocimientos y puntos de vista. También quisiera agradecerle su enorme hospitalidad, haciendo que me sintiera como en casa, pese a estar lejos de ella.

A mi hermanita Lucia, porque no soy capaz de expresar con palabras el agradecimiento que siento de que estés en mi vida. Si estoy aquí es sin duda gracias a ti, tan jóvenes y tan maduros a la vez. Tu arrojo y dulzura a partes iguales han hecho que podamos crecer juntos, enriqueciéndonos mutuamente. Gracias por ser como eres, y gracias por estar siempre tan atenta y traer la alegría a casa.

A la mujer de mi vida, Rocío, gracias por ser mi motor para que pueda mejorar día a día en todos los aspectos. Gracias por tu apoyo incondicional en todas las decisiones que he tomado, así como por escucharme atentamente hora tras hora, día tras día. Aunque si hay algo de valor incalculable, es que siempre has estado a mi lado, en los buenos, pero especialmente en los malos momentos, siempre luchando con fiereza para pueda seguir adelante y no desista nunca. Sin ti hoy no estaría escribiendo estas líneas.

A mi tío José Luis, por cuidarme como a un hijo, y por esas largas e inolvidables horas “arreglando” el mundo juntos. A Melissa, Nadia, Santi e Isaac, por su enorme apoyo, ánimos y comprensión durante todo este tiempo. A mis tíos Daniel y Esther, por estar siempre dispuestos a ayudarme en todo cuanto necesitara. A mi abuela Carmen, por todos los valores que me transmitió y que han sido realmente imprescindibles en esta etapa. A mi abuela Amparo, por su preocupación constante para que no me faltara de nada, así como por sus exquisitas comidas. A mis suegros, Mateo y Victoria, por quererme como a un hijo. Y al resto de miembros de mi familia, tanto sanguínea como política, porque no solamente es la sangre y la carne lo que determina la familia, si no el corazón.

Por último, cabe destacar que una tarea hercúlea, como una tesis doctoral, no puede ser llevada a cabo sin la ayuda de otra gente, ni con los grandes momentos compartidos con amigos y compañeros. Por ello quiero dar las gracias a Ernesto, Miriam, Xavi, Juanan, Rafa, Rubén, Raúl, Héctor, Èric, Claudia, Tesfalem, Selene, Hussam, Pedro, Kawther, Mattia, Sabine, Sergio, Oriol, Ángel, Sara, María, Milena, Ghada, Fátima, Aanchal, y tantos otros con lo que he compartido vivencias e inquietudes durante estos años.

UNIVERSITAT ROVIRA I VIRGILI
GAS SENSING WITH MODIFIED CARBON NANOTUBES, GRAPHENE AND DIAMONDOIDS
Juan Casanova Cháfer

# List of acronyms

| | |
|---|---|
| **WHO** | World Health Organization |
| **TLV** | Threshold Limit Value |
| **PCB** | Printed Circuit Board |
| **EPA** | Environmental Protection Agency |
| **ST** | Short-Time |
| **TWA** | Time-Weighted Average |
| **PAN** | Polyacrylonitrile |
| **CNTs** | Carbon Nanotubes |
| **SWCNTs** | Single-Wall Carbon Nanotubes |
| **MWCNTs** | Multi-Wall Carbon Nanotubes |
| **CVD** | Chemical Vapour Deposition |
| **VOC** | Volatile Organic Compound |
| **LOD** | Limit of Detection |
| **SAM** | Self-assembled Monolayer |
| **VA-CNTs** | Vertically Aligned Carbon Nanotubes |
| **XPS** | X-ray Photoelectron Spectroscopy |
| **HNPs** | Hexagonal-shaped Nanoplates |
| **GO** | Graphene Oxide |
| **rGO** | Reduced Graphene Oxide |
| **NC** | Nanocrystal |
| **FLG** | Few-Layer Graphene |
| **SEM** | Scanning Electron Microscope |
| **SAW** | Surface Acoustic Wave |
| **QCM** | Quartz Crystal Microbalance |
| **BET** | Brunauer-Emmett-Teller theory |
| **UV** | Ultraviolet |

UNIVERSITAT ROVIRA I VIRGILI
GAS SENSING WITH MODIFIED CARBON NANOTUBES, GRAPHENE AND DIAMONDOIDS
Juan Casanova Cháfer

# Table of Contents

UNIVERSITAT ROVIRA I VIRGILI
GAS SENSING WITH MODIFIED CARBON NANOTUBES, GRAPHENE AND DIAMONDOIDS
Juan Casanova Cháfer

# Chapter 1

## Introduction

*The present thesis is focused on the development of gas sensors employing carbon-based nanomaterials. The main goal is to achieve the detection of molecules at trace levels using both, $sp^2$ and $sp^3$ carbon hybridizations. Thus, different approaches will be proposed to enhance crucial sensing parameters such as selectivity, sensitivity or response/recovery times. Additionally, an extensive study of gas sensing mechanisms will be discussed in the journal papers included in the thesis.*

UNIVERSITAT ROVIRA I VIRGILI
GAS SENSING WITH MODIFIED CARBON NANOTUBES, GRAPHENE AND DIAMONDOIDS
Juan Casanova Cháfer

## 1.1. State of art

According to the World Health Organization (WHO), nine out of ten people are exposed to polluted air, which is linked to 7 million deaths every year worldwide [1]. For that reason, this organisation defines the atmospheric pollution as the most significant environmental risk to human health and a key challenge towards climate change. Consequently, stable, sensitive and straightforward electronic sensors are needed for monitoring and detecting pollutants at trace concentrations. Therefore, establishing a widespread sensor network for the continuous monitoring of ambient pollutants is a challenge for our current societies. This requires inexpensive, low-power, sensitive and quite selective devices. Achieving those would undoubtedly fuel their exponential growth. However, most of gas sensing procedures available are frequently associated with high-cost, bulky and complex instrumentation, such as the sampling with sorption tubes or similar approaches to be subsequently analysed by chromatographic techniques [2] or Fourier transform infrared spectroscopy (FTIR) [3]. Those methods provide accurate and selective gas readings, but they involve the use of pumps, require skilled and knowledgeable personnel, and its miniaturisation is still an issue. Some approaches to miniaturise these devices were studied, but their long response time, problems to perform a spatially-distributed and continuous air monitoring and high power consumption are still unsolved [4].

In the last years other options have been extensively studied, such as optical, gravimetric and electrochemical sensors. Optical sensor devices present high sensitivity, enabling the detection at trace concentration levels [5]. However, these devices are expensive and show low portability. Likewise, gravimetric devices such as surface acoustic wave (SAW) sensors and quartz crystal microbalances (QCM) are highly sensitive to gases with short response times [6,7]. Nevertheless, their complexity, high cost and dependence on the temperature and humidity levels [8] constitute limiting parameters to create a vast sensor network able to operate under real conditions. In any case, electrochemical sensing probably is the most popular technique to detect toxic gases due to their low-cost, good selectivity, low power consumption and repeatability [9]. However, electrochemical sensors show significant drawbacks to be employed in real applications for gas monitoring, such as high sensitivity to temperature fluctuations, difficulty for being miniaturised and minimal shell life [10].

In front of these alternatives, chemical resistive (chemiresistive) sensors have emerged as an easy and cheap option to detect pollutants at trace levels [11]. These devices belong to the solid-state gas sensor family, in which a reversible interaction of the target gas with the surface of the solid produces a change in their resistance. During the last decades, chemical sensors were focused on metal oxides, such as $WO_3$, $In_2O_3$, $SnO_2$, and ZnO [12–15]. These nanomaterials show high sensitivities, good reproducibility and low response times [16]. However, metal oxides usually require high operating temperatures to activate the oxidation-reduction processes [17]. In consequence, high power consumption is needed to operate with metal-oxide based sensors. Besides, these temperatures decrease the long-term stability of the sensors due to irreversible changes in their crystalline structure, and the nanostructures tend to agglomerate into large entities, decreasing their surface area and their catalytic properties as well [18]. Additionally, the selectivity of metal oxides is still a key challenge, with believable solutions like the development of sensor arrays, but at the expense of increasing the complexity and the economic cost.

More recently, carbon nanomaterials have been attracting a great deal of research interest in gas sensing. In particular, low-dimensional carbon nanostructures present a high potential to being controlled at the nanoscale, becoming a promising material for the next generation of sensors. This low-dimensionality brings about better properties than that of their bulk materials, mainly because of the dramatically larger surface to volume or weight ratio. Thus, most of their atoms are at the surface, being exposed to the chemical environment, which is advantageous for achieving high sensitivity. Additionally, low-dimensional carbon nanostructures usually have high-quality crystal lattices, high carrier mobility, ease of miniaturisation and low levels of noise [19]. Also, the possibility of carbon nanomaterials to operate at room temperature is an essential parameter that enables the power consumption to be reduced. However, the carbon atoms covalently attached via $sp^2$ bonds entail a low chemical reactivity with the environment, sometimes wasting their characteristic high surface to volume ratio. Defective carbon nanomaterials also present an important lack of selectivity and problems with the recovery of the sensor baseline resistance due to the strong interaction with gas molecules. Nevertheless, selectivity and sensitivity can be engineered in many ways, such as by the controlled creation of defects, grafting functional groups, decorating with metal or metal oxide nanoparticles, among others. Consequently, different approaches were developed in this thesis by engineering the surface of carbon nanomaterials to improve the sensing parameters up to the detection of harmful gases at concentrations below the threshold limit values (TLV) established by the European Union.

## 1.2. Gas sensors

In solid-state gas sensors, the transduction mechanism can be defined as the route to transforming a magnitude from the chemical domain into the electrical or optical domain. In our case, the adsorption/desorption mechanism induces a charge transfer that is transformed into an electrical signal.

For testing the gas sensing properties of the different carbon nanomaterials, they were deposited by several techniques onto silicon substrates previously oxidized. Then, a calibrated alumina hotplate that comprised a platinum screen-printing heating element was connected to the backside of the silicon wafer. Afterwards, the silicon wafer/ceramic hotplate was bonded to a printed circuit board (PCB). Finally, two platinum wire contacts were added on the surface using a silver epoxy paste. Furthermore, the gas sensing experiments were conducted using an airtight Teflon chamber, which was designed and constructed. Its inner volume is 35 $cm^3$ and contains sockets to be placed up to four sensors. Then, this sensing chamber was connected to a gas mixing and delivery systems that used calibrated gas cylinders and pure dry air as balance and carrier gas. In some works, further studies under ambient moisture were made using a computer-controlled evaporator and mixer to humidify gas samples during the measurement. **Figure 1** shows a scheme of the whole system.

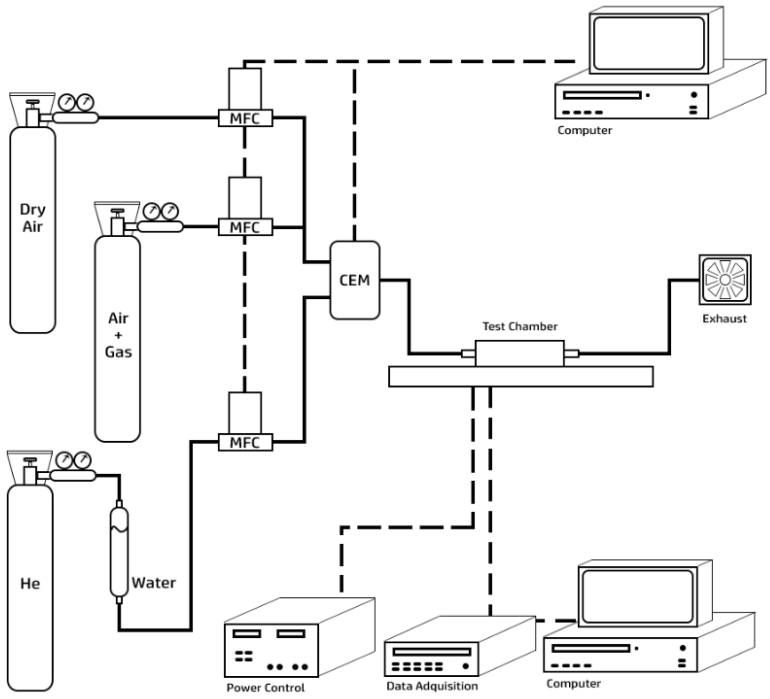


**Figure 1.** Automated gas delivery set-up for characterization of gas sensors. Extracted from [20].

Among the different gases tested, two of them, nitrogen dioxide ($NO_2$) and ammonia ($NH_3$), were measured extensively in our research due to their harmful properties to the human health and their opposite nature. Which means that $NO_2$ is an electron-withdrawing molecule, while $NH_3$ is an electron-donating. On the one hand, nitrogen oxides ($NO_X$) are mainly generated from the high-temperature combustions [21], involved in industrial processes and vehicle exhausts. Short exposure to $NO_2$ can cause minor effects like respiratory irritation and inflammation, but long exposures can cause detrimental health issues such as chronic respiratory and heart disease, acute respiratory infections and lung cancer [22,23].

Additionally, nitrogen dioxide molecules interact with pollen resulting in heightened allergenicity [24]. On the other hand, ammonia is emitted from agricultural processes and livestock [25]. However, some research works also report the emission of this pollutant to the atmosphere derived from the automotive exhaust [26–28]. $NH_3$ is a well-known irritant, and corrosive gas, its inhalation at low concentrations can cause coughing, and nose and throat irritation. Nevertheless, the exposure to high levels of ammonia causes acute toxicity inducing respiratory shocks and burns, even death [29–31]. The reason for this high toxicity is derived from the fact that once ammonia enters the body, it reacts with water molecules, producing ammonium hydroxide, which is a very corrosive and poisoning chemical [32].

Regarding the TLV for $NO_2$ and $NH_3$, **Table 1** summarizes the air quality standards established by the European Commission and the Environmental Protection Agency (EPA) from the US. Among the work described in this thesis, other gases were also measured, such as ethanol, carbon monoxide (CO) or hydrogen, among others. However, these are not particularly harmful to the environment, and human health (e.g. $H_2$) or the sensitivities obtained are not high enough to detect concentrations below the TLV (e.g. CO).

**Table 1**. TLV for NO2 and NH3 exposure correlated with their averaging time. ST = short-time. TWA = Time-Weighted Average). Reproduced from [33].

| | Averaging Time | European Union | United States |
|---|---|---|---|
| $NO_2$ | 1 h | 200 ppb | 100 ppb |
| | 1 year | 40 ppb | 53 ppb |
| $NH_3$ | ST | 50 ppm | 35 ppm |
| | TWA | 20 ppm | 25 ppm |

When carbon nanomaterial based chemoresistors interact with target gases, the result is a charge transfer between adsorbed gas molecules and the nanomaterial, which results in changes in the electrical resistance (R expressed in Ohms) of the chemoresistor. These changes are monitored and quantified; therefore, they can be correlated with the nature of the gaseous species and its concentration. The carbon nanomaterials employed usually behave as a mild p-type semiconductors, which means that holes and free electrons are the majority and minority charge carriers, respectively [34]. Consequently, the adsorption of an electron-withdrawing gas such as nitrogen dioxide ($NO_2$) results in a shift of the Fermi level closer to the valence band in the carbon nanomaterials. Thus, the enriched hole carriers enhance the sample conductance, leading to a lower resistance. Conversely, electron-donating species such as ammonia ($NH_3$) shift the Fermi level away from the valence band, resulting in a hole depletion and leading to a reduced conductance (and a higher resistance).

The response of the sensors to target gases is usually defined as the difference between the initial resistance value ($R_0$) and the change of the measured physical property (R), normalized to $R_0$.

$$\text{Response (\%)} = \frac{R-R_0}{R_0} \cdot 100 = \frac{\Delta R}{R_0}$$

The present thesis introduction is organized in five different sections. Three of them correspond to the different allotropes of carbon (**Figure 2**) that are used in our work (carbon nanotubes, graphene, and diamondoids). The other two sections (carbon black and carbon nanofibers) correspond to carbon nanomaterials that were not studied in this thesis, but they are important to offer a more comprehensive view of the use of all carbon nanomaterials for

gas sensing. Each allotrope shows interesting and unique properties to be employed as gas sensitive material, which depend on their dimensional structure and their physicochemical properties. In the present thesis, their sensing properties, their modification and gas mechanism are extensively studied.

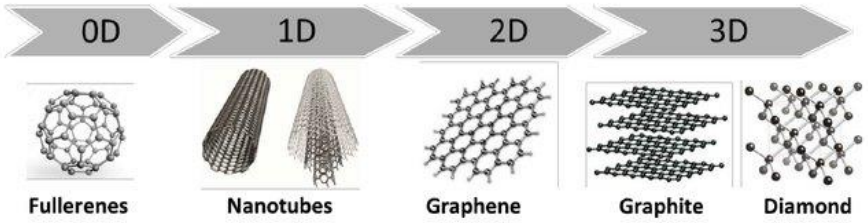


**Figure 2**. Allotropes of the different carbon nanomaterials. Reproduced from [35].

During the lasts 20 years, an increasing research interest has been focused on gas sensors based on carbon nanomaterials (**Figure 3**). In particular, the first works employed carbon nanotubes, showing a continuous increase in the number of publications until five years ago approximately, when graphene took over attracting considerable interest. Although carbon nanotubes keep a stable and high publication rate, in the last years publications related to graphene have experienced a notable and sustained increase. In contrast, carbon black and carbon nanofibers based gas sensors have attracted a fare more limited interest, showing a significantly lower number of publications every year. Additionally, new carbon nanomaterials such a diamondoids, have emerged in 2019 with the first publication employing these nanostructures in gas sensing application.

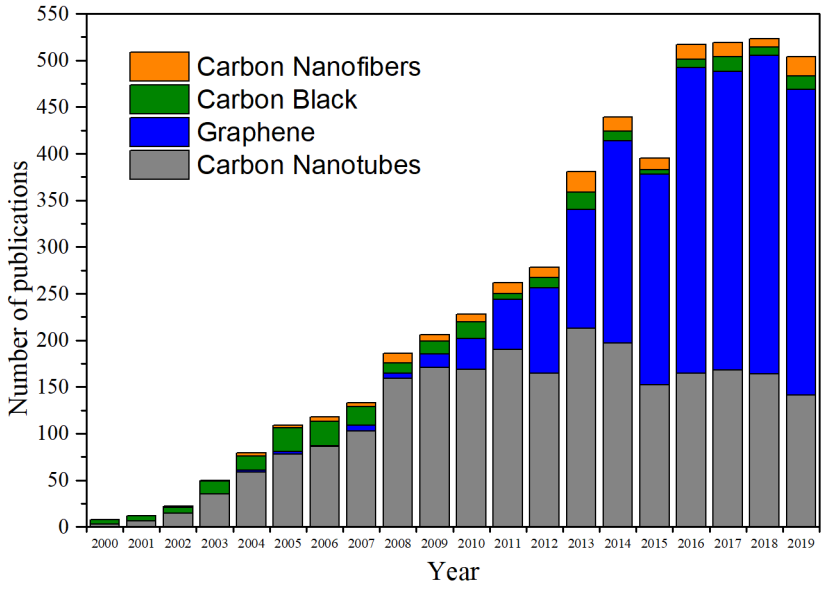


**Figure 3.** Yearly number of publications for gas sensors based on carbon nanotubes, graphene carbon black and carbon nanofibers. Source: Scopus.

## 1.3. Carbon black

Carbon black consists of a finely divided powder of pure elemental carbon, in other words, they can be considered as pure crystalline carbon particles (**Figure 4**). This carbon in the form of colloidal particles can be produced by the incomplete combustion or thermal decomposition of gaseous or liquid hydrocarbons under controlled conditions. Two main carbon black manufacturing processes, furnace black and thermal black, are the methods for its production. The furnace black method involves the use of heavy aromatic oils as feedstock in a closed reactor, in order to atomise the feedstock oil under controlled parameters, such as temperature and pressure. A secondary feedstock (e.g., oil or natural gas) is burned to achieve a hot gas stream, and then, the primary feedstock is introduced on this hot gas stream. The result is the formation of microscopic carbon particles by the vaporisation and pyrolysis of the feedstock. The reaction rate can be controlled by steam or water spray. The carbon black obtained is transported through the reactor, and then cooled and collected in bag filters. During this process, residual gases such as hydrogen and carbon monoxide are generated, however, usually are used to produce heat, steam, or electric power [19].

The thermal black method is carried out by using natural gas as feedstock material, basically heavy aromatic oils or methane. This process usually employs two furnaces, alternating between pre-heating and carbon black production every few minutes. In the absence of air, the natural gas injected into a hot refractory line furnace is decomposed into carbon black and hydrogen. The aerosol material stream is quenched with water sprays and filtered in a bag. Besides, carbon black can be further processed by removing impurities, screened or pelletised. Finally, the residual hydrogen is burned in air to heat the furnaces [19].

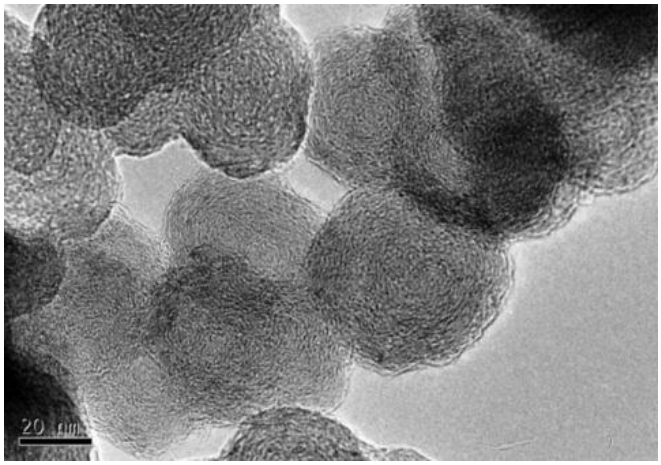


**Figure 4**. TEM image of carbon black particles. Reproduced from [36].

Carbon black usually contains more than 97% of carbon arranged as aciniform particulate matter. This is the main difference of carbon black towards soot or back carbon, which can contain impurities (e.g. dichloromethane, toluene and ash) up to 50% of content [37]. Thus, carbon black show interesting properties such as relatively high surface to volume area and particle size about tens of nanometers. This carbon nanomaterial was successfully employed as a reinforcing agent in tires and industrial rubber products, plastics and coatings.

Carbon black was also reported for gas sensing applications. To perform an electrical conductive film, carbon black should be dispersed into an insulating polymer matrix. In that

way, it is ensured that some conducting pathways are available between the interdigitated electrodes. The resistivity of the film is based on the percolation theory [38]. Thus, if the carbon black content is below the percolation threshold, the film will be insulator and there are not pathways of carbon black (the conductive particles) to connect the interdigitated electrodes. Nevertheless, with enough carbon black content, the resistance decreases dramatically due to the presence of conductive pathways. This point is known as the percolation threshold, and once is reached, small variations in the carbon black content entail huge changes in the resistivity of the film. Additionally, the composite viscosity can be modified by adjusting the solvent parameters, and the resulting paste is deposited by spin coating or screen printing techniques on flat substrates. Afterwards, a drying step is needed to remove the solvents. Then, an easy working principle and simple air monitoring are derived from the fact that polymer swelling upon exposure to gases increases the resistance of the conductive film because some conducting paths are disrupted [39]. For instance, Lewis and co-workers employed an array of carbon black-polymer hybrid sensors to detect several vapours [40,41]. Thus, the diversity between sensor elements is based on the different organic polymers employed. However, gas sensors based on carbon black-polymer hybrids present important drawbacks, such as weak signal transduction, high sensitivity to ambient moisture, moderate sensitivities to gases and remarkable baseline drift [42]. Moreover, the ageing of the polymer matrix, and the changes in the percolation paths, derived from the rearrangement of carbon black particles within the polymer caused by the swelling/shrinking processes, constitute significant drawbacks to employ this nanomaterial in commercial applications.

## 1.4. Carbon nanofibers

Carbon nanofibers can be defined as hollow nanosized structures (**Figure 5**) produced at the surface of catalytic metal particles (Fe, Co and Ni) by using hydrocarbon gases at temperatures between 900˚C and 1500˚C [43]. An initial filament composed of graphitic planes in a "stacked-cup" morphology (diameter of 20-60 nm) is formed. Afterwards, a secondary thickening process can be applied by the deposition of an outer layer using chemical vapour deposition [44]. Resulting to this thickening, undulating graphitic planes are added, lying parallel to the carbon nanofiber outer layer. This method produces carbon nanofibers with diameters ranging from 60 to 200 nm, and as-formed lengths from 1 to 100 mm [19]. However, these processes are usually expensive for mass production. In consequence, other low-cost processes have been emerged, such as electrospinning [45]. This method can use a polymer (e.g. polyacrylonitrile (PAN)) as a carbon source, producing a high conductive polymer solution by using a suitable solvent with a low boiling point. The polymer solution is ejected from a syringe tip onto a rotating collector situated a few centimetres away, and a specific voltage is applied between them. Electrospun material is stabilised via annealing, and afterwards, a carbonisation step is performed by calcinating the samples at high temperature (700-1000˚C) in an inert atmosphere (e.g. Ar or $N_2$). Employing this efficient and low-cost approach, carbon nanofibers around 40-400nm of diameter and lengths above 70 µm can be obtained [46,47].

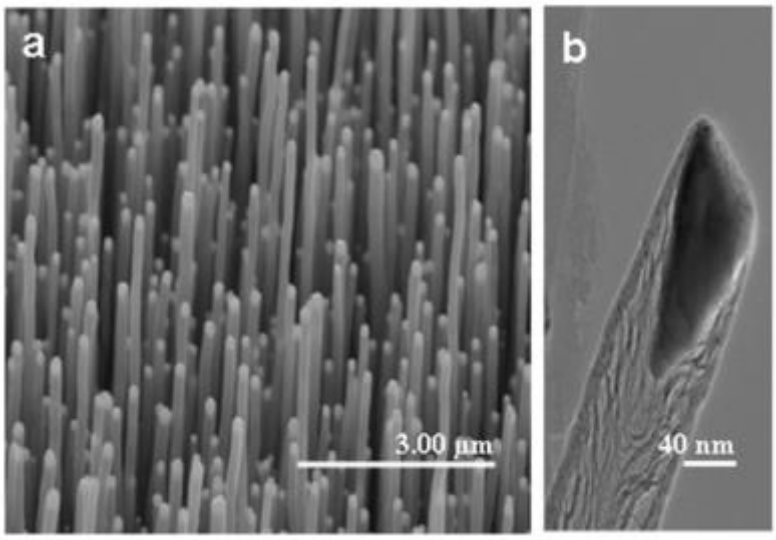


**Figure 5**. (a) SEM image of vertically aligned carbon nanofiber array. (b) TEM image of a stacked cone morphology of carbon nanofibers. Images reproduced from [48].

Since it is well-know the problem of carbon black based gas sensors, the use of carbon nanofibers instead of carbon black particles has been suggested as an alternative to obtaining more stable sensors employing the same detection principle. The sensor instability experienced by using carbon black particles is derived from the aggregation of the particles when the composite increase their volume due to the absorption of gases, and as a result, the matrix viscosity is decreased. In contrast, Pitman and co-workers [49] proposed the dispersion of carbon nanofibers in a polymer matrix to overcome the instability when carbon black particles are used. The reason is that carbon nanofibers are not prone to aggregation within the polymer matrix. In consequence, the percolation pathways are stable during the

absorption/desorption processes. Additionally, mats of carbon nanofibers can be used for developing chemiresistors by depositing them over interdigitated electrodes. In carbon nanofiber mats, the electrical conductivity is mobility-limited by the potential barriers developing at the nanofiber-to-nanofiber junctions [19]. Also, it is possible to perform further modifications over carbon nanofibers to enhance some sensing parameters such as sensitivity or selectivity. For instance, the use of KOH solutions for the chemical activation of carbon nanofibers improve their porous structure. Thus, the sensitivity of the sensor is improved due to an increase of the specific surface area up to 100-fold [50]. Besides, other options to enhance the sensing properties have been explored, such as the carbon nanofiber decoration with metal or metal oxide nanoparticles [51,52]. With this approach, higher sensitivities can be obtained due to the increase in the changes of the electrical resistance, based on a larger rate of gas adsorption.

## 1.5. Carbon nanotubes

Carbon nanotubes (CNTs) are composed of carbon atoms bonded in a hexagonal lattice (exactly as in graphene), creating a hollow structure due to being formed of rolled graphene sheets. CNTs can be classified as a single-wall (SWCNTs), consisting of a single tube, and multi-wall (MWCNTs), constituted by a multiple nanotubes sharing the same axis. The chirality of carbon nanotubes determines their metallic or semiconducting behaviour, and then, modulating their electrical and mechanical properties. The chiral vector (**Figure 6**) is composed of two components (n,m). The (n,0) structure is called "zigzag" when n=m (n,n) is called "armchair" and the structure in which n > m > 0 is called "chiral" [53]. When n-m=3q (where q is an integer or zero) a SWCNT is metallic, whereas semiconducting nanotubes show n-m≠3q [54]. Additionally, for MWCNTs, tube interactions can modify the electronic properties for specific relative positions. Meaning that MWCNTs with a larger diameter than 14nm show a metallic behaviour because, under these conditions, the band-gap energy is lower than the thermal energy at room temperature [55]. In our case, the MWCNTs employed in this thesis have an average diameter of 9 nm, keeping their mild semiconductor behaviour. The chemical bonding of pristine CNTs is composed entirely by $sp^2$ bonds, similarly to graphene. These bonds are stronger than $sp^3$ configuration found in diamondoids, providing a unique strength. However, such strong bonds are characterised by a low chemical reactivity with their surroundings, in our case, the gaseous species. Therefore, further modifications or functionalization over CNTs will be required to employ them as gas sensors, by improving basically the sensitivity and selectivity.

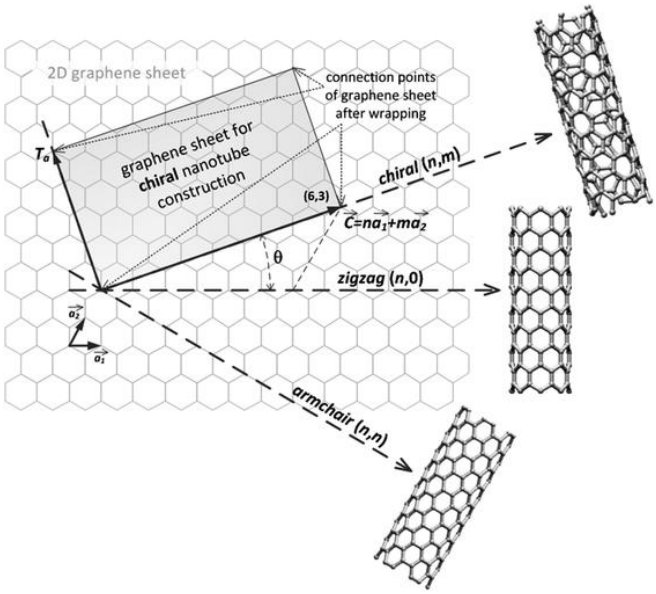


**Figure 6.** Schematic CNT depiction of the roll-up vectors (n,m) reproduced from [53].

CNTs have been synthesised using several techniques, such as arc discharge, laser ablation or chemical vapour deposition. In 1991, CNTs were discovered from the carbon soot of graphite electrodes during an arc discharge process [56]. As a consequence of the high discharge temperatures, the carbon contained in the negative electrode was sublimated. Thus, arc discharge was extensively used during the first years, despite the low yield (around 30%) of this method. Besides, this technique produces both, SWCNTs and MWCNTs with large lengths (up to a few tens of µm) and some structural defects. A few years later, the laser ablation process has been constituted as a new method to create MWCNTs [57] and SWCNTs [58] with

a higher yield (around 70%). In this method, a pulsed laser vaporises a graphite target in a high-temperature reactor, while an inert gas is bled into the chamber. Also, the CNT diameter can be modulated by the reaction temperature. However, in 1993, the catalytic vapour phase deposition of CNTs was reported [59], being the method used for the commercial production of nanotubes. In this chemical vapour deposition (CVD) method, a substrate with a layer of metal catalyst particles (e.g. iron, nickel or cobalt) is used [60]. The strong point of this approach, is the high control over the diameters of the CNTs according to the size of the metal catalyst particles. Thus, the particle size can be modulated by annealing, by plasma etching or by a patterned (or masked) deposition of the metal. Then, the substrate is heated up to 700˚C, and the CNT growth is started by introducing two gases into the reactor. One is the carrier gas, such as nitrogen, and the other is a carbon-containing gas, such as methane, ethylene, acetylene, among others. As a consequence, the carbon-containing gas is broken at the surface of the metal catalyst particles, and the CNTs start their growing at these sites via vapour-liquid-solid mechanism. A high yield (around 90%) can be achieved, and the catalyst particles can stay at the tips or at the base of the nanotubes depending on the adhesion of the particles to the substrate. Although CNT growth without plasma results in a random orientation of them, by adjusting the geometry of the reactor and by applying a plasma is it possible the synthesis of vertically-aligned CNTs, as we sometimes used in this thesis.

Carbon nanotubes are one-dimensional nanostructures with outstanding physical, chemical and mechanical properties such as robustness and remarkable sensitiveness towards changes in their surroundings with suitable functionalization [61], even when being operated at room temperature. Since Sumio Iijima imaged carbon nanotubes in 1991 [56], many researchers demonstrated their outstanding properties by employing them in different applications. For instance, CNTs are used in batteries [62], supercapacitors [63], solar cells [64], automotive parts [65], water filters [66], sporting goods [67] and antifouling paints [68], among others. Recently, carbon nanotubes have been reported as good candidates to replace silicon in electronic devices [69], thanks to their nanoscale structure and relatively low cost in large scale production [70].

In 2000, Kong et al. [71] and Collins et al. [72] demonstrated that SWCNTs showed resistance changes under exposure to gases with extreme sensitivity, even at room temperature. However, it is required the heating of the chemical-sensitive surface to desorb previously adsorbed gas species and return it to initial conditions. Afterwards, the use of ultraviolet light to reach the large adsorption binding energies was shown to be an interesting alternative to the requirement of increasing the sensor temperature [73], allowing a faster baseline recovery with less aggressive treatment.

From about 20 years ago, many works also reported the use of CNTs as gas sensors, detecting a wide variety of gases such as $NO_2$ [74], $NH_3$ [75], $O_2$ [76], humidity [77], Volatile Organic Compounds (VOCs) [78] and chemical warfare agents [79]. Since pristine CNTs are quite inert and show a lack of specificity to target gases, there are several options to achieve the detection of gases at trace levels by further modification of CNTs. These physical or chemical alterations of CNTs can enhance sensing parameters such as sensitivity, the limit of detection (LOD) and selectivity. As a consequence, several strategies were defined, for instance, the decoration of CNTs with metal or metal oxide nanoparticles [80], their surface modification by grafting functional groups [81], the creation of hybrid nanocomposites with polymers [82] or zeolites [83], among others.

Metal oxides nanoclusters exhibit a broad range of electronic and physicochemical properties such as high catalytic activity, efficient charge transfer, robustness, ability to support high temperatures and high adsorption capacity [84]. For that reason, an easy and inexpensive strategy to improve some sensing parameters like sensitivity and selectivity is the decoration of CNTs with metal oxide nanoclusters. In this thesis we report for the first time the use of carbon nanotubes loaded with iridium oxide nanoparticles as gas sensors [80]. The synthesis of $IrO_x$ nanoparticles (NPs) was achieved following the method proposed by Zhao et al. [85], obtaining NPs with an ultra-small diameter (around 1 nm). This nanosize exhibits a high specific area, maximizing the effect of the nanoclusters. In other words, since the catalytic activity of $IrO_x$ had been demonstrated, this nanosize plays an essential role in the sensing mechanism (**Figure 7**). The effect of ambient moisture was also studied to apprehend better the mechanisms involved, especially because two oxidation states of iridium coexist ($IrO_2$ and $Ir_2O_3$).

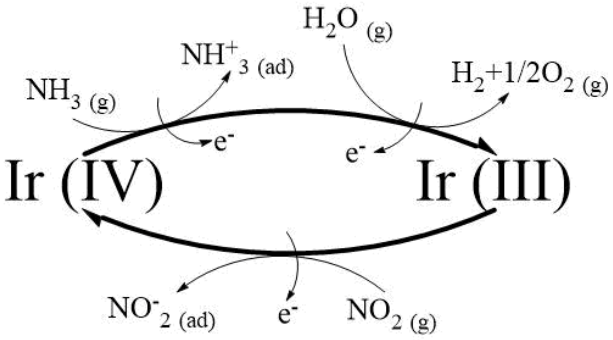


**Figure 7**. Gas sensing mechanism proposed for $IrO_x$ decorated CNTs.

In another work, we report a similar strategy to the $IrO_x$ NPs decoration of CNTs. In this case, the metal oxide nanoclusters that we used to load the carbon nanotubes were iron oxide ($Fe_2O_3$) NPs [86]. Despite the enhancement in some sensing parameters, the main objective of this work is exploring a new, inexpensive and straightforward method for the synthesis of NPs and the subsequent decoration of CNTs (**Figure 8**). Despite conventional CNT decoration techniques (e.g. sputtering) can achieve a homogeneous distribution and controlled particle size, they need expensive facilities. However, this work can offer a simple approach to decorating CNTs based on wet chemistry. We demonstrated that varying the type of solvent, the amount of iron salt or the calcination time, it is possible to modulate the morphology, decoration density and the nanocluster size of the $Fe_2O_3$ NPs. Additionally, a broad characterization using spectroscopic and microscopic techniques was performed. Gas sensing experiments reveal better sensitivities to both, benzene and $NO_2$, using the samples of CNTs decorated with metal oxides nanoclusters, indicating their essential role in the gas sensing mechanism.

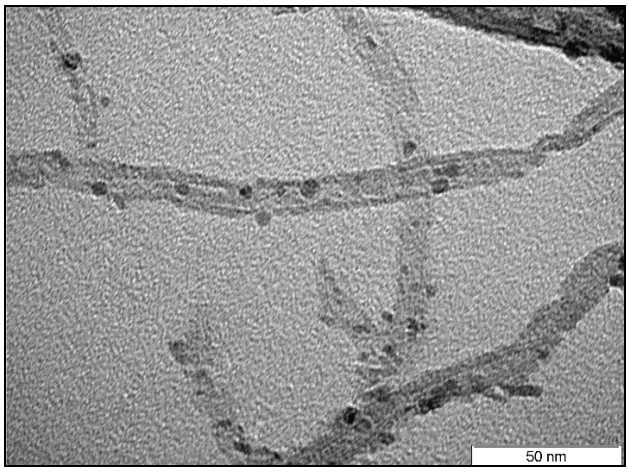


**Figure 8**. Example of the CNTs decoration obtained by using $Fe_2O_3$ NPs.

In a different work of this thesis, the gas sensing properties of MWCNTs functionalized with self-assembled monolayers (SAMs) of different mercaptans were studied [81]. **Figure 9** illustrates the approach developed, in which we employed oxygen-plasma treated MWCNTs, decorated afterwards with gold nanoparticles by sputtering technique. Finally, four different mercaptan SAMs were attached to study the hydrophilicity and carbon chain length effects on the gas sensing properties. **Figure 9** shows the carboxylic acids grafted to the outer walls of nanotubes due to the oxygen-plasma treatment. These oxygenated functional groups are mainly introduced in defect sites of CNTs and will help to anchor the gold NPs during the sputtering process, obtaining a high control in the decoration homogeneity and the size of gold NPs thanks to the avoidance of coalescence effects.

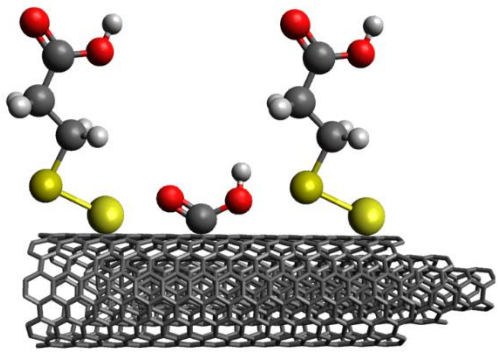

**Figure 9**. Illustration of the functionalized MWCNTs obtained. Atom representation: black = carbon; white = hydrogen; red = oxygen; light yellow = gold; dark yellow = sulphur.

Afterwards, the high affinity between gold and sulphur was taken in advantage to achieve the SAMs using four different thiols. The variation between the four thiols was based on two parameters, one was the different carbon chain length (3 vs 16 carbons), and the other was the head functional group that acted as a gas receptor. The difference in the exposed functional group is based in its hydrophilicity, resulting in two of them with a highly hydrophilic head (carboxyl, COOH) and two with a hydrophobic head (methyl, $CH_3$). **Figure 10** clarifies the structure of the thiols used.

The main objective of this work was to create a chemical-sensitive surface in which the CNTs acted as a support and charge transport transducing element while the functional head groups of SAMs acted as recognition elements of gases. This approach allows us to study the effect of the carbon chain length on the gas sensing performance, showing interesting

differences in the results depending on the use of short or long carbon chain, in our case, 3 and 16 carbons, respectively. Additionally, the nature of the head group had a crucial role in the detection of analytes, demonstrating that selectivity and sensitivity can be tuned based on the reactivity of functional groups. In consequence, this work offers a new approach to developing multisensor arrays capable of being selective and sensitive to different gases, from polar to non-polar species, even under fluctuating ambient moisture. Furthermore, a wide material characterization and detailed study of gas sensing mechanisms were reported in the manuscript.

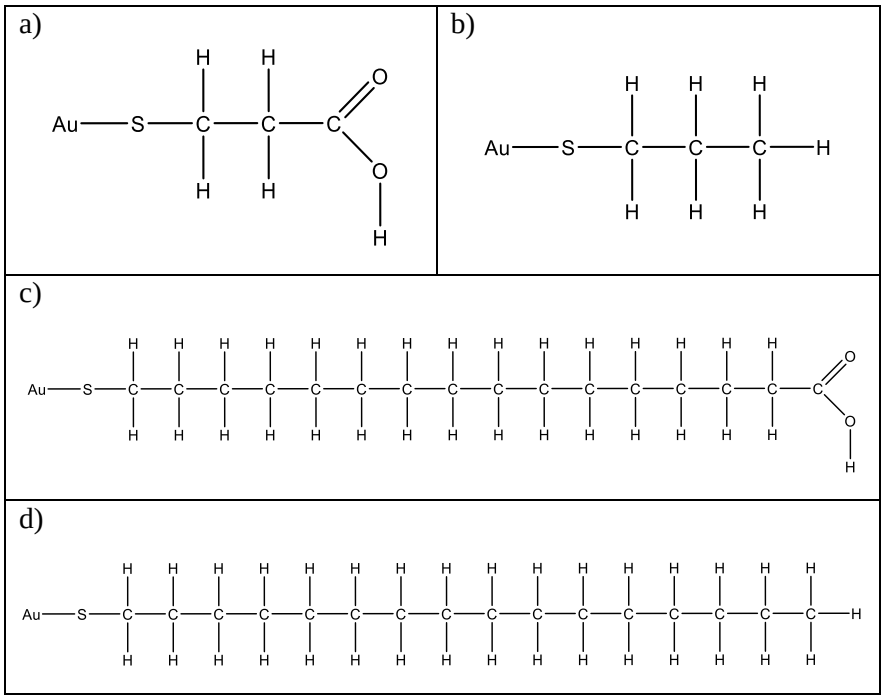


**Figure 10**. Chemical structure of the thiols $C_3H_6O_2S$ (a), $C_3H_8S$ (b), $C_{16}H_{32}O_2S$ (c) and $C_{16}H_{34}S$ (d), bonded to gold atoms.

A complementary work to the previous one was developed by using the 1-Hexadecanethiol functionalization [87]. The main goal was to analyse the suitability of methyl groups to detect non-polar gases such as benzene and toluene. SAMs were growth onto Au decorated graphene as well, detecting these two aromatic VOCs at ppm range. Also, the detection of polar gaseous species, such as methanol and acetone, were evaluated for comparison and better understanding of the mechanisms involved.

Another crucial parameter in gas sensing is the relative humidity influence, especially in the selectivity and sensitivity performance. Thus, the ambient moisture effect should be assessed for optimal environmental monitoring. In consequence, new work was focused on the fluorination of carbon nanotubes [88], in order to hinder the moisture interference, due to the highly hydrophobic character of the covalent C-F bond. Fluorination of CNTs surface was achieved by using $Ar:F_2$ and $CF_4$ plasma. This technology enables fast and reliable chemical functionalization. Even the surface functionalization can be performed after the integration of the CNTs in a device. Then, the electronic and chemical properties of fluorinated CNTs were studied. The gas sensing properties were focused on the surface hydrophobicity effect derived from the presence of fluorine in the CNTs surface (**Figure 11**). Additionally, the effect of the CNTs distribution was also studied. In this case, the sensitivity towards $NO_2$ and $NH_3$ was evaluated by using vertically aligned and randomly distributed CNTs. In summary, carbon nanotube geometry and humidity level influence were extensively studied in order to offer an

optimization towards one of the main problems often experienced with gas sensors, which is the compromised sensor response of carbon nanomaterials in an environment of variable ambient moisture.

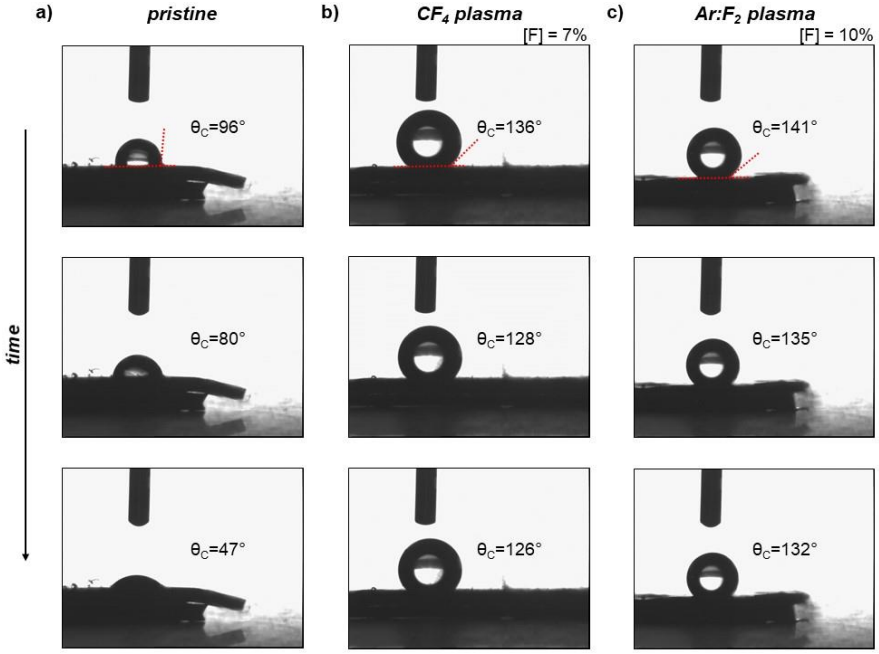


**Figure 11**. Contact angle measurements on bare and fluorinated CNTs. The presence of fluorine increases the surface hydrophobicity.

Once we have demonstrated that vertically-aligned carbon nanotubes (VA-CNTs) show enhanced gas sensing properties such as higher sensitivity and lower response/recovery times, we explored further the use of this geometry. For instance, we developed a new approach to functionalize VA-CNTs with oxygen functional groups employing a low kinetic energy ion irradiation [89]. This ion implantation technique is a non-destructive method to achieve CNTs functionalization with a high content of dopant species. Ion irradiation at low kinetic energies preserves the physical properties and the lattice of CNTs. Thus, oxygen functional groups such as epoxy, carbonyl and carboxyl groups were grafted to the CNTs surface, creating more specific interactions between the gas analytes and the chemical-sensitive film.

An exhaustive X-ray photoelectron spectroscopy (XPS) analysis revealed that the oxygen concentration and the relative abundance among the different oxygen groups grafted can be tuned, by varying the experimental conditions (**Figure 12**). Besides, scanning electron microscope images were obtained before and after the ion irradiation in order to confirm the preservation of the macroscopic structure and the alignment of CNTs. Thus, the highly functionalized VA-CNTs have been identified as a promising nanomaterial to be employed in gas sensing applications.

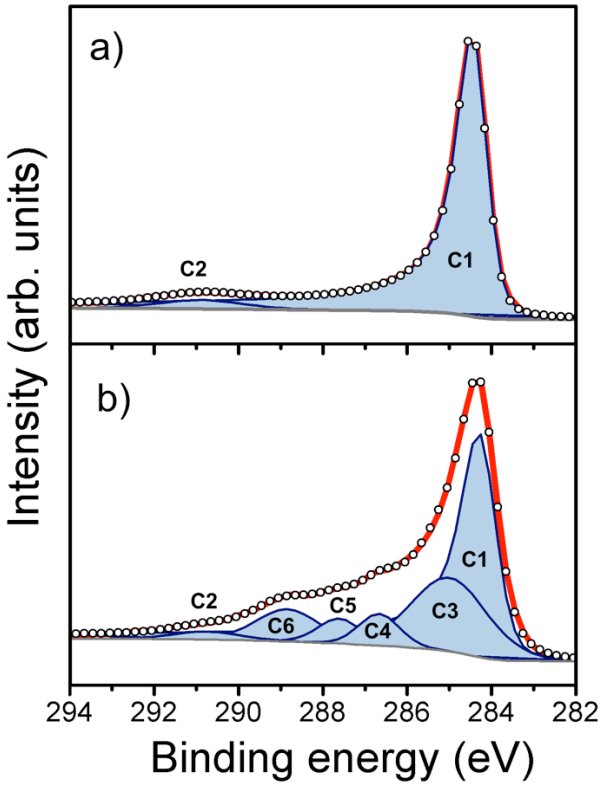


**Figure 12**. XPS analysis of pristine v-CNTs (a) and oxygen ion irradiated CNTs (b) during 10 min at low kinetic energy. C1 is assigned to $sp^2$-C (284.4 eV), C2 to π-plasmon excitations (290.9 eV), C3 to $sp^3$-C (285.0 eV), C4 to epoxy groups (286.6 eV), C5 to carbonyl groups (287.5 eV) and C6 to carboxyl groups (288.8 eV).

Finally, in a different work related to VA-CNTs, we modified nanotubes by forming a film of hexagonally-shaped nanoplates (HNPs) of molybdenum disulphide ($MoS_2$) at their top end [90]. Both nanomaterials, VA-CNTs and $MoS_2$ film were produced by CVD technique, obtaining highly crystalline nanomaterials (**Figure 13**). The particularity of this work is derived from the fact that hexagonally-shaped nanoplates were obtained, entailing a high number of edges exposed to the gas molecules. In consequence, these nanostructures show a high potential to enhance the sensitivity to target gases, and open new possibilities to be employed in other applications such as catalysis.

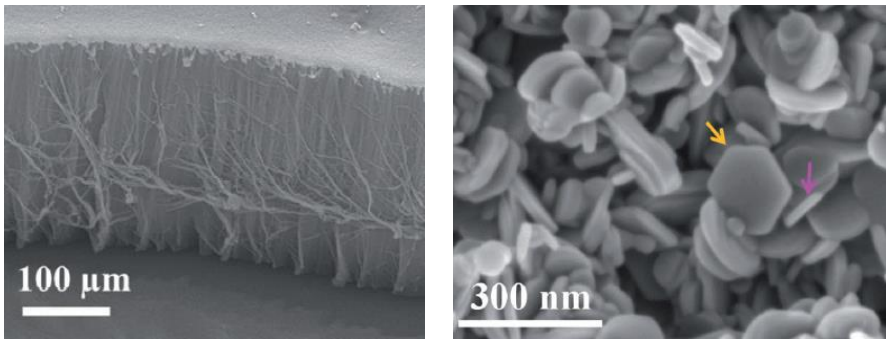


**Figure 13**. SEM images of VA-CNTs with $MoS_2$ film on top (a), and hexagonal-shaped nanoplates of $MoS_2$ obtained by CVD.

## 1.6. Graphene

Graphene consists of a two-dimensional nanomaterial, arranged in a sheet of carbon atoms disposed in a hexagonal lattice. When different sheets are stacked, we are talking about graphite. The structure of pristine graphene is composed by $sp^2$ hybridizations, which means the combination of one s-orbital with only two p-orbitals [91]. Even though crystalline (pristine) graphene can be considered as a zero bandgap (metallic) material [92], the graphene used to behave as a mild p-type semiconductor due to the presence of impurities or defects derived from the synthesis process or post-treatment steps (e.g. ultrasonic bath). In consequence, some defects are created, or some oxygenated or nitrogenated groups are grafted on the surface, inducing p-type doping [93].

Graphene is a promising nanomaterial to be employed in the next generation of electronic devices due to its compatibility with microelectronic technologies such as photolithography. In fact, 2D graphene shows ideally the highest surface area to volume ratio, and superior properties such as low noise levels, and high carrier density and mobility [94]. Besides, it is possible to obtain pristine graphene with a practically defect-free structure, resulting in a low level of 1/f noise caused by their thermal switching [95].

Several routes for graphene synthesis have been developed to both, top-down and bottom-up approaches [96]. The most representative top-down synthesis techniques are mechanical and chemical exfoliation (or cleaving) from graphite material. As remarkable bottom-up approaches, the main ones are CVD and epitaxial growth. This variety of techniques allows obtaining graphene with different qualities and synthesis costs. The mechanical cleaving involves repeated peeling of graphite using adhesive tape, obtaining isolated single layers. This is a straightforward method, however it is not scalable and requires labour-intensive. Regarding to chemical exfoliation of graphite, this method uses strongly acidic solutions to introduce oxygen-containing moieties into graphene sheets, resulting in graphene oxide [97]. Due to the hydrophilic properties of graphene oxide, it can be easily dispersed into an aqueous solution and separated into individual sheets for further processing. Then, graphene oxide can be reduced by chemical or thermal processes, in order to reduce as maximum as possible the presence of oxygen functional groups. With that, the objective is restoring the original properties of graphene, however, reduced graphene oxide usually contains significant amounts of oxygen moieties and defects [98]. Shifting to the bottom-up approaches, the chemical vapour deposition consists of the growth of graphene on metal substrates (e.g. nickel or copper) by using hydrocarbon vapours at high temperature (700-1000˚C). This CVD method can produce large areas of graphene with high-quality, which can then be transferred to other substrates [99]. The growth of graphene by CVD still present some challenges, such as control of the number of layers grown and the contamination avoiding from the metallic substrate. Regarding to the epitaxial growth of graphene, it can be achieved by heating hexagonal silicon carbide crystals to temperatures higher than 1200˚C. Then, the silicon is evaporated and results in the formation of graphene on the basal planes [100]. Although this method produces large areas of graphene layers, the electronic properties can be easily disturbed by disorders introduced by the substrate used [101].

Thus, apart from the superior properties of graphene to be employed in nanotechnology, it can be used in many applications depending on the ratio price/cost needed. For instance, graphene was successfully employed in gas separation and storage (e.g. $CO_2$ and $H_2$), seawater desalination or wastewater treatments. However, more efforts are needed to explore the

graphene potential in battery applications, commercial gas sensors or food processing. Graphene also shows a promising potential to be employed in commercial gas sensors. Developing devices with single layers of graphene, which is a strictly two-dimensional, all the atoms will be exposed to the environment. Additionally, this carbon nanomaterial shows a low Johnson noise, even in the limit of full depletion. Thus, few electrons can produce significant relative changes in the carrier concentration.

Novoselov's group demonstrated for the first time, the use of graphene in gas sensing [102]. Even though pristine graphene was extensively used as a gas sensor, intrinsic problems such as low sensitivity and complicated processability into devices are still present [103]. For that reason, many alternatives have been studied to enhance the sensing properties. The simplest way is the oxidizing treatment of pristine graphene, obtaining graphene oxide (GO), which eases its suspension in aqueous solutions. Sometimes, this oxidizing treatment is followed by a reducing treatment, obtaining reduced graphene oxide (rGO), with different electronic and chemical properties to its precursor. Thus, many works report the use of GO and rGO as gas sensitive materials [104]. However, similarly to carbon nanotubes, some alternatives have been developed to go further by decorating graphene with metal or metal oxide nanoparticles [105], grafting functional groups [106] and organic molecules [107], or creating hybrids/composites with polymers [108], among others. For that reason, graphene-based gas sensors have been widely employed as humidity sensors [109] and also were used to detect harmful pollutants such as VOCs [110], $NO_2$ [111], $NH_3$ [112], even explosives [106] and warfare agents [113], among others.

For gas sensing applications, it is well-know the low reactivity and small charge transfer between graphene and gas molecules when they are operated at room temperature [104]. For that reason, we developed a novel approach by loading, for the first time, graphene with perovskite nanocrystals (NCs) [33]. In our case, we used lead halide perovskite ($CH_3NH_3PbBr_3$) NCs, with an average size of 7.1 ± 2.2 nm. Perovskite crystal structure is derived from $ABX_3$, where A is the cation (for us the methylammonium) and occupies the centre of the unit cell. Moreover, B cation (in our case Pb) and X anion (for us $Br_3$) are arranged at the corners and the edges of the unit cell, respectively (**Figure 14**).

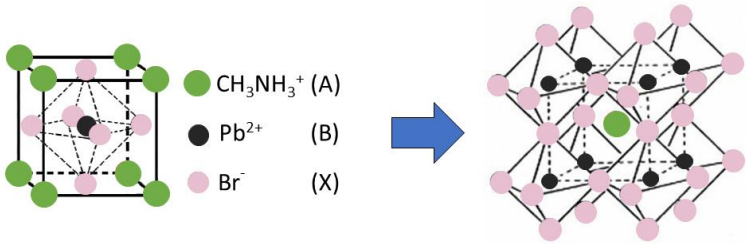


**Figure 14**. Lead halide perovskite ($CH_3NH_3PbBr_3$) unit cell.

Lead halide perovskites are chemical sensitive nanocrystals with ambipolar charge carriers, creating a high concentration of electron-hole pairs [114]. These properties make them ideal candidates to be employed in gas sensors. Although some works report the use of perovskite films as gas sensors [115,116], the main drawback of perovskites is still unsolved. This problem is attributed to its hygroscopic properties, resulting in a fast degradation in the presence of humidity [117].

For that reason, in this work, we tried to use for the first time a stable sensor using perovskites. To demonstrate that, we blocked the perovskite degradation taking advantage of

the protective character of graphene, resulting from its strong hydrophobicity. Then, we have developed a new chemical-sensitive film based on graphene decorated with perovskite NCs for enhanced gas sensing (**Figure 15**) in comparison to bare graphene.

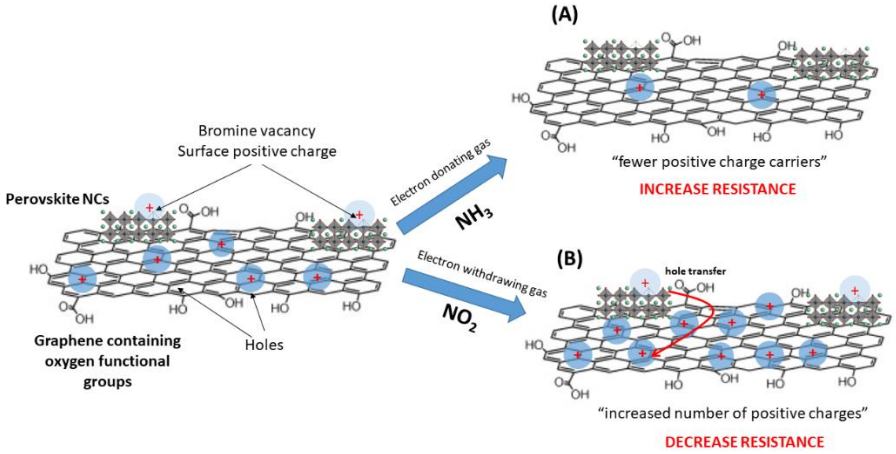


**Figure 15.** Gas sensing mechanism proposed during the exposure to and electron-donating gas (a) and electron-withdrawing (b).

Despite the high potential of graphene to be employed in the next generation of gas sensors, few commercial products are available in the market. The reason is associated with the high economic cost and challenging approach for mass-production of devices with single or few-layer graphene. In other words, the superior electrical, mechanical and physicochemical properties of graphene are not fully exploited with bulky or 3D graphene films.

For that reason, we developed a new approach to growth a wafer-scale (around 50 $cm^2$) of highly crystalline few-layer graphene (FLG) [118]. Then, the FLG was transferred to a substrate composed of an array of silicon nanopillars patterned using lithography (**Figure 16**).

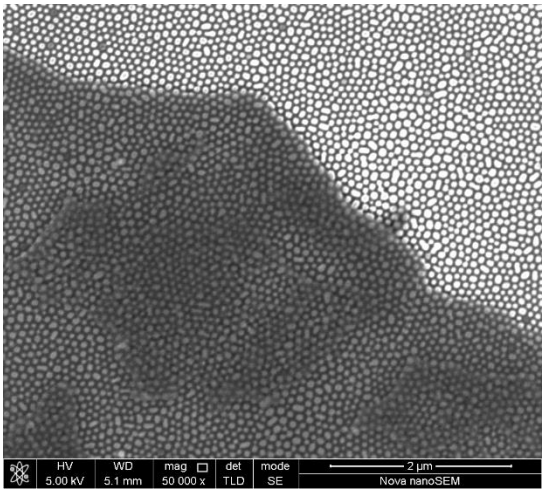


**Figure 16.** High-resolution Scanning Electron Microscope (SEM) around the graphene edge. FLG (darker region) is deposited over the silicon nanopillars arrays (dots across the image). [Note that brighter region in the image has no graphene].

Additionally, unprecedented sensitivity could be achieved with these "suspended" graphene. Also, high reproducibility and stability was observed. The reason is probably the unique configuration used, in which the Si nanopillar arrays provide and access to the backside of the FLG surface. As a consequence, the active surface area available is almost doubled in comparison to flat substrates.

## 1.7. Diamondoids

Carbon-based gas sensor research had been mainly focused on $sp^2$-hybridized structures, such as carbon nanotubes and graphene [11]. However, there is a group of $sp^3$-hybridized carbon semiconductors (**Figure 17**) that have not experienced remarkable attention: pristine nanodiamonds. These diamond nanoparticles are so-called diamondoids, which essentially are $sp^3$-hybridized diamond-like hydrocarbons (hydrogen-terminated) [119]. Diamondoids present carbon atoms bonded in a tetrahedral lattice arrangement with superior properties, such as extraordinarily mechanical and thermodynamic stability [120]. Besides, diamondoids present quantum confinement and tuneable bandgap [121,122], showing a high potential to be employed in the next generation of gas sensors.

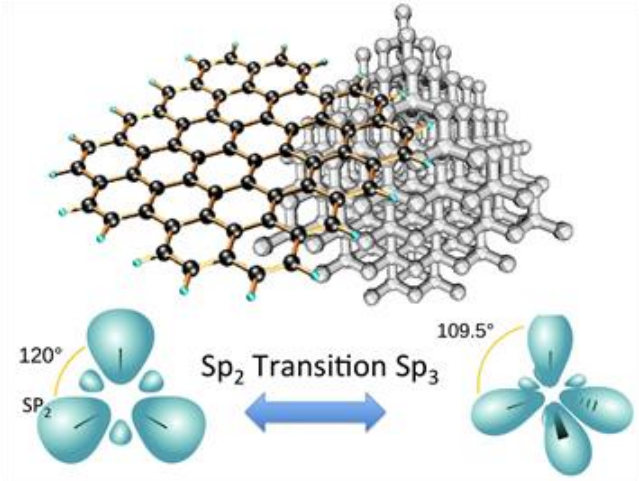


**Figure 17**. Graphite $sp^2$ hybridization on the left side and diamond $sp^3$ hybridization on the right side. Reproduced from [123].

Diamondoids were previously used in biomedical applications, catalysis, polymer materials upgrading, pharmacology and as a 3D building blocks for engineering new materials [119]. Regarding their application for gas sensing, some works report the use of diamonds with much larger sizes [124], $sp^2$-C hybridizations [125] and modified with other materials like Zn nanorods [126]. However, in all these cases, the detection limits obtained were above the TLV, blocking their implementation in real conditions.

Thus, we report the first use of $sp^3$-C-based diamondoids as gas sensors [20] with the capability to detect pollutant concentrations below the TLV. To do that, we coated by CVD $sp^3$-C diamondoids with thin nanolayers of transition metals (**Figure 18**). In particular, from diamantine were synthesized the primary phosphine ($H_2$P-DiamOH, 1) and its oxide ($H_2$(O)P-DiamOH, 2). Additionally, these diamondoids were coated with a thin layer of palladium, obtaining Pd@$H_2$P-DiamOH (3) and Pd@$H_2$(O)P-DiamOH (4).

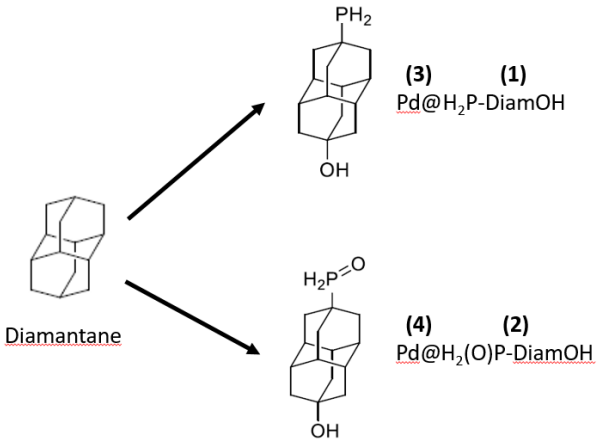


**Figure 18**. Scheme of the four diamondoids derivatives tested as gas sensors. Modified from [20].

Brunauer-Emmett-Teller (BET) surface measurements reveal a remarkably high surface area (up to 140 $m^2/g$) due to a high concentration of channel nanoporosities. These voids are derived from the H-bonding in solid-state; consequently, a high surface is available to interact with gases. Thus, nitrogen dioxide detection at trace levels was conducted with the diamondoids synthesized, demonstrating the capability of these $sp^3$-C nanostructures to be employed in new gas sensors.

## 1.8. References

1. World Health Organization (WHO).

2. Garg, A.; Akbar, M.; Vejerano, E.; Narayanan, S.; Nazhandali, L.; Marr, L.C.; Agah, M. Zebra GC: A mini gas chromatography system for trace-level determination of hazardous air pollutants. *Sensors Actuators, B Chem.* **2015**, *212*, 145–154.

3. Haus, R.; Schäfer, K.; Bautzer, W.; Heland, J.; Mosebach, H.; Bittner, H.; Eisenmann, T. Mobile Fourier-transform infrared spectroscopy monitoring of air pollution. *Appl. Opt.* **1994**, *33*, 5682.

4. Akbar, M.; Restaino, M.; Agah, M. Chip-scale gas chromatography: From injection through detection. *Microsystems Nanoeng.* **2015**, *1*.

5. Hodgkinson, J.; Tatam, R.P. Optical gas sensing: A review. *Meas. Sci. Technol.* 2013, *24*.

6. Viespe, C.; Miu, D. Characteristics of surface acoustic wave sensors with nanoparticles embedded in polymer sensitive layers for VOC detection. *Sensors (Switzerland)* **2018**, *18*.

7. Alassi, A.; Benammar, M.; Brett, D. Quartz crystal microbalance electronic interfacing systems: A review. *Sensors* 2017, *17*.

8. Mujahid, A.; Dickert, F.L. Surface Acoustic Wave (SAW) for Chemical Sensing Applications of Recognition Layers. *Sensors* **2017**, *17*, 2716.

9. Yunusa, Z.; Hamidon, M.N.; Kaiser, A.; Awang, Z. Gas Sensors: A Review. *Sensors & Transducers* **2014**, *168*, 61–75.

10. Khan, M.A.H.; Rao, M. V.; Li, Q. Recent advances in electrochemical sensors for detecting toxic gases: NO2, SO2 and H2S. *Sensors (Switzerland)* 2019, *19*.

11. Schroeder, V.; Savagatrup, S.; He, M.; Lin, S.; Swager, T.M. Carbon nanotube chemical sensors. *Chem. Rev.* **2019**, *119*, 599–663.

12. Shendage, S.S.; Patil, V.L.; Vanalakar, S.A.; Patil, S.P.; Harale, N.S.; Bhosale, J.L.; Kim, J.H.; Patil, P.S. Sensitive and selective NO2 gas sensor based on WO3 nanoplates. *Sensors Actuators, B Chem.* **2017**, *240*, 426–433.

13. Gao, L.; Cheng, Z.; Xiang, Q.; Zhang, Y.; Xu, J. Porous corundum-type In2O3 nanosheets: Synthesis and NO2 sensing properties. *Sensors Actuators, B Chem.* **2015**, *208*, 436–443.

14. Li, T.; Zeng, W.; Long, H.; Wang, Z. Nanosheet-assembled hierarchical SnO2 nanostructures for efficient gas-sensing applications. *Sensors Actuators, B Chem.* **2016**, *231*, 120–128.

15. Wang, J.X.; Sun, X.W.; Yang, Y.; Huang, H.; Lee, Y.C.; Tan, O.K.; Vayssieres, L. Hydrothermally grown oriented ZnO nanorod arrays for gas sensing applications. *Nanotechnology* **2006**, *17*, 4995–4998.

16. Dey, A. Semiconductor metal oxide gas sensors: A review. *Mater. Sci. Eng. B Solid-State Mater. Adv. Technol.* 2018, *229*, 206–217.

17. Lahlalia, A.; Le Neel, O.; Shankar, R.; Selberherr, S.; Filipovic, L. Improved Sensing Capability of Integrated Semiconducting Metal Oxide Gas Sensor Devices. *Sensors* **2019**, *19*.

18. Wang, C.; Yin, L.; Zhang, L.; Xiang, D.; Gao, R. Metal oxide gas sensors: Sensitivity and influencing factors. *Sensors* 2010, *10*, 2088–2106.

19. Llobet, E. Gas sensors using carbon nanomaterials: A review. *Sensors Actuators B Chem.* **2013**, *179*, 32–45.

20. Moncea, O.; Casanova-Chafer, J.; Poinsot, D.; Ochmann, L.; Mboyi, C.D.; Nasrallah, H.O.; Llobet, E.; Makni, I.; El Atrous, M.; Brandès, S.; et al. Diamondoid Nanostructures as sp3-Carbon-Based Gas Sensors. *Angew. Chemie - Int. Ed.* **2019**, *58*, 9933–9938.

21. Park, M.; Shim, S.H.; Jeong, S.H.; Oh, K.J.; Lee, S.S. Nitrogen oxides emissions from the MILD combustion with the conditions of recirculation gas. *J. Air Waste Manag. Assoc.* **2017**, *67*, 402–411.

22. Latza, U.; Gerdes, S.; Baur, X. Effects of nitrogen dioxide on human health: Systematic review of experimental and epidemiological studies conducted between 2002 and 2006. *Int. J. Hyg. Environ. Health* **2009**, *212*, 271–287.

23. Kampa, M.; Castanas, E. Human health effects of air pollution. *Environ. Pollut.* **2008**, *151*, 362–367.

24. Frank, U.; Ernst, D. Effects of NO2 and Ozone on Pollen Allergenicity. *Front. Plant Sci.* **2016**, *7*, 91.

25. McCubbin, D.R.; Apelberg, B.J.; Roe, S.; Divita, F. Livestock ammonia management and particulate-related health benefits. *Environ. Sci. Technol.* **2002**, *36*, 1141–1146.

26. Suarez-Bertoa, R.; Mendoza-Villafuerte, P.; Riccobono, F.; Vojtisek, M.; Pechout, M.; Perujo, A.; Astorga, C. On-road measurement of NH3 emissions from gasoline and diesel passenger cars during real world driving conditions. *Atmos. Environ.* **2017**, *166*, 488–497.

27. Borsari, V.; Assunção, J.V. de Ammonia emissions from a light-duty vehicle. *Transp. Res. Part D Transp. Environ.* **2017**, *51*, 53–61.

28. Suarez-Bertoa, R.; Zardini, A.A.; Astorga, C. Ammonia exhaust emissions from spark ignition vehicles over the New European Driving Cycle. *Atmos. Environ.* **2014**, *97*, 43–53.

29. Weisenburger, D.D. Human health effects of agrichemical use. *Hum. Pathol.* **1993**, *24*, 571–576.

30. Stokstad, E. Ammonia pollution from farming may exact hefty health costs. *Sci.* **2014**, *343*, 238.

31. Sundblad, B.-M.; Larsson, B.-M.; Acevedo, F.; Ernstgård, L.; Johanson, G.; Larsson, K.; Palmberg, L. Acute respiratory effects of exposure to ammonia on healthy subjects. *Scand. J. Work. Environ. Health* **2004**, *30*, 313–321.

32. Agency for Toxic Substances and Disease Registry (ATSDR) https://www.atsdr.cdc.gov/mmg/mmg.asp?id=7&tid=2.

33. Casanova-Cháfer, J.; García-Aboal, R.; Atienzar, P.; Llobet, E. Gas Sensing Properties of Perovskite Decorated Graphene at Room Temperature. *Sensors* **2019**, *19*, 4563.

34. Pearce, R.; Iakimov, T.; Andersson, M.; Hultman, L.; Spetz, A.L.; Yakimova, R. Epitaxially grown graphene based gas sensors for ultra sensitive NO2 detection. *Sensors Actuators B Chem.* **2011**, *155*, 451–455.

35. Kanoun, O.; Müller, C.; Benchirouf, A.; Sanli, A.; Bouhamed, A.; Al-Hamry, A.; Bu, L. Potential of Flexible Carbon Nanotube Films for High Performance Strain and Pressure Sensors. In *Nanotechnology for optics and sensors*; 2014; pp. 148–183.

36. Liu, M. Coating Technology of Nuclear Fuel Kernels: A Multiscale View. In *Modern Surface Engineering Treatments*; InTech, 2013.

37. International Carbon Black Association (ICBA) Available online: http://www.carbon-black.org/.

38. Arshak, K.; Moore, E.; Lyons, G.M.; Harris, J.; Clifford, S. A review of gas sensors employed in electronic nose applications. *Sens. Rev.* 2004, *24*, 181–198.

39. Lundberg, B.; Sundqvist, B. Resistivity of a composite conducting polymer as a function of temperature, pressure, and environment: Applications as a pressure and gas concentration transducer. *J. Appl. Phys.* **1986**, *60*, 1074–1079.

40. Doleman, B.J.; Lonergan, M.C.; Severin, E.J.; Vaid, T.P.; Lewis, N.S. Quantitative Study of the Resolving Power of Arrays of Carbon Black-Polymer Composites in Various Vapor-Sensing Tasks. *Anal. Chem.* **1998**, *70*, 4177–4190.

41. Lonergan, M.C.; Severin, E.J.; Doleman, B.J.; Beaber, S.A.; Grubbs, R.H.; Lewis, N.S. Array-Based Vapor Sensing Using Chemically Sensitive, Carbon Black−Polymer Resistors. *Chem. Mater.* **1996**, *8*, 2298–2312.

42. Albert, K.J.; Lewis, N.S.; Schauer, C.L.; Sotzing, G.A.; Stitzel, S.E.; Vaid, T.P.; Walt, D.R. Cross-Reactive Chemical Sensor Arrays. *Chem. Rev.* **2000**, *100*, 2595–2626.

43. Tibbetts, G.G. Carbon fibers produced by pyrolysis of natural gas in stainless steel tubes. *Appl. Phys. Lett.* **1983**, *42*, 666–668.

44. Oberlin, A.; Endo, M.; Koyama, T. Filamentous growth of carbon through benzene decomposition. *J. Cryst. Growth* **1976**, *32*, 335–349.

45. Kim, C.; Jeong, Y. Il; Ngoc, B.T.N.; Yang, K.S.; Kojima, M.; Kim, Y.A.; Endo, M.; Lee, J.-W. Synthesis and Characterization of Porous Carbon Nanofibers with Hollow Cores Through the Thermal Treatment of Electrospun Copolymeric Nanofiber Webs. *Small* **2007**, *3*, 91–95.

46. Bazilevsky, A. V.; Yarin, A.L.; Megaridis, C.M. Co-electrospinning of Core−Shell Fibers Using a Single-Nozzle Technique. *Langmuir* **2007**, *23*, 2311–2314.

47. Xu, X.; Zhuang, X.; Chen, X.; Wang, X.; Yang, L.; Jing, X. Preparation of Core-Sheath Composite Nanofibers by Emulsion Electrospinning. *Macromol. Rapid Commun.* **2006**, *27*, 1637–1642.

48. Periyakaruppan, A.; Gandhiraman, R.P.; Meyyappan, M.; Koehne, J.E. Label-Free Detection of Cardiac Troponin-I Using Carbon Nanofiber Based Nanoelectrode Arrays. *Anal. Chem.* **2013**, *85*, 3858–3863.

49. Zhang, B.; Fu, R.; Zhang, M.; Dong, X.; Wang, L.; Pittman, C.U. Gas sensitive vapor grown carbon nanofiber/polystyrene sensors. *Mater. Res. Bull.* **2006**, *41*, 553–562.

50. Im, J.S.; Kang, S.C.; Lee, S.H.; Lee, Y.S. Improved gas sensing of electrospun carbon fibers based on pore structure, conductivity and surface modification. *Carbon N. Y.* **2010**, *48*, 2573–2581.

51. Lee, J.S.; Kwon, O.S.; Park, S.J.; Park, E.Y.; You, S.A.; Yoon, H.; Jang, J. Fabrication of Ultrafine Metal-Oxide-Decorated Carbon Nanofibers for DMMP Sensor Application. *ACS Nano* **2011**, *5*, 7992–8001.

52. Lee, J.S.; Kwon, O.S.; Shin, D.H.; Jang, J. WO3 nanonodule-decorated hybrid carbon nanofibers for NO 2 gas sensor application. *J. Mater. Chem. A* **2013**, *1*, 9099–9106.

53. Prasek, J.; Drbohlavova, J.; Chomoucka, J.; Hubalek, J.; Jasek, O.; Adam, V.; Kizek, R. Methods for carbon nanotubes synthesis—review. *J. Mater. Chem.* **2011**, *21*, 15872.

54. Umeno, Y.; Kitamura, T.; Kushima, A. Metallic–semiconducting transition of single-walled carbon nanotubes under high axial strain. *Comput. Mater. Sci.* **2004**, *31*, 33–41.

55. Capaz, R.B.; Spataru, C.D.; Tangney, P.; Cohen, M.L.; Louie, S.G. Temperature dependence of the band gap of semiconducting carbon nanotubes. *Phys. Rev. Lett.* **2005**, *94*, 036801.

56. Iijima, S. Helical microtubules of graphitic carbon. *Nature* **1991**, *354*, 56–58.

57. Guo, T.; Nikolaev, P.; Rinzler, A.G.; Tomanek, D.; Colbert, D.T.; Smalley, R.E. Self-Assembly of Tubular Fullerenes. *J. Phys. Chem.* **1995**, *99*, 10694–10697.

58. Guo, T.; Nikolaev, P.; Thess, A.; Colbert, D.T.; Smalley, R.E. Catalytic growth of single-walled manotubes by laser vaporization. *Chem. Phys. Lett.* **1995**, *243*, 49–54.

59. José-Yacamán, M.; Miki-Yoshida, M.; Rendón, L. Catalytic growth of carbon microtubules with fullerene structure. *Appl. Phys. Lett.* **1993**, *62*, 202.

60. Ishigami, N.; Ago, H.; Imamoto, K.; Tsuji, M.; Iakoubovskii, K.; Minami, N. Crystal Plane Dependent Growth of Aligned Single-Walled Carbon Nanotubes on Sapphire. *J. Am. Chem. Soc.* **2008**, *130*, 9918–9924.

61. Rein, M.D.; Breuer, O.; Wagner, H.D. Sensors and sensitivity: Carbon nanotube buckypaper films as strain sensing devices. *Compos. Sci. Technol.* **2011**, *71*, 373–381.

62. Lee, S.W.; Yabuuchi, N.; Gallant, B.M.; Chen, S.; Kim, B.-S.; Hammond, P.T.; Shao-Horn, Y. High-power lithium batteries from functionalized carbon-nanotube electrodes. *Nat. Nanotechnol.* **2010**, *5*, 531–537.

63. Frackowiak, E. Carbon materials for supercapacitor application. *Phys. Chem. Chem. Phys.* **2007**, *9*, 1774.

64. Lee, J.M.; Park, J.S.; Lee, S.H.; Kim, H.; Yoo, S.; Kim, S.O. Selective Electron- or Hole-Transport Enhancement in Bulk-Heterojunction Organic Solar Cells with N- or B-Doped Carbon Nanotubes. *Adv. Mater.* **2011**, *23*, 629–633.

65. Esawi, A.M.K.; El Borady, M.A. Carbon nanotube-reinforced aluminium strips. *Compos. Sci. Technol.* **2008**, *68*, 486–492.

66. Ihsanullah Carbon nanotube membranes for water purification: Developments, challenges, and prospects for the future. *Sep. Purif. Technol.* **2019**, *209*, 307–337.

67. Suhr, J.; Koratkar, N.; Keblinski, P.; Ajayan, P. Viscoelasticity in carbon nanotube composites. *Nat. Mater.* **2005**, *4*, 134–137.

68. Beigbeder, A.; Degee, P.; Conlan, S.L.; Mutton, R.J.; Clare, A.S.; Pettitt, M.E.; Callow, M.E.; Callow, J.A.; Dubois, P. Preparation and characterisation of silicone-based coatings filled with carbon nanotubes and natural sepiolite and their application as marine fouling-release coatings. *Biofouling* **2008**, *24*, 291–302.

69. Hills, G.; Lau, C.; Wright, A.; Fuller, S.; Bishop, M.D.; Srimani, T.; Kanhaiya, P.; Ho, R.; Amer, A.; Stein, Y.; et al. Modern microprocessor built from complementary carbon nanotube transistors. *Nature* **2019**, *572*, 595–602.

70. Li, W.Z.; Xie, S.S.; Qian, L.X.; Chang, B.H.; Zou, B.S.; Zhou, W.Y.; Zhao, R.A.; Wang, G. Large-Scale Synthesis of Aligned Carbon Nanotubes. *Science (80-. ).* **1996**, *274*, 1701–1703.

71. Kong, J.; Franklin, N.R.; Zhou, C.; Chapline, M.G.; Peng, S.; Cho, K.; Dai, H. Nanotube molecular wires as chemical sensors. *Science (80-. ).* **2000**, *287*, 622–625.

72. Collins, P.G.; Bradley, K.; Ishigami, M.; Zettl, A. Extreme oxygen sensitivity of electronic properties of carbon nanotubes. *Science (80-. ).* **2000**, *287*, 1801–1804.

73. Chen, G.; Paronyan, T.M.; Pigos, E.M.; Harutyunyan, A.R. Enhanced gas sensing in pristine carbon nanotubes under continuous ultraviolet light illumination. *Sci. Rep.* **2012**, *2*.

74. Sayago, I.; Santos, H.; Horrillo, M.C.; Aleixandre, M.; Fernández, M.J.; Terrado, E.; Tacchini, I.; Aroz, R.; Maser, W.K.; Benito, A.M.; et al. Carbon nanotube networks as gas sensors for NO2 detection. *Talanta* **2008**, *77*, 758–764.

75. Panes-Ruiz, L.A.; Shaygan, M.; Fu, Y.; Liu, Y.; Khavrus, V.; Oswald, S.; Gemming, T.; Baraban, L.; Bezugly, V.; Cuniberti, G. Toward Highly Sensitive and Energy Efficient Ammonia Gas Detection with Modified Single-Walled Carbon Nanotubes at Room Temperature. *ACS Sensors* **2018**, *3*, 79–86.

76. Rajavel, K.; Lalitha, M.; Radhakrishnan, J.K.; Senthilkumar, L.; Rajendra Kumar, R.T. Multiwalled Carbon Nanotube Oxygen Sensor: Enhanced Oxygen Sensitivity at Room Temperature and Mechanism of Sensing. *ACS Appl. Mater. Interfaces* **2015**, *7*, 23857–23865.

77. Han, J.W.; Kim, B.; Li, J.; Meyyappan, M. Carbon nanotube based humidity sensor on cellulose paper. *J. Phys. Chem. C* **2012**, *116*, 22094–22097.

78. Thamri, A.; Baccar, H.; Struzzi, C.; Bittencourt, C.; Abdelghani, A.; Llobet, E. MHDA-functionalized multiwall carbon nanotubes for detecting non-aromatic VOCs. *Sci. Rep.* **2016**, *6*.

79. Fennell, J.F.; Hamaguchi, H.; Yoon, B.; Swager, T.M. Chemiresistor Devices for Chemical Warfare Agent Detection Based on Polymer Wrapped Single-Walled Carbon Nanotubes. *Sensors (Basel).* **2017**, *17*.

80. Casanova-Cháfer, J.; Navarrete, E.; Noirfalise, X.; Umek, P.; Bittencourt, C.; Llobet, E. Gas Sensing with Iridium Oxide Nanoparticle Decorated Carbon Nanotubes. *Sensors* **2019**, *19*, 113.

81. Casanova-Cháfer, J.; Bittencourt, C.; Llobet, E. Hydrophilicity and carbon chain length effects on the gas sensing properties of chemoresistive, self-assembled monolayer carbon nanotube sensors. *Beilstein J. Nanotechnol.* **2019**, *10*, 565–577.

82. Chiou, J.C.; Wu, C.C.; Lin, T.M. Sensitivity enhancement of acetone gas sensor using polyethylene glycol/multi-walled carbon nanotubes composite sensing film with thermal treatment. *Polymers (Basel).* **2019**, *11*.

83. Evans, G.P.; Buckley, D.J.; Adedigba, A.L.; Sankar, G.; Skipper, N.T.; Parkin, I.P. Controlling the Cross-Sensitivity of Carbon Nanotube-Based Gas Sensors to Water Using Zeolites. *ACS Appl. Mater. Interfaces* **2016**, *8*, 28096–28104.

84. Kharisov, B.I.; Kharissova, O. V.; Ortiz Méndez, U.; De La Fuente, I.G. Decoration of Carbon Nanotubes With Metal Nanoparticles: Recent Trends. *Synth. React. Inorganic, Met. Nano-Metal Chem.* **2016**, *46*, 55–76.

85. Zhao, Y.; Hernandez-Pagan, E.A.; Vargas-Barbosa, N.M.; Dysart, J.L.; Mallouk, T.E. A High Yield Synthesis of Ligand-Free Iridium Oxide Nanoparticles with High Electrocatalytic Activity. *J. Phys. Chem. Lett.* **2011**, *2*, 402–406.

86. Elnabawy, H.M.; Casanova-Chafer, J.; Anis, B.; Fedawy, M.; Scardamaglia, M.; Bittencourt, C.; Khalil, A.S.G.; Llobet, E.; Vilanova, X. Wet chemistry route for the decoration of carbon nanotubes with iron oxide nanoparticles for gas sensing. *Beilstein J. Nanotechnol.* **2019**, *10*, 105–118.

87. Bohli, N.; Belkilani, M.; Behi, S.; Casanova-Chafer, J.; Llobet, E.; Abdelghani, A. Multiwalled carbon nanotubes based aromatic VOCs sensor: sensitivity enhancement through 1-Hexadecanethiol functionalization. *Beilstein J. Nanotechnol.* **2019**.

88. Struzzi, C.; Scardamaglia, M.; Casanova-Chafer, J.; Calavia, R.; Colomer, J.-F.; Kondyurin, A.; Bilek, M.; Britun, N.; Snyders, R.; Llobet, E.; et al. Exploiting sensor geometry for enhanced gas sensing properties of fluorinated carbon nanotubes under humid environment. *Sensors Actuators B Chem.* **2019**, *281*, 945–952.

89. Acosta, S.; Casanova-Chafer, J.; Sierra-Castillo, A.; Llobet, E.; Snyders, R.; Colomer, J.-F.; Quintana, M.; Bittencourt, C. Low kinetic energy oxigen ion irradiation in vertically aligned carbon nanotubes. *Appl. Sci.* **2019**.

90. Deokar, G.; Vancsó, P.; Arenal, R.; Ravaux, F.; Casanova-Cháfer, J.; Llobet, E.; Makarova, A.; Vyalikh, D.; Struzzi, C.; Lambin, P.; et al. MoS 2 -Carbon Nanotube Hybrid Material Growth and Gas Sensing. *Adv. Mater. Interfaces* **2017**, *4*, 1700801.

91. Georgakilas, V.; Otyepka, M.; Bourlinos, A.B.; Chandra, V.; Kim, N.; Kemp, K.C.; Hobza, P.; Zboril, R.; Kim, K.S. Functionalization of graphene: Covalent and non-covalent approaches, derivatives and applications. *Chem. Rev.* 2012, *112*, 6156–6214.

92. Zhang, Y.; Tang, T.T.; Girit, C.; Hao, Z.; Martin, M.C.; Zettl, A.; Crommie, M.F.; Shen, Y.R.; Wang, F. Direct observation of a widely tunable bandgap in bilayer graphene. *Nature* **2009**, *459*, 820–823.

93. Dobrota, A.S.; Pašti, I.A.; Mentus, S. V.; Skorodumova, N. V. A DFT study of the interplay between dopants and oxygen functional groups over the graphene basal plane - Implications in energy-related applications. *Phys. Chem. Chem. Phys.* **2017**, *19*, 8530–8540.

94. Soldano, C.; Mahmood, A.; Dujardin, E. Production, properties and potential of graphene.

*Carbon N. Y.* 2010, *48*, 2127–2150.

95. Dutta, P.; Horn, P.M. Low-frequency fluctuations in solids: 1f noise. *Rev. Mod. Phys.* **1981**, *53*, 497–516.

96. Ghany, N.A.A.; Elsherif, S.A.; Handal, H.T. Revolution of Graphene for different applications: State-of-the-art. *Surfaces and Interfaces* 2017, *9*, 93–106.

97. Park, S.; Ruoff, R.S. Chemical methods for the production of graphenes. *Nat. Nanotechnol.* **2009**, *4*, 217–224.

98. Yang, D.; Velamakanni, A.; Bozoklu, G.; Park, S.; Stoller, M.; Piner, R.D.; Stankovich, S.; Jung, I.; Field, D.A.; Ventrice, C.A.; et al. Chemical analysis of graphene oxide films after heat and chemical treatments by X-ray photoelectron and Micro-Raman spectroscopy. *Carbon N. Y.* **2009**, *47*, 145–152.

99. Li, X.; Cai, W.; An, J.; Kim, S.; Nah, J.; Yang, D.; Piner, R.; Velamakanni, A.; Jung, I.; Tutuc, E.; et al. Large-area synthesis of high-quality and uniform graphene films on copper foils. *Science (80-. ).* **2009**, *324*, 1312–1314.

100. Deherr, W.; Berger, C.; Wu, X.; First, P.; Conrad, E.; Li, X.; Li, T.; Sprinkle, M.; Hass, J.; Sadowski, M. Epitaxial graphene. *Solid State Commun.* **2007**, *143*, 92–100.

101. Berger, C.; Song, Z.; Li, T.; Li, X.; Ogbazghi, A.Y.; Feng, R.; Dai, Z.; Marchenkov, A.N.; Conrad, E.H.; First, P.N.; et al. Ultrathin Epitaxial Graphite: 2D Electron Gas Properties and a Route toward Graphene-based Nanoelectronics. *J. Phys. Chem. B* **2004**, *108*, 19912–19916.

102. Schedin, F.; Geim, A.K.; Morozov, S. V.; Hill, E.W.; Blake, P.; Katsnelson, M.I.; Novoselov, K.S. Detection of individual gas molecules adsorbed on graphene. *Nat. Mater.* **2007**, *6*, 652–655.

103. Rodríguez-Pérez, L.; Herranz, M.Á.; Martín, N. The chemistry of pristine graphene. *Chem. Commun.* **2013**, *49*, 3721–3735.

104. Varghese, S.S.; Lonkar, S.; Singh, K.K.; Swaminathan, S.; Abdala, A. Recent advances in graphene based gas sensors. *Sensors Actuators, B Chem.* **2015**, *218*, 160–183.

105. Ghanbari, R.; Safaiee, R.; Sheikhi, M.H.; Golshan, M.M.; Horastani, Z.K. Graphene Decorated with Silver Nanoparticles as a Low-Temperature Methane Gas Sensor. *ACS Appl. Mater. Interfaces* **2019**, *11*, 21795–21806.

106. Lee, K.; Yoo, Y.K.; Chae, M.S.; Hwang, K.S.; Lee, J.; Kim, H.; Hur, D.; Lee, J.H. Highly selective reduced graphene oxide (rGO) sensor based on a peptide aptamer receptor for detecting explosives. *Sci. Rep.* **2019**, *9*.

107. Kang, M.A.; Ji, S.; Kim, S.; Park, C.Y.; Myung, S.; Song, W.; Lee, S.S.; Lim, J.; An, K.S. Highly sensitive and wearable gas sensors consisting of chemically functionalized graphene oxide assembled on cotton yarn. *RSC Adv.* **2018**, *8*, 11991–11996.

108. Bhadra, J.; Popelka, A.; Abdulkareem, A.; Ahmad, Z.; Touati, F.; Al-Thani, N. Fabrication of polyaniline-graphene/polystyrene nanocomposites for flexible gas sensors. *RSC Adv.* **2019**, *9*, 12496–12506.

109. Smith, A.D.; Elgammal, K.; Niklaus, F.; Delin, A.; Fischer, A.C.; Vaziri, S.; Forsberg, F.; Råsander, M.; Hugosson, H.; Bergqvist, L.; et al. Resistive graphene humidity sensors with rapid and direct electrical readout. *Nanoscale* **2015**, *7*, 19099–19109.

110. Rodner, M.; Puglisi, D.; Ekeroth, S.; Helmersson, U.; Shtepliuk, I.; Yakimova, R.; Skallberg, A.; Uvdal, K.; Schütze, A.; Eriksson, J. Graphene decorated with iron oxide nanoparticles for highly sensitive interaction with volatile organic compounds. *Sensors (Switzerland)* **2019**, *19*.

111. Chung, M.G.; Kim, D.H.; Lee, H.M.; Kim, T.; Choi, J.H.; Seo, D.K.; Yoo, J.B.; Hong, S.H.; Kang, T.J.; Kim, Y.H. Highly sensitive NO2 gas sensor based on ozone treated graphene. *Sensors Actuators, B Chem.* **2012**, *166–167*, 172–176.

112. Wu, Z.; Chen, X.; Zhu, S.; Zhou, Z.; Yao, Y.; Quan, W.; Liu, B. Enhanced sensitivity of ammonia sensor using graphene/polyaniline nanocomposite. *Sensors Actuators, B Chem.* **2013**, *178*, 485–493.

113. Wiederoder, M.S.; Nallon, E.C.; Weiss, M.; McGraw, S.K.; Schnee, V.P.; Bright, C.J.; Polcha, M.P.; Paffenroth, R.; Uzarski, J.R. Graphene Nanoplatelet-Polymer Chemiresistive Sensor Arrays for the Detection and Discrimination of Chemical Warfare Agent Simulants. *ACS Sensors* **2017**, *2*, 1669–1678.

114. Chen, H.; Zhang, M.; Bo, R.; Barugkin, C.; Zheng, J.; Ma, Q.; Huang, S.; Ho-Baillie, A.W.Y.; Catchpole, K.R.; Tricoli, A. Superior Self-Powered Room-Temperature Chemical Sensing with Light-Activated Inorganic Halides Perovskites. *Small* **2018**, *14*.

115. Zhu, R.; Zhang, Y.; Zhong, H.; Wang, X.; Xiao, H.; Chen, Y.; Li, X. High-performance room-temperature NO2 sensors based on CH3NH3PbBr3 semiconducting films: Effect of surface capping by alkyl chain on sensor performance. *J. Phys. Chem. Solids* **2019**, *129*, 270–276.

116. Fu, X.; Jiao, S.; Dong, N.; Lian, G.; Zhao, T.; Lv, S.; Wang, Q.; Cui, D. A CH3NH3PbI3 film for a room-temperature NO2 gas sensor with quick response and high selectivity. *RSC Adv.* **2018**, *8*, 390–395.

117. Christians, J.A.; Miranda Herrera, P.A.; Kamat, P. V. Transformation of the excited state and photovoltaic efficiency of CH3NH3PbI3 perovskite upon controlled exposure to humidified air. *J. Am. Chem. Soc.* **2015**, *137*, 1530–1538.

118. Deokar, G.; Casanova-Chafer, J.; Rajput, N.S.; Aubry, C.; Llobet, E.; Jouiad, M.; Costa, P.M.F.J. Wafer-scale few layer graphene growth on Cu/Ni films for gas sensing applications. *Sensors Actuators B. Chem.* **2019**.

119. Gunawan, M.A.; Hierso, J.C.; Poinsot, D.; Fokin, A.A.; Fokina, N.A.; Tkachenko, B.A.; Schreiner, P.R. Diamondoids: Functionalization and subsequent applications of perfectly defined molecular cage hydrocarbons. *New J. Chem.* 2014, *38*, 28–41.

120. Moncea, O.; Gunawan, M.A.; Poinsot, D.; Cattey, H.; Becker, J.; Yurchenko, R.I.; Butova, E.D.; Hausmann, H.; Šekutor, M.; Fokin, A.A.; et al. Defying Stereotypes with Nanodiamonds: Stable Primary Diamondoid Phosphines. *J. Org. Chem.* **2016**, *81*, 8759–8769.

121. Fokin, A.A.; Schreiner, P.R. Band gap tuning in nanodiamonds: First principle computational studies. *Mol. Phys.* **2009**, *107*, 823–830.

122. Sofo, J.O.; Chaudhari, A.S.; Barber, G.D. Graphane: A two-dimensional hydrocarbon. *Phys. Rev. B - Condens. Matter Mater. Phys.* **2007**, *75*.

123. Aversa, R.; Petrescu, R.V. V.; Petrescu, F.I.T.; Apicella, A. Nanodiamond for Structural Biomimetic Scaffolds. *J. Mater. Sci. Chem. Eng.* **2018**, *06*, 6–17.

124. Gurbuz, Y.; Kang, W.P.; Davidson, J.L.; Kinser, D.L.; Kerns, D. V. Diamond microelectronic gas sensors. *Sensors Actuators, B Chem.* **1996**, *33*, 100–104.

125. Davydova, M.; Kulha, P.; Laposa, A.; Hruska, K.; Demo, P.; Kromka, A. Gas sensing properties of nanocrystalline diamond at room temperature. *Beilstein J. Nanotechnol.* **2014**, *5*, 2339–2345.

126. Davydova, M.; Laposa, A.; Smarhak, J.; Kromka, A.; Neykova, N.; Nahlik, J.; Kroutil, J.; Drahokoupil, J.; Voves, J. Gas-sensing behaviour of ZnO/diamond nanostructures. *Beilstein J. Nanotechnol.* **2018**, *9*, 22–29.

# Chapter 2

## Carbon Nanotubes

*This chapter provides the articles related to carbon nanotubes included in the thesis*

UNIVERSITAT ROVIRA I VIRGILI
GAS SENSING WITH MODIFIED CARBON NANOTUBES, GRAPHENE AND DIAMONDOIDS
Juan Casanova Cháfer

# Section 2.1

## Gas Sensing with Iridium Oxide Nanoparticle Decorated Carbon Nanotubes

Juan Casanova-Cháfer, Eric Navarrete, Xavier Noirfalise, Polona Umek, Carla Bittencourt, Eduard Llobet

*Sensors, 19 (2019) 113*

DOI: 10.3390/s19010113

UNIVERSITAT ROVIRA I VIRGILI
GAS SENSING WITH MODIFIED CARBON NANOTUBES, GRAPHENE AND DIAMONDOIDS
Juan Casanova Cháfer

sensors

MDPI

*Article*

# Gas Sensing with Iridium Oxide Nanoparticle Decorated Carbon Nanotubes

**Juan Casanova-Cháfer [1], Eric Navarrete [1], Xavier Noirfalise [2], Polona Umek [3], Carla Bittencourt [4] and Eduard Llobet [1,*]**

1 MINOS-EMaS, Universitat Rovira i Virgili, 43007 Tarragona, Spain; juan.casanova@urv.cat (J.C.-C.); eric.navarrete@urv.cat (E.N.)
2 Materia Nova, 7000 Mons, Belgium; xavier.noirfalise@umons.ac.be
3 Jožef Stefan Institute, 10000 Ljubljana, Slovenia; polona.umek@ijs.si
4 ChIPS, University of Mons, 7000 Mons, Belgium; carla.bittencourt@umons.ac.be
* Correspondence: eduard.llobet@urv.cat; Tel.: +34-997-558-502

Received: 21 November 2018; Accepted: 25 December 2018; Published: 31 December 2018


**Abstract:** The properties of multi-wall carbon nanotubes decorated with iridium oxide nanoparticles ($IrO_x$-MWCNTs) are studied to detect harmful gases such as nitrogen dioxide and ammonia. $IrO_x$ nanoparticles were synthetized using a two-step method, based on a hydrolysis and acid condensation growth mechanism. The metal oxide nanoparticles obtained were employed for decorating the sidewalls of carbon nanotubes. Iridium-oxide nanoparticle decorated carbon nanotube material showed higher and more stable responses towards $NH_3$ and $NO_2$ than bare carbon nanotubes under different experimental conditions, establishing the optimal operating temperatures and estimating the limits of detection and quantification. Furthermore, the nanomaterials employed were studied using different morphological and compositional characterization techniques and a gas sensing mechanism is proposed.

**Keywords:** iridium oxide; carbon nanotubes; chemoresistive gas sensor; metal nanoparticles; relative humidity effect

## 1. Introduction

Chemical sensors employing carbon nanomaterials, like carbon nanotubes and graphene, have attracted great research interest. Specifically, carbon nanotubes have been extensively employed in gas sensing applications due to their suitable electronic, physical, and chemical properties, such as nanometer-size, high carrier mobility, and surface area to volume ratio [1]. Additionally, by functionalizing the sidewalls of multi-wall carbon nanotubes (MWCNT), some sensing properties can be enhanced, such as reproducibility, selectivity, and sensitivity [2]. Different options have been widely used to improve gas sensing performance, such as grafting functional groups onto the carbon nanotubes (CNT) surface [3] or decorating them with metal or metal oxide nanoparticles [4]. Nanoparticles present some advantages like high surface area, control over the local environment, and improved mass transport that cannot be achieved at bulk level [5].

Even though many papers have been published on the attachment of metal or metal oxide nanoparticles on carbon nanotube sidewalls [4], to the best of our knowledge this is the first time that the decoration of carbon nanotubes with iridium oxide nanoparticles in chemoresistive gas sensing is studied. For that reason, this paper reports the improvements obtained by loading MWCNTs with $IrO_x$ nanoparticles.

Iridium oxide has been reported for electrochemical sensing and catalyst applications, especially for water splitting at low or moderate temperatures [6] due to its ideal properties such as high

catalytic activity, stability, and selectivity under specific reaction conditions [5]. In addition, $IrO_x$ was employed in biosensing applications [7,8] and as a pH sensor [9,10]. Iridium oxide behaves as a p-type semiconductor with medium band gap energy (3.12 eV) and charge carrier concentration of $4.2 \times 10^{21}$ $cm^{-3}$ [11]. In addition, iridium, has been employed to modify different metal oxides for gas sensing. Even if metal oxides are loaded with iridium metal, it appears in the form of iridium oxide nanoparticles at the high operating temperatures of metal oxide gas sensors. Iridium oxide has been reported to catalyze gallium oxide for detecting ethanol and propane at 600 °C [12], combined to tungsten oxide for detecting ethanol [13], added to titanium oxide films for detecting oxygen [14], or employed in combination with tin oxide in an attempt to diminish moisture cross-sensitivity in the detection of carbon monoxide [15].

As already reported [16], the presence of oxygenated defects and functional groups (e.g., carboxylic acid) on the sidewalls of MWCNTs helps in achieving a stable grafting of metal or metal oxide nanoparticles to carbon nanotubes and enables an efficient charge carrier transfer between them. Therefore, this approach was also employed here for the grafting $IrO_x$ nanoparticles onto carbon nanotubes in view of developing simple, low cost chemoresistive gas sensors.

The hybrid nanomaterial and gas sensors were characterized employing different techniques such as Raman spectroscopy, transmission electron microscopy (TEM), scanning electron microscopy (SEM), and X-ray photoelectron spectroscopy (XPS) to elucidate morphology and chemical composition. The resistance changes during the exposure to different contaminant gases under different experimental conditions were measured.

While it is well-known that carbon nanomaterials show remarkable sensitivity to nitrogen dioxide, the performance of metal or metal oxide NP decorated CNTs in the detection of ammonia vapors remains rather poor. Probably this is due to the significantly weaker affinity between $NH_3$ and carbon nanotubes and its associated poor charge transfer efficiency [17]. However, the capability of $IrO_x$ to detect $NH_3$ has been reported [18] and for that reason, in this paper we explore the possibility of employing $IrO_x$-MWCNTs as gas-sensitive material for detecting $NO_2$ and $NH_3$.

## 2. Materials and Methods

### *2.1. Material Synthesis*

The synthesis of iridium oxide ($IrO_x$) nanoparticles was achieved following the method proposed by Zhao [19], in which a solution of iridium oxide nanoparticles is prepared via a two-step process (Equation (1)). The first step consists of the preparation of 2 mM dissolution using potassium hexachloroiridate (IV) ($K_2IrCl_6$) in 100 mL of distilled water. Then, pH was adjusted to 13 employing sodium hydroxide (NaOH) diluted in distilled water and the product was heated to 90 °C during 30 min to ensure the total hydrolysis of $K_2IrCl_6$, breaking the Ir–Cl bonds and creating the complex $[Ir(OH)_6]^{-2}$. This resulted in a color change of the dissolution from red-brown ($K_2IrCl_6$) to yellow ($[Ir(OH)_6]^{-2}$) (see Equation (1)).

An acid condensation process was conducted in the second step, in which a 3 M nitric acid ($HNO_3$) dissolution was employed to decrease the pH to 1 under vigorous stirring during 90 min in order to avoid the formation of precipitates. In this step, the ($[Ir(OH)_6]^{-2}$) complex forms ligand-free $IrO_x$ nanoparticles dispersed in water, with their characteristic deep blue color (see Figure S1 Supplementary Materials) due to the protonation and condensation of ($[Ir(OH)_6]^{-2}$). Once the iridium nanoparticles are formed, it is important to store the dissolution at 2 °C to avoid the formation of precipitates.

$$[IrCl_6]^{-2} \xrightarrow{OH^-} [Ir(OH)_6]^{-2} \xrightarrow{H^+} IrO_x + nH_2O \quad (1)$$

Once the metal oxide nanoparticles had been obtained, the surface of MWCNTs was decorated by attaching the $IrO_x$ nanoparticles via an impregnation technique. The impregnation technique consists of the dropwise addition of metal nanoparticles to a MWCNTs solution heated at 80 °C under vigorous

stirring. Functionalized MWCNTs were purchased from Nanocyl S.A. (Belgium) with carbonyl and carboxyl functional groups grafted to their surface because these MWCNTs had undergone a cold plasma treatment. As already stated, the presence of these functional groups on the carbon nanotubes sidewalls helps attaching the iridium oxide nanoparticles onto their outer wall.

### *2.2. Material Characterization*

The nanomaterials obtained were analyzed employing several techniques. For instance, both the crystallinity of carbon nanotubes and the confirmation of the presence of iridium oxide nanoparticles in the hybrid samples were evaluated using Raman Spectroscopy. This analysis was performed using a Raman spectrometer from Renishaw, plc. (Wotton-under-Edge, UK), which was coupled to a confocal Leica DM2500 microscope. The laser employed had a wavelength of 514 nm.

The morphology of the hybrid nanomaterial was studied via scanning electron microscopy (SEM) using a SU8020 Microscope from Hitachi (Tokio, Japan) at an operating voltage of 30 kV. In addition, transmission electron microscopy (TEM) using a JEM-1011 from Jeol Ltd. (Tokio, Japan) and high resolution TEM (Jeol 2100, 200 keV) equipped with an energy-dispersive X-ray spectrometer (EDXS) for elemental analysis were also performed. The specimens for high resolution TEM investigation were ultrasonically dispersed in MeOH and a drop of dispersion was deposited onto a lacy carbon film supported by a copper grid. Moreover, a drop of the $IrO_x$ suspension was deposited onto a copper grid and studied by TEM.

The chemical composition of the hybrid sample was studied via X-ray photoelectron spectroscopy (XPS) using a VERSAPROBE PHI 5000 from Physical Electronics Inc. (Chanhassen, MN, USA), equipped with a Monochromatic Al Kα X-ray. The energy resolution was 0.6 eV. For the compensation of built charge during the measurements, a dual beam charge neutralization composed of an electron gun (~1 eV) and an Argon ion gun (<10 eV) was used. All binding energies were calibrated to the Au $4f_{7/2}$ (84.0 eV).

### *2.3. Sensor Fabrication*

A silicon wafer was oxidized in a tubular furnace during 6 h at 1100 °C under continuous flow of dry oxygen. This process results in the growth of a silicon dioxide layer ($SiO_2$) on both sides of the wafer. The wafer was diced. In the polished side of a given die, MWCNTs (either pristine or decorated with iridium oxide nanoparticles) were deposited by an airbrush technique, using a shadow mask. On the other side of the die (non-polished), a platinum screen-printed alumina heater was glued employing a thermally conductive epoxy and subsequently bonded to a 20 × 30 mm printed circuit board (PCB). Finally, two wire contacts were made on the surface of the sensor using a silver epoxy paste (Ag component metallization, Heraeus). The sensor layout was designed and implemented in order to be placed in a Teflon airtight chamber, which was connected to a computer controlled gas mixture and delivery system that employed mass-flow controllers from Bronkhorst High-Tech B.V. (Ruurlo, The Netherlands) and electro-valves (see Figure S2 Supplementary Materials).

### *2.4. Gas Sensing Studies*

Calibrated gas cylinders of the different gases/vapors tested were employed diluted in a balance of synthetic dry air (Air Premier Purity: 99.995%). Pure dry air was also used as carrier gas. To achieve the desired analyte concentrations, successive dilutions were done using synthetic dry air. The total flow was adjusted to 100 mL/min, stabilizing the sensors with synthetic dry air during 1 h between exposures (30 min) to the target gas concentration. Sensor response is defined as $(\Delta R/R_0)$ expressed in percentage, where $\Delta R$ is the resistance change over the 30-min exposure time and $R_0$ is the baseline resistance. The time needed for achieving a stable sensor resistance value after a sudden exposure to nitrogen dioxide or ammonia exceeds one hour. In addition, recovering the initial baseline in dry air, especially after being exposed to nitrogen dioxide, takes a few hours. Therefore, to speed up the characterization process, the exposure and recovery times were arbitrarily set to 30 min and one hour,

respectively. This implies that sensor responses reported are pessimistically biased, since allowing for the full stabilization during response and recovery would result in higher resistance changes than those reported. The different species were tested at three different operating temperatures (i.e., room temperature, 100 °C and 150 °C). Moreover, a controlled evaporator and mixer from Bronkhorst High-Tech B.V. (Ruurlo, The Netherlands) was used to humidify gas samples during the measurements, enabling the study of the relative humidity (R.H.) effect on sensor response. Resistance changes of the different gas sensitive films tested were monitored by an Agilent HP 34972A multimeter.

## 3. Results

At first, the morphology and composition of the hybrid gas sensitive nanomaterial was characterized employing Raman spectroscopy, SEM, TEM, and XPS.

### *3.1. Material Characterization Results*

Figure 1a shows the Raman spectrum of the hybrid nanomaterial with the well-known bands at 1350 $cm^{-1}$ (D), 1580 $cm^{-1}$ (G), 2680 $cm^{-1}$ (2D), and 2950 $cm^{-1}$ (2iTO). D and 2D band are related to the presence of defects such as disorder in the $sp^2$ carbon nanostructure, amorphous carbon or carbonaceous impurities, meanwhile G band represents the in-plane vibrations of $sp^2$ carbon bonds [20]. Taking in consideration the ratio between the intensities of D and G bands (D/G ratio), it was confirmed that the MWCNTs employed here are not highly crystalline. This is due to the presence of defects and oxygenated functional groups attached to the sidewalls of nanotubes resulting from the oxygen plasma treatment. However, the presence of these oxygenated defects plays an essential role in the anchoring process of $IrO_x$ nanoparticles. Besides, the presence of oxygenated species in the surface of MWCNTs enhance their reactivity [16]. In other words, the presence of functional groups (i.e., COOH) contributes to increasing the sensitivity to gas molecules. In addition, Raman measurements revealed the decoration of MWCNTs with $IrO_x$ (see Figure 1b), because the presence of $IrO_x$ active modes ($E_g$, $B_{2g}$, and $A_{1g}$) [21] could be detected.

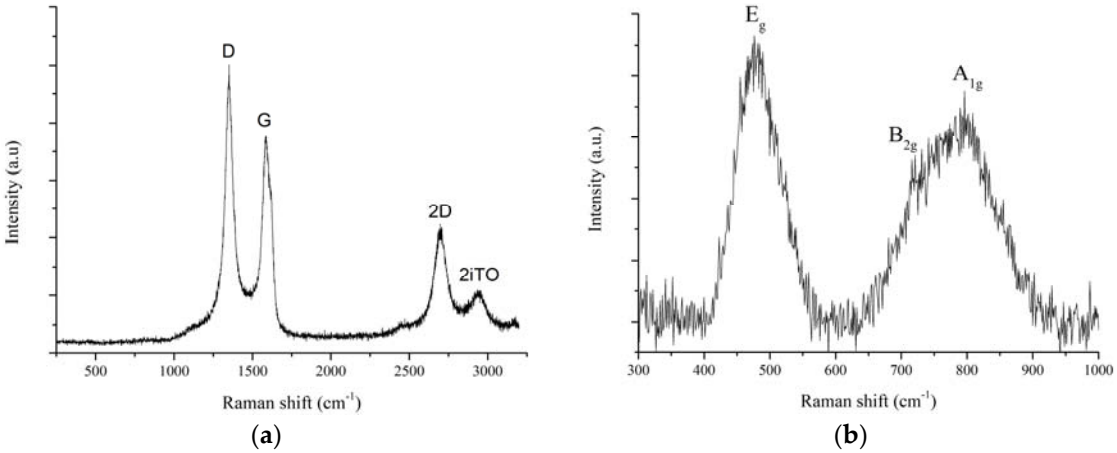


**Figure 1.** Typical Raman spectrum of the multi-wall carbon nanotubes (MWCNTs) used (**a**). Detailed Raman spectrum recorded in the 300–1000 $cm^{-1}$ region corresponding to peaks attributed to the presence iridium oxide nanoparticles in $IrO_x$-MWCNT samples (**b**).

SEM analysis shows that the hybrid nanomaterial consists of mats of disordered MWCNTs (Figure 2a). Some white spots appearing in the SEM micrograph (due to charge accumulation) can be attributed to the presence of semiconductor $IrO_x$ nanoparticles sitting on the rather conductive MWCNTs. The synthesis method produced small nanoparticles, the size of which was $1 \pm 0.3$ nm (see Figure 2a inset). $IrO_x$ nanoparticles appear as dark spots in TEM micrographs. The presence of $IrO_x$ nanoparticles was further confirmed by HR-TEM and EDXS analysis (see Figure 2b and Figure

S3 Supplementary Materials). The HR-TEM image also shows that the structure of the MWCNTs is preserved after the plasma and $IrO_x$ impregnation treatments.

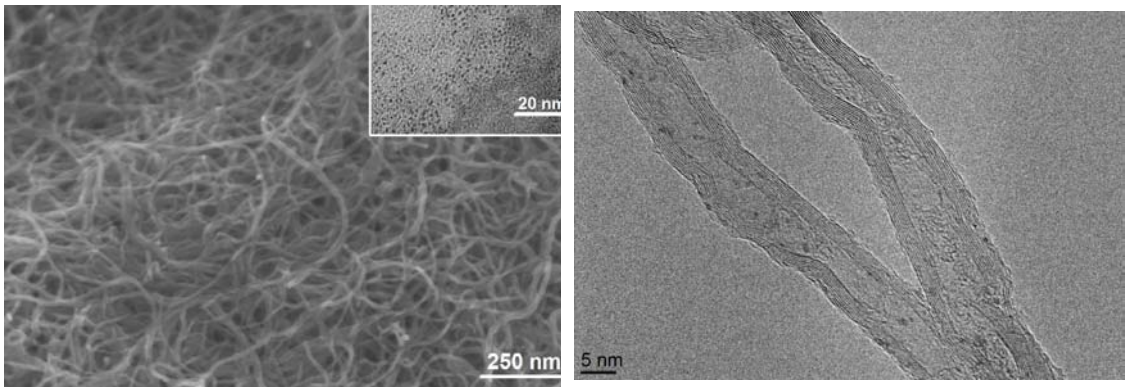


(**a**) (**b**)

**Figure 2.** (**a**) SEM image showing the morphology of the $IrO_x$-MWCNT sample. $IrO_x$ nanoparticles (bright spots) can be observed at the MWCNT surface. The inset shows a TEM image of as synthesized iridium oxide nanoparticles (dark spots). (**b**) HR-TEM image showing MWCNT with $IrO_x$ nanoparticles (dark spots).

The results of the XPS analysis are presented in Figure 3. The C1s spectrum is reproduced by five components centered at binding energy 284.4 eV, 285.5 eV, 287.2 eV, 288.9 eV, and 291.4 eV (Figure 3a). The components at 284.4 eV and 291.0 eV are characteristic of $sp^2$ carbon systems, the first can be associated to photoelectrons emitted from carbon atoms in the carbon nanotube 'graphite-like' walls, while the second reflects the electron energy loss peak due to the collective excitation of $\pi$ electrons, the so-called $\pi$ plasmon [22,23]. The other three components are associated to photoelectrons emitted from carbon atoms at $sp^3$ bonds, oxygen-containing groups such as C–O and in carboxylic groups, respectively [24].

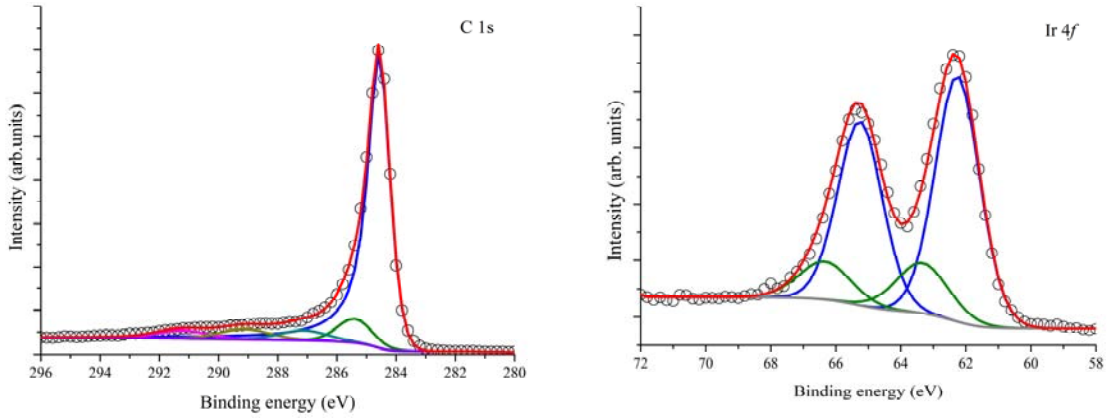


(**a**) (**b**)

**Figure 3.** Deconvolution of the C 1s core level peak for bare MWCNTs (**a**). Deconvolution of the Ir 4f core level peak for iridium oxide nanoparticles (**b**).

Figure 3b shows a typical Ir 4f XPS spectrum recorded on the hybrid nanomaterial and its fitting result. Two doublets of Gaussian-Lorentzian convolution were used to reproduce the experimental data. The spin-orbit doublet binding energy splitting in each doublet was 2.9 eV and the intensity ratio 7:5. The first doublet with components at 62.3 eV ($4f_{7/2}$) and 65.3 eV ($4f_{5/2}$) testifies for the presence of Ir (III) while the second doublet with components centered at 63.4 eV and 66.4 eV the presence of Ir(IV) [25,26]. The fact that Ir presents two oxidation states is favourable for gas sensing, as will be discussed later.

### 3.2. Gas Sensing Results

The ability of the hybrid nanomaterial developed for detecting different gases was evaluated, showing significant results in the detection of $NH_3$ and $NO_2$ at ppm and ppb levels, respectively. Sensors employing decorated MWCNTs with $IrO_x$ nanoparticles showed enhanced sensitivity, stability, and reproducibility than those employing bare carbon nanotubes.

$NH_3$ detection was performed by analyzing repeated response and recovery cycles to four concentrations (25, 50, 75, and 100 ppm, successively), showing an important increase in response (six-fold) for $IrO_x$ loaded carbon nanotubes, compared to bare carbon nanotube sensors. Moreover, apart from the higher response, $IrO_x$-MWCNT presented a better reproducibility and higher stability (see Figure 4a). In addition, the responses were analyzed at three different sensor operating temperatures and $IrO_x$-decorated MWCNT sensors showed higher ammonia responses than bare MWCNT sensors for any of the operating temperatures studied. The best working conditions were found to be 100 °C, considering the higher intensity of response and sensitivity (slope) achieved at this operating temperature (see Figure 4b). Error bars are standard deviations of responses.

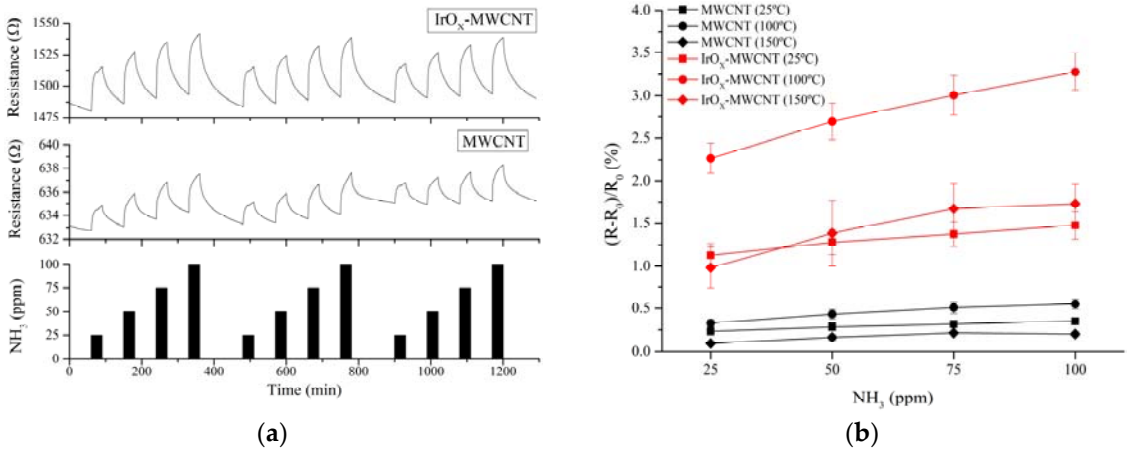


(**a**) (**b**)

**Figure 4.** Typical resistance response obtained when detecting $NH_3$ at a sensor operating temperature of 100 °C (**a**). Calibration curves obtained for $NH_3$ at different operating temperatures (**b**).

The process followed for measuring $NO_2$ was similar to the one employed for $NH_3$. However, in this case four concentrations (see Figure 5a) were analyzed (250, 500, 750, and 1000 ppb), again for three different operating temperatures. It can be observed that a better responsiveness towards $NO_2$ (two-fold increase) was obtained for MWCNTs loaded with $IrO_x$ nanoparticles. Taking in consideration the responses obtained under different working conditions, the optimal operating temperature for detecting $NO_2$ was established at 150 °C (see Figure 5b).

In addition, cross-sensitivity was evaluated measuring other gases. Some aromatic volatile organic compounds (VOCs), such as benzene and toluene were measured at low concentrations and at different operating temperatures without achieving high sensor responses during their exposure to these compounds. Exposure to ethanol ($C_2H_6O$) vapors did not resulted in significant response either. High concentration (100 ppm) of carbon monoxide (CO) was also tested, yet unsuccessfully. Besides, hydrogen was measured until high concentrations (e.g., 1000 ppm) resulting in extremely low response. A comparison of the responses obtained for the different gases tested can be observed in Figure 6. This figure reports a sensitivity coefficient that is defined as the ratio between the response measured and concentration tested for any given species. It can be derived that $IrO_x$-MWCNTs are suitable for detecting $NO_2$ and $NH_3$ with small cross-sensitivity from other species.

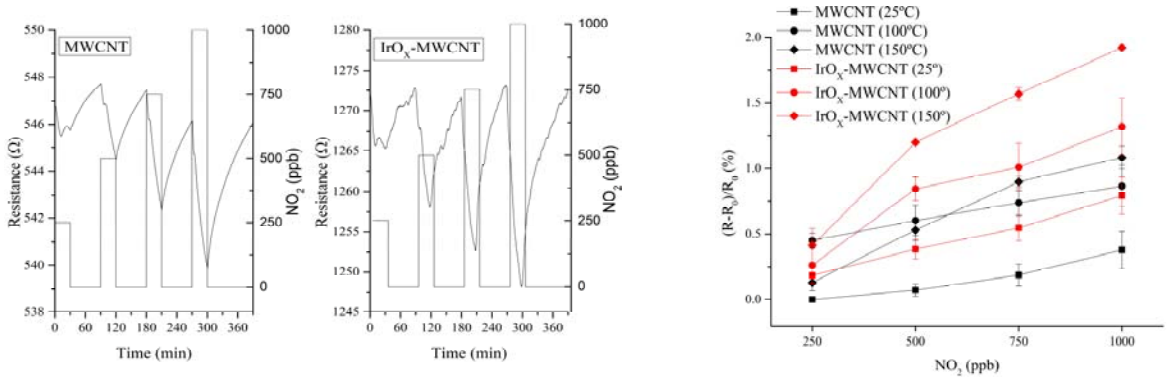


(**a**) (**b**)

**Figure 5.** Typical response and recovery of the resistance signals when the sensors are exposed to different concentrations of $NO_2$ (**a**). Calibration curves obtained for $NO_2$ for bare carbon nanotubes and $IrO_X$-MWCNTs at different operating temperatures under dry conditions. Error bars are standard deviations of responses (**b**).

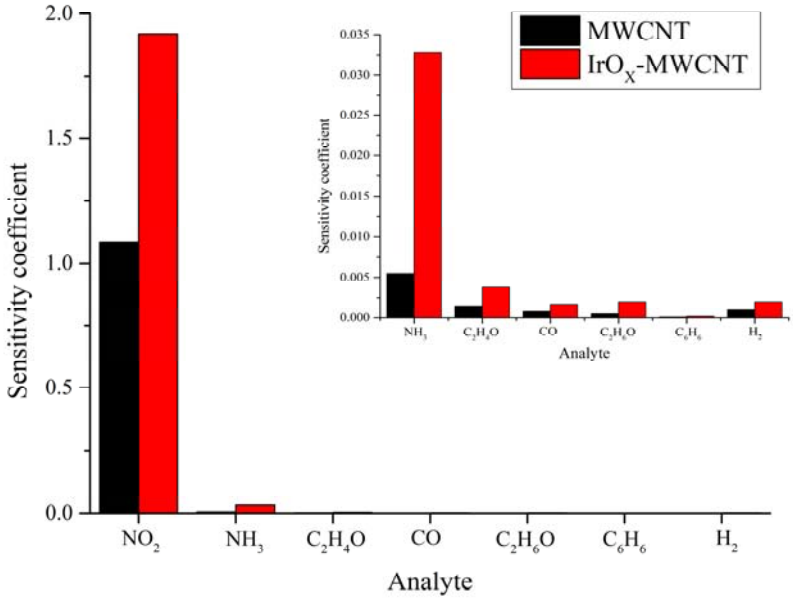


**Figure 6.** Sensitivity coefficient expressed as response/concentration for the different species tested (the inset is an enlargement showing the coefficients for those gaseous species with lower sensitivity coefficients). The sensitivity coefficients were obtained employing the highest response registered at specific concentrations, which were 1 ppm for $NO_2$; 20 ppm for $C_2H_6O$ and $C_6H_6$; 100 ppm for CO, $C_2H_4O$ and $NH_3$; and 1000 ppm for $H_2$.

Acetaldehyde ($C_2H_4O$) was also measured, obtaining a non-conclusive response for bare carbon nanotubes. However, decorated MWCNTs with iridium nanoparticles show a fast and saturated response when $C_2H_4O$ is applied at 100 °C (Figure S4 Supplementary Materials), even at room temperature. However, an important drift can be observed together with a progressive de-sensitization effect over time, probably due to an irreversible adsorption by the repeated exposure of the gas-sensitive film towards $C_2H_4O$ at low temperatures.

The humidity effect on gas sensing performance was also analyzed. When the humidity background changes from dry to 50% R.H., the baseline resistance of $IrO_x$-MWCNTs increases by 3.2% on average. Once this new baseline under humid conditions was reached and stable, which took about 5 min, ammonia and nitrogen dioxide measurements under humid conditions were performed. Bare carbon nanotubes show an important increase in the response towards nitrogen dioxide and ammonia

when humidity is present, probably because of transfer of electronic charge from adsorbed water molecules towards carbon nanotubes depletes carbon nanotubes from holes in p-type carbon nanotube mats [27]. In contrast, during their exposure to $NH_3$, the response of $IrO_x$-decorated MWCNTs remains virtually unaffected by the presence of ambient moisture (see Figure 7). Even that a slight decrease in the response towards $NH_3$ can be observed in Figure 7, this change falls within the range of the measurement uncertainty.

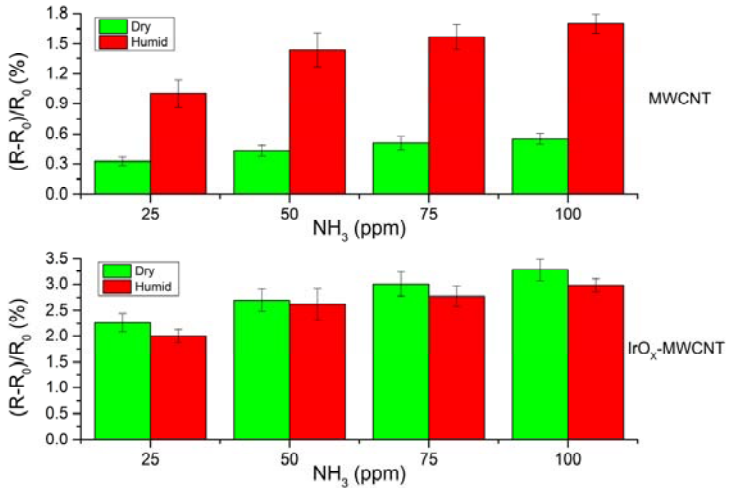


**Figure 7.** Comparison of the response towards ammonia for bare and $IrO_x$-decorated MWCNTs under dry and humid (50% R.H.) conditions. Sensors were operated at 100 °C. For bare carbon nanotubes, the response towards ammonia shows a four-fold increase when under humid conditions. $IrO_x$-MWCNTs present a slightly lower response to ammonia in humid conditions than in dry air.

Similarly, the response to $NO_2$ was evaluated in the presence of ambient moisture (50% R.H.) for a sensor working temperature of 150 °C. Figure 8 shows a high increase in the response towards $NO_2$ of $IrO_x$-MWCNTs when under humid conditions. Figure S5 (Supplementary Materials) shows a typical dynamic response of a sensor for nitrogen dioxide under humid conditions. The possible gas sensing mechanism to explain this effect will be detailed later on, in the discussion section.

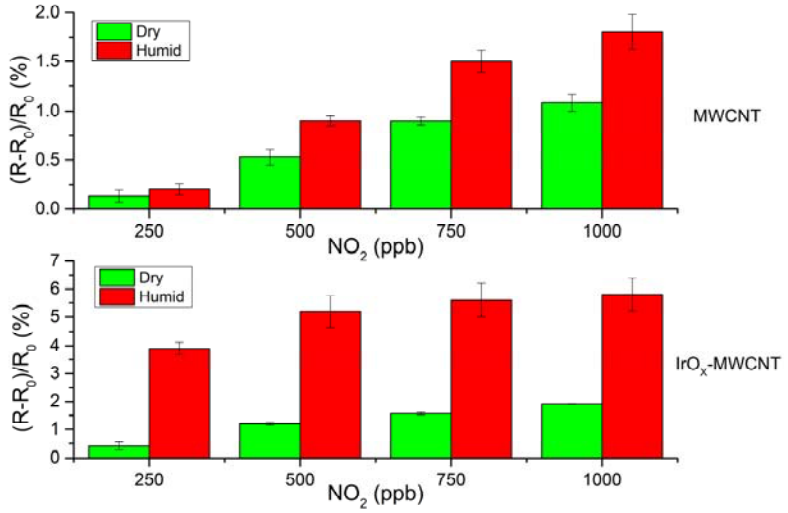


**Figure 8.** Comparison of the responses towards nitrogen dioxide of bare and $IrO_x$-decorated MWCNTs under dry and humid (50% of relative humidity) conditions. Sensors were operated at 150 °C. While for bare carbon nanotubes, the response under humid conditions shows an almost two-fold increase (in comparison to dry conditions), this increase in response is even higher for $IrO_x$-MWCNTs (nearly four-fold).

The long term stability of the response towards nitrogen dioxide was studied as well. For this purpose, repeated nitrogen dioxide measurements were conducted at 1 ppm under dry conditions for both $IrO_x$ loaded and bare MWCNT sensors over a 6-month period. It was found that the response of $IrO_x$-MWCNTs was remarkably stable (variation was below 5%). Figure S6 (Supplementary Materials) shows the details.

It is important to notice that $IrO_x$-MWCNT sensors are able to measure ppm and ppb levels of $NH_3$ and $NO_2$, respectively, with an excellent signal-to-noise ratio. For that reason, it is interesting to estimate the limit of detection (LOD) and limit of quantification (LOQ). In the case of ammonia, it was considered applying a linear regression to the calibration curve, following the method described by Shrivastava and co-workers [28]:

$$\mathrm{LOD} = 3S_a/b \quad (2)$$

$$\mathrm{LOQ} = 10S_a/b \quad (3)$$

where $S_a$ was estimated by the standard deviation of y-intercepts and $b$ is the slope of the regression line obtained from Figure 4b. The theoretical LOD and LOQ for $IrO_x$-MWCNTs were estimated at hundreds of ppb for $NH_3$ detection. These results should be confirmed with measurements at ppb range, however, these levels are much lower than the exposure limit [29] established by the Occupational Safety and Health Administration (OSHA), which is 50 ppm as an 8-h time-weighted average (TWA).

Carbon nanomaterials present high potential to detect very low concentrations of nitrogen dioxide. For that reason, 25 ppb of $NO_2$ were measured (see Figure 9) to check the ability of the sensors to reproducibly detect such a low concentration level. This is the lowest $NO_2$ concentration that our measurement system is able to generate.

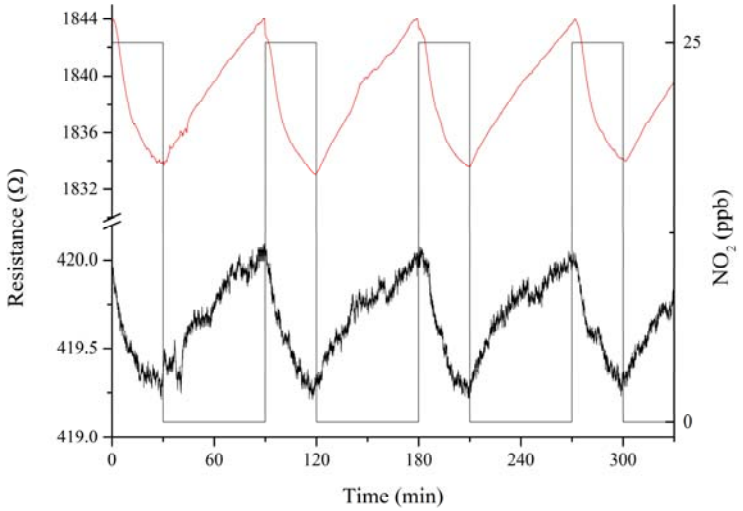


**Figure 9.** Example of the response for bare carbon nanotubes (black line) and $IrO_x$-MWCNTs (red line) to repeated pulses of nitrogen dioxide at 25 ppb. Sensors were operated at 150 °C. A baseline correction was implemented to suppress baseline drift.

To estimate the LOD and LOQ for nitrogen dioxide, a signal-to-noise method was employed [30]. The background noise level was calculated using 50 points during a stabilization step under a flow of dry air. In addition, for each sensor, the response signal for 25 ppb of nitrogen dioxide was computed as the averaged response for 10 nitrogen dioxide pulses. This is illustrated for four pulses in Figure 9. Then, the sensitivity was estimated using the slope of the calibration curve shown in Figure 5b (for the two lowest concentrations measured, i.e., 250 and 500 ppb) obtaining a sensitivity of 0.0032% $ppb^{-1}$ and 0.0015% $ppb^{-1}$ for iridium oxide decorated and bare MWCNTs, respectively. Assuming a signal-to-noise ratio of 3 for LOD, and of 10 for LOQ, the estimated levels are summarized in

Table 1. The lower values obtained with $IrO_x$ loaded MWCNTs are due to the higher response and signal-to-noise ratio for this hybrid nanomaterial than for bare MWCNTs.

**Table 1.** Estimated limits of detection and quantification for $NO_2$. These theoretical levels should be confirmed with experimental measurements at this level of concentration.

| | CNT | IrOx-MWCNT |
|---|---|---|
| LOD | 17.8 ppb | 1 ppb |
| LOQ | 59.1 ppb | 3.2 ppb |

Maximum permitted exposure limits to $NO_2$ are under continuous revision, but nowadays these are established at 200 ppb and 100 ppb (1-h exposure) by the European Union (EU) [31] and the US [32], respectively. Besides, the annual limit mean for primary and secondary exposure is 40 ppb for the EU [31] and 53 ppb for US [32]. Our sensors show clearly the possibility of detecting 25 ppb of nitrogen dioxide and potential for detecting this toxic species even at lower levels. Nevertheless, real exposures to these concentrations of $NO_2$ should be studied in order to confirm the theoretical LOD and LOQ obtained.

## 4. Discussion

Despite the fact that carbon nanotube mats can work at room temperature for gas sensing [33], the presence of metal oxide nanoparticles, which may show catalytic properties above room temperature, has encouraged us to explore the performance of the hybrid nanomaterials at moderate operating temperatures (up to 150 °C). This should help us better apprehend the effect of $IrO_x$ nanoparticles decorating MWCNTs on gas sensing properties [34]. From the gas sensing tests, it was derived that the presence of $IrO_x$ NPs decorating the outer wall of MWCNTs was advantageous for detecting ammonia and nitrogen dioxide. Additionally, ammonia was better detected at an operating temperature of 100 °C, while 150 °C was better for detecting nitrogen dioxide. While MWCNTs offer oxygenated-defect sites and carboxylic acid functional groups to interact with these species, $IrO_x$ nanoparticles present a high content of oxygen species on their surface, improving the sensitivity to some gases.

Ammonia is a reducing agent, acting as electron donor. Then, when p-type carbon nanotube mats interact with $NH_3$, an increase in the film resistance is observed because electronic charge is transferred from adsorbed ammonia molecules towards CNTs [35]. The presence of oxygenated defects on the surface of CNTs favours their interaction with ammonia [36]. In contrast, nitrogen dioxide is a strong oxidizing agent with electrophilic properties, acting as electron acceptor. As a consequence, when nitrogen dioxide is adsorbed on carbon nanotubes, electronic charge is transferred from CNTs towards the adsorbed species and the electrical resistance of the mat decreases. As already discussed for ammonia, oxygenated defects can act as adsorption sites [37]. These mechanisms are detailed below:

$$NH_{3\,(gas)} \rightarrow {NH_3}^{+}{}_{(ads)} + e^{-} \quad (4)$$

$$NO_{2\,(gas)} + e^{-} \rightarrow {NO_2}^{-}{}_{(ads)} \quad (5)$$

At moderate temperatures, the adsorption barrier is further lowered by the presence of oxygen via adsorbed molecular oxygen from the environment and the oxygenated species and defects present on the carbon nanotube sidewalls [20]. These oxygenated species on MWCNTs can be attributed to the presence of functional groups resulting from the plasma treatment and adsorbed oxygen from the sensor environment during the experiments [38].

Moreover, independently of the operating temperature, decorated carbon nanotubes always show a higher response to ammonia or nitrogen dioxide than bare MWCNTs. The presence of $IrO_x$ nanoparticles improves the response and sensitivity offered by carbon nanotubes. The interactions described between gases and oxygenated species for pristine carbon nanotubes can be applied to $IrO_x$ nanoparticles as well. Nanoparticles of oxygen defective iridium oxide (as revealed by XPS) facilitate

the interaction between gas molecules and adsorbed oxygen species ($O_2^-$) [36], which results in the transfer of electronic charge between adsorbed molecules and the NP-MWCNT system.

Nitrogen dioxide and ammonia can react with the oxygen species adsorbed at metal oxide nanoparticles, following the reactions proposed by Rahmani and co-workers [39]:

$$4NH_{3\,(gas)} + 3O_2^- \rightarrow 2N_{2\,(gas)} + 6H_2O + 3e^- \quad (6)$$

$$NO_{2\,(gas)} + O_2^- + 2e^- \rightarrow NO_2^-{}_{(ads)} + 2O^-{}_{(ads)} \quad (7)$$

The release (capture) of electrons upon adsorption of ammonia (nitrogen dioxide) results in the increase (decrease) of the electrical resistance of the $IrO_x$-MWCNT mats. In addition, iridium oxide has been reported as a catalytic material, and the XPS analysis conducted on iridium oxide decorated MWCNT samples (see Figure 3) has shown that two oxidation states coexist for Ir. The presence of both Ir (IV) and Ir (III) was determined, which means that NPs contain $IrO_2$ and $Ir_2O_3$. The coexistence of these two iridium oxides could explain the high response towards ammonia and nitrogen dioxide obtained for $IrO_x$-decorated MWCNT samples in comparison to bare MWCNT samples. The gas sensing mechanism that we propose, derived from the occurrence of different oxidation states for iridium is detailed in Figure 10.

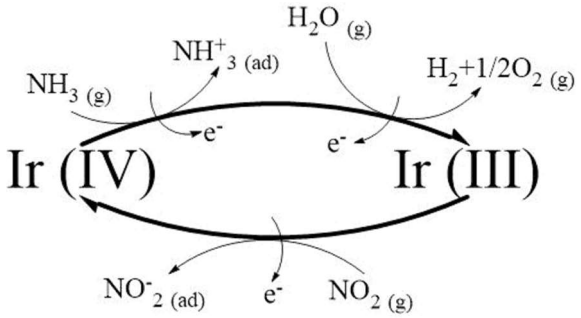


**Figure 10.** Gas sensing mechanism for iridium oxide nanoparticles decorating carbon nanotubes.

Probably iridium oxide nanoparticles present a redox interaction with the analytes, which means that Ir (IV) is reduced by $NH_3$ going to Ir (III) state. However, $NO_2$ can oxidize Ir (III) to Ir (IV). These interactions could explain the higher sensitivity to these gases observed for $IrO_x$-MWCNTs. This is based on the presence of Ir (IV) and Ir (III) in the hybrid sensing material at the same time but in different ratios, depending on the gas tested.

We can consider now the presence of ambient moisture in the sensing mechanism. The high sensitivity of bare nanotubes to ambient moisture is well-known. In fact, carbon nanomaterials such as graphene and carbon nanotubes have been extensively reported as humidity sensors [40–42]. Here the enhancement in the response towards nitrogen dioxide or ammonia observed for bare MWCNT sensors under humid conditions can be attributed to a water mediated adsorption of gas molecules in semiconductor chemoresistors [43]. However, in $IrO_x$-decorated carbon nanotubes the interactions with humidity are more complex. First, $IrO_x$-MWCNTs show a similar response to ammonia under dry or humid conditions, even with ambient moisture the response is slightly lower. Probably the reason for this behaviour is related to the reducing properties of water (see Figure 10):

$$H_2O_{\,(gas)} \rightarrow 2H^+{}_{(gas)} + 1/2O_{2\,(gas)} + 2e^- \quad (8)$$

At 100 °C, which was found optimal for detecting ammonia, $IrO_x$ NPs are able to create a water splitting effect, reducing Ir (IV) to Ir (III). In consequence, reducing molecules such as $NH_3$ and $H_2O$ are taking part in a competitive reaction that favours the reduction of $IrO_x$ towards $Ir_2O_3$, which would explain the similar response observed for ammonia under dry or humid conditions due to the limitation in the number of surface oxygen species to interact with. In contrast, $IrO_x$-MWCNTs

show a higher response to $NO_2$ in a humid environment than in dry air. Figure 10 can explain this behaviour because during any recovery phase under humid air, the occurrence of Ir (III) is favoured, increasing the Ir (III)/Ir (IV) ratio. This higher ratio explains the higher response recorded for a new $NO_2$ exposure event.

Tables 2 and 3 summarize the performance achieved with previously reported metal or metal oxide decorated carbon nanotube materials in the detection of $NO_2$ and $NH_3$, respectively. In addition, these tables also help putting in context the results achieved using $IrO_x$-decorated carbon nanotubes. As described above, the operational sensitivity reported in these tables was estimated using the slope of the calibration curves for the lowest concentrations measured.

**Table 2.** Nitrogen dioxide sensitivities reported as $10^{-3}$% $ppb^{-1}$ for different metal or metal oxide nanoparticles decorating carbon nanotubes. TW = This Work.

| CNT Decoration | Sensitivity | Reference |
|---|---|---|
| $IrO_x$ | 3.2 | TW |
| Au | 8 | [44] |
| Rh | 5 | [37] |
| Pt | 0.094 | [45] |
| Pd | 0.069 | [45] |
| $SnO_2$ | 4.8 | [46] |
| $ZnO_2$ | 0.25 | [47] |

**Table 3.** Ammonia sensitivities reported as $10^{-2}$% $ppm^{-1}$ for different metal nanoparticles decorating carbon nanotubes. TW = This Work.

| CNT Decoration | Sensitivity | Reference |
|---|---|---|
| $IrO_x$ | 1.71 | TW |
| Co | 0.36 | [48] |
| Au | 0.41 | [49] |
| Pd | 1.11 | [50] |
| Pt | 2.80 | [51] |
| Ag | 6.84 | [51] |

## 5. Conclusions

A p-type chemoresistive sensor based on $IrO_x$ nanoparticles decorating MWCNTs was devised to successfully detect harmful gases like $NO_2$ and $NH_3$ at different working temperatures. These loaded carbon nanotubes show enhanced gas sensing properties, such as better reproducibility, higher sensitivity, stability, and lower noise levels in comparison to their bare MWCNT counterparts. In addition, the effect of relative humidity on sensor response was studied, and a detailed gas sensing mechanism was proposed to understand the influence of ambient moisture in the presence of a catalytic nanomaterial like iridium oxide nanoparticles. Finally, low level of cross-sensitivity was observed for a range of different gases and vapors with interfering potential. In consequence, $IrO_x$-MWCNT nanomaterial enables quite a selective detection of nitrogen dioxide or ammonia against other hazardous gases, with low detection limits, making it a potential nanomaterial to be employed in real applications.

**Supplementary Materials:** The following are available online at http://www.mdpi.com/1424-8220/19/1/113/s1. Figure S1: summary of $IrO_x$ NPs synthesis, Figure S2: Gas testing chamber and design of sensor used, Figure S3: TEM-EDXS spectrum of the $IrO_x$-MWCNT sample, Figure S4: Acetaldehyde detection, Figure S5: Response to $NO_2$ in humid conditions for $IrO_x$-MWCNTs, Table S1: Average responses and associated standard deviations, Figure S6: Response stability test.

**Author Contributions:** J.C.-C. synthesized the nanoparticles, performed the experiments and contributed to the discussion and the writing. E.N. assisted to the nanoparticle synthesis. X.N. and C.B. performed and interpreted the SEM and XPS analysis. P.U. performed and interpreted HR-TEM and EDXS analysis. E.L. supervised the work and contributed to the discussion of results.

**Funding:** This research was funded by MINECO and FEDER under grant no. TEC2015-71663-R, AGAUR under grant no. 2017 SGR 418. The project FITTED-FNRS (J 0230.17) is also acknowledged. C.B. and P.U. gratefully acknowledge the financial support provided by COST action CA15107. J.C.-C. is supported by a *Martí i Franquès* pre-doctoral fellowship from Universitat Rovira i Virgili (URV), E.L. is supported by the Catalan Institution for Research and Advanced Studies via the ICREA Academia Award. C.B. is a researcher associate at the FRS-FNRS.

**Acknowledgments:** We are thankful to Moncusí for the help provided with Raman experiments.

**Conflicts of Interest:** The authors declare no conflict of interest.

## References

1. Llobet, E. Gas sensors using carbon nanomaterials: A review. *Sens. Actuators B Chem.* **2013**, *179*, 32–45. [CrossRef]
2. Holzinger, M.; Vostrowsky, O.; Hirsch, A.; Hennrich, F.; Kappes, M.; Weiss, R.; Jellen, F. Sidewall Functionalization of Carbon Nanotubes. *Angew. Chem. Int. Ed.* **2001**, *40*, 4002–4005. [CrossRef]
3. Zhang, Z.; Pfefferle, L.; Haller, G.L. Characterization of functional groups on oxidized multi-wall carbon nanotubes by potentiometric titration. *Catal. Today* **2015**, *249*, 23–29. [CrossRef]
4. Kharisov, B.I.; Kharissova, O.V.; Ortiz Méndez, U.; De La Fuente, I.G. Decoration of Carbon Nanotubes with Metal Nanoparticles: Recent Trends. *Synth. React. Inorg. Met. Nano Met. Chem.* **2016**, *46*, 55–76. [CrossRef]
5. Irfan, M.; Pham, X.-H.; Han, K.N.; Li, C.A.; Hong, M.H.; Seong, G.H. Decoration of carbon nanotube films with iridium nanoparticles and their electrochemical characterization. *BioChip J.* **2014**, *8*, 129–136. [CrossRef]
6. Blakemore, J.D.; Crabtree, R.H.; Brudvig, G.W. Molecular Catalysts for Water Oxidation. *Chem. Rev.* **2015**, *115*, 12974–13005. [CrossRef] [PubMed]
7. Wilson, M.S.; Rauh, R.D. Novel amperometric immunosensors based on iridium oxide matrices. *Biosens. Bioelectron.* **2004**, *19*, 693–699. [CrossRef]
8. Irhayem, E.A.; Elzanowska, H.; Jhas, A.S.; Skrzynecka, B.; Birss, V. Glucose detection based on electrochemically formed Ir oxide films. *J. Electroanal. Chem.* **2002**, *538–539*, 153–164. [CrossRef]
9. Marzouk, S.A.M.; Ufer, S.; Buck, R.P.; Johnson, T.A.; Dunlap, L.A.; Cascio, W.E. Electrodeposited iridium oxide pH electrode for measurement of extracellular myocardial acidosis during Acute Ischemia. *Anal. Chem.* **1998**, *70*, 5054–5061. [CrossRef]
10. Huang, W.D.; Cao, H.; Deb, S.; Chiao, M.; Chiao, J.C. A flexible pH sensor based on the iridium oxide sensing film. *Sens. Actuators A Phys.* **2011**, *169*, 1–11. [CrossRef]
11. Brewer, S.H.; Wicaksana, D.; Maria, J.P.; Kingon, A.I.; Franzen, S. Investigation of the electrical and optical properties of iridium oxide by reflectance FTIR spectroscopy and density functional theory calculations. *Chem. Phys.* **2005**, *313*, 25–31. [CrossRef]
12. Lang, A.C.; Fleischer, M.; Meixner, H. Surface modifications of $Ga_2O_3$ thin film sensors with Rh, Ru and Ir clusters. *Sens. Actuators B Chem.* **2000**, *66*, 80–84. [CrossRef]
13. Bastuck, M.; Puglisi, D.; Huotari, J.; Sauerwald, T.; Lappalainen, J.; Lloyd Spetz, A.; Andersson, M.; Schütze, A. Exploring the selectivity of $WO_3$ with iridium catalyst in an ethanol/naphthalene mixture using multivariate statistics. *Thin Solid Films* **2016**, *618*, 263–270. [CrossRef]
14. Castañeda, L.; Maldonado, A.; Olvera, M.L. Sensing properties of chemically sprayed $TiO_2$ thin films using Ni, Ir, and Rh as catalysts. *Sens. Actuators B Chem.* **2008**, *133*, 687–693. [CrossRef]
15. Ozaki, Y.; Suzuki, S.; Morimitsu, M.; Matsunaga, M. Temperature and humidity dependence of $SnO_2$-based CO gas sensors modified with iridium and ruthenium. *Electrochem. Solid State Lett.* **2000**, *3*, 297–299. [CrossRef]
16. Pisal, S.H.; Harale, N.S.; Bhat, T.S.; Dshmukh, H.P.; Patil, P.S. Functionalized Multi-Walled Carbon Nanotubes for Nitrogen Sensor. *IOSR J. Appl. Chem.* **2014**, *7*, 49–52. [CrossRef]
17. Peng, N.; Zhang, Q.; Chow, C.L.; Tan, O.K.; Marzari, N. Sensing Mechanisms for Carbon Nanotube Based $NH_3$ Gas Detection. *Nano Lett.* **2009**, *9*, 1626–1630. [CrossRef]
18. Karthigeyan, A.; Gupta, R.P.; Scharnagl, K.; Burgmair, M.; Sharma, S.K.; Eisele, I. A room temperature HSGFET ammonia sensor based on iridium oxide thin filmsmall size electronic nose. *Sens. Actuators B Chem.* **2002**, *85*, 145–153. [CrossRef]

19. Zhao, Y.; Hernandez-Pagan, E.A.; Vargas-Barbosa, N.M.; Dysart, J.L.; Mallouk, T.E. A high yield synthesis of ligand-free iridium oxide nanoparticles with high electrocatalytic activity. *J. Phys. Chem. Lett.* **2011**, *2*, 402–406. [CrossRef]
20. Dresselhaus, M.S.; Jorio, A.; Hofmann, M.; Dresselhaus, G.; Saito, R. Perspectives on carbon nanotubes and graphene Raman spectroscopy. *Nano Lett.* **2010**, *10*, 751–758. [CrossRef]
21. Korotcov, A.V.; Huang, Y.-S.; Tiong, K.-K.; Tsai, D.-S. Raman scattering characterization of well-aligned $RuO_2$ and $IrO_2$ nanocrystals. *J. Raman Spectrosc.* **2007**, *38*, 1538–1553. [CrossRef]
22. D'Acunto, G.; Ripanti, F.; Postorino, P.; Betti, M.G.; Scardamaglia, M.; Bittencourt, C.; Mariani, C. Channelling and induced defects at ion-bombarded aligned multiwall carbon nanotubes. *Carbon* **2018**, *139*, 768–775. [CrossRef]
23. Bittencourt, C.; Felten, A.; Douhard, B.; Ghijsen, J.; Johnson, R.L.; Drube, W.; Pireaux, J.-J. Photoemission studies of gold clusters thermally evaporated on multiwall carbon nanotubes. *Chem. Phys.* **2006**, *328*, 385–391. [CrossRef]
24. Chen, C.; Liang, B.; Ogino, A.; Wang, X.; Nagatsu, M. Oxygen Functionalization of Multiwall Carbon Nanotubes by Microwave-Excited Surface-Wave Plasma Treatment. *J. Phys. Chem. C* **2009**, *113*, 7659–7665. [CrossRef]
25. Casella, I.G.; Contursi, M.; Toniolo, R. Anodic electrodeposition of iridium oxide particles on glassy carbon surfaces and their electrochemical/SEM/XPS characterization. *J. Electroanal. Chem.* **2015**, *736*, 147–152. [CrossRef]
26. Kötz, R.; Neff, H.; Stucki, S. Anodic Iridium Oxide Films. *J. Electrochem. Soc.* **1984**, *131*, 72. [CrossRef]
27. Liu, L.; Ye, X.; Wu, K.; Han, R.; Zhou, Z.; Cui, T. Humidity Sensitivity of Multi-Walled Carbon Nanotube Networks Deposited by Dielectrophoresis. *Sensors* **2009**, *9*, 1714–1721. [CrossRef]
28. Shrivastava, A.; Gupta, V.B. Methods for the determination of limit of detection and limit of quantitation of the analytical methods. *Chronicles Young Sci.* **2011**, *2*, 21–25. [CrossRef]
29. Ammonia. Available online: https://www.cdc.gov/niosh/pel88/7664-41.html (accessed on 7 August 2018).
30. Forootan, A.; Sjöback, R.; Björkman, J.; Sjögreen, B.; Linz, L.; Kubista, M. Methods to determine limit of detection and limit of quantification in quantitative real-time PCR (qPCR). *Biomol. Detect. Quantif.* **2017**, *12*, 1–6. [CrossRef]
31. Air Quality Standards. Available online: http://ec.europa.eu/environment/air/quality/standards.htm (accessed on 7 August 2018).
32. NAAQS Table. Available online: https://www.epa.gov/criteria-air-pollutants/naaqs-table (accessed on 7 August 2018).
33. Tang, R.; Shi, Y.; Hou, Z.; Wei, L. Carbon nanotube-based chemiresistive sensors. *Sensors* **2017**, *17*, 882. [CrossRef]
34. Wang, C.; Yin, L.; Zhang, L.; Xiang, D.; Gao, R. Metal oxide gas sensors: Sensitivity and influencing factors. *Sensors* **2010**, *10*, 2088–2106. [CrossRef] [PubMed]
35. Shankar, P.; Bosco, J.; Rayappan, B. Gas sensing mechanism of metal oxides: The role of ambient atmosphere, type of semiconductor and gases—A review. *Sci. Lett. J.* **2015**, *4*, 126.
36. Rout, C.S.; Hegde, M.; Govindaraj, A.; Rao, C.N.R. Ammonia sensors based on metal oxide nanostructures. *Nanotechnology* **2007**, *18*, 205504. [CrossRef]
37. Leghrib, R.; Dufour, T.; Demoisson, F.; Claessens, N.; Reniers, F.; Llobet, E. Gas sensing properties of multiwall carbon nanotubes decorated with rhodium nanoparticles. *Sens. Actuators B Chem.* **2011**, *160*, 974–980. [CrossRef]
38. Sayago, I.; Santos, H.; Horrillo, M.C.; Aleixandre, M.; Fernández, M.J.; Terrado, E.; Tacchini, I.; Aroz, R.; Maser, W.K.; Benito, A.M.; et al. Carbon nanotube networks as gas sensors for $NO_2$ detection. *Talanta* **2008**, *77*, 758–764. [CrossRef]
39. Rahmani, M.B.; Breedon, M.; Lau, D.; Campbell, J.L.; Moafi, A.; McCulloch, D.G.; Wlodarski, W.; Kalantar-Zadeh, K. Gas sensing properties of interconnected ZnO nanowires. *Sens. Lett.* **2011**, *9*, 1–7. [CrossRef]
40. Han, J.W.; Kim, B.; Li, J.; Meyyappan, M. Carbon nanotube based humidity sensor on cellulose paper. *J. Phys. Chem. C* **2012**, *116*, 22094–22097. [CrossRef]
41. Chen, W.-P.; Zhao, Z.-G.; Liu, X.-W.; Zhang, Z.-X.; Suo, C.-G. A Capacitive Humidity Sensor Based on Multi-Wall Carbon Nanotubes (MWCNTs). *Sensors* **2009**, *9*, 7431–7444. [CrossRef]

42. Zhao, Z.G.; Liu, X.W.; Chen, W.P.; Li, T. Carbon nanotubes humidity sensor based on high testing frequencies. *Sens. Actuators A Phys.* **2011**, *168*, 10–13. [CrossRef]
43. Roso, S.; Degler, D.; Llobet, E.; Barsan, N.; Urakawa, A. Temperature-Dependent $NO_2$ Sensing Mechanisms over Indium Oxide. *ACS Sens.* **2017**, *2*, 1272–1277. [CrossRef]
44. Mudimela, P.R.; Scardamaglia, M.; González-León, O.; Reckinger, N.; Snyders, R.; Llobet, E.; Bittencourt, C.; Colomer, J.F. Gas sensing with gold-decorated vertically aligned carbon nanotubes. *Beilstein J. Nanotechnol.* **2014**, *5*, 910–918. [CrossRef] [PubMed]
45. Baccar, H.; Thamri, A.; Clément, P.; Llobet, E.; Abdelghani, A. Pt- and Pd-decorated MWCNTs for vapour and gas detection at room temperature. *Beilstein J. Nanotechnol.* **2015**, *6*, 919–927. [CrossRef] [PubMed]
46. Leghrib, R.; Llobet, E.; Pavelko, R.; Vasiliev, A.A.; Felten, A.; Pireaux, J.J. Gas sensing properties of MWCNTs decorated with gold or tin oxide nanoparticles. *Procedia Chem.* **2009**, *1*, 168–171. [CrossRef]
47. Kwon, Y.J.; Mirzaei, A.; Kang, S.Y.; Choi, M.S.; Bang, J.H.; Kim, S.S.; Kim, H.W. Synthesis, characterization and gas sensing properties of ZnO-decorated MWCNTs. *Appl. Surf. Sci.* **2017**, *413*, 242–252. [CrossRef]
48. Nguyen, L.Q.; Phan, P.Q.; Duong, H.N.; Nguyen, C.D.; Nguyen, L.H. Enhancement of $NH_3$ gas sensitivity at room temperature by carbon nanotube-based sensor coated with Co nanoparticles. *Sensors* **2013**, *13*, 1754–1762. [CrossRef] [PubMed]
49. Young, S.J.; Lin, Z.D. Ammonia gas sensors with Au-decorated carbon nanotubes. *Microsyst. Technol.* **2018**, *24*, 4207–4210. [CrossRef]
50. Choi, H.H.; Lee, J.; Dong, K.Y.; Ju, B.K.; Lee, W. Noxious gas detection using carbon nanotubes with Pd nanoparticles. *Nanoscale Res. Lett.* **2011**, *6*, 1–6. [CrossRef]
51. Lich, N.Q.; Thanh, T.P.; Truong, D.V.; Kien, P.T.; Tu, N.C.; Bac, L.H.; Vuong, D.D.; Chien, N.D.; Lam, N.H. Pt- and Ag-Decorated Carbon Nanotube Network Layers for Enhanced $NH_3$ Gas Sensitivity at Room Temperature. *Mater. Trans.* **2015**, *56*, 1399–1402. [CrossRef]

Section 2.2

# Wet Chemistry Route for the Decoration of Carbon Nanotubes with Iron Oxide Nanoparticles for Gas Sensing

Hussam M. Elnabawy, Juan Casanova-Chafer, Badawi Anis, Mostafa Fedawy, Mattia Scardamaglia, Carla Bittencourt, Ahmed S. G. Khalil, Eduard Llobet, Xavier Vilanova

*Beilstein Journal of Nanotechnology, 10 (2019) 105-118*

DOI: 10.3762/bjnano.10.10

UNIVERSITAT ROVIRA I VIRGILI
GAS SENSING WITH MODIFIED CARBON NANOTUBES, GRAPHENE AND DIAMONDOIDS
Juan Casanova Cháfer

BEILSTEIN JOURNAL OF NANOTECHNOLOGY

# Wet chemistry route for the decoration of carbon nanotubes with iron oxide nanoparticles for gas sensing

Hussam M. Elnabawy[1], Juan Casanova-Chafer[2], Badawi Anis[3], Mostafa Fedawy[1], Mattia Scardamaglia[4], Carla Bittencourt[4], Ahmed S. G. Khalil[5], Eduard Llobet[2] and Xavier Vilanova[*2]

Full Research Paper

Open Access

Address:
[1]Electronics & Communications Department, Faculty of Engineering, Arab Academy for Science and Technology & Maritime Transport, Cairo, Egypt, [2]MINOS-EMaS, Universitat Rovira i Virgili, Avda. Països Catalans, 26, 43007 Tarragona, Spain, [3]Spectroscopy Department, Physics Division, National Research Centre, 33 El Bohouth st. (former El Tahrir st.), P.O. 12622 Dokki, Giza, Egypt, [4]Chemistry of Interaction Plasma Surface (ChIPS), University of Mons, 7000 Mons, Belgium and [5]Physics Department & Center for Environmental and Smart Technology (CEST), Faculty of Science, Fayoum University, Fayoum, Egypt

Email:
Xavier Vilanova[*] - xavier.vilanova@urv.cat

* Corresponding author

Keywords:
benzene detection; doping; gas sensor; metal nanoparticle decoration; multiwalled carbon nanotubes; $NO_2$ detection; room temperature gas sensing; surface modification

*Beilstein J. Nanotechnol.* **2019,** *10,* 105–118.
doi:10.3762/bjnano.10.10

Received: 07 August 2018
Accepted: 29 November 2018
Published: 09 January 2019

Associate Editor: N. Motta



## Abstract

In this work, we investigated the parameters for decorating multiwalled carbon nanotubes with iron oxide nanoparticles using a new, inexpensive approach based on wet chemistry. The effect of process parameters such as the solvent used, the amount of iron salt or the calcination time on the morphology, decoration density and nanocluster size were studied. With the proposed approach, the decoration density can be adjusted by selecting the appropriate ratio of carbon nanotubes/iron salt, while nanoparticle size can be modulated by controlling the calcination period. Pristine and iron-decorated carbon nanotubes were deposited on silicon substrates to investigate their gas sensing properties. It was found that loading with iron oxide nanoparticles substantially ameliorated the response towards nitrogen dioxide.

## Introduction

Carbon nanotubes (CNTs) are considered to be a very interesting material, especially after being rediscovered by Sumio Iijima in 1991 when he found multiwalled CNTs in carbon soot prepared by arc discharge [1]. During the past years, CNTs have proved to possess extraordinary electrical, mechanical, physical and chemical properties [2,3]. In particular, they have been ex-

*Beilstein J. Nanotechnol.* **2019,** *10,* 105–118.

tensively researched in gas sensing applications because of their high thermal and chemical stability, high adsorption capacity and suitability for being functionalized, which enables tailoring (to some extent) their sensitivity and selectivity to the chemical environment [2-5]. CNT gas sensors often exhibit fair sensitivity to gases even when operated at room temperature. Since their electrical conductivity is affected upon the adsorption of gases, their response is often measured as a change in resistance of a CNT film. The fact that CNT gas sensors can be intrinsically low-power devices make them very attractive for their integration in ubiquitous, unattended mobile sensing nodes running on small batteries or on energy harvested from their environment [4].

Among the wide range of functionalization strategies that can be envisaged for tailoring the selectivity of CNTs towards target gases, one of the simplest consists of decorating the outer wall of CNTs with metal or metal oxide nanoparticles [6-9]. In some cases, metal or metal oxide nanoparticles show interesting catalytic properties for the decomposition of target molecules into more reactive species that, in turn, interact with CNTs. In addition, such nanoparticles shift the Fermi level of CNTs, adsorb target molecules, and help in mediating the charge transfer between adsorbates and CNTs [6,10].

Several metal oxides have been reported as useful for decorating CNTs and improving their interaction with gas molecules. Sensitivity and selectivity can be tailored by selecting the type of metal oxide employed, the size of nanoparticles and the decoration density or loading [6,10,11]. Metal oxides have been extensively investigated for sensing a wide range of gases [12-14]. Among them, iron oxide is a semiconductor that has been used in many gas sensing applications because of its low cost and simple preparation [14,15]. This oxide has been used in the detection of acetone, $H_2S$, several alcohols, CO, acetic acid and liquefied petroleum gas (LPG) [16] and forming composites with other materials such as graphene oxide or polyaniline has been reported to detect $NO_2$ [17,18]. The decoration of CNTs with iron oxide has been reported for sensing different species in air such as acetone, $CO_2$ and some volatile organic compounds [19-21]. Moreover, composites made of CNTs and iron oxide have been also used for sensing ammonia and $NO_x$ [22,23]. Among those gases $NO_2$ is considered one of the most dangerous air pollutants occurring both indoors, due to using of gas stoves, and outdoors from fuel powered motor vehicles and power plants especially in long-term exposure conditions. As research studies show, exposure to this gas can lead to an increase in oxidative stress in the body, resulting in behavioral and learning-memory impairments. Also, there is a consistent relationship between $NO_2$ and respiratory and asthmatic problems at mean daily concentrations (20–80 ppb) well below air quality guidelines [24,25], which indicates the importance of fabricating such a gas sensor to be used in different applications.

In this paper, we report on a wet chemistry route that was successfully employed to chemically modify CNTs by decorating them with iron oxide nanoparticles. This inexpensive method allows control of the decoration density and nanoparticle size. The effects of changing the process parameters on the morphology of CNTs, the size of iron oxide nanoparticles and the decoration homogeneity achieved are studied and discussed in detail. The morphology, quality and chemical composition of the iron oxide decorated carbon nanotube samples were investigated employing transmission electron microscopy (TEM), Raman spectroscopy and X-ray photoelectron spectroscopy (XPS).

The differently decorated CNT samples were used to make gas sensors for detecting nitrogen dioxide. A study of the gas sensing properties of the different hybrid nanomaterials was conducted in an effort to determine the optimal functionalization parameters to maximize sensor response. The selectivity of the resulting layer for potential interfering gases such as CO and benzene has also been investigated as well as the effect of ambient humidity.

# Experimental

## Materials

All materials and reagents used (listed below) were of analytical grade and were used as received.

- COOH functionalized multiwalled carbon nanotube (MWCNTs), Nanocyl (C purity higher than 95%)
- Nitric acid, Scharlau ($HNO_3$ 68–70%)
- Sulfuric acid, J. T. Baker ($H_2SO_4$ 95–97%)
- Conductive silver paste, Sigma-Aldrich
- Methanol, Scharlau ($CH_3OH$ 99.9%)
- Ethanol, Scharlau ($C_2H_5OH$ 96% extra pure and 99.5% absolute)
- Acetone, Scharlau ($C_3H_6O$ 99.5%)
- Dimethylformamide (DMF), Alfa Aesar ($C_3H_7NO$ 99.8%)
- Iron(III) nitrate nonahydrate, Sigma-Aldrich ($Fe(NO_3)_3{\cdot}9H_2O$ 99.95% trace metal basic)
- Acetic acid, Fluka Analytical ($CH_3COOH$ 99.8%)

## Decoration and characterization of carbon nanotubes

Commercial CNTs from Nanocyl functionalized with (COOH) groups were further chemically purified by an acidic treatment to remove any traces of catalyst or amorphous carbon. This treatment also helps in creating more active sites (e.g., some

defects) on the side walls of the carbon nanotubes, preparing them for the decoration process. A mixture of $H_2SO_4$ and $HNO_3$ was prepared at a ratio of 3:1. 200 mg of CNTs were mixed with 12 mL of the acidic mixture and were stirred for one hour at room temperature. The reaction was exothermic and no cooling or water baths were used. During the reaction, ultrasonication was employed for the first 15 minutes only to assure the debundling of CNTs without damaging them. During the remaining 45 minutes, the mixture was stirred employing a magnetic stirrer [19,26,27].

When the acidic treatment was completed, the resulting black slurry was filtered out from the acidic mixture using vacuum filtration and then washed with DI water for several washing cycles until the pH was neutralized. Then, the neutral black slurry was dried in a drying oven at 80 °C for 4 hours.

For the decoration of carbon nanotubes, iron(III) nitrate nonahydrate was used as the iron precursor. 50 mg of the acidic-activated carbon nanotubes were added to 50 mL of solvent together with a corresponding amount of $Fe(NO_3)_3{\cdot}9H_2O$ salt. Different solvents, methanol, ethanol, acetone and DMF, as well as different amounts of salt (with ratios 1:1, 1:1.3 and 1:1.5 for CNT/Fe weights) were tested to check the effect of both parameters in the effectiveness of the decoration. The mixtures were stirred using a magnetic stirrer for 60 minutes. In a first attempt, the mixtures were heated to 80 °C to completely evaporate the solvent. This approach did not succeed, as commented in the results and discussion section, so a new approach was designed. In this second attempt, the mixtures were heated to 80 °C until 40 mL of the solvent was evaporated. The remaining solution was then ultrasonicated for 15 minutes then heated at 80 °C on a hotplate with a magnetic stirrer till the complete evaporation of the solvent. Once dried, the resulting powder was exposed to vapors of acetic acid for 15 minutes and later heated for 20 minutes at 80 °C to remove all the physically absorbed acetic acid [28]. Finally, the powder was calcined at 450 °C during either 15 or 30 minutes. In this way the effect of the calcination time on the decoration process was also evaluated.

The chemical composition of the decorated CNTs were measured by X-ray photoelectron spectroscopy (XPS) using a Versaprobe PHI 5000 from Physical Electronics, equipped with a monochromatic Al Kα X-ray source at a base pressure of about $10^{-9}$ mbar. The sample powders were mounted on double-sided conductive vacuum tape. The X-ray photoelectron spectra were collected at a take-off angle of 45° with respect to the electron energy analyzer and the spot size was 200 µm. A pass energy (PE) of 20 eV was used for the high-resolution spectra (Fe 2p, C 1s and O 1s), while PE = 100 eV was used for the survey spectrum, accounting for an overall energy resolution of about 0.5 eV. Different points on each sample were measured in order to ensure the homogeneity. The chemical composition was then evaluated by using CASA XPS software.

TEM images were collected using a JEOL 1011 transmission electron microscope operating at 100 kV. The samples were dispersed in ethanol and a drop of resultant suspension was poured on carbon-coated copper grids.

The Raman spectra for the different samples was characterized using a Renishaw inVia spectrometer as the powder samples were mounted on clean glass slides. The samples were excited with a green (514 nm) laser using 50% laser power and the exposure time was 10 s.

X-ray diffraction (XRD) patterns were recorded at room temperature using a 202964 Panalytical Empryan diffractometer (Central Laboratory, Beni Suef University, Egypt) with a Cu Kα monochromatic radiation ($k$ = 1.54056) operating at 40 kV and 30 mA from 5.0200° to 79.9800° with a 2θ step size of 0.0400 and a scan step time of 0.50 s in a continuous scanning mode.

## Fabrication and testing of gas sensors

In order to check the effect of the different decorations on the gas sensing properties of modified CNTs, simple sensing devices were fabricated. For that purpose, small rectangular pieces of a silicon wafer, previously oxidized at 1100 °C for 6 hours, were used as substrate. Heaters were attached to the back side of the sensor substrate using silver paste from Sigma-Aldrich. The substrates were heated in the oven at 120 °C for 30 minutes to cure the silver paste.

A dispersion in DMF was prepared with a concentration of 0.1 mg/mL of the modified CNT samples to be deposited. Then, the solution was ultrasonicated for 15 minutes before being deposited onto the silicon substrates. Two different approaches were used for depositing iron-loaded CNT films on the substrates: drop coating and air brushing. In drop coating, the substrate was heated on a hot plate up to 160 °C while the dispersion of CNTs in DMF was dropped by means of a pipette (drop by drop). The DMF was instantaneously evaporated when the drop was in contact with the heated silicon substrate, leaving the iron-loaded CNTs physically attached to it. In air brushing, the substrate was also heated to 160 °C while the suspension of CNTs in DMF was airbrushed onto the top of the substrate. As in the previous case, the solvent was instantaneously evaporated when in contact with the heated substrate, leaving the iron-loaded CNTs physically attached to it. To delimitate the area where the CNTs were deposited, a shadow mask of adhesive Kapton was used. This second approach leads to thinner active

layers. The differences in the results for both approaches can be seen in the Supporting Information File 1 (Figure S1).

After the previous steps, heaters and the CNT layer were connected to a printed circuit board (PCB) using platinum wires. Those wires were attached to the heaters and CNT layers using silver paste that was cured in an oven at 120 °C for 30 minutes. To connect the Pt wires to the PCB we used tin wire and a soldering iron.

Wire bonded sensors ready for testing can be seen in the Supporting Information File 2 (Figure S2). The silicon substrates onto which carbon nanotubes were deposited were glued to an alumina substrate that included a platinum heater employing a thermally conductive epoxy.

A teflon chamber, which allowed allocating up to four sensors, was used for testing the gas sensing properties of the different nanomaterials. This chamber is shown in Supporting Information File 3 (Figure S3). A gas cylinder with a 100 ppm $NO_2$ concentration balanced in dry air was used jointly with a set of mass flow controllers to generate the desired concentrations. The gas flux was fixed to 100 sccm during the whole experiments. The sensor response is defined as

$$\left(R_G - R_0\right)/R_0 \quad (1)$$

where $R_G$ is the sensor resistance when exposed to $NO_2$ and $R_0$ is the sensor response when exposed to air.

Before starting any experiment, the sensors were heated while dry synthetic air was flowed in order to clean the sensor surface. Afterwards, different concentrations of $NO_2$ gas (5 ppm, 10 ppm, 20 ppm, 50 ppm and 100 ppm) were successively pumped into the test chamber with the sensors operated at room temperature. The cycles consisted of 30 minutes of exposure to $NO_2$ diluted in air and 3 hours of recovery in dry air.

To determine the selectivity of the sensor for carbon monoxide (CO) and benzene ($C_6H_6$), gas cylinders with a 100 ppm CO and 10 ppm $C_6H_6$ concentrations respectively, balanced in dry air, were used with the previously described set-up. To create the desired humidity in order to check the effect of moisture on the sensor response, a controlled amount of water was mixed with the gas flow by means a liquid mass flow controller.

## Results and Discussion

### Acidic purification and decoration of carbon nanotubes

Figure 1 shows TEM images for the CNTs before and after the acidic treatment and, as shown, no significant changes are visible in the carbon nanotubes.

Since using the first approach for the decoration of CNTs led to the formation of large agglomerates of iron-loaded carbon nanotubes that could not be dispersed even after a sonication process in ethanol for 30 minutes (as can be seen in Figure S4, in Supporting Information File 4), this first approach was discarded and we focused our efforts in the second approach.

Accordingly, the next step was to determine the best solvent for obtaining a well dispersed powder with homogeneous nanoparticle coverage. To analyze the effect of the solvent on the nanoparticle distribution, solutions with the four solvents considered (ethanol, methanol, acetone and DMF) were prepared using a

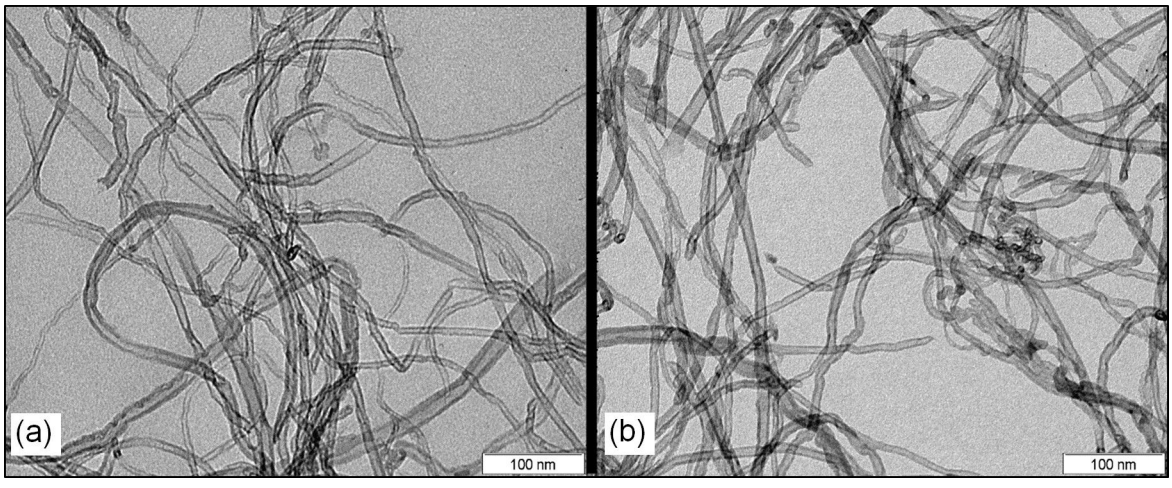


**Figure 1:** TEM images for COOH–CNTs (a) before acidic treatment and (b) after acidic treatment.

1:1.5 proportion in weight between carbon nanotubes and iron(III) nitrate nonahydrate and calcined for 30 minutes. TEM images of the results are summarized in Figure 2. As can be seen, both ethanol and methanol led to a homogenous distribution of the nanoparticles onto the carbon nanotubes. Moreover, the size of the nanoparticles in those cases was also homogeneous. Nevertheless, the decoration homogeneity was slightly better for methanol than for ethanol. On the other hand, acetone and DMF had a negative effect on both the decoration distribution and particle size. As we can see in the case of acetone, the dispersion of the nanoclusters is not uniform or homogenous and some areas have high decoration density while some other areas have very low decoration density. Also, in the case of DMF we can notice that dispersion of the nanoclusters was better than for acetone, but still some areas have a high density of decoration in which agglomerates of large particle size are formed.

According to these results, methanol was chosen as the most suitable solvent to be used in the production of iron-loaded CNT samples for further analysis, including the production of gas sensors.

Once the best solvent was identified, it was necessary to determine the effect of the amount of iron oxide precursor employed on the decoration results (i.e., density and homogeneity of the loading, particle size). TEM images for different samples with different CNT/iron salt ratios were taken to investigate their effect on the decoration density, as shown in Figure 3. We can see that decoration density of CNT/Fe oxide increases by increasing the amount of iron salt, while the particle size was not affected.

Statistical analysis for the three samples shows that the average particle size of the NP does not increase when increasing the decoration dose. The mean particle size was found to be 3.44, 3.46 and 3.31 nm for decoration ratios of 1:1, 1:1.3 and 1:1.5, respectively (size distribution histograms can be found in Supporting Information File 5, Figure S6).

For all the decorated samples we have used the same source of acidic-functionalized MWCNTs. Accordingly, all the MWCNTs used have, more or less, the same defect size and distribution on the side walls. As the amount of iron salt increases, more iron precursor will be able to reach and interact

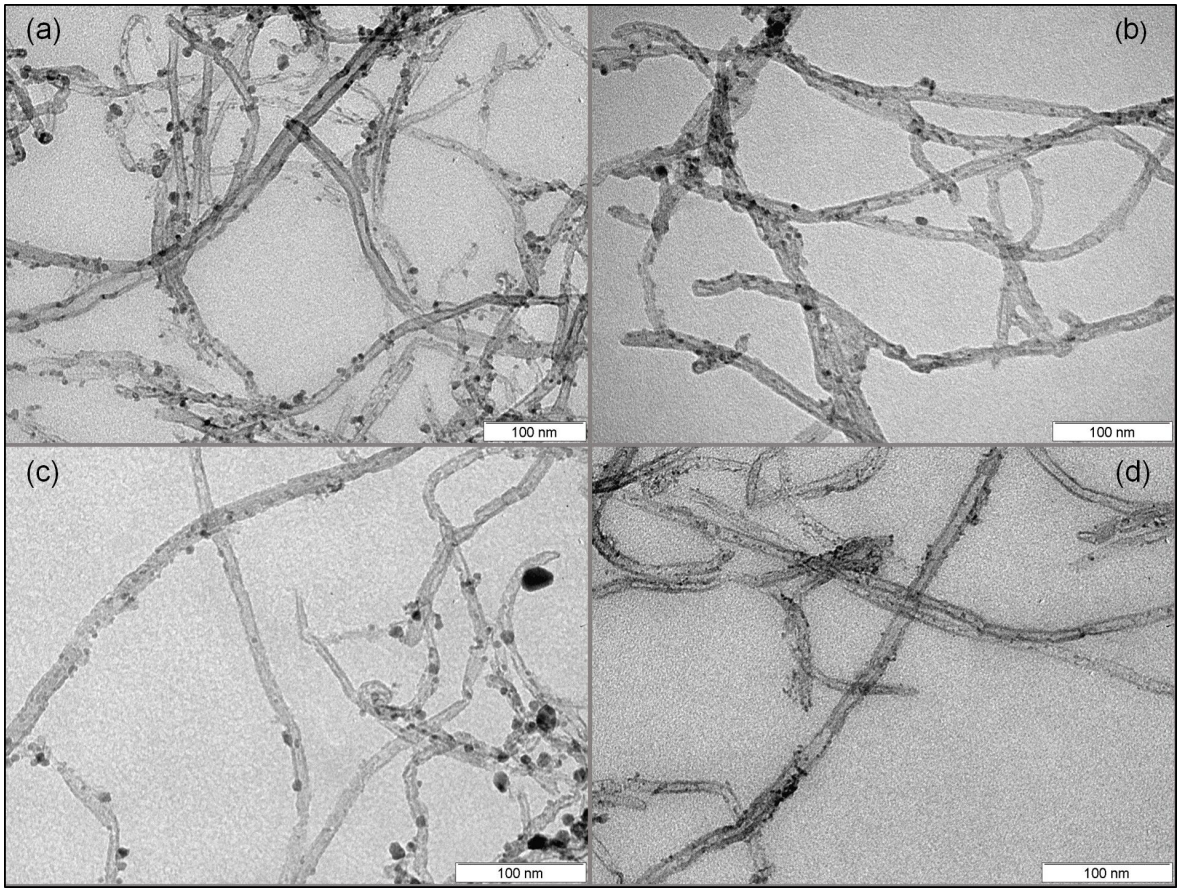


**Figure 2:** Different decoration homogeneity using different solvents, methanol (a), ethanol (b), DMF (c) and acetone (d).

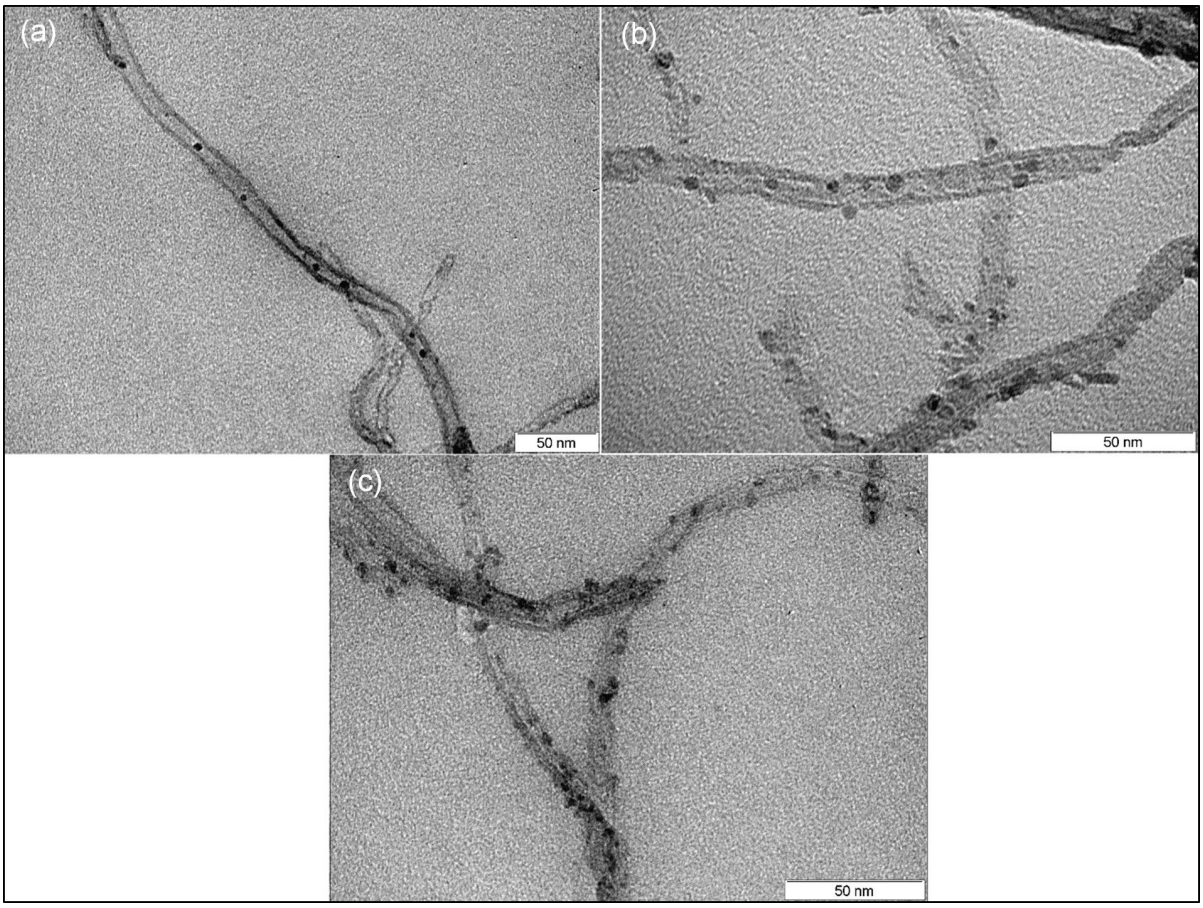


**Figure 3:** Different decoration densities for different decoration ratios of 1:1 (a), 1:1.3 (b) and 1:1.5 (c).

with a larger number of defects on the MWCNTs side walls. Therefore, the density of the formed iron nanoparticles will increase. However, the average particle size of those nanoparticles will be the same because the side defects have the same size distribution for all samples.

In addition, HRTEM imaging for the anchored iron oxide nanoparticles on the MWCNTs surface was performed and the selected area electron diffraction (SAED) pattern for was identified, as shown in Figure 4. The image shows the high crystallinity of the prepared iron oxide nanoparticles and the selected area electron diffraction (SAED) pattern of the iron oxide nanoparticles (see inset of Figure 4) clearly shows the diffraction rings of a typical cubic structure.

XPS was performed to investigate the chemical composition of the samples and, in particular, to determine the oxidation state of iron in the nanoparticles that decorate the CNT sidewalls. These results are shown in Figure 5. A description and coding of the samples analyzed as well as their chemical composition derived from the XPS analysis is summarized in Table 1. The

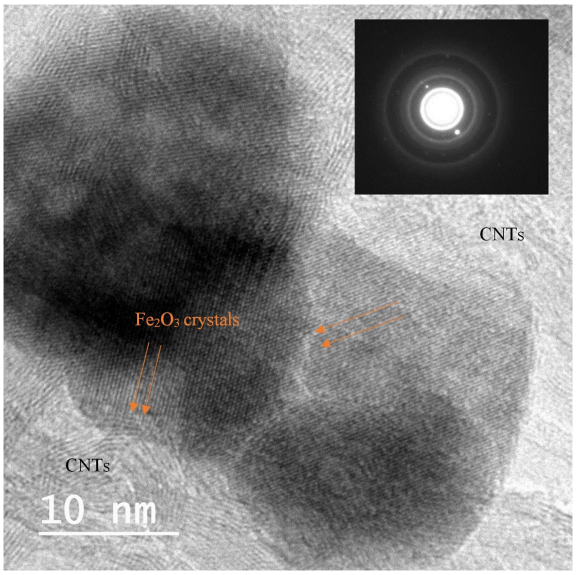


**Figure 4:** High magnification HRTEM images of MWCNTs decorated with $Fe_2O_3$ nanoparticles. The inset shows the electron diffraction pattern (SAED) for the selected area.

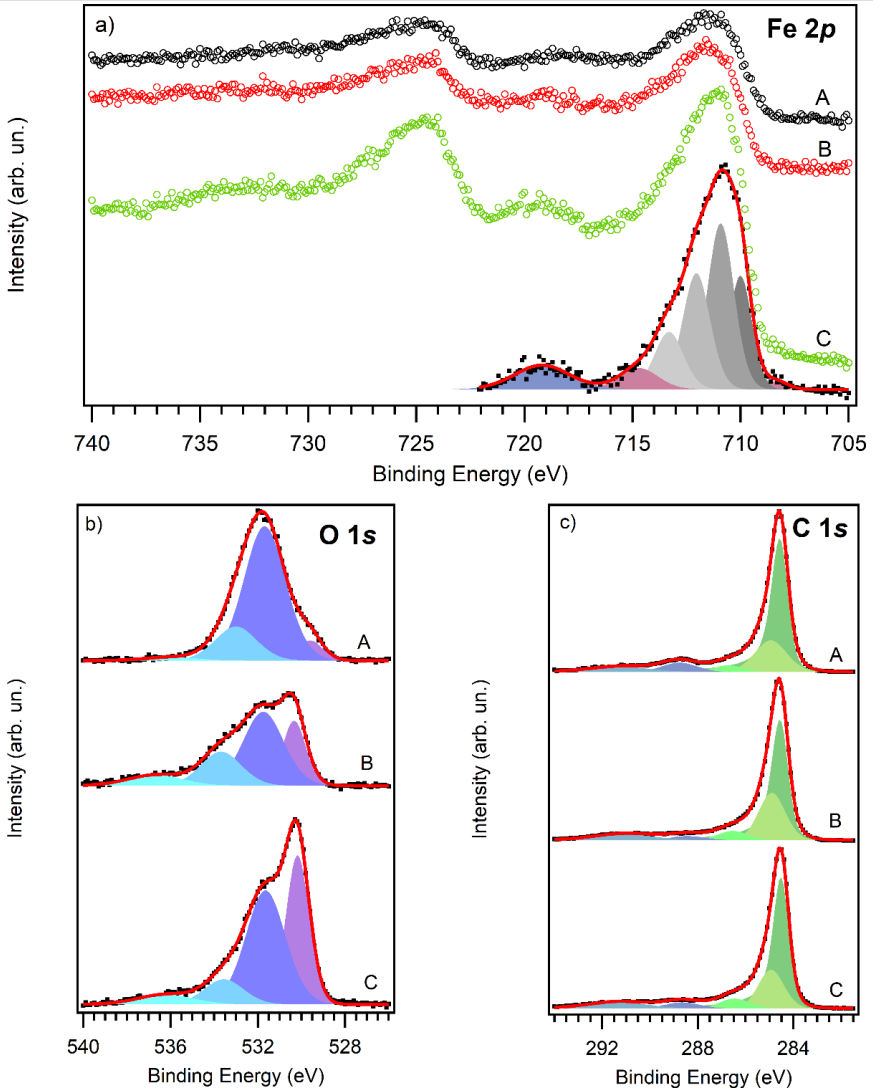


**Figure 5:** XPS core level spectra of Fe 2p with a fitting curve for sample C (a), O 1s (b) and C 1s (c) for the samples A (black curve), B (red curve) and C (green curve). The C 1s spectra has been normalized and aligned.

**Table 1:** Description of the analyzed samples with the percent of different elements in each sample.

| Sample | Description | C (%) | O (%) | Fe (%) |
|---|---|---|---|---|
| A | 2nd decorating approach with a ratio of (1 CNT/1 Fe salt); not calcined | 78.0 | 17.0 | 2.9 |
| B | 2nd decorating approach with a ratio of (1 CNT/1 Fe salt); calcined for 30 minutes | 86.0 | 11.0 | 2.5 |
| C | 2nd decorating approach with a ratio of (1 CNT/1.5 Fe salt); calcined for 30 minutes | 75.0 | 19.0 | 5.7 |

values of the content for each element have been evaluated at different points on the sample and averaged, with an error as low as ±0.5%. The concentration of iron well reflects the decorating ratio, with sample C (1 CNT/1.5 Fe Salt) being the one with the highest Fe content. Residual nitrogen and sodium can be found in samples A and C respectively, which is probably due to some contamination during the fabrication process that we assume will not affect sensor performance.

Figure 5a shows the typical Fe 2p XPS spectrum recorded on the studied samples. The spectrum is composed of two main structures centered at 712 and 725 eV corresponding to photoelectrons emitted from Fe $2p_{3/2}$ and Fe $2p_{1/2}$, respectively. Two satellite structures are also present centered at 719 and 733 eV. As can be seen in the figure, the Fe $2p_{3/2}$ region for sample C can be reproduced using a decomposition of four peaks (grey components), plus a surface peak (purple component) and a

shake-up satellite (blue component) according to Grosvenor et al. [29]. The energy position of these peaks, in particular the first one of the 4-component multiplet (710.0 eV) and the satellite (719.2 eV), indicates the presence of iron in the Fe(III) oxidation state ($Fe^{3+}$), characteristic of $Fe_2O_3$ and oxide-hydroxide. It is reported that the typical value for the satellite peak of $Fe^{2+}$ (FeO) is 715.5 eV [30] and main 2p peak centered at 708 eV [31], while metallic iron has the main peak at much lower binding energy (706.7 eV).

The O 1s core level spectra, shown in Figure 5b, was reproduced using four peaks. The first one at 530.2 eV is attributed to oxygen in iron oxide: its contribution is higher in the spectra recorded on sample C, where the relative amount of iron was found to be the highest. The peak at 531.7 eV is mostly due to hydroxyl OH and O–C groups, while the remaining two peaks are attributed to other O–C groups and adsorbed water [32,33].

C–O contributions can be also observed in the C 1s core level spectra in Figure 5c by the presence of the peak at 288.6 eV. This contribution is higher in the spectrum recorded on sample A, where the highest amount of oxygen was found. The line shape of the C1s spectra recorded is typical for carbon nanotubes, with an asymmetric and narrow $sp^2$ peak at 284.5 eV; this is followed by a second contribution due to carbon in amorphous or $sp^3$ configuration at 285.0 eV [34]. The presence of these peaks associated with C–O bonds indicates that the functionalization of the CNTs (with COOH) is still present after the decoration process.

The fact that the nanoparticles consisted of $Fe_2O_3$ was further confirmed by XRD characterization. For this purpose, pure iron oxide nanoparticles were prepared following the procedure described above. Figure 6 shows the spectra of the iron oxide nanoparticles and iron oxide nanoparticle-decorated nanotubes. These last results correspond to the sample with a 1:1 decoration ratio and calcined for 30 min. As it can be seen, the pattern of the $Fe_2O_3$ nanoparticles corresponds to a cubic crystalline structure, which confirms the HRTEM results. In the XRD pattern for $Fe_2O_3$/CNTs the characteristic peak at 25.994° attributed to plane (002) of the CNTs can be clearly identified. The other diffraction peaks at 35.6°, 43.15°, 53.28°, 57.3°, 63.12° can be attributed to planes (311), (400), (422), (511) and (440) of the cubic $Fe_2O_3$ phase.

## Gas sensing properties

Samples B and C were used to prepare sensors using the drop-coating approach to check the effect of decoration ratio on the response. An additional sensor was prepared using pristine carbon nanotubes with the airbrushing approach. Figure 7 shows electrical resistance against time.

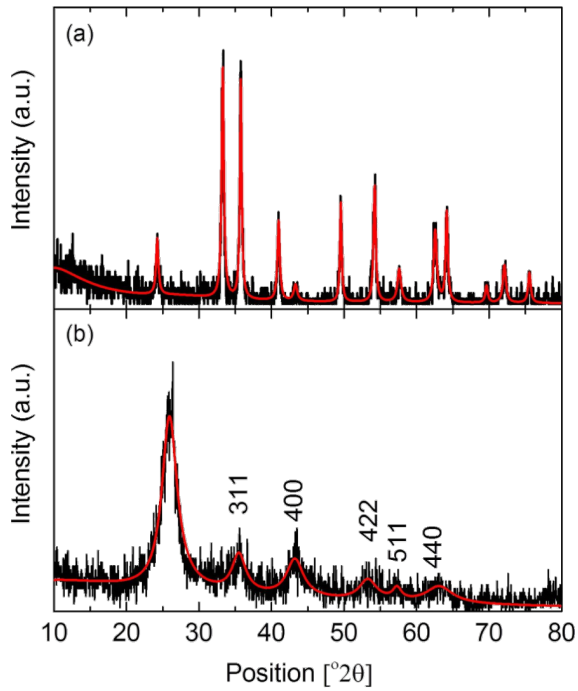


**Figure 6:** XRD pattern for $Fe_2O_3$ nanoparticles (a) and decorated CNTs with $Fe_2O_3$ nanoparticles (b).

Nitrogen dioxide was found to strongly interact with carbon nanotube sensors, and as a result, the sensors did not fully recover their baseline resistance value during the cleaning phase, which was conducted at room temperature without heating. Applying mild heating or UV light have been reported useful for fully recovering the baseline after exposure to nitrogen dioxide [10]. Therefore, for calculating the response to any given nitrogen dioxide concentration, the value of $R_0$ was taken as the value of the sensor resistance before being exposed to the corresponding gas concentration and the value of $R_G$ was fixed as the value of resistance at a fixed time after an $NO_2$ exposure of 10 minutes.

Figure 8 shows the calibration curves for different concentrations of $NO_2$. Response (%) is defined as $100 \times (R_G - R_0)/R_0$. As derived from Figure 8, Sample B with a 1:1 decoration ratio shows better response than sample C and obviously better than pristine CNTs.

These results allow us to conclude that the decoration with iron oxide improves sensor performance in the detection of $NO_2$. Regarding the amount of iron oxide introduced, the best result is obtained for the lower decoration ratio of 1:1 which is considered to be the optimum decoration ratio.

By comparing these results to other results in the literature, we can conclude that there is an optimum decoration ratio which

*Beilstein J. Nanotechnol.* **2019,** *10,* 105–118.

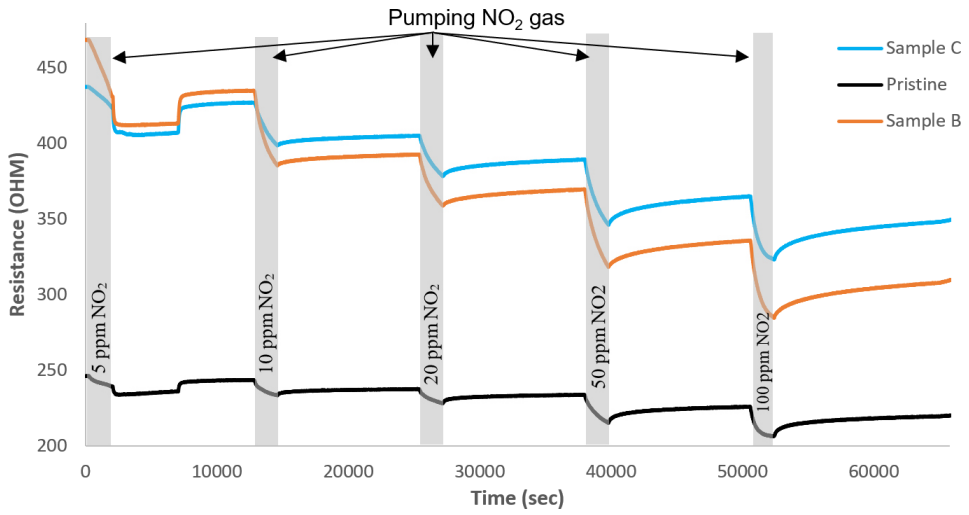


**Figure 7:** Electrical resistance of the samples as a function of time.

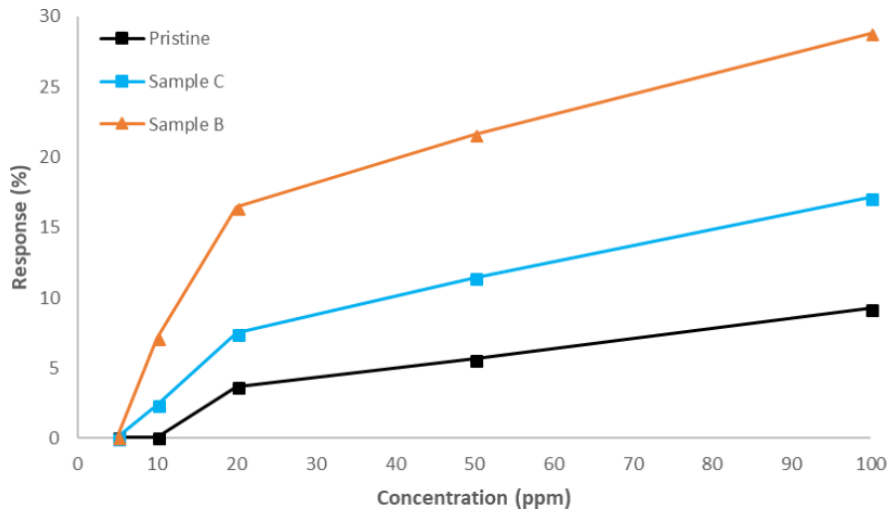


**Figure 8:** Effect of decoration ratio on the gas sensing performance.

gives us the highest response, as the response increases with increasing decoration ratio dose until an optimum decoration density is reached and afterwards the response decreases [6,19,28]. In fact, the obtained results are better regarding the intensity of the sensor response, as compared to those obtained by Chuanfei Hua et al. [23] using a composite of SWCNT–$Fe_2O_3$, although their sensors show faster response time.

## Studying effect of calcination period on nanocluster size

TEM images for two samples with the same decoration ratio (CNT/Fe = 1:1.5) but with different calcination periods of 15 or 30 minutes were taken to investigate the effect of the duration of the calcination on the size of iron nanoclusters. This is shown in Figure 9a. In addition, the nanocluster size distribution can be found in Supporting Information File 5, Figure S5. It can be concluded that the nanocluster size increases with increasing calcination time.

Also, the Raman spectra for pristine CNTs along with decorated samples of CNT/Fe = 1:1.5, which were calcined for 15 or 30 minutes, were studied to determine the effects of the calcination period on the quality of CNTs in comparison to non-calcined decorated CNTs. These results are shown in Figure 9b.

By analyzing the Raman spectra, we conclude that by increasing the calcination time, the quality of the CNTs slightly decreases. We also notice that the change in $I_D/I_G$ between pristine and decorated CNTs is not very high. This is expected because the commercial CNTs provided from Nanocyl are of

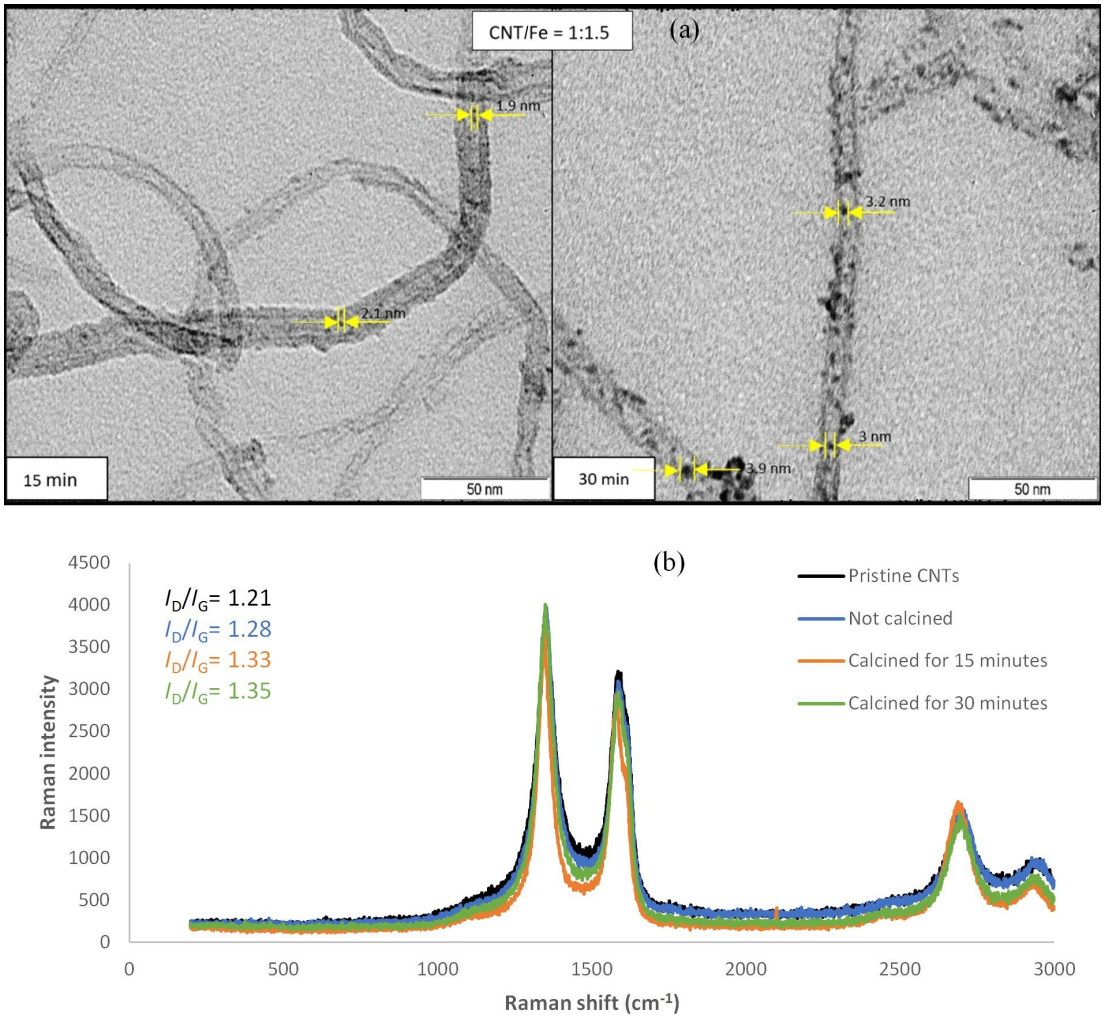


**Figure 9:** TEM images showing nanocluster size (a) after calcination for 15 minutes and 30 minutes for a 1:1.5 decoration ratio and Raman spectra for pristine CNTs and decorated CNTs with different calcination periods for (1:1.5) decorated COOH–CNTs (b).

low purity (95%) in analytical terms. In addition, the CNTs were already functionalized, so it is logical that a relatively high D/G ratio is obtained before performing any treatment or decoration. This low crystallinity means that a high concentration of disordered $sp^2$ carbon in relation to the presence of stretching C–C bonds is already present in as-purchased CNT samples. This makes it difficult to significantly increase defects in CNTs after performing further treatment and decoration.

In order to check the influence of nanoparticle size on the sensing capabilities of the CNTs, carbon nanotubes corresponding to sample A calcined for 15 or 30 minutes were used to implement sensors by the drop-coating approach. The previous sensor based on pristine CNTs was also used for comparison. Two different concentrations of $NO_2$ gas (5 ppm, 10 ppm) were pumped into the test chamber in this case. The results are shown in Figure 10.

As shown in Figure 10, the response of the sensor that employed carbon nanotubes calcined for 30 minutes, i.e., the one with larger iron oxide particles, is higher than the sensor based on iron oxide decorated CNTs calcined for 15 minutes.

These results confirm again that the decoration with iron oxide enhances the sensor response to $NO_2$, obtaining better results for carbon nanotubes decorated with iron oxide nanoparticles of larger size. This is consistent with the literature, in which heat treatment on sensors doped with an optimum doping ratio can cause both an increase in the size of decorating nanoparticles and an enhancement in the response of the sensor [6].

In order to check if the deposition method (drop-coating thick film or airbrushing thin film) has an influence on the sensor behavior, an additional sensor using CNTs corresponding to sample B was prepared by air brushing. Differences in morpholo-

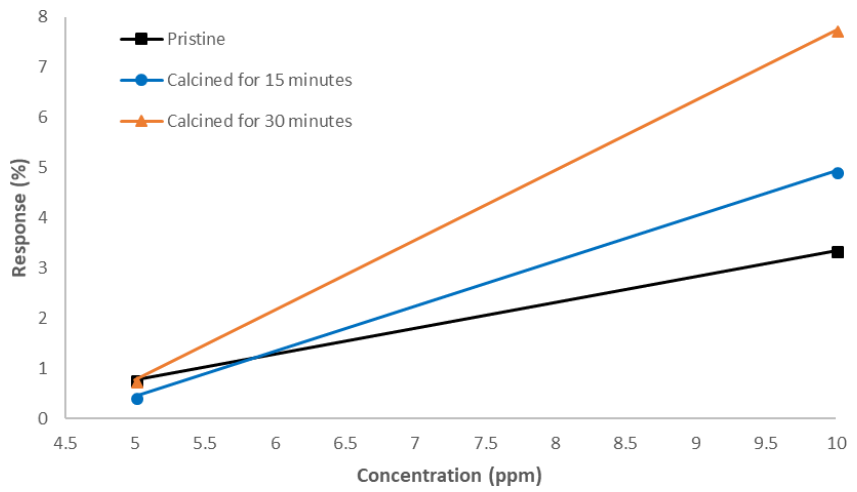


**Figure 10:** Effect of calcination period on the gas sensing performance.

gies between the two approaches followed for the deposition procedure (drop coating and air brushing) can be found in Supporting Information File 1, Figure S1.

This new sensor, together with the one based on pristine nanotubes fabricated using the same approach, and the sensor based on CNTs of sample B, but obtained by drop coating were tested.

The results are shown in Figure 11. As it can be seen, the thin layer sensor obtained by airbrushing decorated nanotubes showed better response than the thick film sensor obtained by drop coating. Once more, the results confirm that the decoration of the nanotubes using iron oxide is a good approach to enhance the sensor response to $NO_2$. In this case, we are comparing sensors implemented employing the same procedure, using both decorated and pristine nanotubes. Moreover, the airbrushed sensor showed the best response.

In order to check the selectivity of the best performing sensor, measurements for 10 ppm of benzene and 100 ppm of CO were performed. Although the concentrations of both gases were quite high, the sensor showed no response to carbon monoxide while the response to benzene was lower than 0.06%, confirming a good selectivity for the target gas (i.e., nitrogen dioxide).

Finally, to check the effect of humidity in the performance of the sensor, a new set of measurements for $NO_2$ were performed. In this case, the relative humidity was set to 50%. Comparing these results with the ones performed with dry air (relative

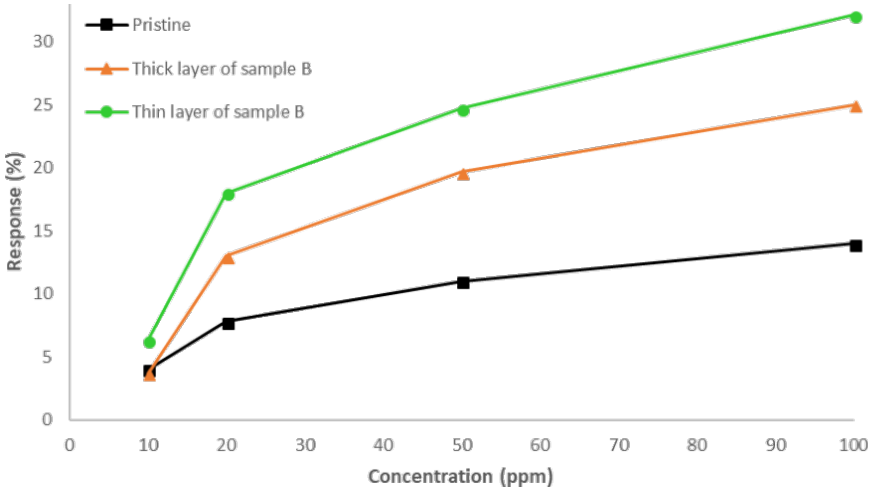


**Figure 11:** Effect of layer homogeneity and thickness on the gas sensing performance.

humidity was around 3%), one can realize that the sensor, when working in a more humid environment, shows faster response. That is, the presence of water vapor improves the performance of the sensor. The results of these measurements are shown in Figure 12. This enhancement in nitrogen dioxide response under humid conditions can be attributed to the water mediated adsorption of $NO_2$ on iron oxide nanoparticles, as previously reported for semiconductor metal oxide chemoresistors [35].

A deeper analysis of the sensor behavior reflected in Figure 7 and Figure 11 shows that both pristine and decorated CNT films behave as a p-type semiconductor. When nitrogen dioxide reacts with the active layer, the molecule traps electrons from the active layer, increasing its conductivity, because this increases the concentration of holes, which act as main charge carriers.

Comparing the behavior of pristine and decorated CNTs, one can clearly see that the decoration process leads to an increase in the electrical resistance of the active layer. This fact can be attributed to the p–n junctions formed between the p-type CNTs and the n-type iron oxide nanoparticles, with the formation of associated depletion layers. The p-type behavior of the decorated nanotubes suggests that, when the sensor is exposed to $NO_2$, the response is mainly due to the CNTs. In this case, the iron oxide NPs contribute to the enhancement of the response via a reduction of their associated depletion layer when $NO_2$ molecules adsorb on the surface of NPs, which increases the conductivity of the layer. Nevertheless, there is another possible explanation. It has been reported that $Fe_2O_3$ can turn from n-type to p-type, especially in oxidizing ambient environments [36]. This possible change in the semiconducting behavior of $Fe_2O_3$ could be the reason why the response to other reducing gases such as benzene or CO has been found to be very low. Nevertheless, a deeper study is necessary to better determine the mechanisms responsible for sensor response.

## Conclusion

The decoration of MWCNTs with $Fe_2O_3$ using an inexpensive method based on wet chemistry has shown to be a good approach for enhancing the detection of $NO_2$. The presence of iron oxide has been confirmed by both XPS and XRD analysis. Parametric studies for the decoration procedure showed that the decoration density is proportional to the ratio of CNT/Fe salt, without affecting particle size. The solvents used in the decoration steps affect the decorated CNT's morphology, decoration uniformity and decoration homogeneity. Methanol and ethanol were found to allow for a more uniform and homogenous decoration along the CNTs and also better powder morphology. On the other hand, DMF and acetone resulted in the formation of agglomeration islands on the CNTs and negatively affected the uniformity and homogeneity of decoration. The effect of the calcination period on the size of the decorating nanoclusters was studied as well. It was found that their size increases by increasing the calcination period. Regarding the gas sensing effect of the decoration, lower decoration density with higher particle size led to the best results.

The effect of the deposition method was also studied and was found to affect the behavior of the sensor. Namely, thinner, homogeneous, layered films obtained by airbrushing showed better response than thicker, non-homogeneous, layered sensors obtained by drop coating.

This last sensor deposited by air brushing showed an excellent selectivity for $NO_2$ when carbon monoxide and benzene vapors were considered as potential interfering gases. Finally, the effect of humidity was studied. It was found that a more humid

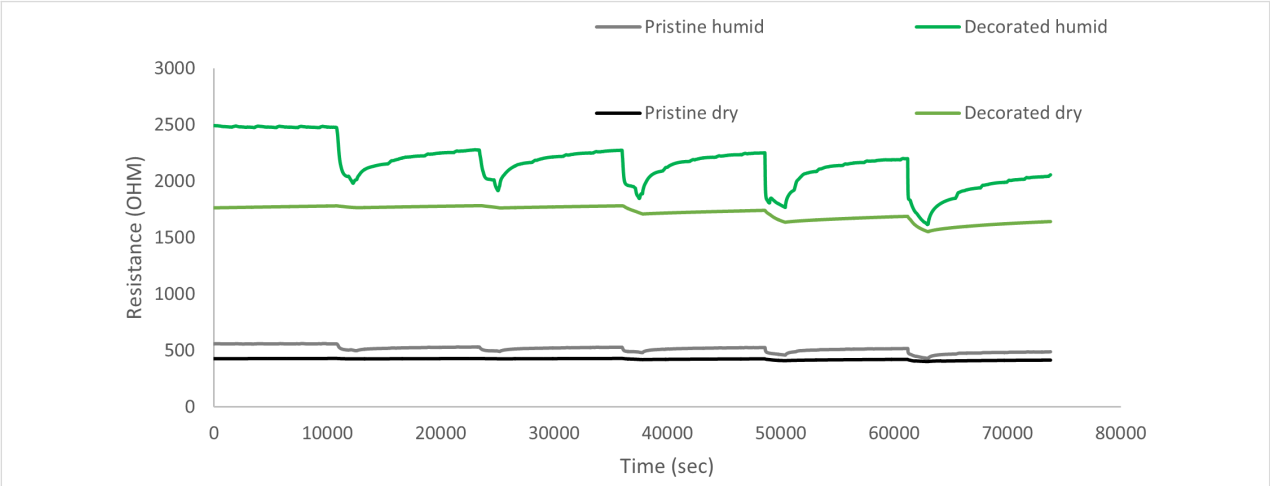


**Figure 12:** Comparison between gas sensors – performance in both dry and humid conditions.

environment resulted in an increased and faster response of the sensor to $NO_2$. This effect was observed for both pristine and decorated sensors.

## Supporting Information

The supporting information features images of the effect of deposition technique on decorated carbon nanotubes, images of the wire bound sensor (both sides), images of the teflon gas sensing chamber, an image of the results from the first decoration method on carbon nanotubes, and a results showing the effect of the calcination period of the nanoparticle size.

### Supporting Information File 1

Effect of deposition technique on decorated carbon nanotube morphology.
[https://www.beilstein-journals.org/bjnano/content/supplementary/2190-4286-10-10-S1.pdf]

### Supporting Information File 2

Wire bonded sensor.
[https://www.beilstein-journals.org/bjnano/content/supplementary/2190-4286-10-10-S2.pdf]

### Supporting Information File 3

Teflon gas sensing chamber allowing for 4 different sensors together for gas sensing.
[https://www.beilstein-journals.org/bjnano/content/supplementary/2190-4286-10-10-S3.pdf]

### Supporting Information File 4

Effect of first decoration step on carbon nanotube morphology.
[https://www.beilstein-journals.org/bjnano/content/supplementary/2190-4286-10-10-S4.pdf]

### Supporting Information File 5

Nanoparticle size distribution histograms.
[https://www.beilstein-journals.org/bjnano/content/supplementary/2190-4286-10-10-S5.pdf]

## Acknowledgements

This work has been funded in part by MINECO under grant no. TEC2015-71663-R, by the European Commission via the European Regional Development Fund (ERDF) and project XNEM 54833-TEMPUS-1-2013-1-EG-TEMPUS-JPCR and by the Catalan agency AGAUR under grant 2017SGR 418. Eduard Llobet is supported by the Catalan Institution for Research and Advanced Studies (ICREA) via the ICREA Academia Award. MS is a FRS Postdoctoral Researcher, CB is Research Associate at the FRS-FNRS.

## Authors Contributions

The chemical synthesis for the CNT decoration was performed by H. M. Elnabawy under the supervision of B. Anis, M. Fedawy, and A. S. G. Khalil. M. Scardamaglia and C. Bittencourt performed the XPS analysis. The preparation and characterization of the gas sensors was performed by H. M. Elnabawy and J. Casanova-Chafer under the supervision of E. Llobet and X. Vilanova. All the authors have collaborated in writing and revising the paper.

## Conflicts of Interest

The authors declare no conflicts of interest. The founding sponsors had no role in the design of the study, in the collection, analyses, or interpretation of data, in the writing of the manuscript, or in the decision to publish the results.

## ORCID® iDs

Juan Casanova-Chafer - https://orcid.org/0000-0002-3508-3462
Badawi Anis - https://orcid.org/0000-0002-7241-3088
Mostafa Fedawy - https://orcid.org/0000-0001-8556-1832
Mattia Scardamaglia - https://orcid.org/0000-0002-1128-7524
Eduard Llobet - https://orcid.org/0000-0001-6164-4342
Xavier Vilanova - https://orcid.org/0000-0002-6245-7933

## References

1. Iijima, S. *Phys. B (Amsterdam, Neth.)* **2002,** *323,* 1–5. doi:10.1016/s0921-4526(02)00869-4
2. Schönenberger, C.; Forró, L. *Phys. World* **2000,** *13,* 37–42. doi:10.1088/2058-7058/13/6/27
3. Kong, J.; Franklin, N. R.; Zhou, C.; Chapline, M. G.; Peng, S.; Cho, K.; Dai, H. *Science* **2000,** *287,* 622–625. doi:10.1126/science.287.5453.622
4. Wang, Y.; Yeow, J. T. W. *J. Sens.* **2009,** *2009,* No. 493904. doi:10.1155/2009/493904
5. Zaporotskova, I. V.; Boroznina, N. P.; Parkhomenko, Y. N.; Kozhitov, L. V. *Mod. Electron. Mater.* **2016,** *2,* 95–105. doi:10.1016/j.moem.2017.02.002
6. Abdelhalim, A.; Abdellah, A.; Scarpa, G.; Lugli, P. *Nanotechnology* **2014,** *25,* 055208. doi:10.1088/0957-4484/25/5/055208
7. Mudimela, P. R.; Scardamaglia, M.; González-León, O.; Reckinger, N.; Snyders, R.; Llobet, E.; Bittencourt, C.; Colomer, J.-F. *Beilstein J. Nanotechnol.* **2014,** *5,* 910–918. doi:10.3762/bjnano.5.104
8. Baccar, H.; Thamri, A.; Clément, P.; Llobet, E.; Abdelghani, A. *Beilstein J. Nanotechnol.* **2015,** *6,* 919–927. doi:10.3762/bjnano.6.95
9. Dilonardo, E.; Penza, M.; Alvisi, M.; Rossi, R.; Cassano, G.; Di Franco, C.; Palmisano, F.; Torsi, L.; Cioffi, N. *Beilstein J. Nanotechnol.* **2017,** *8,* 592–603. doi:10.3762/bjnano.8.64
10. Zanolli, Z.; Leghrib, R.; Felten, A.; Pireaux, J.-J.; Llobet, E.; Charlier, J.-C. *ACS Nano* **2011,** *5,* 4592–4599. doi:10.1021/nn200294h
11. Peng, S.; Cho, K. *Nano Lett.* **2003,** *3,* 513–517. doi:10.1021/nl034064u
12. Liu, L.; Zhang, T.; Li, S. C.; Wang, L. Y.; Tian, Y. X. *Chin. Sci. Bull.* **2009,** *54,* 4371–4375. doi:10.1007/s11434-009-0662-9

13. Lao, C. S.; Liu, J.; Gao, P.; Zhang, L.; Davidovic, D.; Tummala, R.; Wang, Z. L. *Nano Lett.* **2006,** *6,* 263–266. doi:10.1021/nl052239p
14. Cao, Y.; Luo, H.; Jia, D. *Sens. Actuators, B* **2013,** *176,* 618–624. doi:10.1016/j.snb.2012.10.067
15. Sun, P.; Wang, W.; Liu, Y.; Sun, Y.; Ma, J.; Lu, G. *Sens. Actuators, B* **2012,** *173,* 52–57. doi:10.1016/j.snb.2012.05.057
16. Mirzaei, A.; Hashemi, B.; Janghorban, K. *J. Mater. Sci.: Mater. Electron.* **2016,** *27,* 3109–3144. doi:10.1007/s10854-015-4200-z
17. Zhang, H.; Yu, L.; Li, Q.; Du, Y.; Ruan, S. *Sens. Actuators, B* **2017,** *241,* 109–115. doi:10.1016/j.snb.2016.10.059
18. Sonker, R. K.; Yadav, B. C. *J. Taiwan Inst. Chem. Eng.* **2017,** *77,* 276–281. doi:10.1016/j.jtice.2017.04.042
19. Tan, Q.; Fang, J.; Liu, W.; Xiong, J.; Zhang, W. *Sensors* **2015,** *15,* 28502–28512. doi:10.3390/s151128502
20. Tit, N.; Ezzi, M. M. A.; Abdullah, H. M.; Yusupov, M.; Kouser, S.; Bahlouli, H.; Yamani, Z. H. *Mater. Chem. Phys.* **2017,** *186,* 353–364. doi:10.1016/j.matchemphys.2016.11.006
21. Clément, P.; Hafaiedh, I.; Parra, E. J.; Thamri, A.; Guillot, J.; Abdelghani, A.; Llobet, E. *Carbon* **2014,** *78,* 510–520. doi:10.1016/j.carbon.2014.07.032
22. Pistone, A.; Piperno, A.; Iannazzo, D.; Donato, N.; Latino, M.; Spadaro, D.; Neri, G. *Sens. Actuators, B* **2013,** *186,* 333–342. doi:10.1016/j.snb.2013.06.027
23. Hua, C.; Shang, Y.; Wang, Y.; Xu, J.; Zhang, Y.; Li, X.; Cao, A. *Appl. Surf. Sci.* **2017,** *405,* 405–411. doi:10.1016/j.apsusc.2017.01.301
24. Nitschke, M. *Int. J. Environ. Health Res.* **1999,** *9,* 39–53. doi:10.1080/09603129973344
25. Salvi, A.; Patki, G.; Liu, H.; Salim, S. *Sci. Rep.* **2017,** *7,* 8306. doi:10.1038/s41598-017-08859-1
26. Hou, P.-X.; Liu, C.; Cheng, H.-M. *Carbon* **2008,** *46,* 2003–2025. doi:10.1016/j.carbon.2008.09.009
27. Tsoufis, T.; Douvalis, A. P.; Lekka, C. E.; Trikalitis, P. N.; Bakas, T.; Gournis, D. *J. Nanopart. Res.* **2013,** *15,* 1924. doi:10.1007/s11051-013-1924-7
28. Aroutiounian, V. M. *Lith. J. Phys.* **2015,** *55,* 10. doi:10.3952/physics.v55i4.3230
29. Grosvenor, A. P.; Kobe, B. A.; Biesinger, M. C.; McIntyre, N. S. *Surf. Interface Anal.* **2004,** *36,* 1564–1574. doi:10.1002/sia.1984
30. Gota, S.; Guiot, E.; Henriot, M.; Gautier-Soyer, M. *Phys. Rev. B* **1999,** *60,* 14387–14395. doi:10.1103/physrevb.60.14387
31. Biesinger, M. C.; Payne, B. P.; Grosvenor, A. P.; Lau, L. W. M.; Gerson, A. R.; Smart, R. S. C. *Appl. Surf. Sci.* **2011,** *257,* 2717–2730. doi:10.1016/j.apsusc.2010.10.051
32. Sahu, R. K.; Mukherjee, D.; Tiwari, J. P.; Mishra, T.; Roy, S. K.; Pathak, L. C. *J. Mater. Chem.* **2009,** *19,* 6810–6815. doi:10.1039/b908080e
33. Eltouny, N.; Ariya, P. A. *Phys. Chem. Chem. Phys.* **2014,** *16,* 23056–23066. doi:10.1039/c4cp02379j
34. Struzzi, C.; Scardamaglia, M.; Colomer, J.-F.; Verdini, A.; Floreano, L.; Snyders, R.; Bittencourt, C. *Beilstein J. Nanotechnol.* **2017,** *8,* 1723–1733. doi:10.3762/bjnano.8.173
35. Roso, S.; Degler, D.; Llobet, E.; Barsan, N.; Urakawa, A. *ACS Sens.* **2017,** *2,* 1272–1277. doi:10.1021/acssensors.7b00504
36. Lee, Y.-C.; Chueh, Y.-L.; Hsieh, C.-H.; Chang, M.-T.; Chou, L.-J.; Wang, Z. L.; Lan, Y.-W.; Chen, C.-D.; Kurata, H.; Isoda, S. *Small* **2007,** *3,* 1356–1361. doi:10.1002/smll.200700004

## License and Terms

Section 2.3

# Hydrophilicity and Carbon Chain Length Effects on the Gas Sensing Properties of Chemoresistive, Self-Assembled Monolayer Carbon Nanotube Sensors

Juan Casanova-Cháfer, Carla Bittencourt, Eduard Llobet

*Beilstein Journal of Nanotechnology, 10 (2019) 565-577*

DOI: 10.3762/bjnano.10.58

UNIVERSITAT ROVIRA I VIRGILI
GAS SENSING WITH MODIFIED CARBON NANOTUBES, GRAPHENE AND DIAMONDOIDS
Juan Casanova Cháfer

BEILSTEIN JOURNAL OF NANOTECHNOLOGY

# Hydrophilicity and carbon chain length effects on the gas sensing properties of chemoresistive, self-assembled monolayer carbon nanotube sensors

Juan Casanova-Cháfer[1], Carla Bittencourt[2] and Eduard Llobet[*1]

Full Research Paper

Open Access

Address:
[1]MINOS-EMaS, University Rovira i Virgili, Avda. Països Catalans, 26, 43007 Tarragona, Spain and [2]Chimie des Interactions Plasma-Surface (ChIPS), Research Institute for Materials Science and Engineering, Université de Mons, Avenue Copernic 1, Mons, Belgium

Email:
Juan Casanova-Cháfer - juan.casanova@urv.cat;
Carla Bittencourt - carla.bittencourt@umons.ac.be;
Eduard Llobet[*] - eduard.llobet@urv.cat

* Corresponding author

Keywords:
carbon length chain; gas sensing mechanism; hydrophilicity; hydrophobicity; multiwall carbon nanotubes (MWCNTs); self-assembled monolayer (SAM); thiol

*Beilstein J. Nanotechnol.* **2019,** *10,* 565–577.
doi:10.3762/bjnano.10.58

Received: 07 November 2018
Accepted: 07 February 2019
Published: 27 February 2019

Associate Editor: S. A. Claridge



## Abstract

Here we describe the development of chemoresistive sensors employing oxygen-plasma-treated, Au-decorated multiwall carbon nanotubes (MWCNTs) functionalized with self-assembled monolayers (SAMs) of thiols. For the first time, the effects of the length of the carbon chain and its hydrophilicity on the gas sensing properties of SAMs formed on carbon nanotubes are studied, and additionally, the gas sensing mechanisms are discussed. Four thiols differing in the length of the carbon chain and in the hydrophobic or hydrophilic nature of the head functional group are studied. Transmission electron microscopy, Raman spectroscopy and X-ray photoelectron spectroscopy are used to analyze the resulting gas-sensitive hybrid films. Among the different nanomaterials tested, short-chain thiols having a hydrophilic head group, self-assembled onto Au-decorated carbon nanotubes were most responsive to nitrogen dioxide and ethanol vapors, even in the presence of ambient humidity. In particular, this nanomaterial was about eight times more sensitive to nitrogen dioxide than bare Au-decorated carbon nanotubes when operated at room temperature. This response enhancement is attributed to the interaction, via strong hydrogen bonding, of the polar molecules tested to the polar surface of hydrophilic thiols. The approach discussed here could be extended further by combining hydrophilic and hydrophobic thiol SAMs in Au-MWCNT sensor arrays as a helpful strategy for tuning sensor response and selectivity. This would make the detection of polar and nonpolar gas species employing low-power gas sensors easier, even under fluctuating ambient moisture conditions.

*Beilstein J. Nanotechnol.* **2019,** *10,* 565–577.

## Introduction

Carbon nanotubes were first observed by Sumio Iijima in 1991 [1] and since then, this nanostructure has been widely used in chemoresistive gas sensors [2-5] due to the possibility to engineer its sensitivity towards chemicals present in a local environment. One of the reasons for this is their high surface-to-volume ratio and hollow structure in which almost every single carbon atom is on the surface, making them suitable for the adsorption of gas molecules [6]. This capability to detect toxic air pollutants has made them ideal candidates for integration into different types of transducers such as chemoresistors, resonant gravimetric or field effect devices, only to cite a few applications. Bare carbon nanotubes have been employed to detect gases such as nitrogen dioxide [7], ammonia [8], oxygen [9] or ethanol [10]. However, pristine carbon nanotubes (CNTs) present some limitations for gas sensing. For example, carbon nanotube gas sensors often suffer from slow recovery, especially when operated at room temperature, which eventually results in baseline and response drift. For that reason, it is usually necessary to heat up the gas sensitive nanomaterial to higher temperatures [3] or to irradiate the sensor employing ultraviolet (UV) light, in order to promote surface cleaning. Despite these efforts, sometimes CNTs present irreversible resistance changes due to the chemisorption of gas molecules. In addition, other problems such as lack of selectivity, environmental variations (e.g., changes in humidity level) affecting sensor response, or the difficulty to detect gases characterized by low adsorption energies are often encountered [11].

In order to enhance their selectivity and/or their sensitivity, CNTs have been functionalized by introducing reactive groups onto their sidewalls, such as carboxylic acid [12,13], hydroxy [14] or carbonyl [15] groups, by decorating them with metal or metal oxide nanoparticles [10,16-19], or by creating CNT–polymer [20] or CNT–chalcogenide [21] hybrids. Employing these approaches, different carbon nanotube sensors have been reported for detecting toxic pollutants emitted from vehicle exhaust [22,23], hazardous volatile organic compounds (VOCs) [24] or chemical warfare agents (CWAs) [25,26]. Usually, these modified carbon nanotubes improve the selectivity, because the chemical specificity of bonding for target molecules is enhanced. Also sensitivity is improved via a stronger interaction between functionalized carbon nanotubes and target species.

However, apart from improved sensitivity and selectivity, the effective detection of gaseous species in the environment requires gas sensors with other specific properties, such as stability, simplicity, low-cost and fast response [6]. For that reason, the last years have seen the development of approaches in which complex molecules are grafted onto the surface of carbon nanotubes via covalent or non-covalent interactions. In such an approach, carbon nanotubes act as support and charge transport transducing elements while the recognition function is performed by grafted molecules. Two examples of this have consisted of obtaining thiol-functionalized carbon nanotube buckypapers [27] or self-assembled monolayers (SAMs) of thiol molecules onto Au-decorated CNTs [28], in order to enhance the properties required to detect toxic gases. Additionally, the electronic properties of single-wall CNTs heavily depend on chirality, and the conduction properties of single-wall CNT films on top of interdigitated electrodes change dramatically depending on whether metallic nanotubes are above or below the percolation threshold [29,30]. In contrast, multiwall CNT mats always present a mild p-type semiconductor behavior which improves device to device reproducibility without the added burden of sorting nanotubes according to their metallic or semiconducting character before being integrated in gas sensing devices.

In view of developing sensitive, fast-responding, low power consumption and more selective sensors towards nitrogen dioxide or ethanol, in this paper, we combine oxygen plasma treated, Au-decorated MWCNTs with different thiols (see Figure S1, Supporting Information File 1). While thiol molecules behave as a chemoselective material responsible for the recognition of gas species, carbon nanotubes act as efficient charge transport networks, enabling the implementation of a chemoresistive transduction. Different thiols were attached to the gold nanoparticles creating SAMs (see Figure S2, Supporting Information File 1), which differed in their terminal functional groups and in the length of their carbon chain. This enables studying the effects of hydrophilicity or hydrophobicity of terminal functional groups and carbon chain length on the gas sensing properties of SAMs supported on CNTs. The response towards two gases, nitrogen dioxide and ethanol, was investigated. On the one hand, the detection of nitrogen dioxide has attracted great interest because of its adverse consequences for the environment and health risks associated to exposure for humans [18]. In environmental monitoring applications, nitrogen dioxide should be detected in the 20 to 200 ppb range. Some authors have reported the detection of $NO_2$ at such low concentrations using sensors employing carbon nanotubes [31,32]. In addition, sensors can be employed as well to determine nitrogen oxide emission from combustion engines. In this case, the concentrations to be measured range in the tens to hundreds of ppm [33,34]. On the other hand, ethanol sensors can be used in the automotive sector to check the concentration of ethanol in fuel blends, especially in biofuels. Ethanol is added to fuels since it can act as a radical scavenger, improving air quality by diminishing the concentration of pollutants

emitted from combustion engines. However, an excessive amount of ethanol in the blend can damage automotive fuel lines [35]. Additionally, by testing oxidizing (nitrogen dioxide) and reducing (ethanol) species, it is possible to obtain more information about the gas sensing behavior of functionalized carbon nanotube mats. Moreover, the effect of ambient moisture on the chemical response was studied, determining how moisture interference depended on the characteristics of the different thiols considered. Finally, the mechanisms for the interaction between gas molecules and the hybrid nanomaterials, which explain the experimental results obtained with the different sensors tested, are introduced and discussed.

# Results and Discussion

## Material characterization

MWCNTs decorated with Au nanoparticles were analyzed by TEM in order to observe the distribution of metal nanoparticles on the carbon nanotubes. Figure 1 shows that the CNT sidewalls are densely and quite homogeneously decorated with Au nanoparticles (Table S1 in Supporting Information File 1 shows quantitative XPS results indicating that the Au content was 5.7 wt % in these samples). A monomodal distribution of Au nanoparticles is obtained with average diameter of about 4 nm. The gold nanoparticles appear very close one to another (typically 10 nm apart), which will affect the gas sensing mechanism, as will be discussed in detail below.

The crystallinity of oxygen-plasma-treated MWCNTs decorated with gold nanoparticles was characterized by Raman spectroscopy. Taking the intensity ratio of the D/G bands into consideration, the material presents a low level of crystallinity with defects caused by the oxygen plasma treatment. However, the presence of such defects in CNTs is essential, since it has been shown that they play the role of nucleation centers and help to anchor the Au nanoparticles during the sputtering process [36]. In other words, the defects help to achieve a dense and homogenous decoration of CNT sidewalls with Au nanoparticles, preventing their mobility and coalescence.

The different thiols employed in this work were characterized by Raman spectroscopy (see Figure 2). A Peltier cell was used in order to keep samples at 4 °C and stabilize them, because unbound thiols present high volatility, even at room temperature. The Raman analysis of the thiols shows the presence of characteristic peaks in all samples related to the mode of vibration of aliphatic carbon chains at wavenumbers between 250–400 $cm^{-1}$ and 630–790 $cm^{-1}$. Other important bands can be found at the following wavenumbers: 735 $cm^{-1}$, 2580 $cm^{-1}$ and 2900 $cm^{-1}$, which correspond to C–S, S–H and C–H elongations, respectively. In addition, hydrophilic thiols (i.e., $C_3H_6O_2S$ and $C_{16}H_{32}O_2S$) present a characteristic peak at 1680 $cm^{-1}$ attributed to C=O elongation. In contrast, hydrophobic thiols ($C_3H_8S$ and $C_{16}H_{34}S$) show a characteristic peak at 1440 $cm^{-1}$ related to $CH_2$ and $CH_3$ radicals. Note that O–H elongations do not appear in the Raman spectra, probably due to the weak intensity of the O–H peak in Raman spectroscopy.

Once these thiols had been attached to Au-MWCNTs via the SAM technique, it was not possible to detect many of their most characteristic peaks in the resulting hybrid nanomaterials, because the high intensity peaks from MWCNTs had a masking effect in the survey spectra. For this reason, specific regions of the Raman spectrum in which no peaks from MWCNTs appear were acquired in order to confirm the presence of the thiols. Figure 3a shows the region between 550 and 850 $cm^{-1}$ providing information about the C–S and C–C elongations. The first peak appears at 638 and 670 $cm^{-1}$ for Au-MWCNT bound and free $C_3H_6O_2S$, respectively. Two main aspects may be respon-

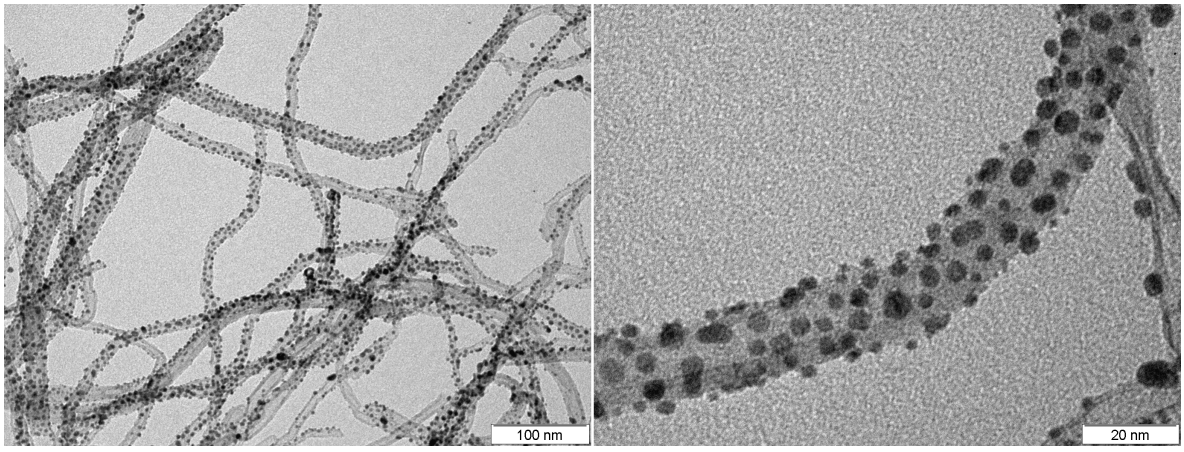


**Figure 1:** TEM images of MWCNTs decorated with gold nanoparticles.

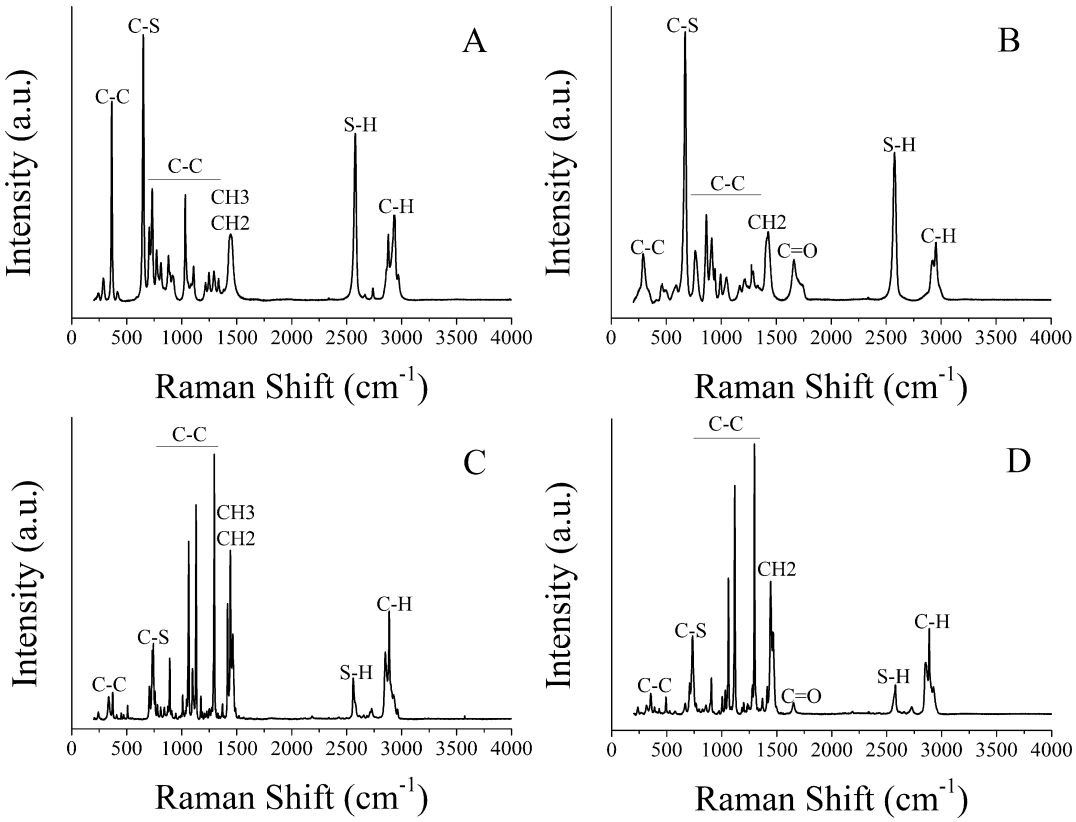


**Figure 2:** Raman spectra for the different thiols studied. A) $C_3H_8S$; B) $C_3H_6O_2S$; C) $C_{16}H_{34}S$; D) $C_{16}H_{32}O_2S$.

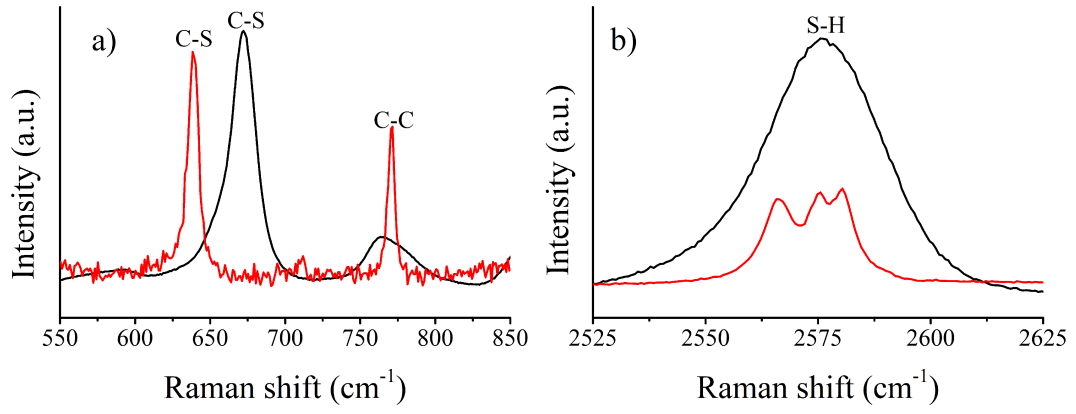


**Figure 3:** a) Comparison between unbound (i.e., free) thiol and hybrid SAM-MWCNTs for C–S and C–C elongations, b) comparison between unbound thiol and hybrid SAM-MWCNTs for S–H elongations. Black line: thiol ($C_2H_6O_2S$); red line: thiol-Au-MWCNTs.

sible for this shift. First, the temperature during the acquisition of the spectra was different. While free $C_3H_6O_2S$ was kept at 4 °C to avoid the fast volatilization that would have happened at room temperature, cooling was not necessary when thiols were attached to Au-MWCNTs and, in this case, the acquisition was conducted at room temperature. Second, the environment of these molecules was absolutely different. In other words, despite the fact that what is detected in both cases is the C–S elongation, the sulfur in free $C_3H_6O_2S$ was bonded in addition to a hydrogen atom, while in thiol attached to Au-MWCNT samples, the sulfur was bonded to a gold atom. Moreover, a second peak can be observed at 770 $cm^{-1}$ indicating the presence of aliphatic carbon chains. This peak is a proof of presence of thiols on the surface of gold decorated CNTs because

this C–C elongation is also registered for unattached thiols. In addition, this peak cannot be attributed to MWCNTs because the vibrations of the aromatic ring carbon chain appear in the region near 1500 $cm^{-1}$.

Figure 3a confirms the presence of thiols in thiol-Au-MWCNT samples, however, Figure 3b shows that some of these thiols remain unattached to Au. The 2550–2600 $cm^{-1}$ region was analyzed in order to find the strong peak corresponding to S–H elongations, which is indicative of the presence of unbound thiols. The intensity of this peak in thiol-Au-MWCNT samples is significantly lower than that found in free thiol samples (both spectra in Figure 3b were measured under identical experimental conditions). The fact that a small peak remains in thiol-Au-MWCNT samples is indicative that basically a SAM is formed, but some thiol molecules remain unattached to gold nanoparticles, despite the cleaning step implemented after the formation of the SAM.

In Figure 3, a clear localized surface plasma resonance (LSPR) effect (e.g., enhancement in signal intensity) cannot be observed. The reason could be due to the extremely low power of the laser used to record the Raman spectra, in order to prevent damaging the SAMs. As a consequence, a possible explanation is that the applied energy was not enough to create an important electromagnetic field around the Au–nanoparticle–dielectric interface. The Raman shift observed can be caused, in part, by LSPR. Further details can be found in Supporting Information File 1 (Figure S3).

Since oxygen-plasma-treated CNTs were employed, a study on the nature of oxygenated species present (acting as nucleation centers for the anchoring the Au NPs) was conducted using XPS. The chemical modification caused by the plasma treatment results in the presence of hydroxy, carbonyl and carboxyl groups [36]. Furthermore, Au nucleation centers occur mainly in the proximity of oxygenated defects created during the plasma treatment [37]. These results are summarized in Supporting Information File 1, Figure S4 and Table S1. The presence of thiols attached to Au NPs was further confirmed by XPS analysis. Figure 4a shows the comparison of the XPS survey spectra recorded on the samples and a reference (gold on CNTs). In the reference sample, the presence of only gold and carbon related peaks is clear; after the reaction with thiols, we can observe the presence of peaks generated by photoelectrons emitted from sulfur atoms for both samples and oxygen atoms for the short-chain thiol. In order to investigate the nature of the bonding of the thiols we investigated the chemical shift of the S 2p core level. The S 2p spectra acquired on the samples show a doublet structure that can be ascribed to the S $2p_{3/2}$ and S $2p_{1/2}$ peaks. All spectra were fitted using a 2:1 peak area ratio and a 1.2 eV splitting, as shown for a short-chain thiol sample in Figure 4b. The S $2p_{3/2}$ peak centered at 161.9 eV is reported to be generated by photoelectrons emitted from sulfur atoms bound to gold atoms at the gold nanoparticle surface as thiolate species [38]. The nonexistence of peaks in the binding energy region above 164 eV suggests the absence (or a non-detectable amount) of unbound thiol molecules (S $2p_{1/2}$ BE ≈ 165 eV), which confirms the correct formation of SAMs. The small amount of unbound thiol molecules detected by Raman spectroscopy were possibly removed under the ultrahigh vacuum needed to perform XPS, which would explain that only thiols attached to Au were detected employing this technique. Table S1 in Supporting Information File 1 reports quantitative XPS results performed before and after the formation of the SAM. These results indicate the almost complete coverage of Au

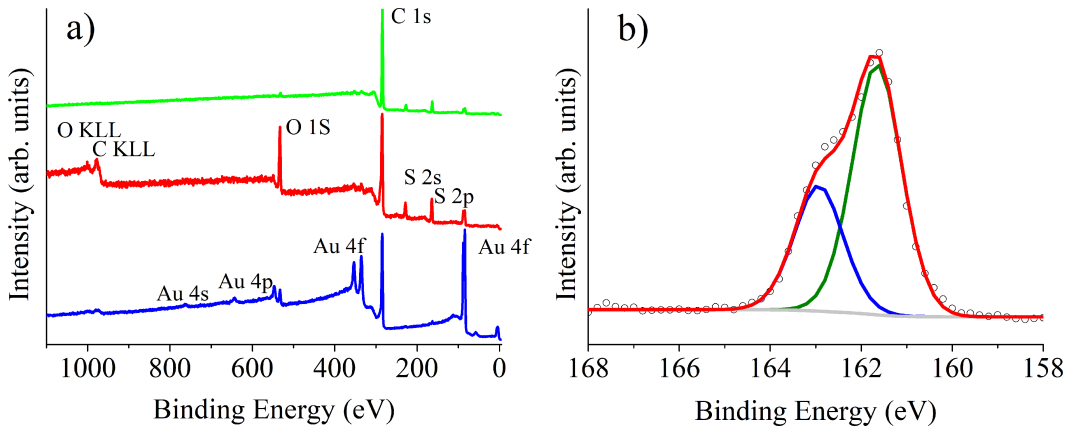


**Figure 4:** (a) X-ray photoelectron survey spectra recorded on Au-CNTs (blue), short-chain thiol-Au-CNTs (red) and long-chain thiol-Au-CNTs (green) samples. (b) S 2p spectrum acquired on a thiol-Au-MWCNT sample. The results for a short-chain thiol ($C_3H_8S$) are shown here, as a typical example of the SAMs obtained.

nanoparticles with thiols, since Au (which accounted for 5.7 wt % in bare samples) is almost no longer "visible" by XPS after the formation of the SAM.

The hydrophilicity of the different coatings was studied via contact angle measurements. It was found that bare Au-MWCNTs showed a hydrophilic character due to the presence of carboxyl groups grafted to their sidewalls. Samples functionalized with SAMS having –COOH head groups showed an increased hydrophilic character and samples functionalized with SAMs having $–CH_3$ head groups possessed a clear hydrophobic character. These results are summarized in Supporting Information File 1 (see Figure S5).

## Gas sensing results

Four different thiols were immobilized, via the SAM technique, on Au-decorated MWCNT mats to obtain gas sensors. The differences between the thiols chosen were in the length of their carbon chain and in their terminal functional group. Two thiols with short-length carbon chains (3 carbons) and two with long-length carbon chains (16 carbons) were used. Moreover, for each one of these two lengths, either a hydrophilic functional group (–COOH) or a more hydrophobic one ($–CH_3$) was selected. Therefore, the following thiols were finally employed to form self-assembled monolayers: 3-mercaptopropanoic acid ($C_3H_6O_2S$) and 16-mercaptohexadecanoic acid ($C_{16}H_{32}O_2S$) as hydrophilic molecules, and 1-propanethiol ($C_3H_8S$) and 1-hexadecanethiol ($C_{16}H_{34}S$) as more hydrophobic molecules. Additionally, control sensors were produced, which integrated bare Au-decorated MWCNTs, in order to better assess the effect of the thiol SAMs on the gas sensing properties of nanomaterials.

Gas measurements were performed under dry air. It is well known that the triple bond in molecular nitrogen makes it chemically inert, however, oxygen presents high electronegativity (3.44 in Pauling scale) making it quite reactive with the sensor surface. Oxygen acts as an electron acceptor due to its lone pairs of valence electrons and can be adsorbed on the sensor surface, p-doping CNTs [39]. To correctly identify the response towards target species (i.e., nitrogen dioxide and ethanol), the oxygen concentration was kept constant at 21% throughout the measurement process. The adsorption of oxygen may result in a slight oxidation of the thiols on the long term.

The sensors were exposed to different concentrations of nitrogen dioxide ($NO_2$) and ethanol ($C_2H_5OH$). The exposure time to gases or vapors was set to 5 minutes in order to obtain a clear enough response for sensors operated at room temperature, which reduces power consumption and increases the sensor lifespan. The sensors were allowed to regain their baseline resistance by flowing dry air through the sensor chamber. Measurements (exposures) were repeated at 4 h intervals. Both during their exposure to the target species (response) and to dry air (recovery), the sensors were operated at room temperature. No heating or UV irradiation was applied to speed up detection and recovery processes. The sensor response (%) is defined as $((R_G - R_0)/R_0) \times 100$.

Nitrogen dioxide is a strong oxidizing agent that acts as an electron acceptor and presents electrophilic properties, which allow these molecules to be adsorbed onto the sensor surface. A control Au-MWCNT sensor and hybrid sensors (SAMs attached on Au-MWCNTs) were measured at four different nitrogen dioxide concentrations. The dynamic response and recovery curves are shown in Figure 5a. The control Au-MWCNT sensor showed the lowest responsiveness to nitrogen dioxide among the different sensors tested. This is in agreement with previous results in which oxygen-plasma-

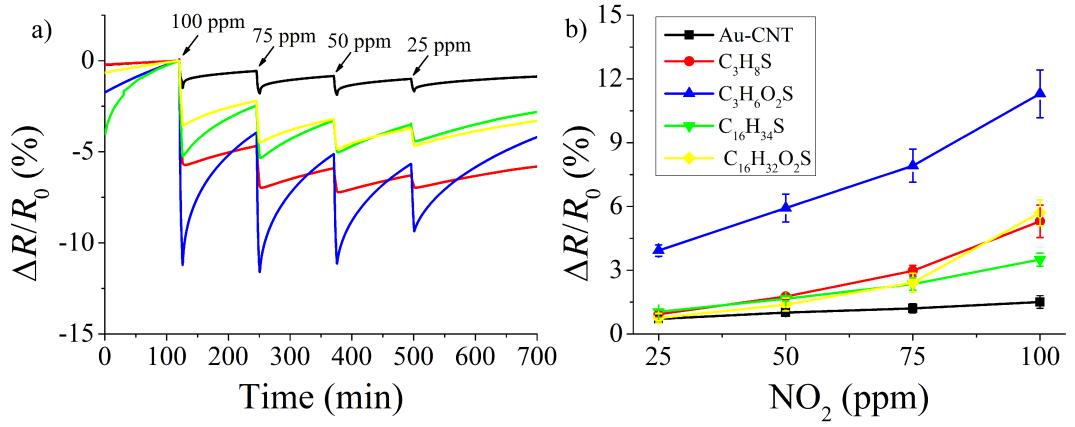


**Figure 5:** a) Sensor response to nitrogen dioxide exposure and recovery cycles in air, and b) calibration curves for the different nitrogen dioxide concentrations tested.

treated CNTs were more responsive to nitrogen dioxide than Au, Pt or Pd-decorated CNTs when operated at room temperature [10,18,40]. This was attributed to a stronger interaction and charge transfer between nitrogen dioxide and oxygenated defects in CNTs than with metal clusters. Possibly the surface of metal clusters requires higher operating temperatures to act as reactive sites for the adsorption of nitrogen dioxide molecules. Therefore, the response obtained for Au-MWCNTs cannot be explained by the catalytic activity of gold clusters at the nanometer range, and instead the resistance changes observed are probably based on the interaction between the carboxylic acid functional groups in MWCNTs and nitrogen dioxide. In contrast, the response to nitrogen dioxide is clearly enhanced (up to an 8-fold increase) when hybrid materials formed by thiol SAMs on Au-MWCNTs are used. Since it was found that Au nanoparticles were completely covered by the SAM of thiols, we assume that thiol–gas interactions dominate the response observed. In other words, the Au nanoparticles for thiol SAMs in Au-MWCNT sensors do not play a significant role in gas detection.

The results show that short length thiols having a hydrophilic head group present higher response and sensitivity to nitrogen dioxide than any other SAM tested (see Figure 5b). A hypothesis to explain this result is based on two main effects. The first one is due to the hydrophilic properties of the surface, given the presence of carboxylic acid in the head group of hydrophilic SAMs. This favors the occurrence of an electrostatic interaction between the nitrogen dioxide molecule and the SAM following two possible pathways. Namely, hydrogen bonding between COOH and nitrogen dioxide molecules (see Figure 6a) and covalent interaction (see Figure 6b). The second effect is related to the length of the carbon chain and, in consequence, to the concentration of carboxyl groups that are accessible to nitrogen dioxide molecules. When short length carbon chain thiols are used (see Figure S2a, Supporting Information File 1) a vertically aligned SAM can be easily formed. Under this configuration, high sensitivity to nitrogen dioxide is obtained because the molecule can interact not only with the COOH groups in the heads of the SAM, but also nitrogen dioxide can diffuse into the SAM and eventually react with the carboxyl groups present on the surface of MWCNTs. In contrast, for SAMs employing long carbon chains (i.e., 16 carbon atoms), such molecules probably collapse and overlap on the surface of CNTs (see Figure S2b, Supporting Information File 1), making it more difficult for gas molecules to access the COOH groups on carbon nanotubes via a steric hindrance effect. This would explain why hydrophilic SAMs with long carbon chains present lower response towards nitrogen dioxide in comparison to hydrophilic, short carbon chain SAMs. In addition, overlapped SAMs can result in the formation of carboxylic acid dimers [41], further decreasing sensitivity.

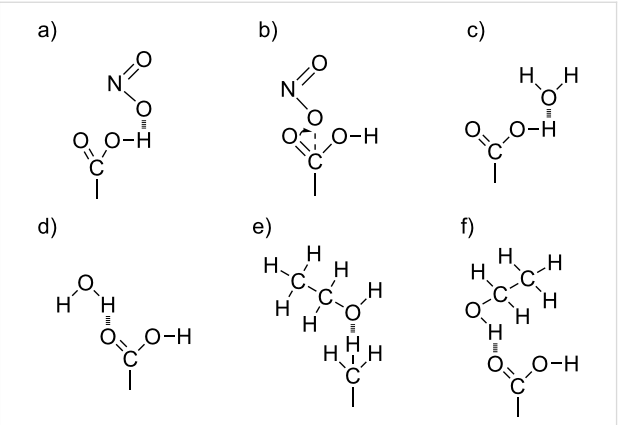


**Figure 6:** Electrostatic interactions pathways between –COOH functional groups and nitrogen dioxide (a, b), water (c, d) and ethanol (e, f).

On the other hand, hydrophobic SAMs present limited responsiveness towards nitrogen dioxide. The fact that the resistive response is far lower than that of hydrophilic SAMs is indicative of the weak chemical affinity between the polar nitrogen dioxide molecule and the methyl functional groups of hydrophobic SAMs. The nature of these interactions is still the subject of debate. While weak intermolecular attractive forces could be responsible for these interactions, some authors maintain that the formation of hydrogen bonds between the methyl groups present in the thiol molecules and the gas species cannot be ruled out [42]. While hydrophilic functional groups (e.g., COOH) present high surface energy due to their high affinity towards polar molecules, such as nitrogen dioxide, hydrophobic functional groups (e.g., $CH_3$) present low surface energy due to their low affinity to polar molecules [43]. The low affinity of hydrophobic thiols towards polar gases explains the lower response observed. Similarly, short-chain thiols present a slightly higher response to nitrogen dioxide than long-chain thiols. This can be attributed, once more, to the molecule being able to diffuse into the SAM of short-chain thiols and reach carboxyl groups present on the surface of CNTs.

With respect to sensor recovery in dry air after a nitrogen dioxide detection event, it was observed that it was more difficult for hydrophilic thiols, especially short carbon chain thiols to regain their baseline resistance than for hydrophobic ones. Probably the cause of this effect is due to the stronger electrostatic interactions between nitrogen dioxide and hydrophilic thiols, leading to the formation of stronger hydrogen bonds.

The effect of ambient moisture on the sensor response was studied. In order to do so, the gas flow was humidified to 50% relative humidity (at 20 °C) and the same nitrogen dioxide con-

centrations that had been studied previously under dry conditions were measured again. These results are shown in Figure 7. As it could be expected, the presence of ambient moisture increases the sensitivity to a polar gas like nitrogen dioxide for sensors employing hydrophilic thiols [44]. In contrast, the response to nitrogen dioxide remains basically unchanged for sensors employing hydrophobic thiols. Ambient moisture can interact with the sensor surface via hydrogen bonds (see Figure 6c,d). However, the COOH groups (in hydrophilic thiols) present higher affinity to $H_2O$ than the $CH_3$ groups (in hydrophobic thiols). The response of carbon nanotubes functionalized with short-chain, hydrophilic thiols towards $NO_2$ increases in humid conditions. While at the lower concentrations tested (i.e., 25 to 75 ppm) the response is almost unaffected by changes in the background humidity; at 100 ppm, nearly a two-fold increase is observed. In hydrophilic thiols, once the saturation of free COOH groups present on the surface of the sensor is reached (because both water and nitrogen dioxide molecules get adsorbed), a water-mediated adsorption of nitrogen dioxide takes place [45], which would explain the highly nonlinear increase in response observed for the highest measured concentration of nitrogen dioxide [46]. Since the presence of ambient moisture only mildly affects the response of short-chain hydrophilic thiols towards the lower concentrations of nitrogen dioxide, in a real application these effects could be compensated for via the use of a humidity sensor and an appropriate calibration.

The presence of an adsorbed water layer on hydrophilic thiol sensors and the reported water-mediated adsorption of nitrogen dioxide could explain the improved response to humid nitrogen dioxide observed for such sensors. The absence of this adsorbed water layer on hydrophobic thiol sensors could explain the fact that, for such sensors, their response to nitrogen dioxide remains basically the same under dry or humid conditions.

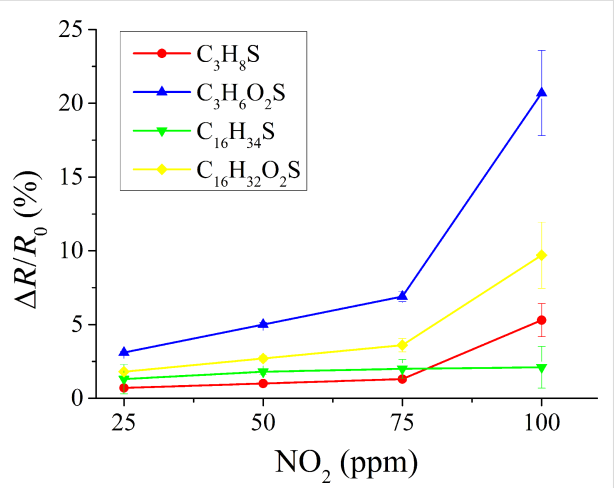


**Figure 7:** Calibration curves for different concentrations of nitrogen dioxide under humid conditions (50% R.H.).

Similarly to the case in which nitrogen dioxide was detected under dry conditions, short-chain hydrophilic thiols present a higher response than long-chain thiols under humid conditions. This behavior can be attributed to the same reasons already discussed for the dry detection of nitrogen dioxide.

A similar experimental approach was employed to study the response towards ethanol vapors. These results are summarized in Figure 8, where it can be observed that the highest sensitivity towards ethanol (i.e., slope of the calibration curves shown in Figure 8b) is obtained for the hydrophilic SAM having a short length carbon chain. The gas sensing mechanism for detecting ethanol is, once more, related to hydrogen bonding (see Figure 6e,f). It is well-known that hydrophilic groups present more affinity to polar compounds (e.g., ethanol) than hydrophobic radicals. This concept can explain why the short hydrophilic chain thiol presents higher response to ethanol

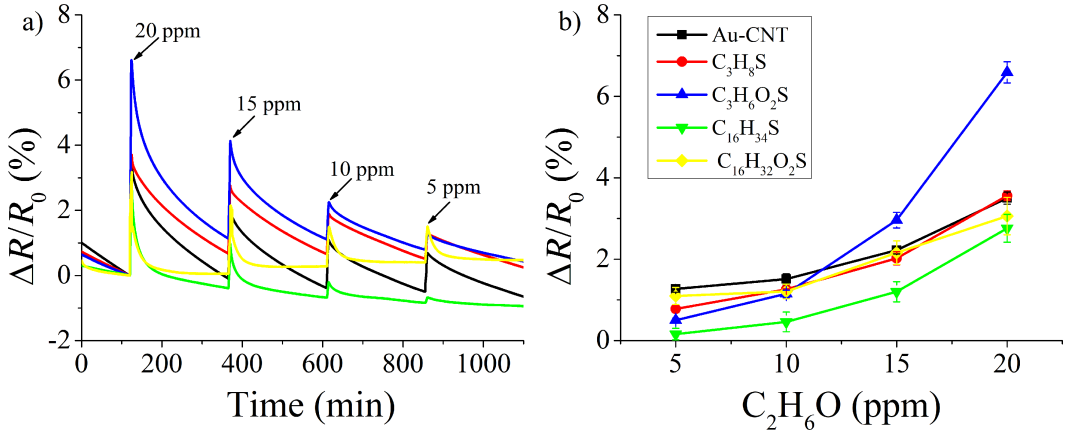


**Figure 8:** a) Sensor response to ethanol exposure and recovery cycles in air. b) Calibration curves for the different ethanol concentrations tested.

vapors, while the other SAMs show similar responses with very little differences. The absence of carboxyl groups in hydrophobic thiols and the combined effects of steric hindrance and formation of carboxylic acid dimers in long-chain, hydrophilic thiols, as already discussed for nitrogen dioxide, could explain the lower ethanol response and sensitivity observed. Finally, the reference sample (i.e., Au-MWCNTs) presents low response and sensitivity to ethanol, showing similar values to those of hydrophobic or long-chain thiols. This is indicative that the mechanism of interaction with ethanol would mainly involve carboxyl groups present on the surface of CNTs. On the other hand, gold nanoparticles probably present a residual contribution to ethanol response, due to these nanoparticles having low affinity to ethanol molecules and remaining catalytically inactive at room temperature.

The extent of energy exchange between gas molecules and the surface of the sensors depends on surface rigidity and mass and also on the forces between the impinging gas molecules and the surface functional groups. Morris and co-workers employed ab initio calculations to estimate the interaction energies between both polar and nonpolar gases with polar (OH-terminated) and nonpolar ($CH_3$-terminated) SAMs [47]. They concluded that interaction forces spanned over a wide range from strong hydrogen bonding between polar gases and polar SAMs to weak dispersion forces for nonpolar gases and nonpolar SAMs. In particular, they found that the magnitude of the interaction energy between methane (nonpolar) and polar or nonpolar terminated SAMs was low and not significantly different. In contrast, the interaction energies between water (polar) and nonpolar or polar-terminated SAMs exhibited a more than one order of magnitude difference in favor of polar SAMs.

Taking into account these theoretical results, strong hydrogen bonding interactions can be assumed between the carboxyl terminals of hydrophilic thiols and the polar species studied here (i.e., ethanol vapors or nitrogen dioxide). This results in high sensor response at room temperature and difficulties for sensors to regain their baseline values. This interaction is weaker with the methyl terminals of hydrophobic thiols, which translates into lower sensor response. In that sense, the combination of hydrophilic and hydrophobic short-chain SAMs in a sensor array should be helpful for detecting polar and nonpolar species and to fight ambient moisture interference.

Finally, some examples of functionalized and pristine MWCNTs employed in gas sensors operating at room temperature are summarized in Table 1, showing a comparison of sensitivities obtained in similar approaches.

## Conclusion

This paper describes the development of chemoresistive sensors employing oxygen-plasma-treated, Au-decorated MWCNTs functionalized with self-assembled monolayers of thiols. The four different thiols studied differ in the length of their carbon chain (either 3 or 16 carbons) and in the head group (either carboxylic acid or methyl). This has enabled the study of the effects of hydrophilicity or hydrophobicity of terminal functional groups and carbon chain length on the gas sensing properties of SAMs supported on CNTs. Under this approach, thiols should, in principle, behave as a chemoselective material responsible for the recognition of gas species. In contrast, carbon nanotubes should not play a major role as receptors for target gas molecules, but instead act as efficient charge transport networks, enabling the efficient implementation of chemoresistive sensors.

It was found that short-chain thiols having a hydrophilic head group (carboxylic acid) were the most responsive to the oxidizing (nitrogen dioxide) and reducing (ethanol vapors) tested. This was attributed to the interaction, via strong hydrogen bonding, of the polar molecules tested to the polar surface of hydrophilic thiols. The contribution to the sensor response of oxygenated defects present on the surface of carbon nanotubes could not be ruled out for CNTs functionalized with short-chain thiols. However, this contribution should be moderate, since Au-MWCNTs functionalized with hydrophilic short-chain thiols showed an 8-fold increase in response to nitrogen dioxide

**Table 1:** Response (($\Delta R/R_0$) × 100) to nitrogen dioxide and ethanol with differently functionalized MWCNTs. N/T: Not tested.

| Sample | $NO_2$/RT[a] | Ref. | Ethanol/RT[a] | Ref. |
|---|---|---|---|---|
| SAM/Au/MWCNT | 11.4 (100 ppm)/5 min | this work | 6.4 (20 ppm)/5 min | this work |
| Au/MWCNT | 1.5 (100 ppm)/5 min | | 3.5 (20 ppm)/5 min | |
| SAM/Au/MWCNT | N/T | – | 22 (20 ppm)/30 min | [28] |
| MWCNT | 10.8 (100 ppm)/5 min | [21] | 0.4 (100 ppm)/5 min | [48] |
| coated Au MWCNT | N/T | – | 1.2 (50 ppm)/5 min | [48] |
| Au/MWCNT | 12.0 (6.5 ppm)/20 min | [49] | 0.4 (50 ppm)/15 min | [36] |

[a]RT = reaction time, is defined as the exposure time to a target gas.

in comparison to bare Au-MWCNTs. Long-chain thiols having a hydrophilic head group were significantly less responsive to the species tested than their short-chain counterparts. Given the distance between neighboring Au nanoparticles, long-chain thiols collapse and overlap, generating a steric hindrance effect and favoring the formation of carboxylic acid dimers, which would explain the decreased sensitivity observed.

In a second step, the effect of ambient moisture on the response towards nitrogen dioxide was studied. It was observed that the presence of moisture adsorbed on the surface of the sensors increased the response of short-chain, hydrophilic thiol and carbon nanotube hybrids. This enhancement in the nitrogen dioxide response under humid conditions can be attributed to a water-mediated adsorption of nitrogen dioxide, already reported for semiconductor chemoresistors.

From an applications perspective, the range of nitrogen dioxide concentrations tested here (tens of ppm) is still too high for monitoring this species in ambient conditions (tens of ppb). However, there is room for improving these results, for example, by using single-walled carbon nanotubes instead of MWCNTs and by further optimizing the chain length, head functional groups and the amount of the carbon nanotube sidewall functionalization. Also, the time needed for recovering the baseline should be improved as well. A few well-known options to diminish the recovery time include heating or UV irradiating the gas-sensitive film during the recovery phase to ease desorption of molecules from the surface, increasing the flow rate during both detection and recovery phases or further optimizing the sensor parameters such as electrode design or CNT density.

According to the experimental results discussed here and in previously reported theoretical studies, the combination of hydrophilic and hydrophobic short-chain SAMs in Au-CNT sensor arrays should be helpful for detecting polar and nonpolar gases, even under fluctuating ambient moisture conditions.

# Experimental

## Functionalization of carbon nanotubes

Multiwall carbon nanotubes (MWCNTs) functionalized with carboxylic acid (COOH) were purchased from Nanocyl S.A. (Belgium). These nanotubes were produced by a catalytic chemical vapor deposition (c-CVD method) and purified to greater than 95%. The average length of these carbon nanotubes is 1.5 μm and the average diameter is 9.5 nm. The surface of the carbon nanotubes was modified with –COOH groups, with a value of mass greater than 8%. This surface modification was performed by Nanocyl S.A. via an oxygen-plasma treatment.

An attempt to decorate pristine CNTs with Au nanoparticles would lead to poor results [36]. Au is mobile on the surface of pristine CNTs, resulting in coalescence effects (uncontrolled size of particles and bad homogeneity in the decoration). Previous works have reported the benefits of employing oxygen-plasma-treated CNTs, which need to be subsequently decorated with Au nanoparticles. Oxygenated defects act as anchoring and nucleation sites. Therefore, high control in the decoration homogeneity and the size of Au nanoparticles (avoiding coalescence effects) have been reported in oxygen-plasma-treated CNTs [37]. Since oxygenated defects are homogeneously distributed in the CNTs used, we expect Au NPs to be homogeneously distributed on the whole surface, that is, not in direct contact to the substrate.

A suspension of these functionalized MWCNTs was prepared using *N*,*N*-dimethylformamide (DMF) purchased from Alfa Aesar (99.8% purity). Then, the suspension was placed in an ultrasonic bath during 30 min at room temperature. Thereafter, the suspension was deposited onto screen-printed alumina substrates by employing an airbrushing technique. Finally, the MWCNTs were decorated with gold nanoparticles by a sputtering method. An ATC Orion 8-HV sputtering machine (AJA International, Inc., USA) was used for this purpose. In this process, an RF inductively coupled plasma was used at a frequency of 13.56 MHz. The sputtering parameters were adjusted to 30 W under argon plasma during 10 s at a pressure of 0.1 Torr [50].

Au-decorated MWCNTs were further functionalized by employing SAMs of different thiols. Four thiols were used, namely, 1-propanethiol ($C_3H_8S$), 3-mercaptopropanoic acid ($C_3H_6O_2S$), 1-hexadecanethiol ($C_{16}H_{34}S$) and 16-mercaptohexadecanoic acid ($C_{16}H_{32}O_2S$), all purchased from Sigma-Aldrich. These thiols were chosen based on two main differences, the length of the carbon chain and the terminal functional group. Thiols with short (3 carbons) and long (16 carbons) length carbon chains were used. In addition, for each length of carbon chain, a hydrophilic functional group (–COOH) and other more hydrophobic ($–CH_3$) groups were studied.

The affinity between sulfur and gold, which results in a strong bond [51], has been extensively reported. Therefore, sensors based on MWCNTs decorated with gold nanoparticles were immersed in a thiol solution. The different thiols employed were dissolved in ethanol to produce 0.1 mM solutions. Then, sensors consisting of mats of Au-decorated MWCNTs on alumina substrates were immersed in these solutions and kept at 4 °C during 24 h in order to ensure the correct formation of SAMs. Finally, the sensors were rinsed three times

with ethanol and dried under a $N_2$ flow to remove unbound thiols [28].

### Material characterization

The hydrophilicity of the gas-sensitive coatings was evaluated using an optical tensiometer from Biolin Scientific. Their chemical composition was characterized by Raman spectroscopy and X-ray photoelectron spectroscopy (XPS). Raman spectrometry was performed employing an instrument from Renishaw, Inc., (U.K.), which was coupled to a confocal Leica DM2500 microscope. The laser wavelength applied to the samples was 785 nm. The samples under inspection were held on a Peltier cell and kept at low temperature (4 °C) in order to ensure the stability of SAMs under laser irradiation. The chemical composition and, particularly, the presence of the Au–S bond were evaluated using a Versaprobe Phi 5000 instrument from Physical Electronics equipped with a monochromatic Al Kα X-ray source. The binding energy (BE) scales were referenced by setting the Au $4f_{7/2}$ to 84.0 eV. The XPS spectra were collected at a take-off angle of 45° with respect to the electron energy analyzer. The X-ray beam diameter was 200 µm. The energy resolution was 0.5 eV. For the compensation of built-up charge on the sample surface during the measurements, a dual-beam charge neutralization composed of an electron gun (1 eV) and an Ar ion gun (≤10 eV) was used.

The structural characterization of Au-decorated MWCNTs was performed using a JEM-1011 transmission electron microscope (TEM) from JEOL Ltd. (Japan). A copper grid was used onto which a suspension of Au-MWCNTs was dropped. The images were taken at 80 kV.

### Fabrication of the sensor substrate

A 10 × 10 $mm^2$ alumina substrate was employed. Interdigitated electrodes and a heating resistor were screen-printed on either side of the substrate employing a platinum ink (see Supporting Information File 1, Figure S6). The electrode area was coated with a mat of CNTs via airbrushing through a shadow mask. Once the sensors were sputtered with gold and functionalized with thiols, two-wire contacts were made on the samples using a conductive epoxy (Ag component metallization, Heraeus) and platinum wires. The samples were bonded to a 20 × 30 $mm^2$ printed circuit board (PCB), which was then plugged inside a test chamber (see Supporting Information File 1, Figure S7).

#### Gas sensing measurements

A 35 mL airtight test chamber in Teflon was connected to an automated gas mixture delivery system controlled by Bronkhorst mass-flow controllers and calibrated gas cylinders. The experimental conditions were set to deliver different concentrations of ethanol vapors and nitrogen dioxide gas at room temperature (20 °C) under a constant flow of 100 mL/min. Unless otherwise specified, the measurements were performed under dry conditions. For studying the effect of ambient moisture on the sensor response, the gas flow was humidified to a relative humidity of about 50%. The evolution of the sensor resistance was measured with an Agilent HP 34972A multimeter.

## Supporting Information

The chemical structure of the different thiols tested. Representation of self-assembled monolayers. Raman spectroscopy of carbon nanotubes. Deconvolution of the C 1s core level peak for Au-MWCNTs using XPS. Table with the relative abundance (%) analyzed by XPS technique. Contact angle measurements. Sensor fabrication process detailed. Alumina heater description and sensor wire-bonded to a PCB.

### Supporting Information File 1

Figures related to thiol-Au-carbon nanotubes and experimental data obtained during the material characterization.
[https://www.beilstein-journals.org/bjnano/content/supplementary/2190-4286-10-58-S1.pdf]

## Acknowledgements

J. Casanova-Cháfer is supported by a Martí i Franquès predoctoral fellowship from Universitat Rovira i Virgili (URV), and E. Llobet is supported by the Catalan Institution for Research and Advanced Studies via the ICREA Academia Award. C. Bittencourt is a Research Associate of the National Funds for Scientific Research (FRS-FNRS, Belgium). This work is funded in part by MINECO under grant no. TEC2015-71663-R, by AGAUR under grant no. 2017SGR 418 and by the Belgian Fund for Scientific Research under FRFC contracts "FITTED and PLAFON". We are thankful to Dr. Calavia and Mr. Blanch for helpful discussions.

## ORCID® iDs

Juan Casanova-Cháfer - https://orcid.org/0000-0002-3508-3462
Carla Bittencourt - https://orcid.org/0000-0002-3330-6693
Eduard Llobet - https://orcid.org/0000-0001-6164-4342

## References

1. Iijima, S. *Nature* **1991,** *354,* 56–58. doi:10.1038/354056a0
2. Valentini, L.; Armentano, I.; Kenny, J. M.; Cantalini, C.; Lozzi, L.; Santucci, S. *Appl. Phys. Lett.* **2003,** *82,* 961–963. doi:10.1063/1.1545166

3. Kong, J.; Franklin, N. R.; Zhou, C.; Chapline, M. G.; Peng, S.; Cho, K.; Dai, H. *Science* **2000,** *287,* 622–625. doi:10.1126/science.287.5453.622
4. Sayago, I.; Terrado, E.; Lafuente, E.; Horrillo, M. C.; Maser, W. K.; Benito, A. M.; Navarro, R.; Urriolabeitia, E. P.; Martinez, M. T.; Gutierrez, J. *Synth. Met.* **2005,** *148,* 15–19. doi:10.1016/j.synthmet.2004.09.013
5. Cantalini, C.; Valentini, L.; Lozzi, L.; Armentano, I.; Kenny, J. M.; Santucci, S. *Sens. Actuators, B* **2003,** *93,* 333–337. doi:10.1016/s0925-4005(03)00224-7
6. Wang, Y.; Yeow, J. T. W. *J. Sens.* **2009,** *2009,* No. 493904. doi:10.1155/2009/493904
7. Helbling, T.; Pohle, R.; Durrer, L.; Stampfer, C.; Roman, C.; Jungen, A.; Fleischer, M.; Hierold, C. *Sens. Actuators, B* **2008,** *132,* 491–497. doi:10.1016/j.snb.2007.11.036
8. Chopra, S.; Pham, A.; Gaillard, J.; Parker, A.; Rao, A. M. *Appl. Phys. Lett.* **2002,** *80,* 4632–4634. doi:10.1063/1.1486481
9. Collins, P. G.; Bradley, K.; Ishigami, M.; Zettl, A. *Science* **2000,** *287,* 1801–1804. doi:10.1126/science.287.5459.1801
10. Young, S. J.; Lin, Z. D. *Microsyst. Technol.* **2018,** *24,* 55–58. doi:10.1007/s00542-016-3154-2
11. Zaporotskova, I. V.; Boroznina, N. P.; Parkhomenko, Y. N.; Kozhitov, L. V. *Mod. Electron. Mater.* **2016,** *2,* 95–105. doi:10.1016/j.moem.2017.02.002
12. Hsu, H.-L.; Jehng, J.-M.; Sung, Y.; Wang, L.-C.; Yang, S.-R. *Mater. Chem. Phys.* **2008,** *109,* 148–155. doi:10.1016/j.matchemphys.2007.11.006
13. Sin, M. L. Y.; Chow, G. C. T.; Wong, G. M. K.; Li, W. J.; Leong, P. H. W.; Wong, K. W. *IEEE Trans. Nanotechnol.* **2007,** *6,* 571–577. doi:10.1109/tnano.2007.900511
14. Wang, W.-H.; Huang, B.-C.; Wang, L.-S.; Ye, D.-Q. *Surf. Coat. Technol.* **2011,** *205,* 4896–4901. doi:10.1016/j.surfcoat.2011.04.100
15. Clément, P.; Ramos, A.; Lazaro, A.; Molina-Luna, L.; Bittencourt, C.; Girbau, D.; Llobet, E. *Sens. Actuators, B* **2015,** *208,* 444–449. doi:10.1016/j.snb.2014.11.059
16. Kharisov, B. I.; Kharissova, O. V.; Ortiz Méndez, U.; De La Fuente, I. G. *Synth. React. Inorg., Met.-Org., Nano-Met. Chem.* **2016,** *46,* 55–76. doi:10.1080/15533174.2014.900635
17. Star, A.; Joshi, V.; Skarupo, S.; Thomas, D.; Gabriel, J.-C. P. *J. Phys. Chem. B* **2006,** *110,* 21014–21020. doi:10.1021/jp064371z
18. Mudimela, P. R.; Scardamaglia, M.; González-León, O.; Reckinger, N.; Snyders, R.; Llobet, E.; Bittencourt, C.; Colomer, J. F. *Beilstein J. Nanotechnol.* **2014,** *5,* 910–918. doi:10.3762/bjnano.5.104
19. Lin, Z.-D.; Hsiao, C.-H.; Young, S.-J.; Huang, C.-S.; Chang, S.-J.; Wang, S.-B. *IEEE Sens. J.* **2013,** *13,* 2423–2427. doi:10.1109/jsen.2013.2256124
20. Hinds, B. J.; Chopra, N.; Rantell, T.; Andrews, R.; Gavalas, V.; Bachas, L. G. *Science* **2004,** *303,* 62–65. doi:10.1126/science.1092048
21. Deokar, G.; Vancsó, P.; Arenal, R.; Ravaux, F.; Casanova-Cháfer, J.; Llobet, E.; Makarova, A.; Vyalikh, D.; Struzzi, C.; Lambin, P.; Jouiad, M.; Colomer, J.-F. *Adv. Mater. Interfaces* **2017,** *4,* 1700801. doi:10.1002/admi.201700801
22. Albiss, B. A.; Sakhaneh, W. A.; Jumah, I.; Obaidat, I. M. *IEEE Sens. J.* **2010,** *10,* 1807–1812. doi:10.1109/jsen.2010.2049739
23. Cho, W.-S.; Moon, S.-I.; Paek, K.-K.; Lee, Y.-H.; Park, J.-H.; Ju, B.-K. *Sens. Actuators, B* **2006,** *119,* 180–185. doi:10.1016/j.snb.2005.12.004
24. Ahmadnia-Feyzabad, S.; Khodadadi, A. A.; Vesali-Naseh, M.; Mortazavi, Y. *Sens. Actuators, B* **2012,** *166–167,* 150–155. doi:10.1016/j.snb.2012.02.024
25. Novak, J. P.; Snow, E. S.; Houser, E. J.; Park, D.; Stepnowski, J. L.; McGill, R. A. *Appl. Phys. Lett.* **2003,** *83,* 4026–4028. doi:10.1063/1.1626265
26. Cattanach, K.; Kulkarni, R. D.; Kozlov, M.; Manohar, S. K. *Nanotechnology* **2006,** *17,* 4123–4128. doi:10.1088/0957-4484/17/16/022
27. Afrin, R.; Shah, N. A. *Diamond Relat. Mater.* **2015,** *60,* 42–49. doi:10.1016/j.diamond.2015.10.010
28. Thamri, A.; Baccar, H.; Struzzi, C.; Bittencourt, C.; Abdelghani, A.; Llobet, E. *Sci. Rep.* **2016,** *6,* No. 35130. doi:10.1038/srep35130
29. Hu, L.; Hecht, D. S.; Grüner, G. *Nano Lett.* **2004,** *4,* 2513–2517. doi:10.1021/nl048435y
30. Jang, H.-K.; Jin, J. E.; Choi, J. H.; Kang, P.-S.; Kim, D.-H.; Kim, G. T. *Phys. Chem. Chem. Phys.* **2015,** *17,* 6874–6880. doi:10.1039/c4cp05964f
31. Penza, M.; Rossi, R.; Alvisi, M.; Signore, M. A.; Cassano, G.; Dimaio, D.; Pentassuglia, R.; Piscopiello, E.; Serra, E.; Falconieri, M. *Thin Solid Films* **2009,** *517,* 6211–6216. doi:10.1016/j.tsf.2009.04.009
32. Sharma, A.; Tomar, M.; Gupta, V. *J. Mater. Chem.* **2012,** *22,* 23608–23616. doi:10.1039/c2jm35172b
33. Lenner, M. *Atmos. Environ. (1967-1989)* **1987,** *21,* 37–43. doi:10.1016/0004-6981(87)90268-x
34. The International Council on Clean Transportation, Vehicle NOx emmissions. https://www.theicct.org/cards/stack/vehicle-nox-emissions-basics (accessed Jan 23, 2019).
35. Latif, U.; Najafi, B.; Glanznig, G.; Dickert, F. L. *Sens. Actuators, B* **2013,** *188,* 584–589. doi:10.1016/j.snb.2013.07.065
36. Charlier, J.-C.; Arnaud, L.; Avilov, I. V.; Delgado, M.; Demoisson, F.; Espinosa, E. H.; Ewels, C. P.; Felten, A.; Guillot, J.; Ionescu, R.; Leghrib, R.; Llobet, E.; Mansour, A.; Migeon, H.-N.; Pireaux, J.-J.; Reniers, F.; Suarez-Martinez, I.; Watson, G. E.; Zanolli, Z. *Nanotechnology* **2009,** *20,* 375501. doi:10.1088/0957-4484/20/37/375501
37. Suarez-Martinez, I.; Bittencourt, C.; Ke, X.; Felten, A.; Pireaux, J. J.; Ghijsen, J.; Drube, W.; Van Tendeloo, G.; Ewels, C. P. *Carbon* **2009,** *47,* 1549–1554. doi:10.1016/j.carbon.2009.02.002
38. Mikhlin, Y.; Likhatski, M.; Tomashevich, Y.; Romanchenko, A.; Erenburg, S.; Trubina, S. *J. Electron Spectrosc. Relat. Phenom.* **2010,** *177,* 24–29. doi:10.1016/j.elspec.2009.12.007
39. Shankar, P.; Rayappan, J. B. B. *Sci. Lett. J.* **2015,** *4,* 126.
40. Baccar, H.; Thamri, A.; Clément, P.; Llobet, E.; Abdelghani, A. *Beilstein J. Nanotechnol.* **2015,** *6,* 919–927. doi:10.3762/bjnano.6.95
41. Carot, M. L.; Macagno, V. A.; Paredes-Olivera, P.; Patrito, E. M. *J. Phys. Chem. C* **2007,** *111,* 4294–4304. doi:10.1021/jp066513v
42. Knak Jensen, S. J.; Tang, T.-H.; Csizmadia, I. G. *J. Phys. Chem. A* **2003,** *107,* 8975–8979. doi:10.1021/jp035024h
43. Zhang, H.-L.; Evans, S. D.; Henderson, J. R.; Miles, R. E.; Shen, T.-H. *Nanotechnology* **2002,** *13,* 339. doi:10.1088/0957-4484/13/3/339
44. Su, P.-G.; Kuo, X.-R. *Sens. Actuators, A* **2014,** *205,* 126–132. doi:10.1016/j.sna.2013.10.024
45. Roso, S.; Degler, D.; Llobet, E.; Barsan, N.; Urakawa, A. *ACS Sens.* **2017,** *2,* 1272–1277. doi:10.1021/acssensors.7b00504
46. Fei, T.; Jiang, K.; Jiang, F.; Mu, R.; Zhang, T. *J. Appl. Polym. Sci.* **2014,** *131,* 39726. doi:10.1002/app.39726
47. Bennett, M. E.; Alexander, W. A.; Lu, J. W.; Troya, D.; Morris, J. R. *J. Phys. Chem. C* **2008,** *112,* 17272–17280. doi:10.1021/jp801476f
48. Young, S.-J.; Lin, Z.-D.; Hsiao, C.-H.; Huang, C.-S. *Int. J. Electrochem. Sci.* **2012,** *7,* 11634–11640.

49. Espinosa, E. H.; Ionescu, R.; Bittencourt, C.; Felten, A.; Erni, R.; Van Tendeloo, G.; Pireaux, J.-J.; Llobet, E. *Thin Solid Films* **2007,** *515,* 8322–8327. doi:10.1016/j.tsf.2007.03.017
50. Clément, P.; Korom, S.; Struzzi, C.; Parra, E. J.; Bittencourt, C.; Ballester, P.; Llobet, E. *Adv. Funct. Mater.* **2015,** *25,* 4011–4020. doi:10.1002/adfm.201501234
51. Pensa, E.; Cortés, E.; Corthey, G.; Carro, P.; Vericat, C.; Fonticelli, M. H.; Benítez, G.; Rubert, A. A.; Salvarezza, R. C. *Acc. Chem. Res.* **2012,** *45,* 1183–1192. doi:10.1021/ar200260p

## License and Terms

Section 2.4

# Multiwalled Carbon Nanotubes Based Aromatic VOCs Sensor: Sensitivity Enhancement Through 1-Hexadecanethiol Functionalization

Nadra Bohli, Meryem Belkilani, Syrine Behi, Juan Casanova-Chafer, Eduard Llobet, Adnane Abdelghani

*Beilstein Journal of Nanotechnology 2019 (in press)*

DOI: in process

UNIVERSITAT ROVIRA I VIRGILI
GAS SENSING WITH MODIFIED CARBON NANOTUBES, GRAPHENE AND DIAMONDOIDS
Juan Casanova Cháfer

# Multiwalled Carbon Nanotubes Based Aromatic VOCs Sensor: Sensitivity Enhancement Through 1-Hexadecanethiol Functionalization

Nadra Bohli*[1], Meryem Belkilani[1,2], Syrine Behi[1], Juan Casanova-Chafer[3], Eduard Llobet[3] and Adnane Abdelghani[1]

[1]Carthage University, National Institute of Applied Science and Technology, Research Unit of Nanobiotechnology and Valorisation of Medicinal Plants UR17ES22, Bp 676, Centre Urbain Nord, 1080 Charguia Cedex, Tunisia ; [2]Tunis University, ENSIT, Avenue Taha Hussein, Montfleury, 1008 Tunis, Tunisia and [3]MINOS-EMaS, Universitat Rovira i Virgili, Avda. Països Catalans, 26, 43007 Tarragona, Spain.

Email: nadra.bohli@insat.u-carthage.tn

* Corresponding author

## Abstract

Aromatic VOCs sensors are attracting a growing interest in the research community as a response to a pressing market need of sensitive, fast response, low power consumption and stable sensors. Benzene and Toluene detection is subject to several potential applications such as air monitoring in chemical industries or even biosensing of human breath. In this work, we report the fabrication of a room temperature toluene and benzene sensor based on multiwall carbon nanotubes

(MWCNTs) decorated with gold nanoparticles and functionalized with a long chain thiol self-assembled monolayer, 1-hexadecanethiol (HDT). High Resolution Transmission Electron Microscopy (HRTEM) and Fourier Transform Infra-Red spectroscopy (FTIR) were performed to characterize the gold nanoparticles decoration and to check the thiol monolayer bonding to the MWCNTs. The detection of aromatic vapours with electric measurements on Au-MWCNTs and HDT/Au-MWCNTs in ppm range shows that the presence of the self-assembled layer increases sensitivity (up to 17 times), selectivity and improves response dynamics of the sensors.

## Keywords

SAMs; Vapour sensor; Gold decorated MWCNTs; Sensitivity; Selectivity.

## Introduction

Aromatic volatile organic compounds (VOCs) such as Benzene and Toluene, are hazardous vapours causing considerable damage to human health upon extended exposure. Benzene, for example, is known to have a carcinogenic effect on exposed humans. Since 2008, Toluene and Benzene monitoring is mandatory by the European Air Quality Directive, where the upper and lower assessment thresholds for Benzene are respectively limited to 0.6 ppb and 1.05 ppb. The monitoring method to be used according to the European directive is complex, expensive and time-consuming. It is carried out through active/online sampling, using desorption and gas chromatography, which are hardly portable or practical methods to be extended for indoor mass production monitoring [1]. All these facts boosted the scientific

community to work intensively on the development of cost effective, sensitive and reliable sensors for environmental pollution monitoring.

Moreover, besides the prevention of indoor exposure to harmful aromatic VOCs, a new application has arisen recently for the development of such gas sensors. In fact, recent scientific evidence proved a correlation between the presence of some VOCs in exhaled human breath and the presence of a disease. For instance, the presence of trace concentration of toluene in exhaled breath is associated with lung cancer and can therefore be considered as a biomarker to this pathology [2-4].

A gas sensor is generally composed of an active sensing film or material deposited on an electrode. Its sensing performances are strongly correlated to that active sensing film/material used. Various nanomaterials-based gas sensors have been investigated to monitor the presence of aromatic VOCs. The ones mainly studied are based on metal oxides, carbon nanotubes, graphene and hybrid materials [5, 6].

Carbon nanotube based gas sensors (single wall carbon nanotube (SWCNT), Multiwall carbon nanotubes (MWCNTs), graphene, graphene oxide (GO), etc.) present a sensitive active layer exhibiting an electrical resistance change while in contact with the target gas due to interactions at the molecular level [7, 8]. These interactions, depending whether they are strong covalent ones (chemisorption) or weak (physisorption) highly impact the sensor performance: sensitivity, response and recovery times, detection range. Unlike metal oxide-based gas sensors, CNTs based ones operate at room temperature (low activation energy) and can therefore lead to the development of commercially affordable sensors [9,10]. However, they suffer from some limitations such as their poor selectivity, partial recovery and long response recovery times [11]. To overcome these issues, several strategies were reported including, but not limited to, metal decoration or chemical functionalization [12].

In the present work, we investigated the effect of gold nanoparticle decorated multiwall carbon nanotubes functionalized with 1-hexadecanethiol on the sensor selectivity and sensitivity towards Benzene and Toluene vapours.

# Experimental

## Materials

Multiwall carbon nanotubes (MWCNTs) were purchased from Nanocyl S.A. (Belgium) with a minimum purity of 95 wt.%. They have an average length of 50 μm and average inner / outer diameters of 3 and 15 nm, respectively. 1-Hexadecanethiol (HDT) was purchased from Sigma Aldrich.

## Sensors fabrication

### MWCNTs Gold nanoparticles decoration

Prior to their deposition on the interdigitated electrode surface, MWCNTs were treated by oxygen plasma to create oxygen vacancies on the walls of CNTs in order to enhance their surface reactivity [13, 14]. The detailed description of the experimental steps undertaken is presented in the Supporting Information File 1 [15-17]. The MWCNTs were then dispersed in dimethylformamide (DMF) (0.1 mg MWCNTs in 1 mL of DMF) using an ultrasonic bath for 20 minutes at room temperature. Then, they were deposited on platinum interdigitated electrodes of an alumina substrate by air-brushing. They were then decorated with gold nanoparticles via the "sputtering" technique with "Sputtering ATC Orion 8-HV-AJA International machine" [18]. This technique consists of bombarding the surface of a gold disc by a plasma beam, enabling the nanoparticles to cling to the walls of MWCNTs under the effect of nucleation. The power and time required for the plasma beam aperture within the cell were optimized and fixed to 30 W and 10 seconds respectively.

### Functionalization with self-assembled monolayers (SAMs)

The Au decorated MWCNTs substrate was further functionalized with an alkanethiol self-assembled monolayer of 1-Hexadecanethiol (HDT). The sensor functionalization was undertaken through its immersion for 4 hours at room temperature in a solution of 5 mM of HDT diluted in ethanol. The sensor is then rinsed with ethanol to wash out the unbound thiol molecules and dried under a nitrogen stream [19]. Figure 1 shows the synoptic structure of the sensor before and after the HDT deposition.

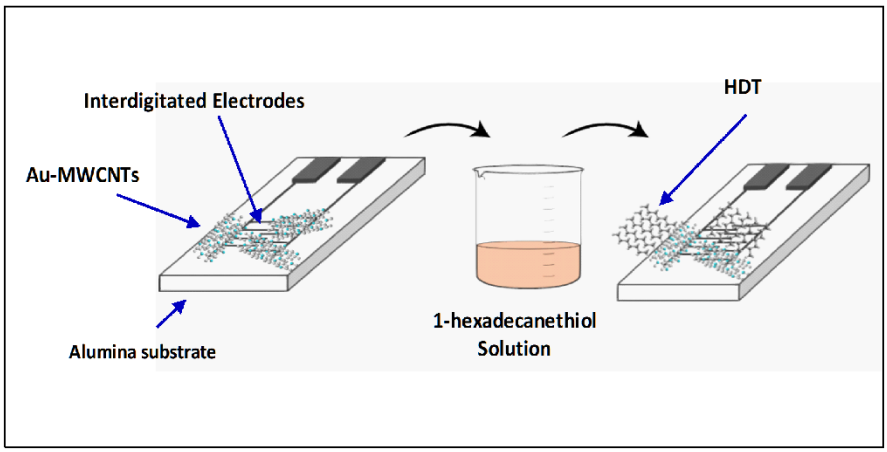


**Figure 1:** Synoptic structure of the sensor before and after the HDT deposition.

## HRTEM and FTIR characterizations

The analysis of the quantity and distribution of the gold nanoparticles attached to the MWCNTs was undertaken with a high-resolution transmission electron microscope (JEOL 1011), operating at 100 kV. An Alpha FTIR spectrometer (Bruker, France) equipped with an ATR Platinum crystal diamond module was used, in absorbance mode, to obtain the infrared spectra of the gold decorated MWCNTs before and after the deposition of the SAMs monolayer. This technique provides useful information on the various chemical bonds present on the sensor structure.

## Vapour sensing experimental setup

The sensors developed, based on Au-MWCNTs and HDT/Au-MWCNTs, were tested for the detection of aromatic VOCs (Toluene and Benzene). The vapours were generated by a dilution bench consisting of a chemical vaporization cell for solvents and two flowmeters to generate reproducible concentrations of the different vapours tested. These were coupled to a sensor cell (35 $cm^3$ volume) which can support up to 6 sensors at a time. Sensor resistance was measured using an Agilent HP 34972A Multimeter at a fixed operating frequency of 1kHz. Once a stable electrical resistance was achieved in the presence of the carrier gas (pure dry air, bought from Air Liquide), we injected the adequate concentration of the target VOC. The flow rate was set to 200 standard cubic centimeters per minute. All measurements were carried out at room temperature and the response of the sensors was defined as the normalized resistance variation, presented in equation 1 [20, 21].

$$\frac{\Delta R}{R_0}(\%) = \left[\frac{R_g - R_0}{R_0}\right] * 100 \qquad (1)$$

Where $R_0$ and $R_g$ are respectively the resistance under the carrier gas and the aromatic VOC.

# Results and Discussion

## Morphological and compositional characterization

### Transmission electron microscopy characterization

In order to carry out high-resolution transmission electron microscope characterization, the MWCNTs were diluted in ethanol and then deposited on a grid and decorated by the same method and at the same time as the substrates. Figure 2 displays HRTEM images at 20 nm scale. The image clearly shows a successful and homogenous grafting of the Au nanoparticles onto the sidewalls of the MWCNTs. The HRTEM analysis indicates an average gold nanoparticle size of 2 nm.

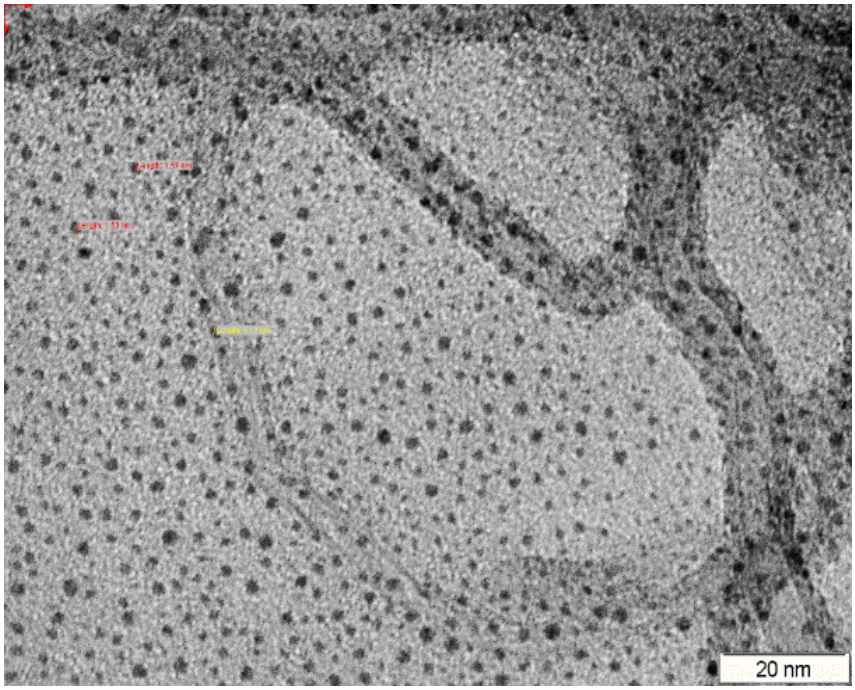


**Figure 2:** HRTEM image of MWCNTs decorated with Au nanoparticles at 20 nm scale.

**FTIR characterization**

In order to ensure that the HDT monolayers are formed and well immobilized on the Au-MWCNTs layers, we used the FTIR characterization. Figure 3 shows the infrared spectra, in absorbance mode, of both Au-MWCNTs and HDT/Au-MWCNTs layers.

When analyzing and comparing the infrared spectra of Au-MWCNTs and SAMs/Au-MWCNTs layers, we found common bands and peaks associated with the carbonyl, carboxyl and hydroxyl groups attached to the MWCNTs side walls during the oxygen plasma treatment. We found also common bands and peaks associated with the C-H bonds present in both layers. The corresponding bands are found at 2960, 1730, 1470, 1290 and 1076 $cm^{-1}$, that can be assigned respectively to C–H stretching, C=O stretching, C-H bending, C– O stretching and C–H anti-stretching vibration mode. The existence of the Au–S bond associated weak intensity peak positioned at 2360 $cm^{-1}$ which proves the attachment of 1-Hexadecanethiol on the Au-MWCNTs sensor layer [22-25]. Moreover, other techniques were used for thiol monolayer

characterization. In previous work [26, 27], different thiol chains were characterized by Raman spectroscopy, X-ray Photoelectron Spectroscopy (XPS) and contact angle measurement. In summary, the obtained FTIR results confirm the covalent functionalization of Au-decorated MWCNTs with HDT.

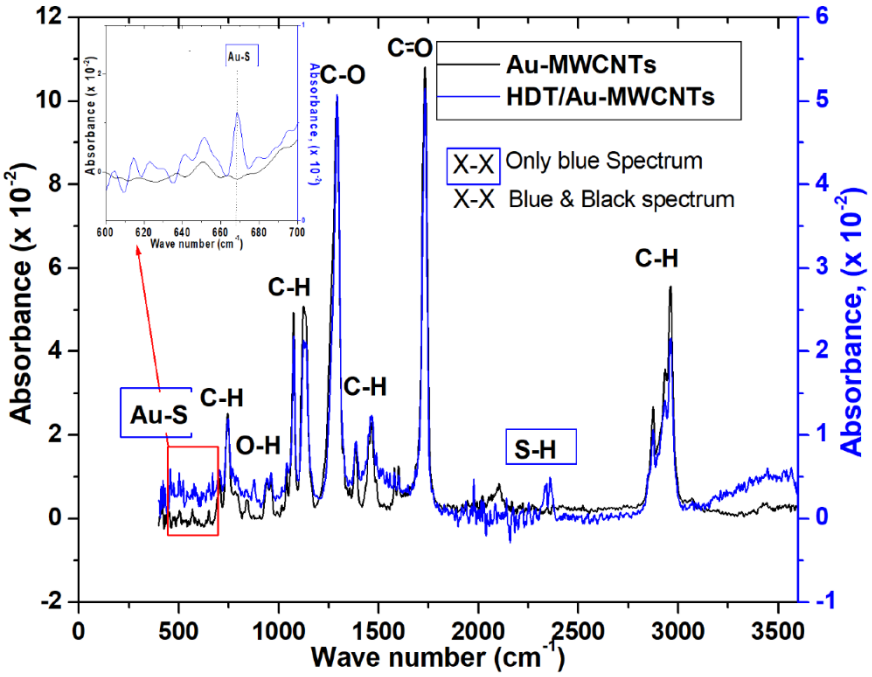


**Figure 3:** Infrared spectra of Au-MWCNTs and SAMs/Au-MWCNTs layers.

## Sensing results

### Au-MWCNTs sensing of aromatic VOCs

Figure 4 shows the response of the Au-MWCNTs sensor to the benzene and toluene for various vapours concentrations injected at room temperature.

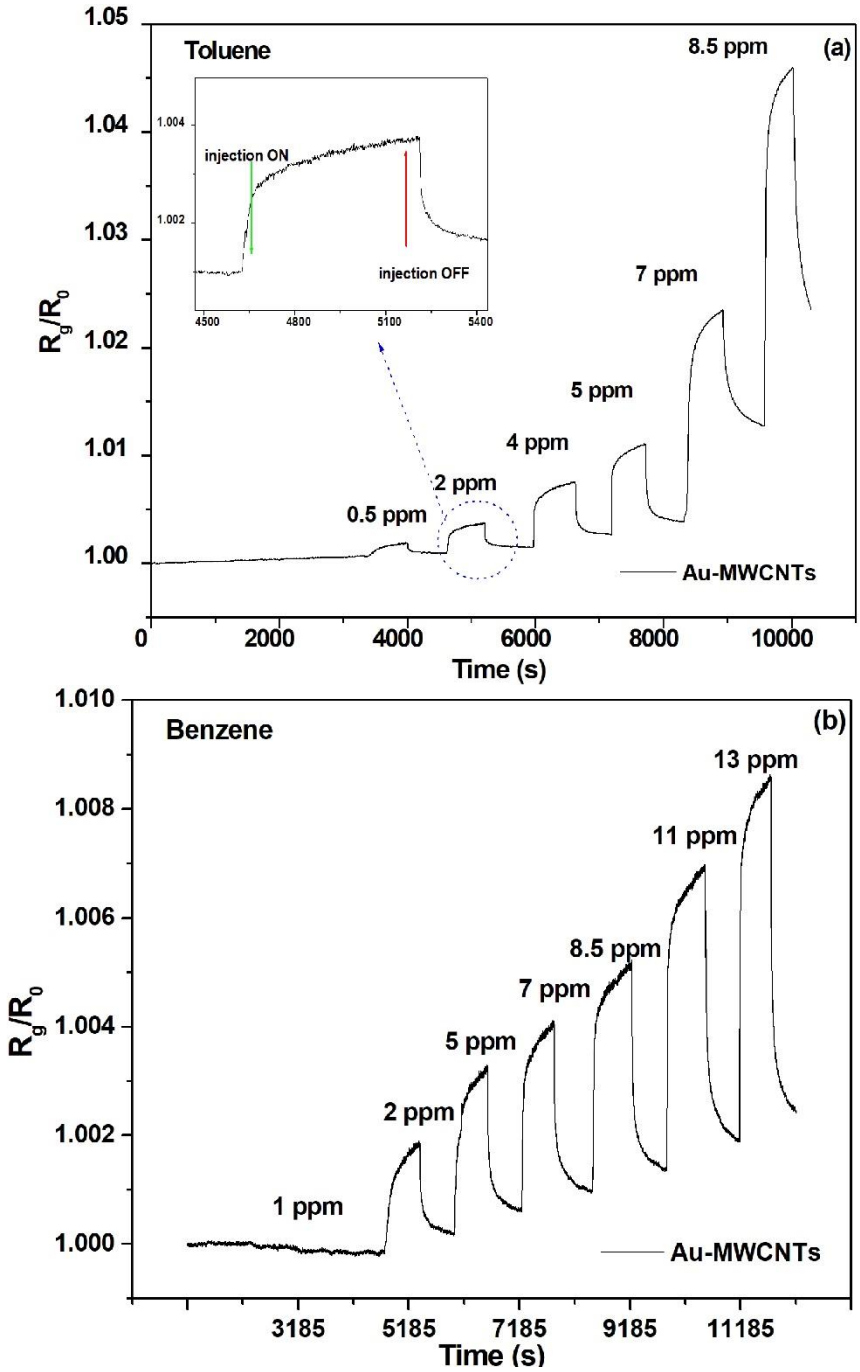


**Figure 4:** Au-MWCNT sensor responses for different concentrations of the injected vapours of (a) Toluene and (b) Benzene;

The results show an increasing resistance alongside with the increasing concentrations of the injected vapours. The adsorption of these vapours on the Au-MWCNTs films leads to a reduction of global sensor electrical conductivity. The lowest concentrations measured were 2 ppm for Benzene and 0.5 ppm for Toluene. A physisorption is observed for Toluene at concentrations below 7 ppm (below 5ppm

for Benzene), indicating weak interaction forces between the vapour molecules and the Au-MWCNTs active sensor layer and the signal return to the baseline. For higher concentration, a drift was observed in the baseline due to the higher interaction with toluene (respectively Benzene). This stronger interaction suggests slower baseline overlaps, which can be accelerated with short heating for few seconds at 70 °C (Figure 5).

**HDT/Au-MWCNTs sensing of aromatic VOCs**

Figure 5 shows the response of the HDT/Au-MWCNTs sensor to the Benzene and Toluene vapours concentrations injected at room temperature.

The detection results of the various injected vapours show a considerable decrease in the electrical conductivity of the HDT/Au-MWCNT sensor compared with the non-functionalized sensor. The same kinetics were also observed, where a physisorption is visible for Toluene below 7 ppm concentration (below 5 ppm for Benzene). A short heating at 70°C for few seconds is sufficient for un-saturating the sensor (desorbing the vapour molecules) and its return to the baseline. The figure's insets represent sensors response after heating and after a storage for several months (8 months). It clearly shows that our sensors respond after heating and after several months.

This weak interaction with both type of sensors surface can be explained by the hydrophobic-hydrophobic interaction between the functional groups of the monolayer ($CH_3$ groups) and the $CH_3$ group of the Toluene molecule. The considerable decrease in the conductivity is due to the oxidizing nature of the injected vapours. As the tested oxygen-treated and gold decorated MWCNTs are "p" type semiconductors, the adsorption of the oxidant vapour molecules leads to a transfer of the majority carriers of "p" type semiconductors towards the adsorbed vapours molecules. This transfer results in a decrease of the majority carriers in the valence band of the

decorated carbon nanotubes, and thus the decrease of the measured conductivity [28].

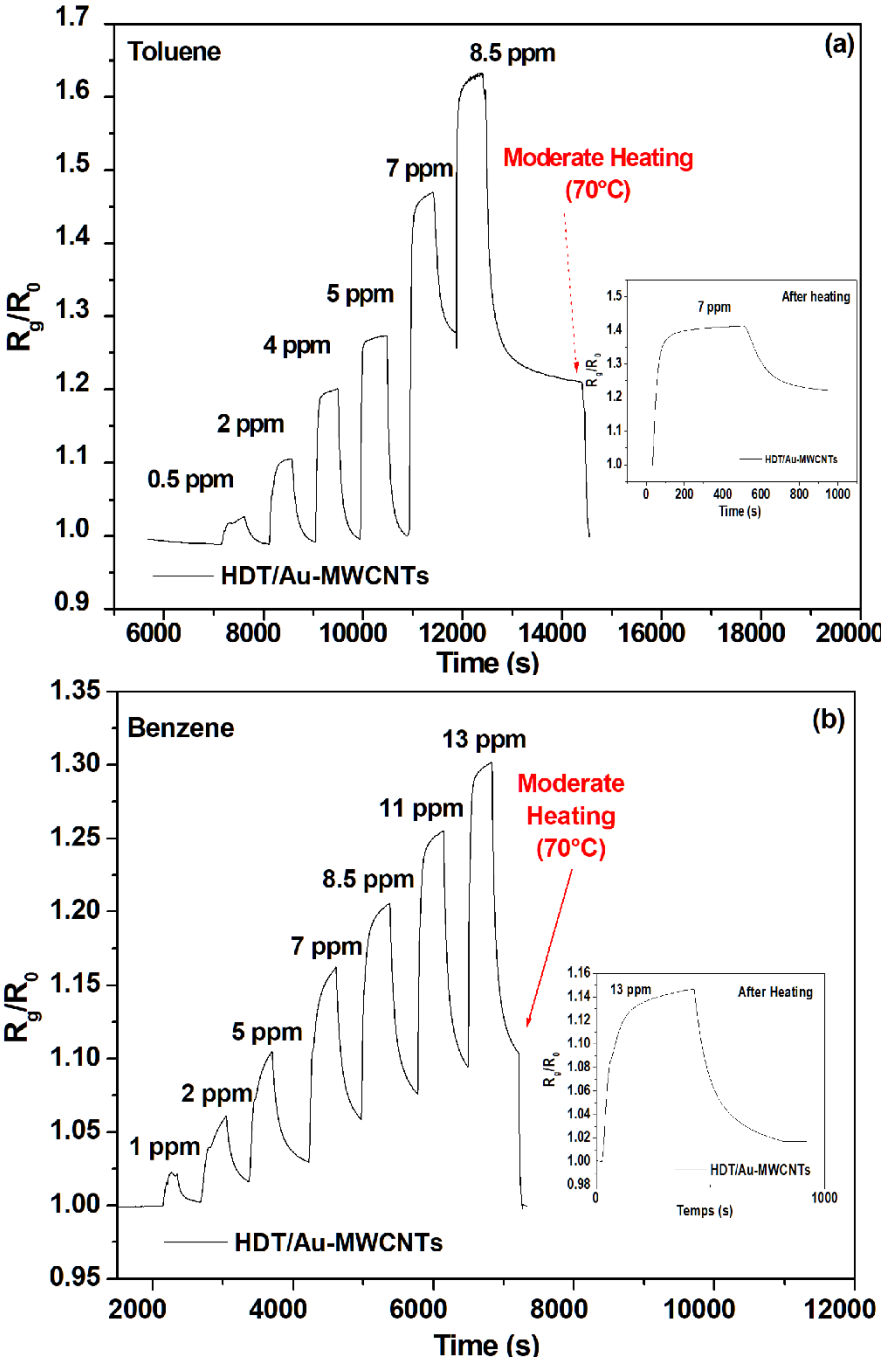


**Figure 5:** HDT/Au-MWCNTs sensor responses for different concentrations of the injected vapours of (a) Toluene and (b) Benzene.

## Sensor performance

The calibration curves, expressing the normalized sensors resistance versus the vapour concentration for Toluene and Benzene are presented respectively in Figure 6 (a) and (b) for both tested sensors.

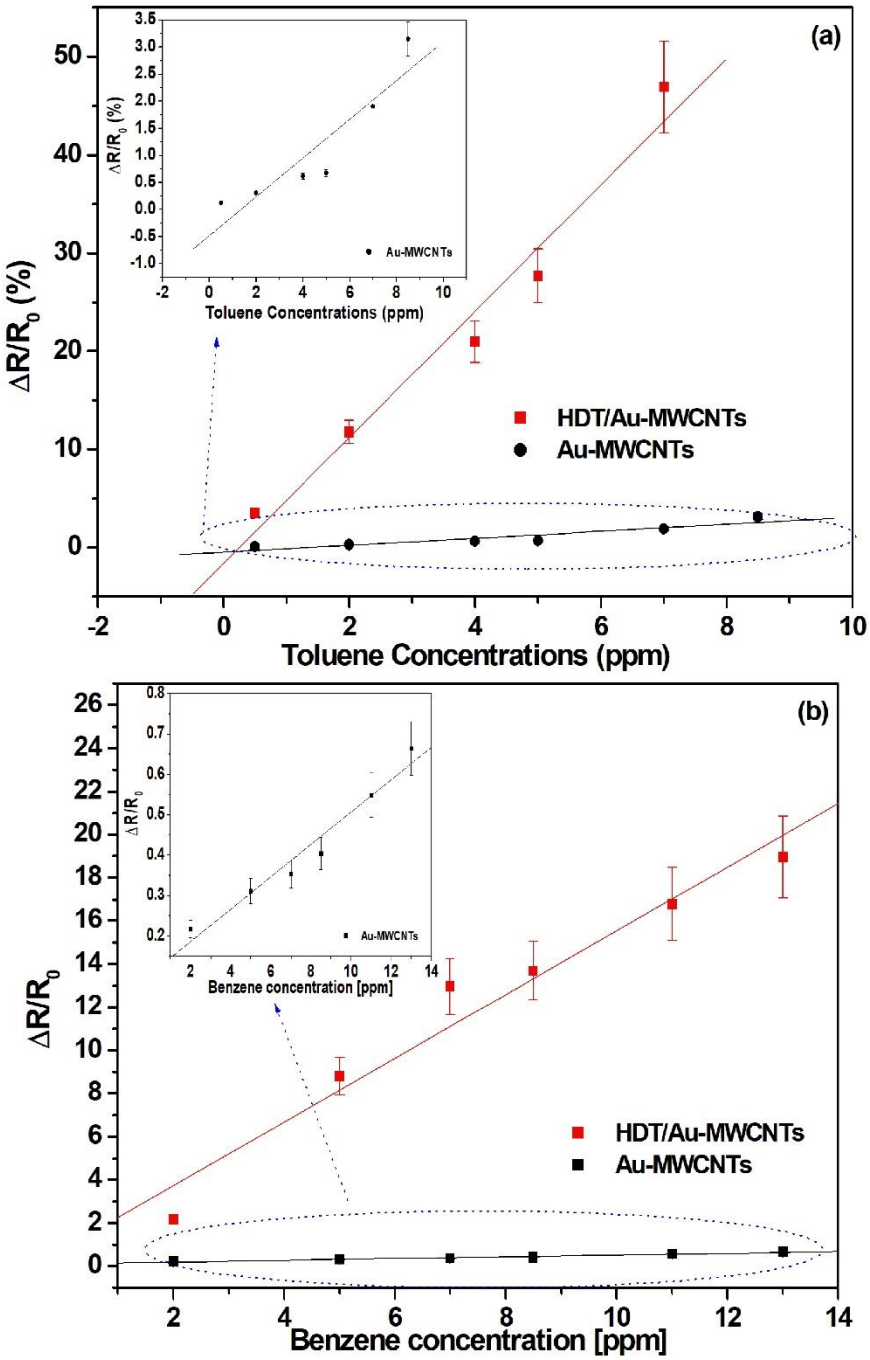


**Figure 6:** Calibration curves for Au-MWCNTs and HDT/Au-MWCNTs sensors for (a) Toluene and (b) Benzene Aromatic VOCs detection.

The associated sensitivities are displayed in Table 1.

**Table 1:** Au-MWCNTs and HDT/Au-MWCNTs sensors sensitivity for aromatic and non-aromatic vapours.

| Sensitivity ($10^{-2}$x $ppm^{-1}$) | Toluene | Benzene | Methanol | Acetone |
|---|---|---|---|---|
| Au-MWCNT | 35.8 | 4.8 | 3.15 | 0.84 |
| HDT/Au-MWCNT | 642.17 | 147 | 78.91 | 20.48 |

A dramatic increase in the HDT functionalized sensor sensitivity is observed for both vapours. The increase goes from 4.79 $10^{-2}$ %. $ppm^{-1}$ to 147 $10^{-2}$ %. $ppm^{-1}$ for Benzene and from 35.82 $10^{-2}$ %. $ppm^{-1}$ to 642.17 $10^{-2}$ %. $ppm^{-1}$ for Toluene. It is noteworthy to point out that $CH_3$ group in the HDT molecule seems to have a high affinity towards aromatic vapour, in contrast with the results presented in a previous work, where a 16-Mercaptohexadecanoic acid (MHDA) showed no response to aromatic vapours [21]. As presented in Table 1, the vapours tested are non-polar in nature and have therefore a high affinity with the hydrophobic $CH_3$ group of the HDT. On the contrary, MHDA are carboxylic acid terminated thiol, which are hydrophilic, and have little possible interactions with the non-polar vapours. In order to prove the improved selectivity of the developed sensor toward benzene and Toluene vapours, we tested the sensors response to methanol and acetone vapours, which are polar solvents. The sensor responses to these nonaromatic VOCs vapours are summarized in the Supporting Information File 1 (See figures S1 and S2). The associated calibration curves and compared sensitivities are respectively presented in Figure 7 and Table 1. The sensitivity for aromatic solvent for the HDT sensors is bigger in comparison with methanol and acetone. This can be explained by the fact that the assembled $CH_3$ group acts as a Lewis acid and the latter one (Benzene and Toluene) as a Lewis base [29]. The sensitivity for Toluene is bigger than to Benzene due to the difference in their dipole moment (Toluene: 0.375; Benzene: 0).

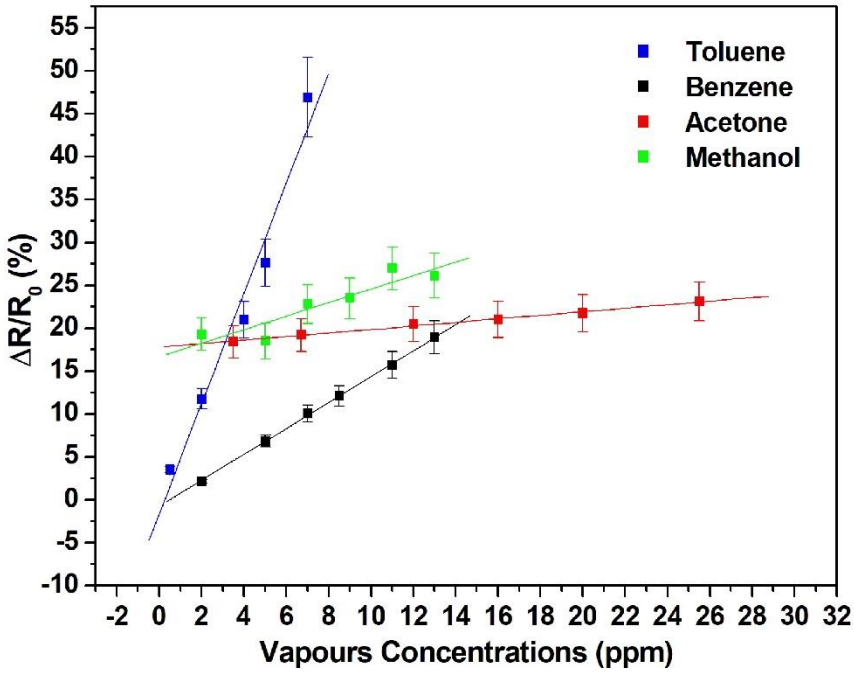


**Figure 7:** Calibration curves of HDT/Au-MWCNTs sensor for Methanol and Acetone nonaromatic VOCs detection.

The effect of ambient moisture on the sensor response was studied in previous work [27]. The response to vapours remains basically unchanged for sensors employing hydrophobic thiols due to their hydrophobicity [26]. Such long-chain alkanethiols functionalized decorated multiwall carbon nanotubes showed a high contact angle with water which remains stable after a one month stay in aqueous media [26].

Figure 8 presents the response and recovery times of Au-MWCNTs and HDT/Au-MWCNTs sensors toward aromatic and non-aromatic vapours. The results show a faster response and recovery times for the HDT functionalized Au-MWCNTs sensor with Benzene and Toluene vapours.

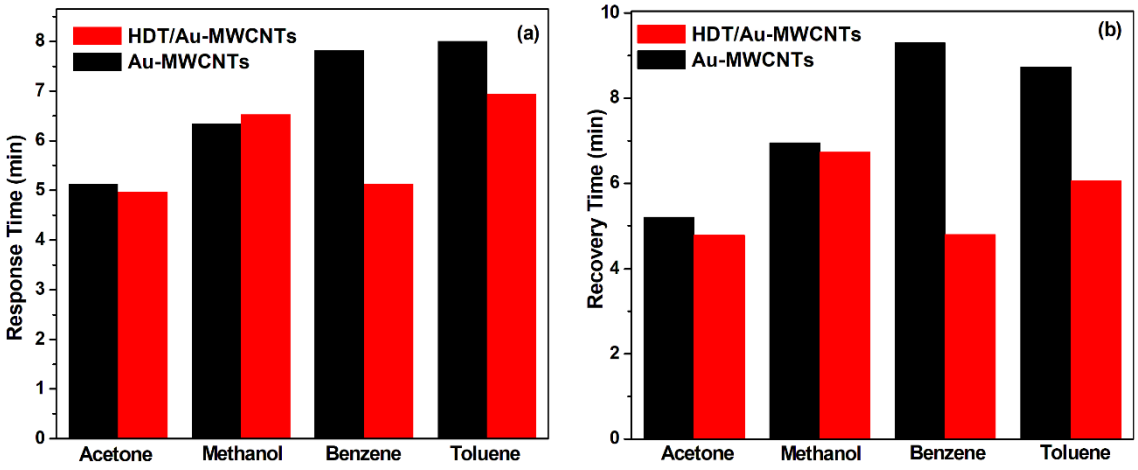


**Figure 8:** (a) Response and (b) Recovery times of Au-MWCNTs and HDT/Au-MWCNTs sensors towards tested vapours.

# Conclusion

In this work, we studied the detection of aromatic vapours in ppm range with a sensor composed of HDT functionalized gold decorated multiwall carbon nanotubes. The studied self-assembled monolayer, with its $CH_3$ functional group increased the sensor's sensitivity (up to 17 times) and selectivity. It also improves the sensor response dynamics. These results combined with previous results [21, 27] could be interesting for the development of functionalized multisensors arrays combined with artificial intelligence algorithm for selectivity enhancement.

# Supporting Information

Details on HDT/Au-MWCNTs sensor fabrication process and its response to methanol and acetone vapours.

Supporting Information File 1: Details on HDT/Au-MWCNTs sensor fabrication process and its response to methanol and acetone vapours.

File Name: Supporting information File 1

File Format: Text

Title: Details on HDT/Au-MWCNTs sensor fabrication process and its response to methanol and acetone vapours.

## Acknowledgements

The authors thank the Alexander Von Humboldt Foundation (Bonn, Germany) for material donation. This work is funded by the Science for Peace and Security Program of the North Atlantic Treaty Organization under grant no. SFP 984511.

## References

1. Spinelle, L.; Gerboles, M.; Kok, G.; Persijn, S.; Sauerwald, T. Sens. **2017**, 17, 1520–1550. http://dx.doi.org/10.3390/s17071520

2. Haick, H.; Broza, Y. Y.; Mochalski, P.; Ruzsanyi, V.; Amann, A. Chem. Soc. Rev., **2014**, 43, 1423−1449. https://doi.org/10.1039/c3cs60329f

3. Ju, S.; Lee, K.-Y.; Min, S.-J.; Yoo, Y. K.; Hwang, K. S.; Kim, S. K.; Yi, H. Sci. Rep., **2015**, 5, 9196–9202. https://doi.org/10.1038/srep09196

4. Xing, R.; Xu, L.; Song, J.; Zhou, C.; Li, Q.; Liu, D.; Song, H. W. Sci. Rep. **2015**, 5, 10717–10731. https://doi.org/10.1038/srep10717

5. Xu, K.; Fu, C.; Gao, Z.; Wei, F.; Ying, Y.; Xu, C.; & Fu, G. Instrum. Sci. Technol. **2018,** 46, 115. https://doi.org/10.1080/10739149.2017.1340896

6. Aroutiounian, V. M.; Adamyan, Z. N.; Sayunts, A. G.; Khachaturyan, E. A.; Adamyan, A. Z. AMA Conferences 2015 – SENSOR 2015 and IRS2 2015, 836-841. http://dx.doi.org/10.5162/sensor2015/P8.3

7. Wang, Y.; Yeow, J. T. W. J. Sens. **2009**, 1-24. http://dx.doi.org/10.1155/2009/493904

8. Collins, P.G.; Bradley, K.; Ishigami, M.; Zettl, A. Sci. **2000**, 287, 1801–1804. http://dx.doi.org/10.1126/science.287.5459.1801

9. Ueda, T.; Katsuki, S.; Takahashi, K.; Narges, H. A.; Ikegami, T.; Mitsugi, F. Diamond and Related Materials. **2008,** 17, 1586–1589. http://dx.doi.org/10.1016/j.diamond.2008.03.009

10. Wei-De Zhang, W.D.; Zhang, W. H. J. Sensors. 2009, Article ID 160698, 16 pages. http://dx.doi.org/10.1155/2009/160698

11. Li, J. Nano lett. **2003**, 3, 7, 929-933. https://doi.org/10.1021/nl034220x

12. Zanolli, Z.; Leghrib, R.; Felten, A.; Pireaux, J.-J.; Llobet, E.; Charlier, J.-C. ACS nano. **2011**, VOL. 5 (NO. 6), 4592–4599. https://doi.org/10.1021/nn200294h

13. Valentini, L.; Cantalini, C.; Armentano, I.; Kenny, J.M.; Lozzi, L.; Santucci, S. Diam. Relat. Mater. **2004**, 13, 1301–1305. http://dx.doi.org/10.1016/j.diamond.2003.11.011

14. Hafaiedh, I.; Clément, P.; Baccar, H.; Llobet, E.; Abdelghani, A. Int. J. Nanotechnol. **2013**, 10, 485-495. http://dx.doi.org/10.1504/IJNT.2013.053518

15. Thamri, A.; Baccar, H.; Clément, P.; Llobet, E.; Abdelghani, A. Int. J. Nanotechnol. **2015**,12, 562–571. http://dx.doi.org/10.1504/IJNT.2015.068878

16. Clement, P.; Hafaiedh, I.; Parra, E.J.; Thamri, A.; Guillot, J.; Abdelghani, A. ; Llobet, E. Carbon. **2014**, 78, 510–520. http://dx.doi.org/10.1016/j.carbon.2014.07.032

17. Hafaiedh, I.; El Euch, W.; Clement, P.; Llobet, E.; Abdelghani, A. Sensor. Actuat. B: Chem. **2013**, 182, 344– 350. http://dx.doi.org/10.1016/j.snb.2013.03.020

18. Leghrib, R.; Clement, P.; Llobet, E. Procedia Eng. **2011,** 25, 223–226. http://dx.doi.org/10.1016/j.proeng.2011.12.055

19. Techane, D. S.; Gamble, L. J.; Castner, D. G.; J. Phys. Chem. C Nanomater. Interfaces. **2011,** 115, 9432–9441. http://dx.doi.org/10.1021/jp201213g

20. Baccar, H.; Thamri, A.; Clément, P.; Llobet, E.; Abdelghani, A. Beilstein J. Nanotechnol., **2015**, 6, 919–927. http://dx.doi.org/10.3762/bjnano.6.95

21. Thamri, A.; Baccar, H.; Struzzi, C.; Bittencourt, C.; Abdelghani, A.& Llobet, E. Sci. Rep., **2016**, 6, 35130-35142. http://dx.doi.org/10.1038/srep35130

22. Nawaz, M. A. N; Rauf, S.; Catanante, G.; Nawaz, M.H.; Nunes, G.; Marty, J.L.; Hayat, A. Sensors, **2016**, 16, 1651. http://dx.doi.org/10.3390/s16101651

23. Rajalingam, K.; Hallmann, L. ; Strunskus, T. ; Bashir, A.; Woll, C.; Tuczek, F. Phys. Chem. Chem. Phys., **2010**, 12, 4390–4399. http://dx.doi.org/10.1039/b923628g

24. Deręgowska, A. et al. Study of optical properties of a glutathione capped gold nanoparticles using linker (MHDA) by Fourier transform infra-red spectroscopy and surface enhanced Raman scattering. Int. J. Math. Comput. Phys. Electr. Comput. Eng. **2013,** 7, 1.

25. Chiou, B. S.; Khan, S. A. Macromolecules, **1997**, 30, 7322-7328.

26. Abdelghani, A; Chovelon, J.M.; Krafft, J.M.; Jaffrezic-Renault, N.; Trouillet, A.; Veillas, C.; Ronot-Trioli, C.; Gagnaire, H. Thin Solid Films, **1996**, 284-285, 157-161. https://doi.org/10.1016/S0040-6090(95)08295-6

27. Casanova-Cháfer, J; Bittencourt, C; Llobet, E. Beilstein J. Nanotechnol. **2019**, 10, 565–577. https://doi.org/10.3762/bjnano.10.58

28. Kwon, Y. J.; Na, H. G.; Kang, S. Y.; Choi, S.W.; Kim, S. S.; Kim, H. W.; Sensor Actuat. B-Chem, **2016**, 227,157–168. http://dx.doi.org/10.1016/j.snb.2015.12.024

29. Zhuo, H. Y.; Jiang, L. X.; Li, Q. Z.; Li, W. Z.; Cheng, J.B. Chem. Phys. Lett. **2014**, 608, 90-94. https://doi.org/10.1016/j.cplett.2014.05.074

Section 2.5

# Exploiting Sensor Geometry for Enhanced Gas Sensing Properties of Fluorinated Carbon Nanotubes Under Humid Environment

Claudia Struzzi, Mattia Scardamaglia, Juan Casanova-Chafer, Raul Calavia, Jean-Francois Colomer, Alexey Kondyurin, Marcela Bilek, Nikolay Britun, Rony Snyders, Eduard Llobet, Carla Bittencourt

*Sensors and Actuators B: Chemical, 281 (2019) 945-952*

DOI: 10.1016/j.snb.2018.10.159

UNIVERSITAT ROVIRA I VIRGILI
GAS SENSING WITH MODIFIED CARBON NANOTUBES, GRAPHENE AND DIAMONDOIDS
Juan Casanova Cháfer

Sensors & Actuators: B. Chemical 281 (2019) 945–952

Contents lists available at ScienceDirect

Sensors and Actuators B: Chemical

journal homepage: www.elsevier.com/locate/snb

# Exploiting sensor geometry for enhanced gas sensing properties of fluorinated carbon nanotubes under humid environment

C. Struzzi[a,b,*], M. Scardamaglia[a,c], J. Casanova-Chafer[d], R. Calavia[d], J.-F. Colomer[e], A. Kondyurin[c,f], M. Bilek[c], N. Britun[a], R. Snyders[a,g], E. Llobet[d,**], C. Bittencourt[a]

[a] Chimie des Interactions Plasma-Surface, CIRMAP, University of Mons, 7000, Mons, Belgium
[b] MAX IV Laboratory, University of Lund, 22100, Lund, Sweden
[c] Applied and Plasma Physics Group, Physics Department, University of Sydney, Sydney, Australia
[d] MINOS Group, Universitat Rovira i Virgili, Tarragona, Spain
[e] Research Group on Carbon Nanostructures (CARBONNAGe), University of Namur, 5000, Namur, Belgium
[f] Farm, Ewingar, 2469, NSW, Australia
[g] Materia Nova Research Center, 7000, Mons, Belgium

ARTICLE INFO

*Keywords:*
Fluorinated carbon nanotubes
Sensing response to $NO_2$ and $NH_3$
Room temperature gas sensors
Increased response reproducibility under humid conditions

ABSTRACT

Modification of the surface electronic properties of vertically aligned and randomly distributed carbon nanotubes and the hydrophobic character after exposure to Ar:$F_2$ and $CF_4$ plasma are exploited to optimize the sensing characteristics of these materials. The sensing properties of fluorinated carbon nanotubes are disclosed by probing their stability and responsiveness towards the detection of two selected pollutants such as nitrogen dioxide and ammonia ($NO_2$ and $NH_3$). The effects of both humidity level and geometry of the sensing layer are assessed. It is demonstrated that fluorination, by increasing the surface hydrophobicity, results in increased response reproducibility and enhanced sensor response towards $NH_3$ when using vertically aligned carbon nanotubes.

## 1. Introduction

Nitrogen dioxide ($NO_2$) and ammonia ($NH_3$) are critical air pollutants, the former resulting from combustion or automotive emissions while the second is a dangerous analyte that has both natural and industrial derivation. In the perspective of real-time analysis, miniaturization and cost effectiveness, semiconducting metal oxide films, capacitive polymers and silicon devices have represented the most common active layers for detection of hazardous gases [1,2]. More recently, the implementation of carbon allotropes in gas sensor technology has been suggested to meet the demand of improved criteria as sensitivity, selectivity, long-term stability and reduced fabrication cost [3–7]. Among the peculiar characteristics of carbon nanomaterials, their high aspect ratio is a key aspect promoting them as potentially excellent sensing platforms as the whole surface is involved in the process leading to a maximization of the sensing performance upon exposure to adsorbates. The introduction of active sites on the pristine carbon structure has been explored largely to boost the reactivity to gases while improving both the selectivity and the sensitivity during the detection of hazardous molecules [8,9]. Devices based on doped graphene have already shown competitive efficiency in detecting glucose [10], thus enlarging its applicability in bio-sensing technology as well. The deposition of metal [6,11,12] and metal oxide nanoparticles on carbon allotropes [13] has been proposed to improve their sensing performances. In a recent study, quinoxaline-walled thioether-legged deep cavitand functionalized multiwall carbon nanotubes have shown unprecedented sensitivity towards traces of benzene vapours [14]. However, the sensor response toward aromatic volatile organic compounds diminished as the relative humidity in the gas flow was increased due to the oxygenated defective sites at the nanotubes surface.

For optimal environmental monitoring, the humidity effects must be assessed in order to extend the use of a performant sensing device to humid working environments as well. In this respect, fluorination of carbon nanomaterials could represent a valuable solution to hinder the moisture interference as the polarity of the covalent C–F bond favours an enhanced hydrophobic character [15]. Besides the hydrophobicity, the tuning of the density of states in fluorinated carbon nanomaterials and the thermal stability of the F–C bond play a key role in several

* Corresponding author at: Chimie des Interactions Plasma-Surface, CIRMAP, University of Mons, 7000, Mons, Belgium.
** Corresponding author.
*E-mail addresses:* claudia.struzzi@maxiv.lu.se (C. Struzzi), eduard.llobet@urv.cat (E. Llobet).

https://doi.org/10.1016/j.snb.2018.10.159
Received 28 June 2018; Received in revised form 23 October 2018; Accepted 30 October 2018
Available online 08 November 2018
0925-4005/ 

application fields [16], including gas sensing experiments. The improved ambient and thermal stabilities of fluorine functionalities grafted at the carbon nanostructures surface promote such materials as potential room temperature sensing devices substituting graphene oxide or oxidized carbon nanotubes, whose performances as selective gas sensor can be compromised by the high response to variable relative humidity level and by the reduced electrical conductivity [17–19]. Recent measurements on fluorinated graphite have reported a good sensing response to several hundreds of ppm concentration of ammonia and nitrogen dioxide [20,21]. However, the sensing measurements of fluorinated carbon nanomaterials were only performed under controlled dry air, Ar or $N_2$ atmosphere, or in vacuum and these conditions do not reproduce the realistic working condition requested for a commercialized gas sensor.

In the present work, two fluorine-based gas precursors are used for the plasma fluorination of carbon nanotubes, namely Ar:$F_2$ and $CF_4$, since multiple fluorinated carbon groups, as $CF_3$, are also grafted at the carbon nanotubes surface when using the latter precursor [22,23]. After the fluorination, the carbon nanotubes are integrated in home-made chemical gas sensors platforms to address three main factors. Firstly, the possible role played by the different patterning of the fluorinated carbon sites obtained with the two plasma treatments is unravelled. Secondly, the influence of fluorine functionalities over the pristine sensor response is probed. Thirdly, the interference of humidity in the environment is addressed, as it represents the main drawback hindering the functionalized carbon-based sensing properties. The increased hydrophobicity of the carbon surfaces after fluorination is exploited, leading to an increased response reproducibility under variable humidity level. The sensing mechanism and the geometry of the sensing layer are also investigated showing an enhanced response when vertically aligned carbon nanotube forests are used as sensing layer compared to the randomly distributed, spaghetti-like nanotube mats due to the remarkable role played by the exposed tips in the vertical configuration of the forest.

## 2. Materials and methods

Vertically aligned carbon nanotubes (vCNT) are synthesized by catalytic chemical vapour deposition (CCVD) at atmospheric pressure using Fe nanoparticles as catalyst. More details on the synthesis can be found in previous reports [24,25]. The as-synthesized close-packed vCNT are well-aligned multiwalled carbon nanotubes of 150–200 μm length, a dozen walls are found on average. To fabricate spaghetti-like carbon nanotube mats with random distribution, the CNT powder (Nanocyl®, purity level 95%) is sonicated in isopropanol for 30 min and the CNT mat is obtained by drop casting the suspension on silicon wafers kept at T = 100 °C to facilitate solvent evaporation.

Fluorination of the CNT surface is achieved in a post-discharge of a microwave (MW) plasma reactor where the discharge is sustained in a quartz tube by a surface wave (surfaguide type) launcher. A SAIREM 6 kW pulsed microwave generator working at 2.45 GHz has been used [26]. The gas flow rate is set to 100 sccm for both $CF_4$ and for the Ar:$F_2$ mixture (95:5) giving a post-discharge pressure of about 1 mbar. The power is maintained to 0.55 kW and the frequency to 1 kHz with a duty ratio fixed to 80%. The samples are placed on a supporting stage at a distance of 30 cm from the end of the discharge tube. To obtain different fluorination yields, the exposure time is changed ranging from 2.5 to 20 min. No changes are observed in the weight and in the structure of the carbon nanotubes.

The contact angle measurements are conducted using the static sessile drop method based on a direct optical measurement. The experimental set-up consists of a movable horizontal stage where the sample is placed, an automatized micrometre pipette system to generate the few microliter liquid drop of Milli-Q water, and an integrated camera for acquisition of real time images. Several points over each sample surface are analysed for accuracy and reproducibility during the drop profile analysis.

The photoemission studies are carried out at the Soft X-ray beamline of the Australian Synchrotron in Melbourne. The valence band spectra are collected using a photon energy of 110 eV, while a photon energy of 800 eV is used for the acquisition of the F1 s core levels to enhance the surface sensitivity. Spectroscopy data are acquired in normal emission geometry. The carbon (C) and fluorine (F) K-edge NEXAFS spectra are obtained in the partial electron yield mode. The NEXAFS measurements are performed by positioning the samples at the magic angle, that is the angle at which the measured intensity distribution is independent from the molecular orientation.

The chemical composition of the fluorinated samples after the sensing measurements is probed by using a VERSAPROBE PHI 5000 from Physical Electronics, equipped with a monochromatic Al Kα X-ray source. The experimental geometry of the data collection allows the analysis of carbon nanotube surface with an energy resolution better than 0.5 eV. For the compensation of built-up charge on the sample surface during the measurements, a dual beam charge neutralization composed of an electron gun ($\approx$1 eV) and an Ar ion gun ($\leq$10 eV) is used.

For the sensing measurements, a customization of the device is used to prepare the sensors. A commercial Ag paste (Heraeus AD 1688-06) is employed to glue a screen-printed Pt resistor, working as a heater, on the backside of the sample. Pt wires connect the heater resistor to a PCB board that can be plugged into the sensor test chamber through soldered connections. Parallel silver electrodes are realized on top of the sample surface and connected to the PCB board through Pt wires. At each step, the contacts are cured at 100 °C for 30 min in the oven.

The measurement rig comprises a set of computer-controlled mass flow meters and electro-valve systems to ensure reproducible concentrations of the gases that are delivered to the miniaturized Teflon chamber (35 mL). The DC resistance of the sensors is continuously measured with an Agilent 34,972 A multimeter. In a typical measurement cycle, pure dry air (Air Products) is flowed through the chamber until the sample resistance is stabilized, corresponding to a constant baseline $R_0$. Successively, given concentrations of $NO_2$ or $NH_3$ vapours are fed into the test chamber and kept flowing during the chosen exposure time, that is usually fixed to 10 min unless otherwise specified. The total flow is fixed to 100 sccm during the detection and recovery phases. During the detection time, the samples are kept at room temperature. After the detection measurements, the gas flow is switched again to pure dry air and the samples are allowed to re-stabilize to the room temperature baseline resistance. The relative humidity (RH) is constantly monitored using a thermo-hygrometer ICT-7 M from Ecological Sensors and Systems (ES&S). This sensor is located at the output of the test chamber recording both temperature and ambient moisture. It is considered dry condition when a residual amount of about RH = 4 ± 1% is measured. Under humid conditions, a specific amount of water in mg/h is introduced in the test chamber using a dedicated liquid mass flow system (Environics series 4000), which allowed generating humidified gas mixtures at different moisture levels.

The operational principle of resistive sensing devices consists of the variation of the electrical resistivity as a result of the adsorption of gas molecules on the sensor surface. The measurement of the resistance is continuously running, thus allowing a real-time acquisition of its variation from the initial value, which is the sensor baseline resistance $R_0$, during a complete exposure cycle. The sensor response, expressed as a percentage, is defined (unless otherwise specified) as the normalized resistance variation, $|(R_f - R_0)/R_0| \times 100$, where $R_f$ is the resistance value measured when the gas flow is switched to pure air. The sign of the resistance variation depends on the type of semiconducting layer (n- or p- type depending on the electron or hole doping) and on the donor/acceptor behaviour of the detected molecule. Since holes are the major charge carriers in fluorinated carbon nanotubes, the fluorinated surface behaves as a p-type semiconductor.

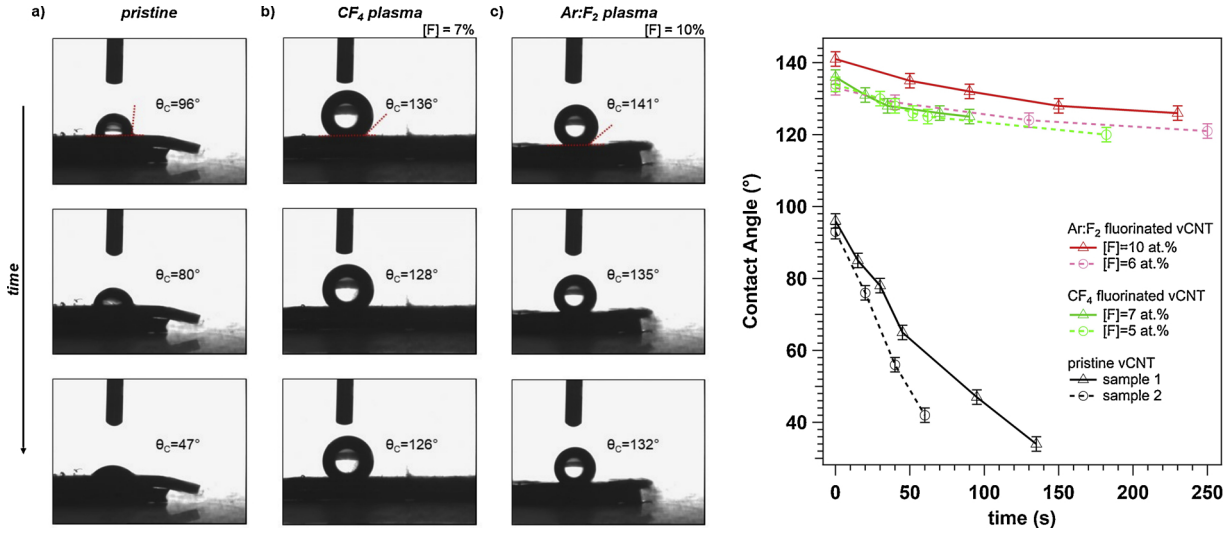


**Fig. 1.** (Left) Contact angle measurements on vertically aligned carbon nanotubes are shown for increasing fluorine content. The pictures along each column illustrate the time evolution of the water droplet. (Right) Contact angle values are acquired at increasing time to trace the water droplet evolution on two pristine samples (black curves) and on different plasma fluorinated samples, Ar:$F_2$ and $CF_4$, with various fluorine content (red and green curves) (For interpretation of the references to colour in this figure legend, the reader is referred to the web version of this article).

## 3. Results and discussion

The wettability of pristine and fluorinated vCNT is probed by measuring the contact angle at the interface with a liquid Milli-Q water drop, as shown on the left side of Fig. 1 (upper row). The initial contact angle value of pristine vCNT ($\theta_C$ = 96°) gradually rises with increasing fluorine content up to a value of $\theta_C$ = 141° for 10 at.% of F, thus reflecting the increased hydrophobic character introduced through the functionalization. The wettability is strongly dictated by the oriented dipole-dipole interactions in partially fluorinated vCNT (first row, left side of Fig. 1). The successive rows in Fig. 1 (left) correspond to the time evolution of the water droplet, each picture is collected after 30 s from the corresponding previous image. The variation of the contact angle decay rate of the pristine and functionalized samples indicates a different impedance of water diffusion into the nanotube forests. The water droplet deposited on the pristine surface is not stable and penetrates the forest, this process is further facilitated by the presence of voids on a submicron scale within the vCNT. On the contrary, the fluorinated carbon nanotubes show only a moderate reduction of the contact angle values exhibiting a higher stability with time for increasing fluorine yield at the surface. Additional data showing the contact angle trends with time for other pristine and fluorinated samples are shown on the right side of Fig. 1.

In correspondence to the remarkable changes in the surface energy induced by the fluorination, the nature of the pristine electronic properties is also largely modified. The valence band spectra are outlined for each sample in Fig. 2a. The grafting of fluorine atoms on the vCNT surface provokes a strong quenching of the C-C π states at 3 eV in concomitance with the suppression of the density of states near the Fermi level and the appearance of an intense contribution at about 10 eV, associated to the F2p-like states, which dominates the spectrum [25]. The F1 s core level spectra are shown in Fig. 2b. Interestingly, the F1 s core level acquired on the $CF_4$ plasma fluorinated sample shift towards higher binding energy values with respect to the Ar:$F_2$ plasma

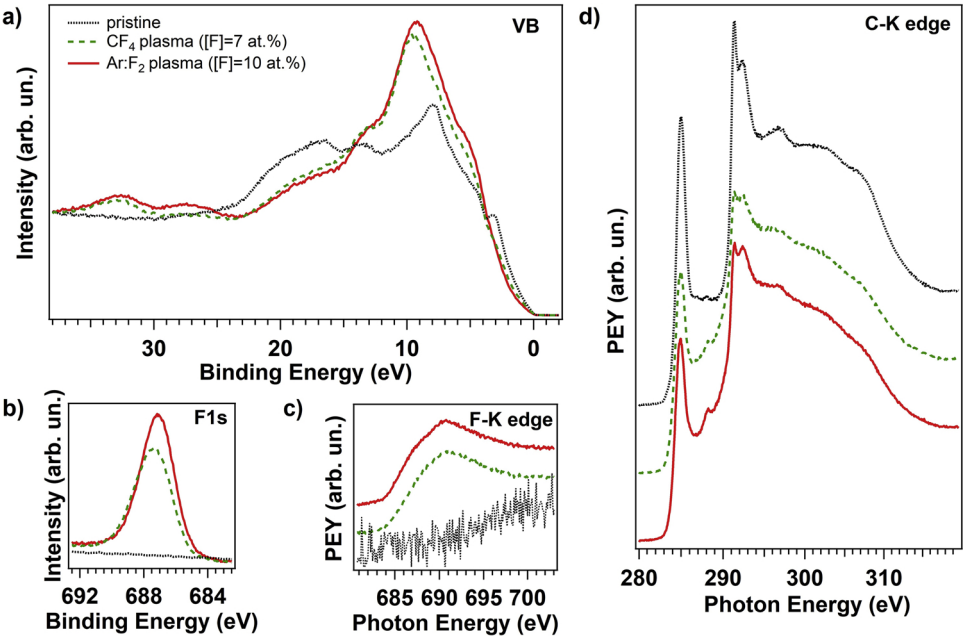


**Fig. 2.** Synchrotron-based measurements are performed on pristine (black dotted line) and on functionalized vCNT using different gas precursors. The fluorine contents are 7 and 10 at.% for the green dotted and red curves, respectively. Photoemission data are collected on the valence band (a) and the F1 s core level (b). Absorption spectra are shown for the F–K edge (c) and C–K edge (d). (For interpretation of the references to colour in this figure legend, the reader is referred to the web version of this article).

fluorinated vCNT, in line with the shift observed in the F2p-like states in the respective valence band spectrum. This shift is associated to the diverse chemical environment introduced at the surface by the multiple fluorinated carbon functionalities grafted on the vCNT [22].

The absorption spectra at the F–K and C–K edges are reported in Fig. 2c and d, respectively. The F–K edge signatures display broad structures composed of resonances at about 688 and 690 eV that are accompanied by weaker contributions at their sides, indicating dissimilar coordination for the fluorine atoms after both plasma treatments [23]. The large features at photon energy higher than 688 eV correspond to excitation from the F1 s to $\sigma^*$ states due to the covalent interaction between fluorine and carbon atoms [27]. On the contrary, the resonances of $\pi^*$ character are located at lower photon energies and they are associated to the interaction of fluorine with carbon atoms in the local vicinity of C–F groups (686 eV) [28].

The signals in the C–K edge can be divided into π and σ resonances. The absorption intensity associated to the transition from the C1 s level to the unoccupied $\pi^*$ states (285 eV) decreases after the functionalization. The covalent C–F bond formation is confirmed by the peak at 288 eV increasing in intensity with higher fluorine content. The states corresponding to the transition from C1 s to $\sigma^*$ suggest a limited extent of C–F bond formation with σ symmetry, thus supporting the evidence that the carbon nanotube structure is not destroyed by the plasma but it preserves the $sp^2$ character.

Pristine and fluorinated vCNT are then used as sensing layers for $NO_2$ and $NH_3$ detection at the ppm concentration range to test whether the fluorine functionalities affect the pristine sensor response for variable humidity level. The use of $Ar:F_2$ and $CF_4$ gas precursor for the plasma fluorination allows understanding the eventual role played by the multiple fluorinated carbon groups, as $CF_3$, during sensing mechanism as these species are mainly produced on the carbon nanotubes surface when using the $CF_4$ plasma [22,23].

The sensing experiments presented hereafter are performed at room temperature due to the observed desorption process of the functionalities, which is already activated when annealing at T = 250 °C in UHV condition, as shown in Fig. S1 in Supporting information where spectroscopic and absorption data are acquired as a function of the annealing temperature.

Due to the vertical geometry of the sensors the electrodes are placed on top of the densely packed nanotubes, therefore the sensing properties are only due to the intrinsic properties of the carbon nanotubes, *i.e.* the substrate is not playing any role.

The typical sensor response curves are illustrated in Fig. 3 where the normalized response (left axis) is plotted as a function of exposure time (bottom axis) to various analyte concentrations (right axis) at dry condition, corresponding to RH = 5% humidity level. The black dotted curves in Fig. 3 correspond to the pristine vCNT sensor (no trace of oxygen detectable on the surface), the red curves are obtained from the fluorinated vCNT using $Ar:F_2$ plasma, while the sensing responses of the $CF_4$ plasma functionalized sample are depicted as green dotted curves. The fluorine concentrations on these two samples are evaluated by XPS immediately after the fluorination process: 15 at.% of fluorine and about 2.5 at.% of oxygen contents are detected on the surface of the $Ar:F_2$ fluorinated sample (10 min of plasma treatment), while a fluorine concentration of 16 at.% and 1.5 at.% of oxygen is found after $CF_4$ plasma (10 min of plasma treatment).

All samples behave as p-type materials due to the increased conductivity (reduced resistance) when exposed to $NO_2$, and *vice versa* a decrease in the conductivity is measured when $NH_3$ flows in the chamber. The pristine vCNT sensor shows a fast reaction to the presence of nitrogen dioxide, but the response is characterized by a low recovery time once the gas flow is switched to pure air. On the contrary, the pristine sample is not sensitive to the ammonia molecule, neither at higher concentration (100 ppm), in agreement with previous results where the pristine nanotubes showed sensitivity to ammonia only after an intensive oxygen plasma treatment [29]. The fluorinated vCNT using $Ar:F_2$ plasma exhibits a good response to both gases with an improved recovery time for the release of $NO_2$ molecule once the gas flow is switched to pure air. The instantaneous response of all vCNT sensors can be attributed to both the full exposure of the nanotube surface area to the two chemical environments and to the mobility of the charge carriers leading to a fast transmission of the signal. Additionally, a better recovery (about 50%) of the fluorinated sensors is observed after $NO_2$ detection with respect to $NH_3$ experiments. The slow recovery process after ammonia exposure suggests a slower molecular desorption of $NH_3$ from the nanotube due to a stronger chemical interaction occurring mainly between the fluorinated sites on the carbon surface and the ammonia molecules. Further, diffusion process may occur into the three-dimensional porous architecture of the vCNT forest and additional external energy would be consequently required, for example in the form of heating treatment, to favour the release of this pollutant. However, a heating treatment would promote the desorption process of fluorine atoms from the surface in the present case (see Fig. S1 in Supporting information).

Compared to the absence of ammonia detection for the pristine sample, the fluorinated carbon nanotubes exhibit stronger adsorption capacities and better sensing properties. The improvement in the sensing performance of fluorinated vCNT is associated to both the strong polarity and the reactivity of F atoms in interacting with the hydrogen atoms of the analyte resulting in hydrogen bonding interactions. On the other side, also the interaction with $NO_2$ is not negligible considering the incomplete resistance baseline recovery at room temperature, analogous to previous results where a rather strong interaction was found [29]. This observation implies that complete $NO_2$ desorption is

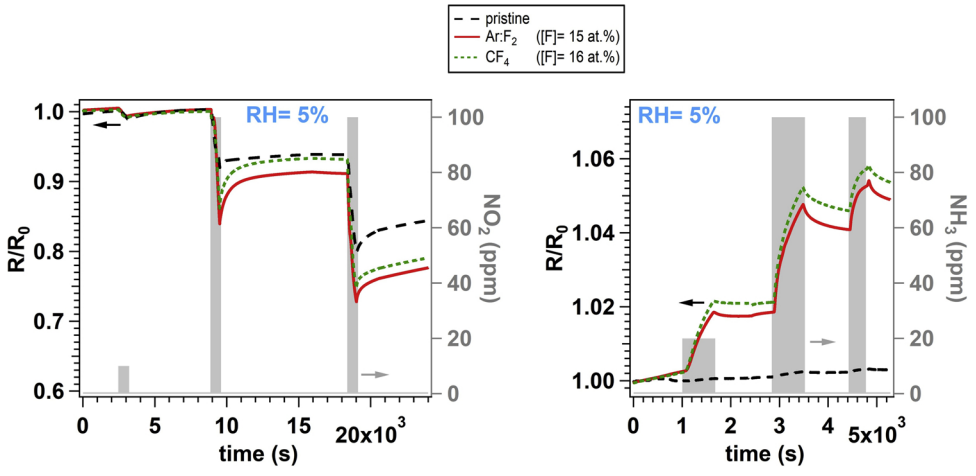


**Fig. 3.** The typical response and recovery curves of pristine and fluorinated vCNT sensors are shown for low (10 or 20 ppm) and high (100 ppm) concentration of the two analytes shown as grey bar (right axis). The measured resistance curves are normalized to the relative baseline value $R_0$ of each sensor (left axis). The experimental data are collected with a relative humidity level of RH = 5%.

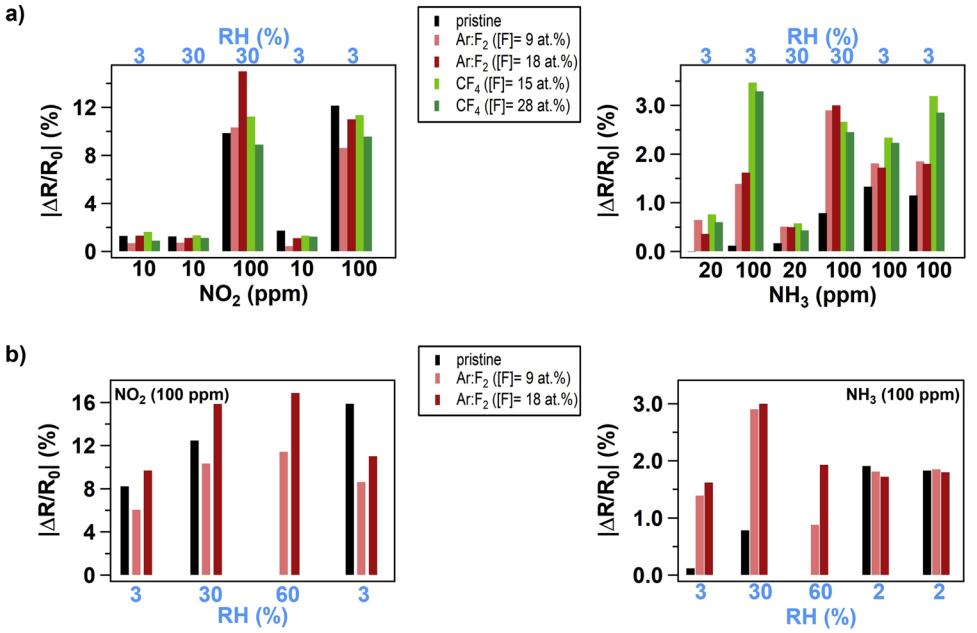


**Fig. 4.** a) The relative sensor responses to low and high concentrations of $NO_2$ and $NH_3$ are shown for pristine and fluorinated vCNT with different fluorination yields, as indicated in the legend, and for switching humidity levels (RH = 3/30%). b) The relative sensor response to 100 ppm of $NO_2$ and $NH_3$ at variable humidity levels (RH) is shown for pristine and Ar:$F_2$ plasma fluorinated vCNT with different fluorination yields, as indicated in the legend.

not achievable at room temperature and that stronger interaction than Van der Waals interaction with the carbon nanotubes, as chemisorption, cannot be ruled out for this analyte. At the same time, the diffusion of $NO_2$ down the nanotube forest may also hinder the complete release of the analyte during recovery phase.

The increased hydrophobicity of the carbon surfaces after fluorination is exploited to probe the gas sensing reproducibility under variable humidity level and the relative sensor responses are shown in Fig. 4. The response values are calculated over 10 min of exposure and expressed as a percentage.

In Fig. 4a, the moisture effect is analysed for the pristine and for the differently plasma fluorinated vCNT (Ar:$F_2$ and $CF_4$ plasma) thus allowing the investigation of a possible dependence of the sensor response on the functionalization used. In this experiment, the humidity level is switched from RH = 3% to RH = 30% while measuring the responses to low and high concentrations of $NO_2$ and $NH_3$. All sensor responses to traces of nitrogen dioxide are near to three times higher than the detection capability towards similar concentrations of ammonia. The response of pristine nanotubes towards $NH_3$ is rather dependent on the humidity content, increasing with increasing concentration of water molecules in the environment. When humidity is diminished from 30% to 3%, the response to ammonia remains almost identical to the one for 30% in the pristine sample. Most probably, the adsorbed moisture penetrated deeper in the forest (as observed during contact angle measurements) and the water contamination of the pristine surface could lead to a charge redistribution affecting the current through the layer. On the other hand, when the surface of the forest is fluorinated, the hydrophobic character is significantly higher than that of the pristine vCNT surface resulting in a reproducible response of the fluorinated films under variable humidity levels.

Variations in the amount of fluorine functionalities grafted on the sample surface does not impact the sensor response to $NO_2$. The response of fluorinated vCNT sensors towards nitrogen dioxide is, in essence, the same as that measured with the pristine samples in line with the fluorination content affecting less than a third of the sample surfaces in all cases. This result suggests that reducing the interaction of carbon nanotubes with water *via* fluorination does not alter their interaction with $NO_2$, thus promoting the plasma fluorination as a valuable substitution to $O_2$ plasma treatment and pioneering the anchoring of recognition elements to improve selectivity and sensitivity, similarly to previous works [14,30].

In addition, the particular gas precursor used during fluorination does not have a strong effect on the sensor performance, therefore the relative response can be measured within a wider humidity range, from dry air (RH = 3%) up to RH = 60%, testing one pristine and two Ar:$F_2$ plasma fluorinated samples, as illustrated in Fig. 4b. The strong influence of the moisture concentration on the pristine sample response (black bars) is further confirmed: the resistance variation continuously raises upon successive nitrogen dioxide exposures and an emerging response to $NH_3$ is detected under humid condition, though the pristine sample did not show sensitivity to ammonia during the first measurements in dry condition. No recovery of the starting pristine performance is observed in the successive measurements under dry air, suggesting that the humidity can be considered as the primary interfering analyte responsible for the performance deterioration with time in this sensor. Once exposed to water, the active material changes dramatically the response intensity to the pollutants and there is a strong memory effect when exposed again to a flow of dry air, *i.e.* the response remains altered as if humidity was still present due to the penetration of water molecules deeply in the carbon nanotubes forest. This memory effect prevents the use of such a sensor in a scenario in which ambient humidity may change, given the impossibility of calibrating the sensor.

In contrast to the pristine vCNT sensor, when the concentration of water molecules is increased to 30%, the fluorinated vCNT response is enhanced, implying that the presence of water does not block the interaction between adsorbed molecules and the vCNT. Although the response is affected by humidity being different under dry or humid conditions due to the presence of water molecules on top of the forest, fluorinated vCNT do not experience the memory effect. The response nearly returns to the original value as soon as the dry condition is re-established and it remains unvaried during the successive measurements at RH = 2–3%, suggesting that the adsorbed water molecules are easily evacuated without heating the sensors or without the necessity of using an inert gas flow. As a result, sensor response becomes reproducible and a humidity-calibrated response could be possible, *e.g.* including a humidity sensor.

Reproducible results are obtained after repeated sensing measurements over time indicating good sensor performance when working in ambient condition. Nevertheless, the relative response measured with fluorinated vCNT should be further improved to reach the high level of detection measured in metal decorated carbon nanotubes, especially when detecting ammonia [6,11,12]. However, the response of the

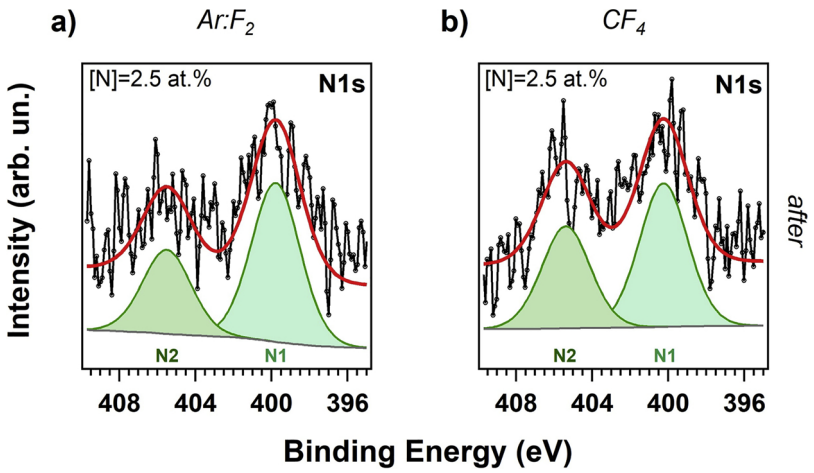


**Fig. 5.** The N1 s core level signals are measured after implementing the functionalized samples in a gas sensing device (after test gas exposure). The N1 s signal is only detected after the sensing measurements and exclusively on fluorinated vCNT.

fluorinated vertically aligned carbon nanotubes to $NH_3$ is higher compared with recent results from fluorinated graphene layers [20], where a maximal response of 11% on detection of 10,000 ppm of $NH_3$ in argon atmosphere was achieved after more than 10 min of exposure and with a recovery time longer than 30 min. In the same experiment, the response decreased to 2% when a concentration of 600 ppm of ammonia was detected.

The sensor response, the selectivity to ammonia and the response reproducibility in humid environments have been demonstrated so far, showing a satisfactory performance of the plasma fluorinated sensors. To probe the effect of the sensing measurement on the chemical composition of the surface and determine the nature of the interaction with the target gases, the nitrogen content has been monitored by XPS. The N1 s core level signal is only detected after the sensing measurements and exclusively on fluorinated vCNT surface. In Fig. 5, the N1 s core level spectra are illustrated for the (a) Ar:$F_2$ sample (F concentration of 15 at.%) and for the (b) $CF_4$ plasma functionalized vCNT (F concentration of 16 at.%). The nitrogen concentration evaluated by XPS is 2.5 at.% in both samples. The N1 s spectra are composed of two main components: N1 located around 400 eV and N2 near 406 eV binding energy. The former is commonly associated to amines [31] indicating the presence of $NH_3$ still adsorbed on the sample surface due to the higher interaction. The second component N2 is instead assigned to nitrogen dioxide molecules adsorbed on the nanotubes [32] likely as a pyridinic-*N*-oxide configuration [33] consistent with the presence of $NO_2$ on the vCNT surface. This observation is supported by the evidence of an increased uptake of oxygen on the surface after the sensor tests, in fact the oxygen concentrations increased from 2.5 (a) and 1 at.% (b) to 4 at.% in both cases.

The relative intensity of the two nitrogen components confirms that a higher amount of ammonia is adsorbed on the surface due to the stronger interaction with the fluorinated surface, in agreement also with the hindered recovery of the baseline during $NH_3$ sensing measurements.

According to theoretical calculations, the estimated adsorption energy of ammonia on pristine graphene is lower than the adsorption energy of nitrogen dioxide molecule [21,34,35], while the adsorption energy of $NH_3$ on fluorinated graphene is one order of magnitude higher than on the pristine surface [20,36]. Experimentally, we have measured a remarkably higher response to $NO_2$ with respect to the ammonia detection regardless of the fluorination as a consequence of the large charge transfer from the sensing layer to the analyte. This mechanism is sustained by the appearance of the LUMO state of nitrogen dioxide below the Dirac point [37] with a favoured orientation of the $NO_2$ molecule exhibiting the N atom pointing towards the F atom [38]. Reversely, the fluorination introduces a moderate sensing response towards ammonia in agreement with the predicted decrease in the distance between the analyte and the fluorinated carbon surface [39] that promotes a stronger interaction *via* the formation of hydrogen bonding as a result of a dipolar electrostatic interaction providing an enhanced charge transfer with the fluorinated carbon layer [20].

To further investigate the possible role played by the geometry of the sensing layer, randomly dispersed CNTs are tested. The carbon nanotubes are first drop-casted on a silicon wafer adopting a spaghetti-like distribution, the SEM images are shown in Fig. 6. Subsequently, the samples are inserted in the μ-wave plasma chamber and they are subjected to the plasma fluorination treatments. Finally, the contacts are realized on the surface following the experimental method used for the vCNT sensors and the sensing performance of the samples are tested in the same experimental chamber as used for the vCNT.

Under this arrangement, the sparse carbon nanotube mesh is not regular and it does not cover homogeneously the silicon surface therefore the response can be influenced by the substrate (extrinsic gas response). The response curves to variable $NO_2$ and $NH_3$ concentration

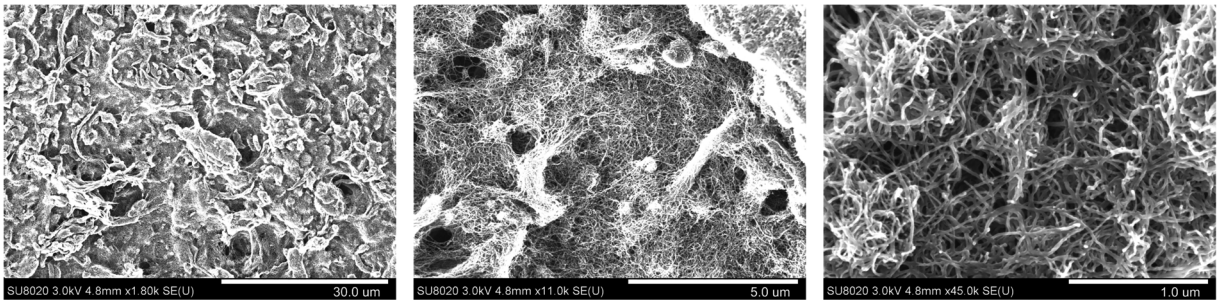


**Fig. 6.** The SEM images show the random distribution of the pristine multi-walled nanotubes drop-casted on a silicon wafer.

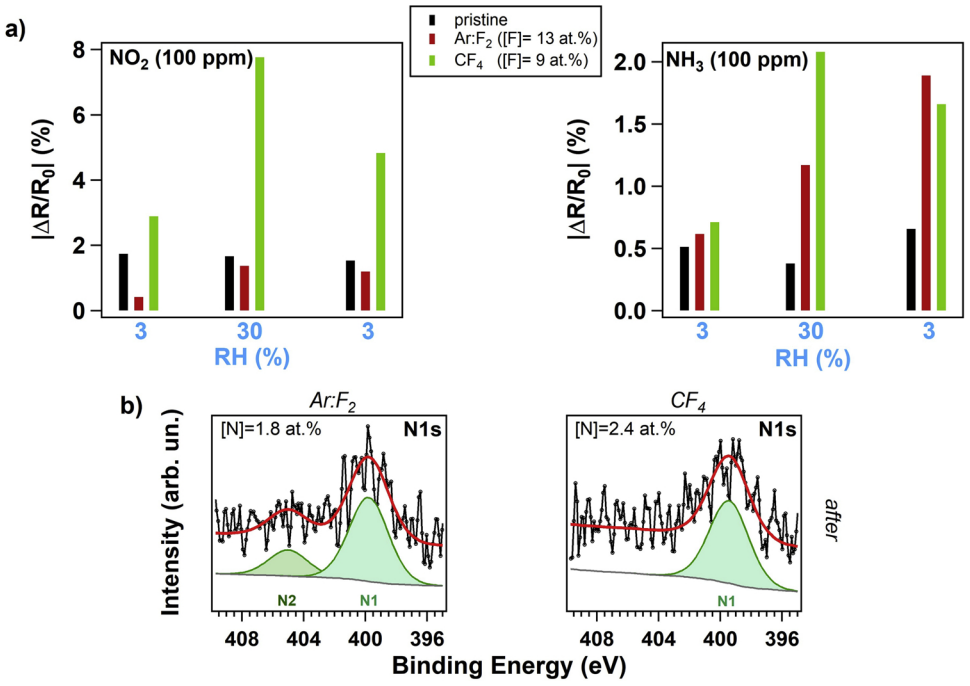


**Fig. 7.** a) The relative sensor response to 100 ppm of $NO_2$ and $NH_3$ is shown for pristine and fluorinated random CNT with different fluorination yield, as indicated in the legend, and switchable humidity level (RH = 3/30%). b) The N1 s core level signals are recorded after the sensing measurements performed using the fluorinated samples ($Ar:F_2$, left panel, and $CF_4$, right panel). The N1 s signal is detected only on fluorinated carbon nanotubes.

and different humidity levels are shown in Figs. S2 and S3 of the Supporting Information for pristine and plasma fluorinated samples.

The relative sensor responses are illustrated in Fig. 7a for pristine nanotubes (with an oxygen content of 4 at.%) and fluorinated samples containing a F concentration equal to 13 at.% ($Ar:F_2$ plasma) and 9 at.% ($CF_4$ plasma). Before the sensing measurements, the oxygen concentration on the two fluorinated sensors was 4.2 at.% and 1.5 at.%, respectively.

The response to $NO_2$ is notably lower than that of vCNT forest, confirming the remarkable role played by the tips that are directly exposed to the target gas in the vertical geometry. Furthermore, the change in the humidity concentration in the environment has a larger impact on the sensor performance for the sparse carbon nanotube mesh. The fluorination, especially using $CF_4$ plasma, seems to increase the influence of humidity level on the response towards $NO_2$ and $NH_3$ similarly to graphene oxide performance under wet condition [19]. The observed higher response of the $CF_4$ functionalized sample when RH = 30% is associated to an improved ammonia adsorption on the surface due to the presence of water molecules confined by the hydrophobic and highly dense fluorinated areas. Therefore, the inhomogeneous hydrophobic path could be a competitive counterpart leading to the production of an ionic current that facilitates local space charge creation. On the other side, the pristine random CNT samples are responsive to ammonia already under dry condition due to the presence of native oxygen on the surface.

The surface of the random CNT-based sensors is analysed by XPS after running the gas sensing measurements, the N1 s core level spectra are reported in Fig. 7b for the two fluorinated carbon nanotubes samples. The nitrogen signal is not detected on the pristine sensors, while the N1 s spectra are dominated by the N1 component in the plasma fluorinated nanotubes used for the sensing measurements. The N2 peak is visible in the $Ar:F_2$ plasma fluorinated sample (left panel): this observation combined with the slower recovery of the baseline during $NO_2$ measurements for this sensor (see Fig. S2 in Supporting information) confirms the assignment of the component to nitrogen dioxide molecule adsorbed on the surface. In analogy, the N2 component is not found on the $CF_4$ plasma fluorinated sensor (right panel) as the analyte desorbs faster from it (see Fig. S3 in Supporting information). The nitrogen uptake corresponds to a final concentration of 1.8 at.% for the $Ar:F_2$ plasma fluorinated sample and 2.4 at.% for the $CF_4$ plasma fluorinated sample, respectively.

## 4. Conclusion

The room temperature efficiency, the reliability and the high sensitivity towards detection of different gases have triggered great interest in the use of both pristine and functionalized carbon nanotubes as sensing layers. In the present work, a controlled plasma fluorination of carbon nanotubes is obtained using different fluorine-based gas precursors, namely $Ar:F_2$ and $CF_4$. The hydrophobicity of the pristine carbon nanotube forest is strongly increased and the water diffusion process inside the forest, observed for pristine vCNT, is largely impeded even at a fluorine content of only 7 at.%. The sensing response of the fluorinated carbon nanotube samples is investigated upon exposure to nitrogen dioxide and ammonia being representative for the opposite acceptor/donor behaviour. If from one side the fluorination does not alter the high response to $NO_2$ molecules, the improved sensing performance in detecting ammonia is associated to an increased interaction between $NH_3$ and the fluorinated carbon nanotubes surface, as confirmed by XPS measurements. A hydrogen bonding interaction favours the charge transfer to the fluorinated carbon-based sensor. The vertically aligned carbon nanotube forests show an enhanced sensor response compared to the planar distribution of spaghetti-like nanotubes. The vertical geometry is thus a preferable layer for the sensing platform due to the remarkable role played by the tips in the vCNT. Contrary to the pristine samples, improved response reproducibility in a variable ambient moisture levels is observed when testing fluorinated vCNT. This property makes fluorinated vCNT as potential material to be employed in practical commercial applications after sensor calibration: once the response changes *versus* variations in relative humidity are known, it will be possible to compensate this effect and implement them as room temperature gas detectors.

## Acknowledgements

CS is grateful to the “Fonds pour la Formation à la Recherche dans l’Industrie et dans l’Agriculture” (F.R.I.A.) for financial support. CS also acknowledges the Stiftelsen för Strategisk Forskning (SSF) (Project no.

RMA15-0024). MS is FRS-FNRS post-doctoral researcher, J-FC and CB are Researcher Associates at the FRS-FNRS. The authors thank the Australian synchrotron radiation lightsource for the funding (grant no. AS161/SXR/10421) and the staff of the Soft X-Ray beamline. This work is supported by the Belgian Fund for Scientific Research (FRS-FNRS) under the FRFC contract "CHEMOGRAPHENE" (convention no. 2.4577.11). This research is also supported by a Marie Curie International Research Staff Exchange Scheme Fellowship within the 7th European Community Framework Programme "NanoCF" (grant agreement number: PIRSES-GA-2013-612577). Funded in part by MINECO and FEDER *via* grant no. TEC2015-71663-R and by AGAUR under grant no. 2017SGR 418. E.L. is supported by the Catalan institution for Research and Advanced Studies *via* the 2012 Edition of the ICREA Academia Award.

Declarations of interest: none.

## Appendix A. Supplementary data

Supplementary material related to this article can be found, in the online version, at doi:https://doi.org/10.1016/j.snb.2018.10.159.

## References

[1] X. Liu, S. Cheng, H. Liu, S. Hu, D. Zhang, H. Ning, A survey on gas sensing technology, Sensors (Switzerland) 12 (2012) 9635–9665, https://doi.org/10.3390/s120709635.
[2] J. Zhang, X. Liu, G. Neri, N. Pinna, Nanostructured materials for room-temperature gas sensors, Adv. Mater. 28 (2016) 795–831, https://doi.org/10.1002/adma.201503825.
[3] J. Kong, N.R. Franklin, C. Zhou, M.G. Chapline, S. Peng, K. Cho, H. Dai, Nanotube molecular wires as chemical sensors, Science 287 (2000) 622–625, https://doi.org/10.1126/science.287.5453.622.
[4] F. Schedin, A.K. Geim, S.V. Morozov, E.W. Hill, P. Blake, M.I. Katsnelson, K.S. Novoselov, Detection of individual gas molecules adsorbed on graphene, Nat. Mater. 6 (2007) 652–655, https://doi.org/10.1038/nmat1967.
[5] E. Llobet, Gas sensors using carbon nanomaterials: a review, Sens. Actuators B: Chem. 179 (2013) 32–45, https://doi.org/10.1016/j.snb.2012.11.014.
[6] P.R. Mudimela, M. Scardamaglia, O. González-León, N. Reckinger, R. Snyders, E. Llobet, C. Bittencourt, J.-F. Colomer, Gas sensing with gold-decorated vertically aligned carbon nanotubes, Beilstein J. Nanotechnol. 5 (2014) 910–918, https://doi.org/10.3762/bjnano.5.104.
[7] M. Meyyappan, Carbon nanotube-based chemical sensors, Small 12 (2016) 2118–2129, https://doi.org/10.1002/smll.201502555.
[8] J. Kong, M.G. Chapline, H. Dai, Functionalized carbon nanotubes for molecular hydrogen sensors, Adv. Mater. 13 (2001) 1384–1386, https://doi.org/10.1002/1521-4095(200109)13:18<1384::AID-ADMA1384>3.0.CO;2-8.
[9] P. Clément, A. Ramos, A. Lazaro, L. Molina-Luna, C. Bittencourt, D. Girbau, E. Llobet, Oxygen plasma treated carbon nanotubes for the wireless monitoring of nitrogen dioxide levels, Sens. Actuators B: Chem. 208 (2015) 444–449, https://doi.org/10.1016/j.snb.2014.11.059.
[10] G. Chen, Y. Liu, Y. Liu, Y. Tian, X. Zhang, Nitrogen and sulfur dual-doped graphene for glucose biosensor application, J. Electroanal. Chem. 738 (2015) 100–107, https://doi.org/10.1016/j.jelechem.2014.11.020.
[11] M. Penza, R. Rossi, M. Alvisi, E. Serra, Metal-modified and vertically aligned carbon nanotube sensors array for landfill gas monitoring applications, Nanotechnology 21 (2010) 105501, https://doi.org/10.1088/0957-4484/21/10/105501.
[12] Z. Zanolli, R. Leghrib, A. Felten, J.-J. Pireaux, E. Llobet, J.-C. Charlier, Gas sensing with Au-decorated carbon nanotubes, ACS Nano 5 (2011) 4592–4599, https://doi.org/10.1021/nn200294h.
[13] F. Rigoni, G. Drera, S. Pagliara, E. Perghem, C. Pintossi, A. Goldoni, L. Sangaletti, Gas sensing at the nanoscale: engineering SWCNT-ITO nano-heterojunctions for the selective detection of NH 3 and NO 2 target molecules, Nanotechnology 28 (2017) 035502, https://doi.org/10.1088/1361-6528/28/3/035502.
[14] P. Clément, S. Korom, C. Struzzi, E.J. Parra, C. Bittencourt, P. Ballester, E. Llobet, Deep cavitand self-assembled on Au NPs-MWCNT as highly sensitive benzene sensing interface, Adv. Funct. Mater. 25 (2015) 4011–4020, https://doi.org/10.1002/adfm.201501234.
[15] V. Mazánek, O. Jankovský, J. Luxa, D. Sedmidubský, Z. Janoušek, F. Šembera, M. Mikulics, Z. Sofer, Tuning of fluorine content in graphene: towards large-scale production of stoichiometric fluorographene, Nanoscale 7 (2015) 13646–13655, https://doi.org/10.1039/C5NR03243A.
[16] D.D. Chronopoulos, A. Bakandritsos, M. Pykal, R. Zbořil, M. Otyepka, Chemistry, properties, and applications of fluorographene, Appl. Mater. Today 9 (2017) 60–70, https://doi.org/10.1016/j.apmt.2017.05.004.
[17] S. Prezioso, F. Perrozzi, L. Giancaterini, C. Cantalini, E. Treossi, V. Palermo, M. Nardone, S. Santucci, L. Ottaviano, Graphene oxide as a practical solution to high sensitivity gas sensing, J. Phys. Chem. 117 (2013), https://doi.org/10.1021/jp3085759.
[18] H. Bi, K. Yin, X. Xie, J. Ji, S. Wan, L. Sun, M. Terrones, Ultrahigh humidity sensitivity of graphene oxide, Sci. Rep. 3 (2013) 1–7, https://doi.org/10.1038/srep02714.
[19] A. Bannov, J. Prášek, O. Jašek, L. Zajícková, Investigation of pristine graphite oxide as room-temperature chemiresistive ammonia gas sensing material, Sensors 17 (2017) 320, https://doi.org/10.3390/s17020320.
[20] M.V. Katkov, V.I. Sysoev, A.V. Gusel'nikov, I.P. Asanov, L.G. Bulusheva, A.V. Okotrub, A backside fluorine-functionalized graphene layer for ammonia detection, Phys. Chem. Chem. Phys. 17 (2015) 444–450, https://doi.org/10.1039/C4CP03552F.
[21] V.I. Sysoev, L.G. Bulusheva, I.P. Asanov, Y.V. Shubin, A.V. Okotrub, Thermally exfoliated fluorinated graphite for NO2 gas sensing, Phys. Status Solidi Basic Res. 253 (2016) 2492–2498, https://doi.org/10.1002/pssb.201600270.
[22] C. Struzzi, M. Scardamaglia, J.-F. Colomer, A. Verdini, L. Floreano, R. Snyders, C. Bittencourt, Fluorination of vertically aligned carbon nanotubes: from $CF_4$ plasma chemistry to surface functionalization, Beilstein J. Nanotechnol. 8 (2017) 1723–1733, https://doi.org/10.3762/bjnano.8.173.
[23] L.G. Bulusheva, Y.V. Fedoseeva, E. Flahaut, J. Rio, C.P. Ewels, V.O. Koroteev, G. Van Lier, D.V. Vyalikh, A.V. Okotrub, Effect of the fluorination technique on the surface-fluorination patterning of double-walled carbon nanotubes, Beilstein J. Nanotechnol. 8 (2017) 1688–1698, https://doi.org/10.3762/bjnano.8.169.
[24] M. Scardamaglia, M. Amati, B. Llorente, P. Mudimela, J.-F. Colomer, J. Ghijsen, C. Ewels, R. Snyders, L. Gregoratti, C. Bittencourt, Nitrogen ion casting on vertically aligned carbon nanotubes: tip and sidewall chemical modification, Carbon 77 (2014) 319–328, https://doi.org/10.1016/j.carbon.2014.05.035.
[25] C. Struzzi, M. Scardamaglia, A. Hemberg, L. Petaccia, J.F. Colomer, R. Snyders, C. Bittencourt, Plasma fluorination of vertically aligned carbon nanotubes: functionalization and thermal stability, Beilstein J. Nanotechnol. 6 (2015) 2263–2271, https://doi.org/10.3762/bjnano.6.232.
[26] T. Silva, N. Britun, T. Godfroid, R. Snyders, Optical characterization of a microwave pulsed discharge used for dissociation of CO2, Plasma Sources Sci. Technol. 23 (2014) 025009, https://doi.org/10.1088/0963-0252/23/2/025009.
[27] M. Klues, P. Jerabek, T. Breuer, M. Oehzelt, K. Hermann, R. Berger, G. Witte, Understanding the F 1s NEXAFS dichroism in fluorinated organic semiconductors, J. Phys. Chem. C 120 (2016) 12693–12705, https://doi.org/10.1021/acs.jpcc.6b04048.
[28] A.V. Okotrub, N.F. Yudanov, I.P. Asanov, D.V. Vyalikh, L.G. Bulusheva, Anisotropy of chemical bonding in semifluorinated graphite C2F revealed spectroscopy, ACS Nano 7 (2013) 65–74.
[29] R. Ionescu, E.H. Espinosa, E. Sotter, E. Llobet, X. Vilanova, X. Correig, A. Felten, C. Bittencourt, G. Van Lier, J.C. Charlier, J.J. Pireaux, Oxygen functionalisation of MWNT and their use as gas sensitive thick-film layers, Sens. Actuators B: Chem. 113 (2006) 36–46, https://doi.org/10.1016/j.snb.2005.02.020.
[30] A. Thamri, H. Baccar, C. Struzzi, C. Bittencourt, A. Abdelghani, E. Llobet, MHDA-functionalized multiwall carbon nanotubes for detecting non-aromatic VOCs, Sci. Rep. 6 (2016) 35130, https://doi.org/10.1038/srep35130.
[31] D. Zeng, X. Yu, Y. Zhan, L. Cao, X. Wu, B. Zhang, J. Huang, Z. Lin, F. Xie, W. Zhang, J. Chen, W. Xie, W. Mai, H. Meng, Insight into the nitrogen-doped carbon as oxygen reduction reaction catalyst: the choice of carbon/nitrogen source and active sites, Int. J. Hydrogen Energy 41 (2016) 8563–8575, https://doi.org/10.1016/j.ijhydene.2016.03.072.
[32] G. Ruiz-Soria, A. Pérez Paz, M. Sauer, D.J. Mowbray, P. Lacovig, M. Dalmiglio, S. Lizzit, K. Yanagi, A. Rubio, A. Goldoni, P. Ayala, T. Pichler, Revealing the adsorption mechanisms of nitroxides on ultrapure, metallicity-sorted carbon nanotubes, ACS Nano 8 (2014) 1375–1383, https://doi.org/10.1021/nn405114z.
[33] S. Kundu, W. Xia, W. Busser, M. Becker, D.A. Schmidt, M. Havenith, M. Muhler, The formation of nitrogen-containing functional groups on carbon nanotube surfaces: a quantitative XPS and TPD study, Phys. Chem. Chem. Phys. 12 (2010) 4351, https://doi.org/10.1039/b923651a.
[34] Y.-H. Zhang, Y.-B. Chen, K.-G. Zhou, C.-H. Liu, J. Zeng, H.-L. Zhang, Y. Peng, Improving gas sensing properties of graphene by introducing dopants and defects: a first-principles study, Nanotechnology 20 (2009) 185504, https://doi.org/10.1088/0957-4484/20/18/185504.
[35] S.S. Varghese, S. Lonkar, K.K. Singh, S. Swaminathan, A. Abdala, Recent advances in graphene based gas sensors, Sens. Actuators B: Chem. 218 (2015) 160–183, https://doi.org/10.1016/j.snb.2015.04.062.
[36] H. Zhang, L. Fan, H. Dong, P. Zhang, K. Nie, J. Zhong, Y. Li, J. Guo, X. Sun, Spectroscopic investigation of plasma-fluorinated monolayer graphene and application for gas sensing, ACS Appl. Mater. Interfaces 8 (2016) 8652–8661, https://doi.org/10.1021/acsami.5b11872.
[37] O. Leenaerts, B. Partoens, F.M. Peeters, Adsorption of H2O, NH3, CO, NO2, and NO on graphene: a first-principles study, Phys. Rev. B 77 (2008) 125416, , https://doi.org/10.1103/PhysRevB.77.125416.
[38] V.I. Sysoev, A.V. Okotrub, I.P. Asanov, P.N. Gevko, L.G. Bulusheva, Advantage of graphene fluorination instead of oxygenation for restorable adsorption of gaseous ammonia and nitrogen dioxide, Carbon 118 (2017) 225–232, https://doi.org/10.1016/j.carbon.2017.03.026.
[39] K.K. Tadi, S. Pal, T.N. Narayanan, Fluorographene based ultrasensitive ammonia sensor, Sci. Rep. 6 (2016) 25221, https://doi.org/10.1038/srep25221.

Section 2.6

# Low Kinetic Energy Oxigen Ion Irradiation in Vertically Aligned Carbon Nanotubes

Selene Acosta, Juan Casanova-Chafer, Ayrton Sierra-Castillo, Eduard Llobet, Rony Snyders, Jean-François Colomer, Mildred Quintana, Carla Bittencourt

*Applied Sciences 2019 (in press)*

DOI: in process

UNIVERSITAT ROVIRA I VIRGILI
GAS SENSING WITH MODIFIED CARBON NANOTUBES, GRAPHENE AND DIAMONDOIDS
Juan Casanova Cháfer

MDPI

*Article*

# Low kinetic energy oxygen ion irradiation of vertically aligned carbon nanotubes

**Selene Acosta[1,4]*, Juan Casanova-Chafer[2], Ayrton Sierra-Castillo[3], Eduard Llobet[2], Rony Snyders[1], Jean-François Colomer[3], Mildred Quintana[4], Chris Ewels[5] and Carla Bittencourt[1]**

[1] Chimie des Interactions Plasma – Surface (ChIPS), Research Institute for Materials Science and Engineering, Université de Mons, 7000 Mons, Belgium; Carla.BITTENCOURT@umons.ac.be; rony.snyders@umons.ac.be
[2] MINOS Group, Universitat Rovira i Virgili, Tarragona, Spain; juan.casanova@urv.cat; eduard.llobet@urv.cat
[3] Research Group on Carbon Nanostructures (CARBONNAGe), University of Namur, 5000 Namur, Belgium; ayrton.sierracastillo@unamur.be; jean-francois.colomer@unamur.be
[4] Centro de Investigación en Ciencias de la Salud y Biomedicina, Universidad Autónoma de San Luis Potosí., San Luis Potosí, México; mildred@ifisica.uaslp.mx
[5] Institut des Matèriaux Jean Rouxel (IMN), CNRS UMR6502, Université de Nantes, Nantes, France; chris.ewels@cnrs-imn.fr

* Correspondence: Selene.ACOSTAMORALES@umons.ac.be; Tel: +52 489 41 56 68

Received: date; Accepted: date; Published: date

**Abstract:** Vertically aligned multiwalled carbon nanotubes (v-CNTs) were functionalized with oxygen groups using low kinetic energy oxygen ion irradiation. X-ray photoelectron spectroscopy (XPS) analysis indicates that oxygen ion irradiation produces three different types of oxygen functional groups at the CNTs surface: epoxide, carbonyl and carboxyl groups. The relative concentration of these groups depends on the parameters used for oxygen ion irradiation. Scanning electron microscopy (SEM) shows that the macroscopic structure and alignment of v-CNTS are not affected by the ion irradiation and transmission electron microscopy (TEM) proves tip functionalization of v-CNTs. We observed that in comparison to oxygen plasma treatment, oxygen ion irradiation shows higher functionalization efficiency and versatility. Ion irradiation leads to higher amount of oxygen grafting at the v-CNTs surface, besides different functional groups and their relative concentration can be tuned varying the irradiation parameters.

**Keywords:** ion irradiation; functionalization; carbon nanotubes.

## 1. Introduction

Carbon nanotubes (CNTs) are nanostructured material with high technological importance owing to their unique chemical and electronic properties. They have been reported as good candidates to replace silicon in different electronic devices due to their higher carrier velocity, nanoscale structure and relative low-cost large scale production [1]. Nevertheless, their inert surface limits their use in several applications, such as biological and gas sensor devices [2-4]. To tackle this issue, the CNTs surface properties can be altered through changes of their surface chemistry by functionalization. It has been shown that CNTs functionalization with oxygen groups can enhance their surface chemical reactivity [5,6] and change their hydrophobicity improving their dispersion in aqueous media [7,8], property that is of vital importance for their integration in biological systems. Moreover, oxygen groups can act as active sites for further functionalization increasing their potential applications in a vast variety of fields, such as drug delivery, bio imaging, water purification, catalysis, among others [9]. Vuković *et al.* reported in 2010 [10] that amino functionalization of CNTs can be easily implemented by chemical modification of carboxyl groups in oxidized CNTs, engineering CNTs capable of removing $Cd^{2+}$ from water solutions. Regarding electronic properties,

oxygen groups grafted at the CNTs surface can convert metallic CNTs into semiconducting [11]. Barinov *et al.* [11], showed that even a very small oxygen amount can alter the electronic structure of CNTs without alter their morphology.

Functionalization of CNTs has been achieved via different techniques such as wet chemistry, surface plasma treatment, simultaneous functionalization during synthesis or ion irradiation [12-15]. In order to obtain an optimal tailoring of the CNTs chemical and electronic properties, the functionalization technique used must be fully controlled. In this context, low kinetic ion irradiation consists in irradiate a target with ions of low kinetic energy, these ions interact with the sample in two different ways, they can bond directly to the atoms in the target, mainly in the intrinsic defects, or crosswise the sample creating new defects that can be used by other ions to create new functional groups.

Ion irradiation can alter the structure and the chemical, electronic and magnetic properties of carbon materials [16]. Additionally, junctions among carbon nanotubes can be created which may have application in the reinforcement of materials for construction among others [17]. The ion kinetic energy during ion irradiation is an important parameter for optimal functionalization. It is considered low kinetic energy ion irradiation if the ions have an energy range from 100 eV to a few keV, and high kinetic energy ion irradiation if the range is of several keV to MeV [18, 17]. The degree of interaction of the ions with the sample also depends on the displacement threshold energy $T_d$ of the sample, that is, the minimum energy required by an atom through the impact of an energetic particle to be ejected from its original position [16]. Only if the kinetic energy imparted by the ions is higher than the $T_d$ of the irradiated material the atoms will be moved and defects created.

Unlike others functionalization techniques, low energy ion irradiation is a clean, efficient and site-selective post-growth technique that does not generate liquid waste and allows functionalizing with a precise ion dose control, adjusting the quantity and energy of ions arriving to the sample surface [19]. In addition, this technique offers the possibility of scaling up to produce large quantities of functionalized CNTs for commercial use. Furthermore, different parameters for ion irradiation can be varied reducing the creation of defects on the structure of nanomaterials. Depending on the kinetic energy and the ion mass, the ions can traverse the nanomaterial without interaction with the target, contrary to bulk materials where all ions will interact with the sample [20]. Besides, ion irradiation of graphitic networks is of high interest in nano-engineering due to their ability of structural reorganization after irradiation, like no other material; during the reorganization new bonds around the defects are created restructuring the lattice [21].

Low kinetic energy ion irradiation of CNTs has been described mainly in theoretical works [22-24] and the limited experimental works reported are mostly in boron and nitrogen ion irradiation [25, 26, 19]. In this work, vertically aligned multi-walled carbon nanotubes (v-CNTs) are functionalized with oxygen groups using low kinetic energy ion irradiation, we evaluate the influence of the ion kinetic energy and irradiation time in the resulting oxygen functionalization. Vertically aligned nanotubes with their unidirectional electron transport facilitate the transducer operation in sensors [27]. Besides, their vertical geometry avoids the use of wet chemistry preventing contamination of the CNTs walls during integration of the active layer in the transducer. The v-CNTs were synthetized by thermal catalytic chemical vapor deposition technique. The structure and alignment of v-CNTs was observed before and after ion irradiation using scanning electron microscopy and transmission electron microscopy. The chemical functionalization of v-CNTs was characterized using X-ray photoelectron spectroscopy and Raman spectroscopy.

## 2. Materials and Methods

Vertically aligned multi-walled carbon nanotubes (v-CNTs) were synthesized by thermal catalytic chemical vapor deposition technique using $C_2H_4$ as carbon source [27]. A multilayer system composed of Si/Al/Fe was the catalyst. Si wafers are used as substrates. An Al thin film (30nm) is deposited on Si wafers and then, after its oxidation, a 1.5 nm Fe layer is deposited and heated to 300ºC for three hours to form nanoparticles which are responsible for the CNTs growth. The Al and Fe layers are prepared by magnetron sputtering using a Quorum device. For the v-CNTs growth, the

reactor is heated to 750 °C in atmospheric pressure under He flow (500 sccm). The catalyst is placed inside the reactor and $H_2$ flow (200 sccm) is introduced into the reactor for 20 min. After that, $C_2H_4$ flow (60 sccm) is introduced into the reactor for 24 min. After the growth, $H_2$ and $C_2H_4$ flows are switched off and a flow of He is used to clean the reactor (500 sccm).

The low energy oxygen ion irradiation in v-CNTs was performed in a vacuum chamber system (PREVAC-541) using as ion source a Tectra plasma source TPIS, where microwave energy is used to create a gas plasma at the plasma cup from which ions are extracted. Microwaves with a frequency of 2.45 GHz are generated by a magnetron coupled to a coaxial feedthrough structure which guides the microwaves into the plasma cup containing low pressure $O_2$ gas. The electrons generated in the plasma undergo cyclotron resonance motion increasing their perpendicular kinetic energy due to a magnetic quadrupole arranged around the discharge chamber. Subsequently, when the energized free electrons collide with the gas in the volume, they cause ionization of the gas if their kinetic energy is larger than the ionization energy of the atoms or molecules. The ion extraction optics is composed of two grids located at the open end of the plasma cup, a positive voltage is applied to the first grid to accelerate ions extracting them from the plasma out to the sample, the other grid has a negative voltage and assist in the ion extraction and the beam current.

Oxygen ion irradiation was performed varying separately the irradiation time and the ion kinetic energy. For the samples functionalized with different irradiation time the ion kinetic energy was fixed at 1 keV and the time was varied from 1, 2.5, 5 and 10 minutes. The samples functionalized varying the ion kinetic energy had irradiation time fixed to 5 minutes, the different ion kinetic energies were 0.1, 0.25, 0.5, 1, 1.5 and 2 keV. For all samples the current induced by the ion irradiation energy was 10μA, certifying that the number of ions reaching the samples were the same (Table 1).

**Table 1.** Summary of irradiation parameters used for oxygen functionalization of v-CNTs, oxygen (at. %) and carbon (at. %) relative concentration obtained by XPS.

| Irradiation time (min) | Ion kinetic energy (keV) | Oxygen content (at. %) | Carbon content (at. %) |
|---|---|---|---|
| 0 | - | 1.7 | 98.3 |
| 1 | 1 | 6.7 | 93.3 |
| 2.5 | 1 | 10.0 | 90.0 |
| 5 | 1 | 14.2 | 85.8 |
| 10 | 1 | 20.0 | 80.0 |
| 5 | 0 | 8.0 | 92.0 |
| 5 | 0.1 | 8.4 | 91.6 |
| 5 | 0.25 | 9.8 | 90.2 |
| 5 | 0.5 | 15.4 | 84.6 |
| 5 | 1.5 | 14.5 | 85.5 |
| 5 | 2 | 16.0 | 84.0 |

The vertical alignment and the morphology of v-CNTs were characterized before and after oxygen ion irradiation by scanning electron microscopy (SEM) using a JEOL-JSM-7500F-Field Emission Scanning Electron Microscope operated at 15 kV and transmission electron microscopy (TEM) using a JEM-1011 Jeol Ltd.

The chemical composition of the v-CNTs was studied with X-ray photoelectron spectroscopy (XPS) using a VERSAPROBE PHI 5000 from Physical Electronics, equipped with a monochromatic Al K$\alpha$ X-ray source. The XPS analysis chamber is connected to the ion irradiation vacuum chamber

system to avoid contaminations. C1s and O1s core level spectra were recorded for each sample with an energy resolution of 0.6 eV.

Raman spectroscopy was collected using a Micro-Raman system (Senterra Bruker Optik GmbH) with a resolution of $3cm^{-1}$ using as excitation source a laser with a wavelength of 532 nm and 20mW of power.

## 3. Results and discussion

The macroscopic morphology and alignment of v-CNTs were evaluated with SEM microscopy before and after the oxygen ion irradiation in order to estimate if disorder was induced by ions impacting onto the sample surface. We observe that neither the density or the alignment of CNTs are affected by the ion irradiation treatment (Figure 1).

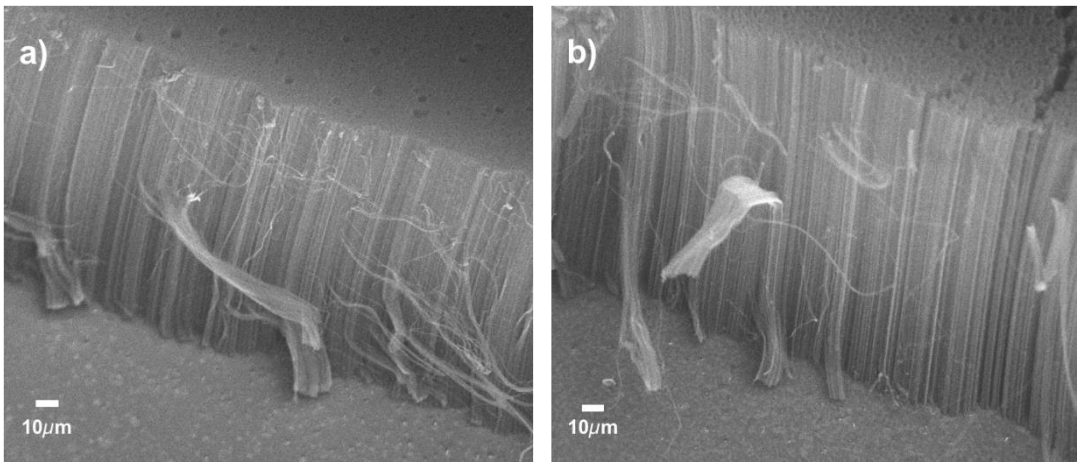


**Figure. 1.** Cross section SEM images of v-CNTs before (**a**) and after 5 minutes of irradiation with oxygen ions with 1 keV of kinetic energy (**b**).

The understanding of the dependency of the oxygen bonding configurations in v-CNTs on the different parameters used during ion irradiation is a key step for optimal controlling functionalization and, consequently tailoring CNTs properties for applications such as in sensing. X-ray photoelectron spectroscopy (XPS) is a surface technique that, besides providing information on the relative atomic concentration of the elements present on a sample, is also suitable to characterize changes in the bonding configuration of the atoms via the chemical shift, i.e. via the analysis of the shift in the binding energy of the core electrons of the different atoms composing a sample.

We first record XPS survey spectra to evaluate if the oxygen ion irradiation had grafted undesired elements other than oxygen at the CNT surface. Figure 2 shows typical survey spectra recorded on v-CNTs before and after 5 minutes of irradiation with oxygen ions with 1 keV of kinetic energy. We can observe in the spectrum recorded before the ion irradiation a high intensity peak centered at 284.4 eV, generated by photoelectrons emitted from the C1s electronic level, and a very low intensity peak at 532.6 eV associated to oxygen contamination during the v-CNTs synthesis, evaluated to be 1.7 at. %. After ion irradiation the relative intensity of the peak generated by C1s photoelectrons decreases and the intensity of the peak at 532.6 eV corresponding to O1s photoelectrons increases remarkably. No other elements were found in the samples.

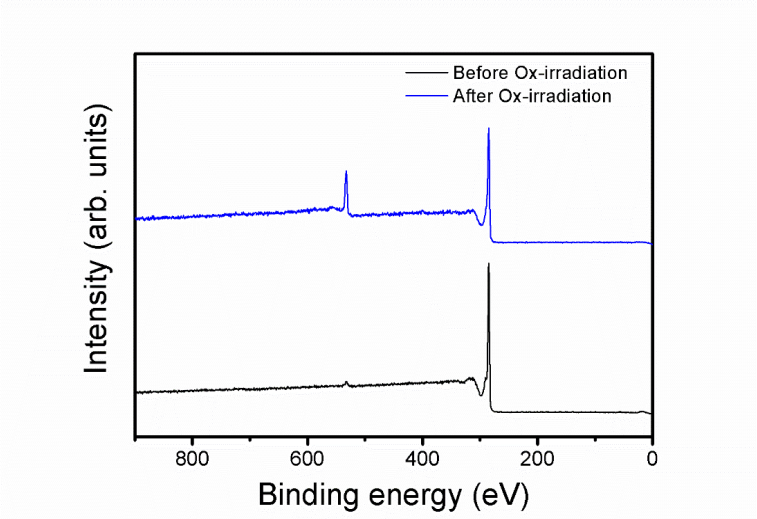


**Figure 2**. XPS survey spectra comparison between v-CNTs before (black line) and after 5 minutes of irradiation with oxygen ions with 1 keV of kinetic energy (blue line).

Figure 3 summarizes the change in the relative oxygen concentration when v-CNTs are irradiated with oxygen ions with different kinetic energies and irradiation times. Increasing the irradiation time (1, 2.5, 5 and 10 min) the relative concentration of oxygen increases from 1.7 at. % to 20.0 at. % (Figure 3a). For a fixed irradiation time (5 minutes) we can divide the resulting amount of oxygen ion grafting in two regimes (Figure 3b): from 0.5 to 2 keV, the relative oxygen concentration remains almost constant (~ 15.0 at.%) independent of the ion energy. As the number of oxygen ions arriving at the sample surface was fixed throughout the experiment, we can conclude that the ion kinetic energy in this range does not affect the rate of ions grafted at the CNT surface. The amount of oxygen ions implanted thus depends only on the treatment time. The second regime is observed for oxygen ion irradiation from 0 keV up to 0.5 keV (Figure 3b), it is clear that when CNTs are irradiated with ions with 0 keV kinetic energy, i.e. the grid supply at the extractor is set to 0 keV, the amount of oxygen grafted is lower. Under these conditions no specific ion kinetic energy is selected, and all types of species generated inside the plasma chamber are able to reach the sample surface, including neutrals species. It is important to mention that the distance between the exit of the plasma cup in the Tectra ion source and the surface of the sample is about 12 cm, thus it is a remote plasma treatment in which the species with short-life time recombine before reaching the sample surface [28]. Under these conditions instead of ion irradiation, functionalization occurs via a plasma treatment. The quantity of oxygen grafted during this remote oxygen plasma treatment was 8.0 at. % about half that produced by ion energy irradiation, with ion kinetic energies from 0.5 to 2 keV (Figure 3b). The increase in the grafting of oxygen for increasing ion kinetic energy can be associated to an increase in the probability of defect creation as discussed by Lehtinen *et al.* in 2010 [29]. These authors, using atomistic computer simulations based on analytical potential and density-functional theory models, showed that for carbon nanostructures the probability of defect creation during low-mass ion irradiation, has a sharp increase up to 0.5 keV kinetic energy followed by a gradual decrease. This shows that the functionalization efficiency using low kinetic energy ion irradiation is higher than in the remote plasma treatment, since the impacting oxygen species are more energetic increasing the probability of creating defect sites into the CNT lattice [30]. Additionally, the oxygen species shorter lifetimes increase the possibility for recombination into stable gas-phase species unlikely to react with

the tubes.

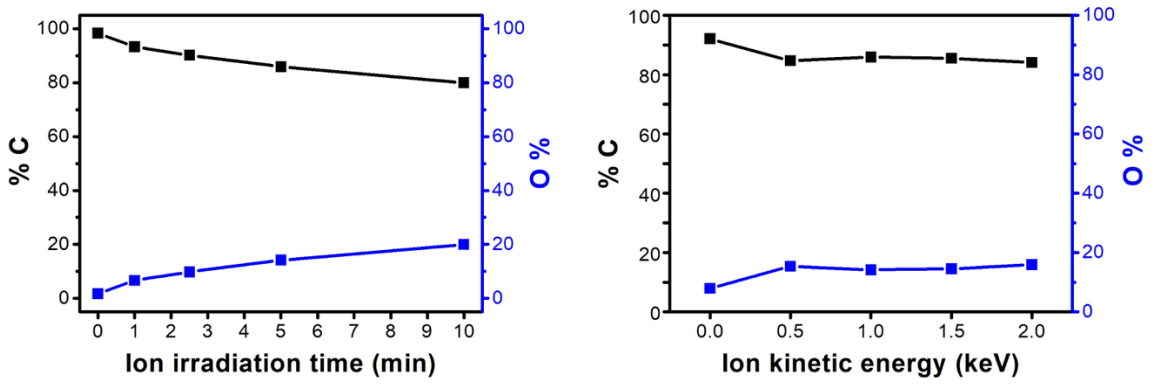


**Figure 3**. Carbon and oxygen content in v-CNTs before and after oxygen functionalization in function of ion irradiation time (**a**) and ion kinetic energy (for a fixed time: 5 minutes) (**b**). When the ion irradiation time is zero it corresponds to v-CNTs pristine. For ion energy equal to 0 keV the oxidation occurs through a remote plasma treatment rather than to an ion-implantation process.

A detailed analysis of the C1s XPS spectrum gives information on the chemical configuration of the oxygen grafted in the graphitic network. Figure 4 shows a comparison between the C1s spectra recorded on the pristine v-CNTs and after 10 minutes of oxygen ion irradiation at 1 keV of ion kinetic energy and the result of the curve fitting reproducing each spectrum.

The pristine C1s spectrum is asymmetric, due to a re-adjustment of the Fermi level caused by electron-hole interaction after the electron scattering. In order to reproduce this asymmetry, the fitting of C1s peak was made with the Doniach-Sunjic function [31]. The peak has a binding energy of 284.4 eV and is reported to be generated by photoelectrons emitted from $sp^2$ carbon atoms [11]. We also observe a low intensity broad peak centered at 290.9 eV, corresponding to photoelectrons that lose kinetic energy to π-plasmon excitations. To reproduce this peak a Gaussian-Lorentzian was used (Figure 4a).

The C1s XPS spectra recorded after v-CNTs irradiation with oxygen ions show a drastic change, widening in the range 285 to 290 eV, due to the bonding of oxygen to carbon atoms (Figure 4b, supplementary). To reproduce the spectrum for the sample irradiated 10 minutes it was necessary to use six components, the two used in the fitting of pristine v-CNTs and four other symmetric peaks (Gaussian-Lorentzian). These components are centered at binding energies of 285.0 eV, 286.6 eV, 287.5 eV and 288.8 eV.

The component at 285.0 eV is assigned to $sp^3$ carbon bonding occurring at defects introduced in the carbon lattice by ion irradiation. This can include interlayer and intertube cross-linking defects, amorphization, and carbon bonding to $CO_x$ species. Induced in a controllable way, these defects can cause beneficial changes in chemical and electronic properties of the CNTs, promoting their application in different fields [16]. The components at 286.6 eV, 287.5 eV and 288.8 eV are associated to carbon bonded to oxygen. The electronegative oxygen atoms induce a positive charge in the carbon atoms thus changing the electron screening of their nucleus. This increases consequently the binding energy of the electrons, explaining the shift to higher binding energies for the components in the C1s spectra. Using spin polarized density functional calculations within the local density approximation (LDA) for the interpretation of the C1s XPS peak of oxygen functionalized carbon nanotubes, Bittencourt *et al* [12], assigned the component at 286.6 eV to epoxide groups (C-O-C), the component 287.5 eV to carbonyl groups (C=O) and 288.8 eV to carboxyl groups (-COOH).

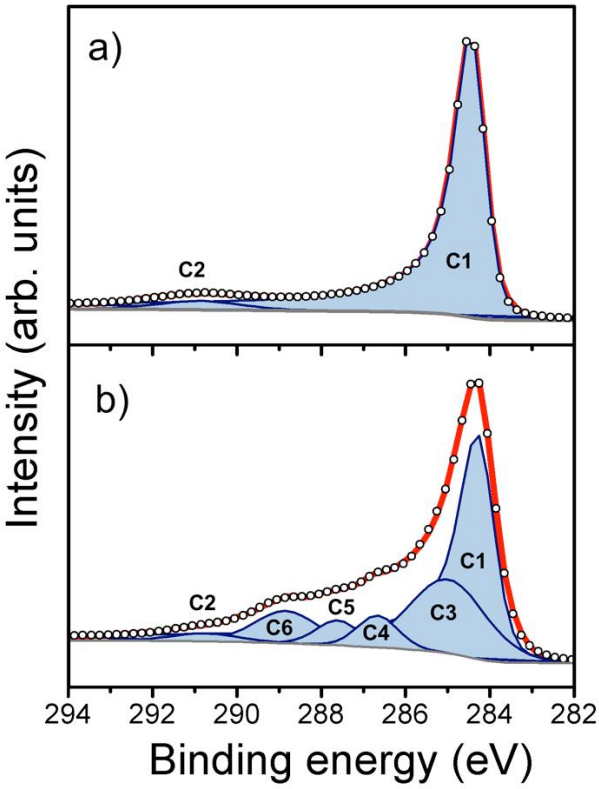


**Figure 4**. XPS analysis of v-CNTs pristine (**a**) and v-CNTs after 10 min of irradiation with oxygen ions with ion kinetic energy of 1 keV (**b**). C1 is assigned to $sp^2$-C (284.4 eV), C2 to π-plasmon excitations (290.9 eV), C3 to $sp^3$-C (285.0 eV), C4 to epoxide groups C-O-C (286.6 eV), C5 to carbonyl groups C=O (287.5 eV) and C6 to carboxyl groups -COOH (288.8 eV). Components peaks result from a least-squares fitting procedure.

In order to understand the effect of varying the ion irradiation parameters in the chemistry of the v-CNTs, we analyzed the C1s XPS spectrum of each sample (Table 2, Figures S1-S7). To corroborate our results, the analysis of O1s XPS spectra was also performed (Figures S8-S17). The same number of C-O components were obtained in C1s and O1s analysis.

Table 2. Relative area (%A) of the components used the reproduce the C1s peak. The binding energy assignments was reported by Bittencourt *et al.* 2011.

| **Irradiation time (min)** | **Ion kinetic energy (keV)** | **$sp^2$-C (%A) C1 284.4 eV** | **$sp^3$-C (%A) C3 285.0 eV** | **C-O-C (%A) C4 286.6 eV** | **C=O (%A) C5 287.5 eV** | **-COOH (%A) C6 288.8 eV** | **Plasmon (%A) C2 290.9 eV** |
|---|---|---|---|---|---|---|---|
| 0 | - | 96.3 | 0 | 0 | 0 | 0 | 3.7 |
| 1 | 1 | 86.2 | 9.0 | 0.7 | 1.9 | 0 | 2.2 |
| 2.5 | 1 | 83.0 | 11.5 | 1.7 | 2.4 | 0 | 1.4 |
| 5 | 1 | 71.7 | 16.8 | 3.1 | 4.7 | 2.9 | 0.8 |
| 10 | 1 | 62.7 | 20.0 | 4.5 | 3.8 | 7.2 | 1.9 |
| 5 | 0 | 85.2 | 8.8 | 5.5 | 0 | 0 | 0.5 |
| 5 | 0.1 | 92.9 | 5.5 | 1.3 | 0 | 0.3 | 0 |
| 5 | 0.25 | 84.2 | 9.8 | 2.6 | 0 | 1.9 | 1.5 |
| 5 | 0.5 | 71.2 | 15.7 | 3.3 | 2 | 5.7 | 2.1 |
| 5 | 1.5 | 69.7 | 19.0 | 4.2 | 2.4 | 3.7 | 1.1 |
| 5 | 2 | 72.0 | 15.5 | 3.9 | 4.2 | 2.7 | 1.7 |

Figure 5 shows the variation in the relative area of each component used to reproduce the C1s peak as a function of the treatment time and the ion kinetic energy. The relative contribution of component C1 (graphitic carbon ($sp^2$-C)) decreases from the 96.3 % in pristine v-CNTs to 62.7 % when the treatment time reaches 10 minutes, indicating that the oxygen functionalization occurs through breakdown of π bonding in the $sp^2$-C bond. The relative area of component C2 ($sp^3$-C) increases to 20% after 10 minutes of treatment (Figure 5a).

When the treatment time was fixed to 5 minutes and the ion kinetic energy was the variant parameter, we observed that the ion energy does not significantly affect the relative area of the graphitic carbon component (C1), remaining in a range from 69.7 to 72.0 % (for the range of energies form 0.5 to 2 keV). Similarly, the area of the component C2 ($sp^3$-C) remains in a range from 15.7 to 19.0 %.

These results suggest that for the samples irradiated with ion kinetic energy varying from 0.5 to 2 keV, approximately the same number of ions interact with the carbon nanotubes. At 0 keV kinetic energy (a remote plasma treatment [32]), only 8.8 % of the $sp^2$ carbon (C1) is transformed into $sp^3$ (C3) and 5.5% into oxygen-bound carbon species (C4), confirming that the remote plasma treatment generates less defects at the CNT surface than ion irradiation (Figure 5b), with much lower oxygen grafting at the CNT surface (Figure 3b).

It is interesting to compare the grafting of oxygen atoms for 0 keV (remote plasma functionalization) with the ion irradiation results (Figure 6 and 7b). In the case of remote plasma functionalization, the only C-O bonding observed comes from epoxide groups. These consist of single oxygen atoms bonded covalently to a $sp^2$-C surface, forming covalent bonds with two carbon neighbors with the oxygen atom sitting above the C-C bond centre. This is the least disruptive oxygen functional group (indeed epoxide groups can be added to graphene simple trough ozone exposure with UV light [33]), since they do not require carbon dangling bonds, and hence associated hole or edge formation. This therefore confirms that the remote plasma is only adding very low energy isolated oxygen atoms to the nanotube surface (probably primarily neutrals) with minimal damage and disruption of the carbon layers. Epoxide oxygen can also be removed through relatively gentle reducing processes.

In contrast, the ion-implantation results show high concentrations of carbonyl and carboxyl groups, demonstrating that the lattice is being disrupted and carbon dangling bonds created which are being oxygenated. This is consistent with a picture where incoming charged oxygen ions are arriving with kinetic energies far above the knock-on threshold energies of the lattice carbon, resulting in carbon displacements and increased local damage. This is also visible in the production of $sp^3$-C carbon atoms as collateral damage. Thus the two processes are complementary, allowing choice of oxygen chemical functional group addition depending on end-application requirements.

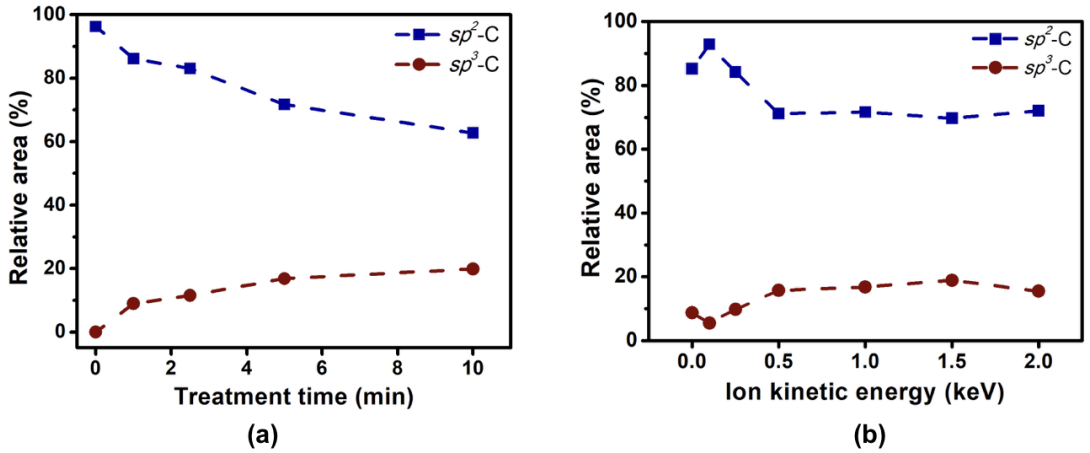


**Figure 5.** Variation in relative area of the components of carbon $sp^2$-C (C1) and carbon $sp^3$-C (C3) used to reproduce the C1s XPS spectrum of v-CNTs as a function of the treatment time (ion kinetic energy 1keV) (**a**) and the ion kinetic energy (fixed treatment time: 5 minutes) (**b**).

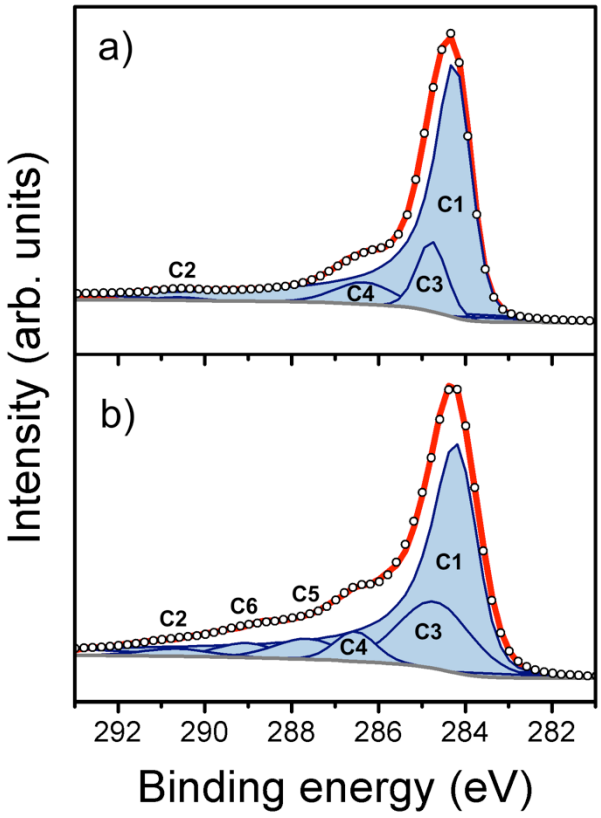


**Figure 6.** XPS analysis of v-CNTs functionalized by plasma treatment (0 keV of ion kinetic energy) (**a**) and by ion irradiation with 2 keV of ion kinetic energy (**b**). The treatment time was 5 min for the two samples. C1 is assigned to $sp^2$-C (284.4 eV), C2 to π-plasmon excitations (290.9 eV), C3 to $sp^3$-C (285.0 eV), C4 to epoxide groups C-O-C (286.6 eV), C5 to carbonyl groups C=O (287.5 eV) and C6 to carboxyl groups -COOH (288.8 eV). Components peaks result from a least-squares fitting procedure.

We can further understand the oxidation processes occurring during ion irradiation by exploring the change in relative concentration of different C-O species over time (Figure 7a). Just as for the plasma treatment, epoxide species start forming on the basal plane from the beginning of the treatment, and gradually increase in concentration over the time. In parallel there is an extremely initial rapid formation of carbonyl groups. This presumably involves functionalization of tube tips which are much more chemically reactive than the tube sidewalls and represent preferential addition sites [34]. During this period there is a gradual increase in $sp^3$-C indicating the ion irradiation process is beginning to damage the nanotube carbon network (Figure 5a). After 5 minutes the network is sufficiently damaged that holes and internal edges are formed. These are C=O and -COOH edge-terminated, giving rise to a corresponding increase in the C=O and -COOH C1s peaks in the XPS.

The carbonyl groups are intermediate states and can oxygen saturate, transforming to carboxyl groups, helping to explain the relative stability in carbonyl concentration and large increase in -COOH in the C1s peak from 5 to 10 minutes. This process will be kinetically dependent on the rate of damage site and hole formation (i.e. new dangling bond creation rate), and is also reflected in the ion energy study (Figure 7b). As the ion kinetic energy increases there is a steady decrease in epoxide concentration, primarily because at higher energies there is an increased chance of damaging the lattice and so inserting oxygen as other (carbonyl or carboxyl) forms. The slight decrease in the $sp^3$-C

component observed when the sample was irradiated with 0.1 keV ions can be associated to a preferential removal of physically adsorbed species (amorphous carbon and oxygen species including water) occurring during the synthesis and due to the exposure to ambient air.

Raman spectroscopy data shows variations in the relative intensity of the primary G- and D-peaks consistent with the interpretation we present here based on the XPS data (see Supplementary Figure S18 and associated supplementary discussion).

Figure 8 shows the typical TEM images recorded on carbon nanotubes pristine (Figure 8a) and carbon nanotubes irradiated for 5 minutes with oxygen ions with kinetic energy of 2 keV (Figure 8b) samples. Carbon nanotubes pristine exhibit closed tips, as was expected, contrary to carbon nanotubes irradiated with oxygen ions where open tips were observed, the presence of open tips on carbon nanotubes is an evidence of oxygen functionalization of the tips. No significant damage was found on the nanotube walls.

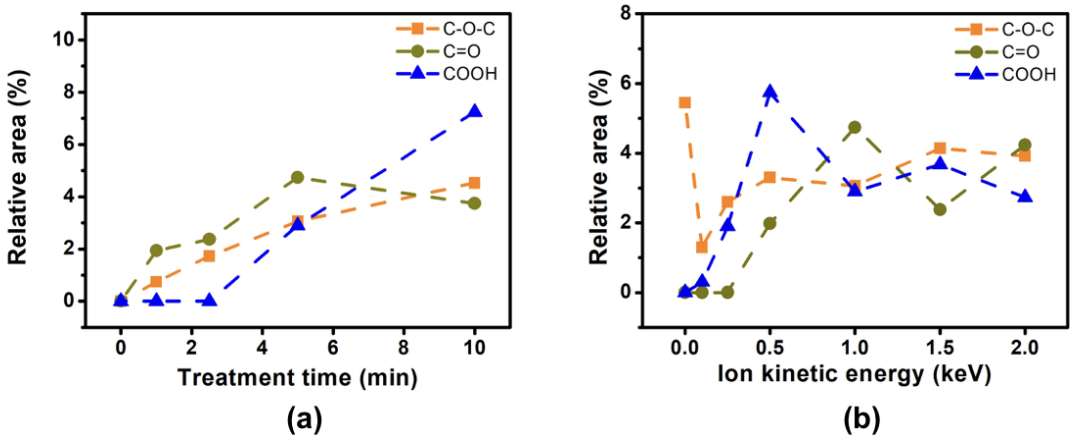


**Figure 7**. Variation in relative area of the components of carbon bonded to oxygen (C4 (C-O-C), C5 (C=O), C6 (-COOH)) used to reproduce the C1s XPS spectrum of v-CNTs as a function of the treatment time (ion energy 1 keV) (**a**) and the ion kinetic energy (treatment time 5 minutes) (**b**).

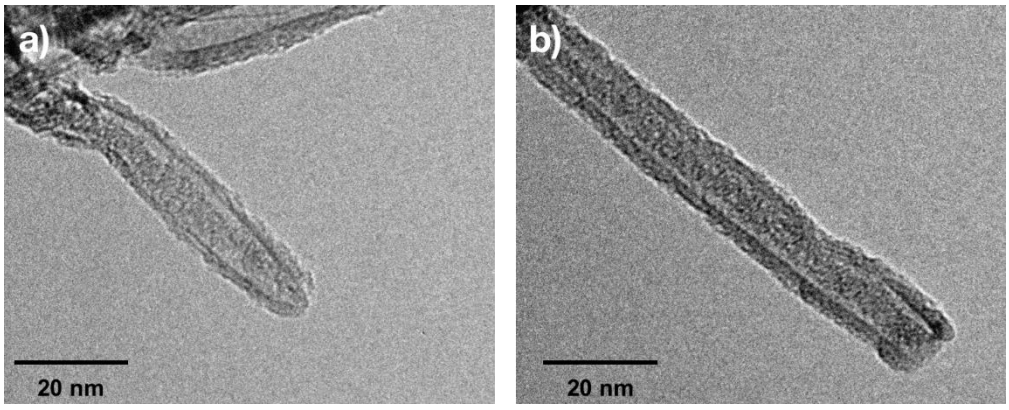


**Figure 8**. TEM microscopy of carbon nanotubes pristine (**a**) and carbon nanotubes irradiated for 5 minutes with oxygen ions with kinetic energy of 2 keV (**b**).

## 4. Conclusions

Different oxygen functional groups can be created at the surface of vertically aligned carbon nanotubes by low kinetic energy oxygen ion irradiation. We show that defect creation, the chemical nature, and concentration of functional groups depend on the irradiation time and the ion kinetic energy, indicating that low kinetic energy ion irradiation is an optimal functionalization method that can be used to fine tune the type and concentration of functional groups grafted at the carbon

nanotube surface. The versatility of the method is a very clear advantage in comparison to other functionalization techniques, because using low kinetic ion irradiation we can tailor the surface reactivity of carbon nanotubes specifically for different applications, in a clean way and employing very short treatment times.

**Supplementary Materials:** The following are available online at www.mdpi.com/xxx/s1, Figure S1. XPS analysis of v-CNTs after 1 minute of ion implantation with 1 keV of ion kinetic energy, Figure S2. XPS analysis of v-CNTs after 2.5 minutes of ion implantation with 1 keV of ion kinetic energy, Figure S3. XPS analysis of v-CNTs after 5 minutes of ion implantation with 1 keV of ion kinetic energy, Figure S4. XPS analysis of v-CNTs after 5 minutes of ion implantation with 0.1 keV of ion kinetic energy Figure S5. XPS analysis of v-CNTs after 5 minutes of ion implantation with 0.25 keV of ion kinetic energy, Figure S6. XPS analysis of v-CNTs after 5 minutes of ion implantation with 0.5 keV of ion kinetic energy, Figure S7. XPS analysis of v-CNTs after 5 minutes of ion implantation with 1.5 keV of ion kinetic energy, Figure S8. XPS analysis of O1s spectrum of v-CNTs after 1 minute of ion implantation with 1 keV of ion kinetic energy, Figure S9. XPS analysis of O1s spectrum of v-CNTs after 2.5 minutes of ion implantation with 1 keV of ion kinetic energy, Figure S10. XPS analysis of O1s spectrum of v-CNTs after 5 minutes of ion implantation with 1 keV of ion kinetic energy, Figure S11. XPS analysis of O1s spectrum of v-CNTs after 10 minutes of ion implantation with 1 keV of ion kinetic energy, Figure S12. XPS analysis of O1s spectrum of v-CNTs after 5 minutes of ion implantation with 0 keV of ion kinetic energy, Figure S13. XPS analysis of O1s spectrum of v-CNTs after 5 minutes of ion implantation with 0.1 keV of ion kinetic energy, Figure S14. XPS analysis of O1s spectrum of v-CNTs after 5 minutes of ion implantation with 0.25 keV of ion kinetic energy, Figure S15. XPS analysis of O1s spectrum of v-CNTs after 5 minutes of ion implantation with 0.5 keV of ion kinetic energy, Figure S16. XPS analysis of O1s spectrum of v-CNTs after 5 minutes of ion implantation with 1.5 keV of ion kinetic energy, Figure S17. XPS analysis of O1s spectrum of v-CNTs after 5 minutes of ion implantation with 2 keV of ion kinetic energy, Figure S18**.** Raman spectrum of v-CNTs functionalized with low kinetic energy oxygen ion irradiation with different treatment time (**a**) and ion kinetic energy (**b**).

**Funding:** This work is funded by the Belgian Fund for Scientific Research under FRFC contracts "SNOW - J001019 and PLAFON - UN003.18" and by MINECO under grant no. TEC2015-71663-R, by AGAUR under grant no. 2017SGR 418. J. Casanova-Cháfer is supported by a Martí i Franquès pre-doctoral fellowship from Universitat Rovira i Virgili (URV), and E. Llobet is supported by the Catalan Institution for Research and Advanced Studies via the ICREA Academia Award. C. Bittencourt and J.–F Colomer are Research Associates of the National Funds for Scientific Research (FRS-FNRS, Belgium).

**Conflicts of Interest:** "The authors declare no conflict of interest." "The funders had no role in the design of the study; in the collection, analyses, or interpretation of data; in the writing of the manuscript, or in the decision to publish the results".

## References

1. Li, W. Z., Xie, S. S., Qian, L. X., Chang, B. H., Zou, B. S., Zhou, W. Y., Zhao, R. A., & Wang, G. Large-scale synthesis of aligned carbon nanotubes. *Science*, **1996** *274(5293)*, 1701-1703. DOI: 10.1126/science.274.5293.1701.
2. Fam, D. W. H., Palaniappan, A., Tok, A. I. Y., Liedberg, B., & Moochhala, S. M. A review on technological aspects influencing commercialization of carbon nanotube sensors. *Sensors and Actuators B: Chemical*, **2011** *157(1)*, 1-7. DOI: 10.1016/j.snb.2011.03.040.
3. Bondavalli, P., Legagneux, P., & Pribat, D. Carbon nanotubes based transistors as gas sensors: state of the art and critical review. *Sensors and Actuators B: Chemical* **2009**, *140(1)*, 304-318. DOI: 10.1016/j.snb.2009.04.025.
4. Vardharajula, S., Ali, S. Z., Tiwari, P. M., Eroğlu, E., Vig, K., Dennis, V. A., & Singh, S. R. Functionalized carbon nanotubes: biomedical applications. *International journal of nanomedicine* **2012**, *7*, 5361. DOI: 10.2147/IJN.S35832.
5. Yoo, K. P., Kwon, K. H., Min, N. K., Lee, M. J., & Lee, C. J. Effects of O2 plasma treatment on NH3 sensing characteristics of multiwall carbon nanotube/polyaniline composite films. *Sensors and Actuators B: Chemical* **2009**,*143(1)*, 333-340. DOI: 10.1016/j.snb.2009.09.029.
6. Malik, R., McConnell, C., Alvarez, N. T., Haase, M., Gbordzoe, S., & Shanov, V. Rapid, in situ plasma functionalization of carbon nanotubes for improved CNT/epoxy composites. *RSC Advances* **2016**, *6(110)*, 108840-108850. DOI: 10.1039/C6RA23103A.

7. Lobo, A. O., Ramos, S. C., Antunes, E. F., Marciano, F. R., Trava-Airoldi, V. J., & Corat, E. J. Fast functionalization of vertically aligned multiwalled carbon nanotubes using oxygen plasma. *Materials Letters* **2012**, *70*, 89-93. DOI: 10.1016/j.matlet.2011.11.071.
8. Trulli, M. G., Sardella, E., Palumbo, F., Palazzo, G., Giannossa, L. C., Mangone, A., Comparelli, R., Musso, S., & Favia, P. Towards highly stable aqueous dispersions of multi-walled carbon nanotubes: the effect of oxygen plasma functionalization. *Journal of colloid and interface science* **2017**, *491*, 255-264. DOI: 10.1016/j.jcis.2016.12.039
9. Muhulet, A., Miculescu, F., Voicu, S. I., Schütt, F., Thakur, V. K., & Mishra, Y. K. Fundamentals and scopes of doped carbon nanotubes towards energy and biosensing applications. *Materials today energy* **2018**, *9*, 154-186. DOI: 10.1016/j.mtener.2018.05.002.
10. Vuković, G. D., Marinković, A. D., Čolić, M., Ristić, M. Đ., Aleksić, R., Perić-Grujić, A. A., & Uskoković, P. S. Removal of cadmium from aqueous solutions by oxidized and ethylenediamine-functionalized multi-walled carbon nanotubes. *Chemical Engineering Journal* **2010**, *157(1),* 238-248. DOI: 10.1016/j.cej.2009.11.026
11. Barinov, A., Gregoratti, L., Dudin, P., La Rosa, S., & Kiskinova, M. Imaging and spectroscopy of multiwalled carbon nanotubes during oxidation: defects and oxygen bonding. *Advanced Materials* **2009**, *21(19),* 1916-1920. DOI: 10.1002/adma.200803003.
12. Bittencourt, C., Navio, C., Nicolay, A., Ruelle, B., Godfroid, T., Snyders, R., Colomer, J.-F., Lagos, M. J., Ke, X., Van Tendeloo, G., Suarez-Martinez, I., & Ewels, C. P. Atomic oxygen functionalization of vertically aligned carbon nanotubes. *The Journal of Physical Chemistry C* **2011**, *115(42),* 20412-20418. DOI: 10.1021/jp2057699.
13. Datsyuk, V., Kalyva, M., Papagelis, K., Parthenios, J., Tasis, D., Siokou, A., Kallitsis, I., & Galiotis, C. Chemical oxidation of multiwalled carbon nanotubes. *Carbon*, **2008**, *46(6)*, 833-840. DOI: 10.1016/j.carbon.2008.02.012.
14. Korusenko, P. M., Nesov, S. N., Povoroznyuk, S. N., Bolotov, V. V., & Knyazev, E. V. Functionalization of multi-walled carbon nanotubes using ion beams of various intensities. *AIP Conference Proceedings*, **2018**, *2007(1)*, 040008. DOI: 10.1063/1.5051935.
15. Xia, W., Schlüter, O. F. K., Liang, C., van den Berg, M. W., Guraya, M., & Muhler, MThe synthesis of structured Pd/C hydrogenation catalysts by the chemical vapor deposition of Pd (allyl) Cp onto functionalized carbon nanotubes anchored to vapor grown carbon microfibers. *Catalysis today* **2005**, *102*, 34-39. DOI: 10.1016/j.cattod.2005.02.002.
16. Krasheninnikov, A. V., & Banhart, F. J. N. M. Engineering of nanostructured carbon materials with electron or ion beams. *Nature materials* **2007**, *6(10)*, 723. DOI: 10.1038/nmat1996.
17. Krasheninnikov, A. V., & Nordlund, K. Irradiation effects in carbon nanotubes. *Nuclear Instruments and Methods in Physics Research Section B: Beam Interactions with Materials and Atoms* **2004**, *216*, 355-366. DOI: 10.1016/j.nimb.2003.11.061
18. Kamimura, T., Yamamoto, K., Kawai, T., & Matsumoto, K. n-type doping for single-walled carbon nanotubes by oxygen ion implantation with 25 eV ultralow-energy ion beam. *Japanese journal of applied physics* **2005**, *44(11R)*, 8237. DOI: 10.1143/JJAP.44.8237
19. Bangert, U., Bleloch, A., Gass, M. H., Seepujak, A., & Van den Berg, J. Doping of few-layered graphene and carbon nanotubes using ion irradiation. *Physical Review B* **2010**, *81(24)*, 245423. DOI: 10.1103/PhysRevB.81.245423.
20. Krasheninnikov, A. V., & Nordlund, K. Ion and electron irradiation-induced effects in nanostructured materials. *Journal of applied physics* **2010**, *107(7)*, 3. DOI: 10.1063/1.3318261
21. Krasheninnikov, A. V., Nordlund, K., & Keinonen, J. Production of defects in supported carbon nanotubes under ion irradiation. *Physical Review B* **2002**, *65(16)*, 165423. DOI: 10.1103/PhysRevB.65.165423
22. Shemukhin, A. A., Stepanov, A. V., Nazarov, A. V., & Balakshin, Y. V. Simulation of defects formation in nanotubes under ion irradiation. *Nuclear Instruments and Methods in Physics Research Section B: Beam Interactions with Materials and Atoms* **2019**. DOI: 10.1016/j.nimb.2019.03.055.
23. Krasheninnikov, A. V., Nordlund, K., Sirviö, M., Salonen, E., & Keinonen, J. Formation of ion-irradiation-induced atomic-scale defects on walls of carbon nanotubes. *Physical Review B* **2001,** *63*(24), 245405. DOI: 10.1103/PhysRevB.63.245405.
24. Salonen, E., Krasheninnikov, A. V., & Nordlund, K. Ion-irradiation-induced defects in bundles of carbon nanotubes. *Nuclear Instruments and Methods in Physics Research Section B: Beam Interactions with Materials and Atoms* **2002**, *193*(1-4), 603-608. DOI: 10.1016/S0168-583X(02)00861-3.

25. Scardamaglia, M., Struzzi, C., Rebollo, F. J. A., De Marco, P., Mudimela, P. R., Colomer, J. F., Amati, M., Gregoratti, L., Petaccia, L., Snyders, R., & Bittencourt, C. Tuning electronic properties of carbon nanotubes by nitrogen grafting: chemistry and chemical stability. *Carbon* **2015**, *83*, 118-127. DOI: 10.1016/j.carbon.2014.11.009.
26. Xu, F., Minniti, M., Giallombardo, C., Cupolillo, A., Barone, P., Oliva, A., & Papagno, L. Nitrogen ion implantation in single wall carbon nanotubes. *Surface science* **2007**, *601*(13), 2819-2822.
27. Colomer, J. F., Ruelle, B., Moreau, N., Lucas, S., Snyders, R., Godfroid, T., Navio, C., & Bittencourt, C. Vertically aligned carbon nanotubes: synthesis and atomic oxygen functionalization. *Surface and Coatings Technology* **2011**, *205*, S592-S596. DOI: 10.1016/j.surfcoat.2011.03.040.
28. Ruelle, B., Felten, A., Ghijsen, J., Drube, W., Johnson, R. L., Liang, D., Erni, R., Van Tendeloo, G., Peeterbroeck, S., Dubois, P., Godfroid, T., Hecq, M., & Bittencourt, C. Functionalization of MWCNTs with atomic nitrogen. *Micron* **2009**, *40*(1), 85-88. DOI: 10.1016/j.micron.2008.01.003.
29. Lehtinen, O., Kotakoski, J., Krasheninnikov, A. V., Tolvanen, A., Nordlund, K., & Keinonen, J. Effects of ion bombardment on a two-dimensional target: Atomistic simulations of graphene irradiation. *Physical review B* **2010**, *81*(15), 153401. DOI: 10.1103/PhysRevB.81.153401.
30. Tessonnier, J. P., Villa, A., Majoulet, O., Su, D. S., & Schlögl, R. Defect-mediated functionalization of carbon nanotubes as a route to design single-site basic heterogeneous catalysts for biomass conversion. *Angewandte Chemie International Edition* **2009**, *48*(35), 6543-6546. DOI: 10.1002/anie.200901658.
31. Doniach, S., & Sunjic, M. Many-electron singularity in X-ray photoemission and X-ray line spectra from metals. *Journal of Physics C: Solid State Physics* **1970**, *3(2)*, 285. DOI: 10.1088/0022-3719/3/2/010.
32. Zhu, H., Qin, X., Cheng, L., Azcatl, A., Kim, J., & Wallace, R. M. Remote plasma oxidation and atomic layer etching of MoS2. *ACS applied materials & interfaces* **2016**, *8(29)*, 19119-19126. DOI: 10.1021/acsami.6b04719
33. GÜNEŞ, F., Han, G. H., Shin, H. J., Lee, S. Y., Jin, M., Duong, D. L., Chae, S.J., Kim, E. S., Yao, F., Benayad, A., Choi, J. Y., & Lee, Y. H. UV-light-assisted oxidative sp3 hybridization of graphene. *Nano* **2011**, *6(05)*, 409-418. DOI: 10.1142/S1793292011002780.
34. Scardamaglia, M., Amati, M., Llorente, B., Mudimela, P., Colomer, J. F., Ghijsen, J., Ewels, C., Snyders, R., Gregoratti, L., & Bittencourt, C. Nitrogen ion casting on vertically aligned carbon nanotubes: tip and sidewall chemical modification. *Carbon* **2014**, *77*, 319-328. DOI: 10.1016/j.carbon.2014.05.035.

Section 2.7

# $MoS_2$-Carbon Nanotube Hybrid Material Growth and Gas Sensing

Geetanjali Deokar, Péter Vancsó, Raul Arenal, Florent Ravaux, Juan Casanova-Cháfer, Eduard Llobet, Anna Makarova, Denis Vyalikh, Claudia Struzzi, Philippe Lambin, Mustapha Jouiad, Jean-Francois Colomer

*Advanced Materials Interfaces, 4 (2017) 1700801*

DOI: 10.1002/admi.201700801

UNIVERSITAT ROVIRA I VIRGILI
GAS SENSING WITH MODIFIED CARBON NANOTUBES, GRAPHENE AND DIAMONDOIDS
Juan Casanova Cháfer

ADVANCED MATERIALS INTERFACES
www.advmatinterfaces.de

# $MoS_2$–Carbon Nanotube Hybrid Material Growth and Gas Sensing

*Geetanjali Deokar,* Péter Vancsó, Raul Arenal, Florent Ravaux, Juan Casanova-Cháfer, Eduard Llobet,* Anna Makarova, Denis Vyalikh, Claudia Struzzi, Philippe Lambin, Mustapha Jouiad,* and Jean-Francois Colomer*

**Hexagonal-shaped nanoplates (HNPs) of $MoS_2$ on vertically aligned carbon nanotubes (CNTs) over a patterned area (a circular area of 1 $cm^2$ diameter) are produced by chemical vapor deposition technique. With an optimized initial Mo film thickness, a uniform coverage of $MoS_2$ HNPs with a thickness around 20 nm is achieved. The results confirm that the CNT template plays an important role in the $MoS_2$ HNPs growth. Each $MoS_2$ HNP consists of abundant exposed edges, interesting for sensing and catalysis applications. High crystallinity and quality of the as-produced material are revealed by X-ray photoelectron and Raman spectroscopies. Furthermore, $NO_2$ gas-sensing studies show better sensitivity and recovery for $MoS_2$/CNT samples as compared to pristine CNTs. The detection of $NO_2$ gas in a few tens of parts per million to a few hundreds of parts per billion range, at room temperature, is achieved. Density-functional theory calculation indicates that the exposed edges of $MoS_2$ play a significant role in the $NO_2$ sensing as compared to horizontally aligned $MoS_2$ layers. The present report can promote the research toward the fabrication of efficient and reliable $MoS_2$-based hybrid materials for toxic gas-sensing applications for air quality monitoring in various environments.**

## 1. Introduction

Unlike the zero band-gap graphene, semiconductor materials[1–4] with reactive sites for redox reactions are particularly interesting for gas sensors. Among the various other possible active materials in gas-sensing devices, carbon nanotubes (CNTs) are good candidates. For more than a decade, quite detailed studies have been devoted to use CNTs for gas-sensing applications.[2] Using CNTs as an $NO_2$ gas sensor was first proposed by Kong et al.[5] The functionalization of CNTs by organic polymers or catalytic metal nanoparticles was found to be a good strategy to enhance the sensitivity and the selectivity of the CNT-based sensors.[2] Metal functionalized sensors can operate at higher temperatures and in harsh environments, as they are both mechanically and chemically

Dr. G. Deokar, Dr. P. Vancsó, Prof. P. Lambin, Dr. J.-F. Colomer
Research Group on Carbon Nanostructures (CARBONNAGe)
University of Namur
61 Rue de Bruxelles, 5000 Namur, Belgium
E-mail: geetanjali.deokar@unamur.be

Dr. G. Deokar, Dr. F. Ravaux, Prof. M. Jouiad
Department of Mechanical and Materials Engineering
Masdar Institute of Science and Technology
A part of Khalifa University of Science and Technology
54224 Abu Dhabi, United Arab Emirates
E-mail: mjouiad@masdar.ac.ae

Dr. R. Arenal
Laboratory of Advanced Microscopies (LMA)
Institute of Nanoscience of Aragón (INA)
Universidad de Zaragoza
c/Mariano Esquillor 50018, Zaragoza, Spain

Dr. R. Arenal
Department of Electronic Engineering
Fundacion ARAID
50004 Zaragoza, Spain

The ORCID identification number(s) for the author(s) of this article can be found under https://doi.org/10.1002/admi.201700801.

**DOI: 10.1002/admi.201700801**

J. Casanova-Cháfer, Prof. E. Llobet
MINOS-EMaS
Universitat Rovira i Virgili
43007 Tarragona, Spain
E-mail: eduard.llobet@urv.cat

Dr. A. Makarova
Institut für Festkörperphysik
Technische Universität Dresden
D-01062 Dresden, Germany

Prof. D. Vyalikh
Physics Department
Saint-Petersburg State University
Saint Petersburg 198504, Russia

Prof. D. Vyalikh
Donostia International Physics Center (DIPC)
Departamento de Fisica de Materiales, CFM-MPC UPV/EHU
20080 San Sebastian, Spain

Prof. D. Vyalikh
IKERBASQUE
Basque Foundation for Science
48011 Bilbao, Spain

C. Struzzi
Chimie des Interactions Plasma-Surface (ChIPS)
CIRMAP
Research Institute for Materials Science and Engineering
University of Mons
7000 Mons, Belgium

 

robust and stable, as compared to polymer-based functionalized sensors. It has been shown that the sensitivity of the CNT gas sensor functionalized using metal-nanostructures, depends on nanocluster size and shape.[6] Indeed, the size of the metal clusters is necessary to maximize the effect of the gas adsorption at the corners and edges and so to affect the electron transport in the CNTs by the charge transfer.[6]

In the past few years, it has been emphasized experimentally[7,8] and theoretically[4,9,10] that semiconductive $MoS_2$ is a potential candidate material for gas-sensing applications. It has been reported that $MoS_2$ structural defects, including point defects,[11] grain boundaries,[12] and edges[3,13] play significant roles in sensing applications. However, large-scale fabrication of sensors, their selectivity tuning, and noise reduction are still a challenge. Therefore, there is significant scope remained to explore new materials with advanced properties. New materials often generate entirely new possibilities, pushing the limits of the accepted boundaries of material properties within which engineers operate.[14] With the increasing demand of highly sensitive, fast, and stable sensors, a series of sensing applications of nanoscale $MoS_2$-based composites and hybrids have been of growing interest.[15] Out of various methods for $MoS_2$-based hybrid nanomaterials growth, chemical vapor deposition (CVD) is a promising approach to achieve high-quality $MoS_2$ nanosheets (NSs) with good control on shape, size and number of horizontally or vertically stacked $MoS_2$ layers.[16,17]

Here, we present our work on the functionalization of vertically aligned CNTs (va-CNTs) by a growth of $MoS_2$ hexagonal-shaped nanoplate (HNP) and their use for gas sensing. The hybrid material produced using CVD technique was characterized by employing various microscopy and spectroscopy characterization tools. The obtained $MoS_2$ HNPs consist of highly crystalline structures and have abundant exposed edges, which can be very useful in applications such as sensing,[3] catalysis,[18] Li-ion battery,[19] etc. We have explored the gas ($NO_2$ and $NH_3$) sensing performance for the $MoS_2$/CNT hybrid system. The hybrid samples containing $MoS_2$ HNPs with exposed edges exhibit relatively rapid detection of $NO_2$ as compared to the pristine va-CNT and monolayer $MoS_2$ making it a potential candidate for sensor device application. The obtained results are discussed based on density-functional theory (DFT) calculation results.

## 2. Results and Discussion

### 2.1. Material Characterization

In the present work, patterned growth of $MoS_2$/CNT hybrid material was achieved. The Mo film with defined thickness (10 to 50 nm) deposited on the va-CNT sample and sulfurized for 60 min at 850 °C resulted in $MoS_2$ growth on CNTs (refer to the Experimental Section). The morphology of the synthesized material was examined by scanning electron microscope (SEM), and the images are shown in **Figure 1**. The inset of Figure 1a shows a typical patterned (circular area with 1 $cm^2$ diameter) CNT growth on Si substrate. In Figure 1a,b, cross-section SEM images of the sample are shown where the $MoS_2$ material can be clearly seen, especially on the top of the CNTs. Furthermore, the plan-view SEM images (Figure 1c,d) show that the synthesized material consists of well-defined HNPs with uniform size. The thickness of the nanoplates is about 20 nm, estimated from standing HNPs. The average length of the HNP along the diagonal of the hexagon is about 200–300 nm, as it can be measured from SEM images, and further confirmed by transmission

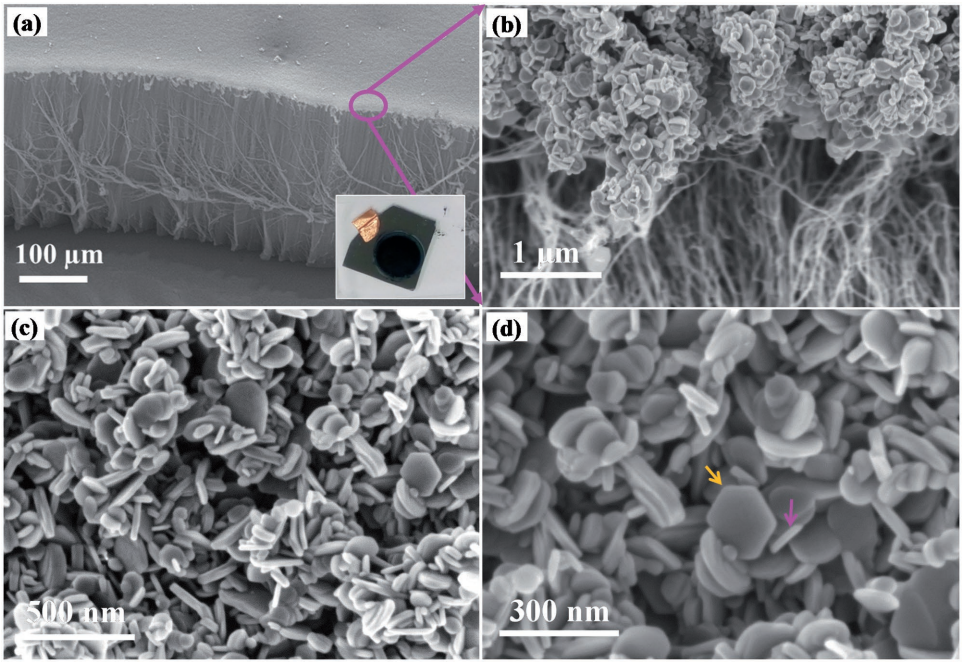


**Figure 1.** SEM images of $MoS_2$/CNT sample synthesized by a 50 nm Mo film sulfurized at 850 °C with 420 mg of S powder for 60 min. a,b) Low and high resolution cross-section view SEM images with a typical patterned CNT/Si sample photo in the inset of panel (a). c,d) Surface view SEM images. The typical standing and flat lying HNPs are marked with magenta and orange arrows, respectively.

 

electron microscopy (TEM) (Figure 3a). Two morphologies of $MoS_2$ were observed when Mo film was deposited on the full sample (CNT and Si surface without CNT). On CNT free Si substrate, vertically aligned $MoS_2$ nanosheet growth was seen as reported previously.[20] By contrast, on the va-CNTs growth of $MoS_2$ HNPs was noticed. An equilibrium morphology of 2H-$MoS_2$ has a triangular shape. However, other morphologies such as nanowires,[21] nanotubes,[22] nanoplates,[23] etc., by changing the growth parameter had been reported previously. In our studies, the CNT template seems to play an important role in the nucleation and growth of $MoS_2$ HNPs similar in the case of epitaxially grown $MoS_2$ on graphene substrates where hexagonal $MoS_2$ flakes have been reported.[24] Selective growth of $MoS_2$ HNP can be achieved by depositing Mo film on the patterned CNT by putting a mask to cover the bare-Si substrate sample. In further studies, the Si substrate with a mask on CNT free area (during Mo film deposition) was used for $MoS_2$ growth.

The Raman measurements revealed the growth of 2H-$MoS_2$ on va-CNTs (**Figure 2**).[25] In micro-Raman spectroscopy, a sample volume with an illuminated area of 0.6 µm can be investigated, which provides clear information on the overall composition of the material in the given volume (for 2–3 µm depth). In the low-energy region, the Raman spectrum of the $MoS_2$/CNT heterostructure exhibits the two most intense peaks at 376.8 and 402.4 $cm^{-1}$ corresponds to the $E^1_{2g}$ and $A_{1g}$ modes of 2H-$MoS_2$ (Figure 2). The presence of the sharp peaks indicates a high crystalline nature of the formed $MoS_2$ deposit. The intensity ratios for $E^1_{2g}$ and $A_{1g}$ peaks are ≈0.63 and ≈0.45 for the $MoS_2$ HNP and bulk $MoS_2$, respectively. The frequency difference between $E^1_{2g}$ and $A_{1g}$ modes can be used as a robust and convenient diagnostic of the number of $MoS_2$ layers.[26,27] The observed difference of 25.6 $cm^{-1}$ indicates that the $MoS_2$ HNPs consist of five or more $MoS_2$ layers. Additionally, the presence of Raman modes of first order at 1350 $cm^{-1}$ (D band) and 1580 $cm^{-1}$ (G band) and second order at 2780 $cm^{-1}$ (2D band) corresponding to crystalline multiwalled CNTs was observed.[19]

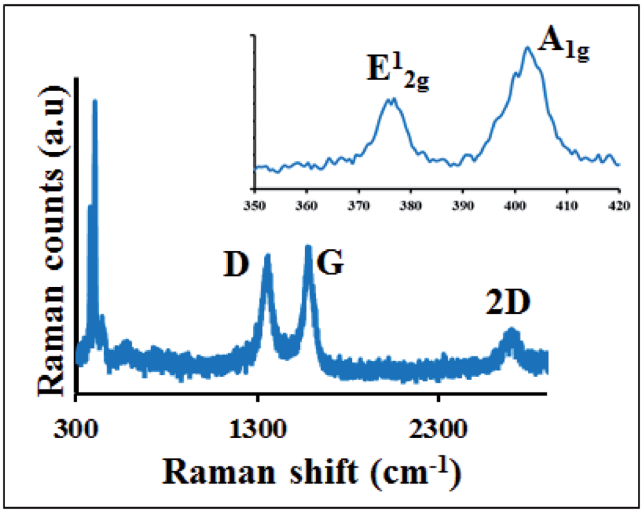


**Figure 2.** Raman spectra with zoom in over 350–420 $cm^{-1}$ in the inset for $MoS_2$/CNT sample synthesized by a 50 nm Mo film sulfurized at 850 °C with 420 mg of S powder for 60 min.

SEM results for samples of different Mo film thicknesses were treated while keeping the other growth parameters constant is presented in Figure S1 (Supporting Information). We found that the Mo film thickness significantly influences the size and density of HNPs. In the case of a 50 nm sulfurized-Mo-film HNP growth with higher density and higher substrate surface (va-CNT top-surface) coverage was observed as compared to that for 25 nm sulfurized-Mo film and 10 nm sulfurized-Mo-film samples. For 10 nm sulfurized-Mo-film sample, a growth of a few large (250 nm) size HNPs was observed. Additionally, the presence of a few tens of nm (10–30 nm) HNPs was observed for the same sample by low-resolution TEM imaging (Figure S2a, Supporting Information). It can be noted that the as-grown HNPs were produced only in a 1 h, as compared to the previously reported lengthy (≥27 h) and two-step method for growth of $MoS_2$ HNPs by calcination of $MoS_2$ nanosheets.[23]

Typical TEM observations of as-grown material are presented in **Figure 3**. The nanoplates with hexagonal shape (schematic in the inset of Figure 3a) in agreement with the SEM results (Figure 1c) can be observed from Figure 3a (also, Figure S2a, Supporting Information). The presence of multiwalled CNTs of 5–10 nm outer diameter can be easily noticed from Figure 3a and Figure S2. The relatively dark and thin objects in Figure 3a are standing HNPs. In Figure 3b, the high resolution scanning transmission electron microscopy (HR-STEM) image is taken on standing HNP, where the $MoS_2$ layers with exposed edges are separated by 0.63 nm. (In the inset the view-plane is highlighted by blue on the schematic of HNP.) The interlayer spacing is slightly higher than the *d*-spacing of the (002) planes of a hexagonal $MoS_2$ bulk lattice (0.62 nm). Figure 3c shows an HR-TEM image of the flat lying HNP. The HR-TEM image (Figure 3d) over the orange squared area in Figure 3c, indicates that the typical hexagonal pattern of $MoS_2$ is maintained without any defects in the grain. Moreover, the presence of bright hexagonal spots as it can be seen from the fast Fourier transform (FFT) pattern displayed in Figure 3e for the same area indicating good crystalline quality of the NSs. From the TEM imaging analysis, it can be seen that each $MoS_2$ HNP bearing eight surfaces consists of abundant exposed edges. Such a material with the huge active surface is particularly highly interesting for catalysis and sensing applications.

We have investigated the pristine CNTs and $MoS_2$/CNT samples using angular-resolved near-edge X-ray absorption fine structure (NEXAFS). **Figure 4** shows the C K-edge spectra of the 10 nm Mo film on CNT sulfurized sample. The angle between the incident photon beam and the sample surface plane was changed between 20° and 90°. The analysis of the angular-dependent C K-edge NEXAFS spectra reveals a reasonable degree of order with an orientation parameter close to that of the pristine CNTs (refer to Figure S3, Supporting Information). The data indicate that the vertical alignment of the CNT is preserved even after the $MoS_2$ formation on top of them.

Additionally, the $MoS_2$/CNT hybrid samples chemical composition was analyzed by using X-ray photoelectron spectroscopy (XPS). **Figure 5**a shows the C 1s spectra taken for the pristine CNT sample and for the $MoS_2$/CNT sample with

 

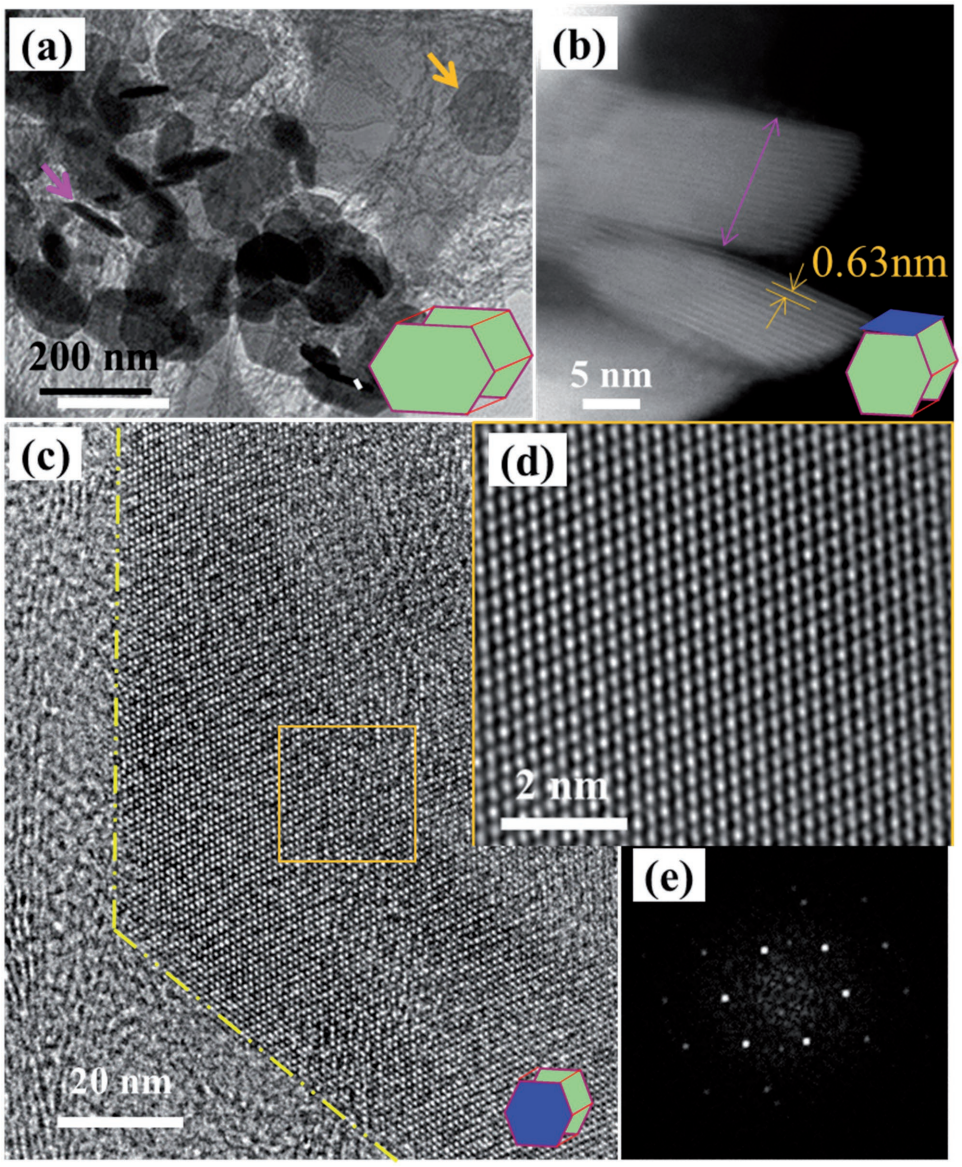


**Figure 3.** $MoS_2$/CNT sample synthesized by a 50 nm Mo film sulfurized at 850 °C with 420 mg of S powder for 60 min. a) Low-resolution TEM image of HNPs and CNTs on Cu grid with a schematic of HNP shape in the inset. The standing and flat HNPs are marked with magenta and orange arrows, respectively. b) HR-STEM image of $MoS_2$ HNP along the edge (view-plane highlighted by blue, on the schematic of HNP in the inset). The typical thickness of 11.3 with (18 $MoS_2$ layers) nm of the HNPs marked by a magenta arrow. c) HR-TEM images of flat HNP corner (view-plane highlighted by blue on the schematic of HNP in the inset) and its border marked by a yellow line. d) HR-TEM image for the area marked with an orange square in panel (c). e) FFT patterns for the orange squared area marked in panel (c).

25 nm initial Mo film thickness. Both spectra are characterized by a single peak structure, implying that chemical environment of carbon atoms was not dramatically changed upon CNT functionalization. However, lower binding energy shift of 0.1 eV of the hybrid sample spectrum as compared to the pristine CNT implies p-doping of CNTs by $MoS_2$. In Figure 5b,c, the core level spectra of Mo 3d and S 2s and S 2p are presented for samples with of 10, 25, and 50 nm initial Mo thickness (see Figure S4 of the Supporting Information for data fitting analysis). Since we have not observed Mo oxide and polysulfide ($S_n^{2-}$ and $S^{4+}$) species in the case of $MoS_2$/CNT with 50 nm initial Mo film, these samples were used for the gas-sensing studies.

### 2.2. Gas-Sensing Results

Successive detection and recovery cycles to increasing concentrations of $NO_2$ and to $NH_3$ for an $MoS_2$/CNT sample are shown in **Figure 6**a,b, respectively. While detection is performed at room temperature, the two-step recovery process (see the Experimental Section), including heating at 100 °C, is needed for fully restoring the baseline resistance during the cleaning phase (Figure S5a, Supporting Information). This is clearly visible for $NO_2$ in Figure 6a. The heating step was not applied during $NH_3$ detection (Figure 6b), which resulted in a lack of baseline recovery after the detection cycles. In agreement with

 

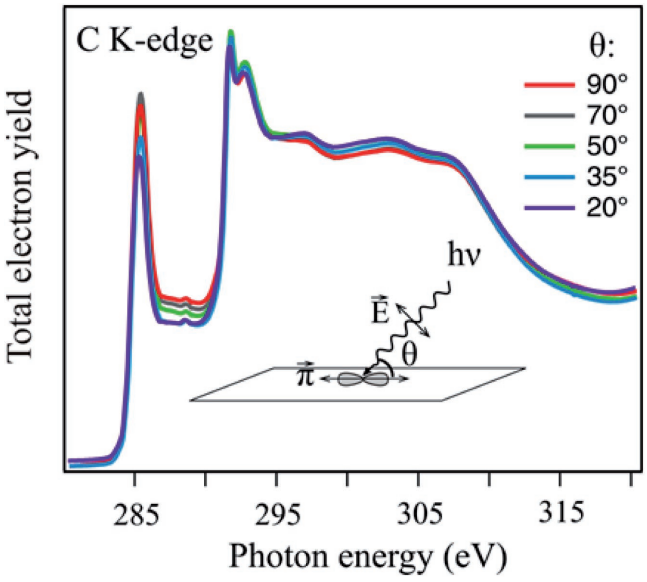


**Figure 4.** C K-edge NEXAFS spectrum of the $MoS_2$/CNT hybrid (for 10 nm Mo film on CNT and sulfurized) taken at different angles of incidence. Experimental geometry is shown in the inset.

previous experimental findings,[7] $MoS_2$–CNT hybrids are also more sensitive to $NO_2$ than to $NH_3$ (Figure 6c), which may be attributed to the different binding energies and charge transfers of the molecules to $MoS_2$.[9,10] The sensitivity to $NO_2$ (slope of the calibration curve shown in Figure 6d) is $0.192\% \times ppm^{-1}$ in the range from 25 to 100 ppm. The response of the hybrid nanomaterial to lower $NO_2$ concentrations was also investigated. **Figure 7** shows the responses to 25 and 100 ppb. In this range, the sensitivity is $0.023\% \times ppb^{-1}$. Considering the noise levels, present in the signals (about 1 mΩ) shown in Figure 7 and assuming a signal-to-noise ratio of 3 as required to be properly distinguished a response from the noise, the limit of detection for $NO_2$ can be estimated to be near 2 ppb.

The $MoS_2$/CNT system performance for $NO_2$ sensing was also tested in humidity conditions (Figure S6, Supporting Information). In the presence of humidity, the response toward 50 ppm of $NO_2$ significantly increases. It raises from 12.6% under dry conditions to 21% at 30% relative humidity (RH) at 20 °C (Figure S6, Supporting Information). The response further increases to 22.2% when the moisture level reaches 50% RH (20 °C). The change from dry conditions to a moderate humidity level (i.e., 30%) results in a very significant increase in response (1.7-fold). A further increase in humidity level (e.g., from 30% to 50%) yields a smaller additional increase of the response to $NO_2$ (1.05-fold). Because water vapor is an electron acceptor like $NO_2$, the further increase of the response for $NO_2$ at higher RH values can be qualitatively understood.

A comparison between the responses toward 100 ppm of $NO_2$ for $MoS_2$/CNT hybrids and pristine va-CNTs operated at room temperature is shown in Figure S6d (Supporting Information). $MoS_2$/CNTs show higher response and better baseline recovery properties than pristine va-CNTs. It is in agreement with previously reported results of better performance of $MoS_2$ over carbon-based materials when used as a chemical sensor.[28,29] Additionally, the performance of $MoS_2$/CNTs is superior to that of pristine va-CNTs in humidity conditions (Figure S6e, Supporting Information), where the response slightly decreases in the presence of humidity (Figure S6e, Supporting Information). It can be derived that the $MoS_2$/CNT system is more suitable for detecting $NO_2$ under real conditions in which ambient humidity is present. It should be noted that the conductive measurements were performed with top contacts (Ag) where the $MoS_2$ HNPs are situated (Figure S5b,c, Supporting Information). This top contact geometry (Figure 9) implies that a significant part of the current measured between the contacts actually flows through the $MoS_2$ HNP layer. However, the response to $NO_2$ can be attributed to the hybrid $MoS_2$ HNPs-CNT film because; (1) the CNTs act as a support to $MoS_2$ HNPs and, (2) increases the accessibility of $NO_2$ molecules to reach the exposed edges of $MoS_2$ HNPs where they adsorb. To the best of our knowledge, a successful detection of 25 ppb of $NO_2$ employing $MoS_2$ has never been reported previously. The $MoS_2$/CNT hybrid material exhibits a much larger detection range as compared to the previously reported sensor

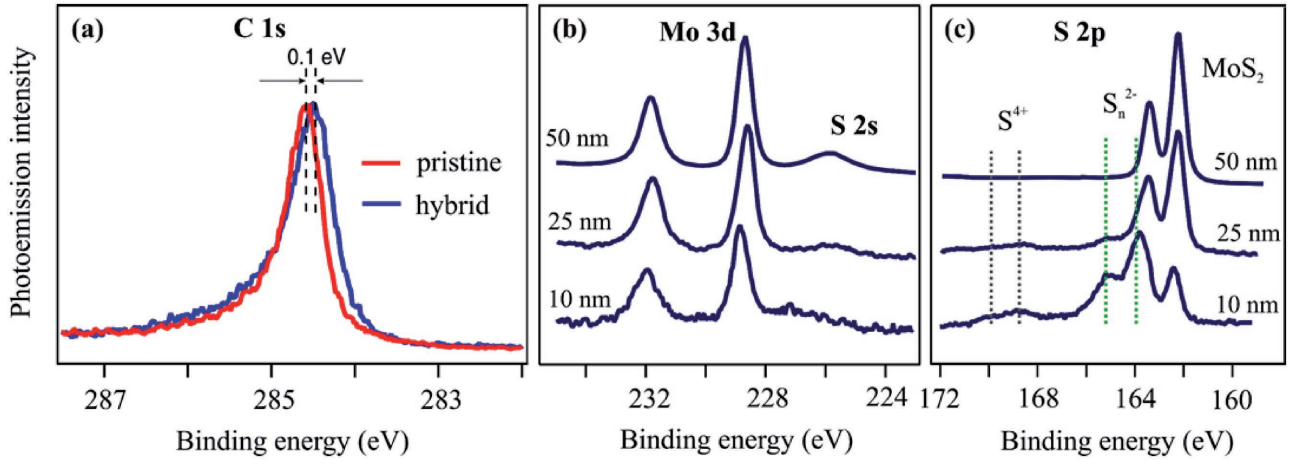


**Figure 5.** XPS spectra: Binding energy (eV) versus photoemission intensity (arbitrary unit) plots for the $MoS_2$/CNT samples. a) The C1s core level spectra for pristine CNT sample and for 25 nm Mo film on CNT sulfurized sample. b,c) The core level spectra for Mo 3d, S 2p from three samples with initial Mo film thickness 10, 50, and 300 nm on CNT sulfurized.

 

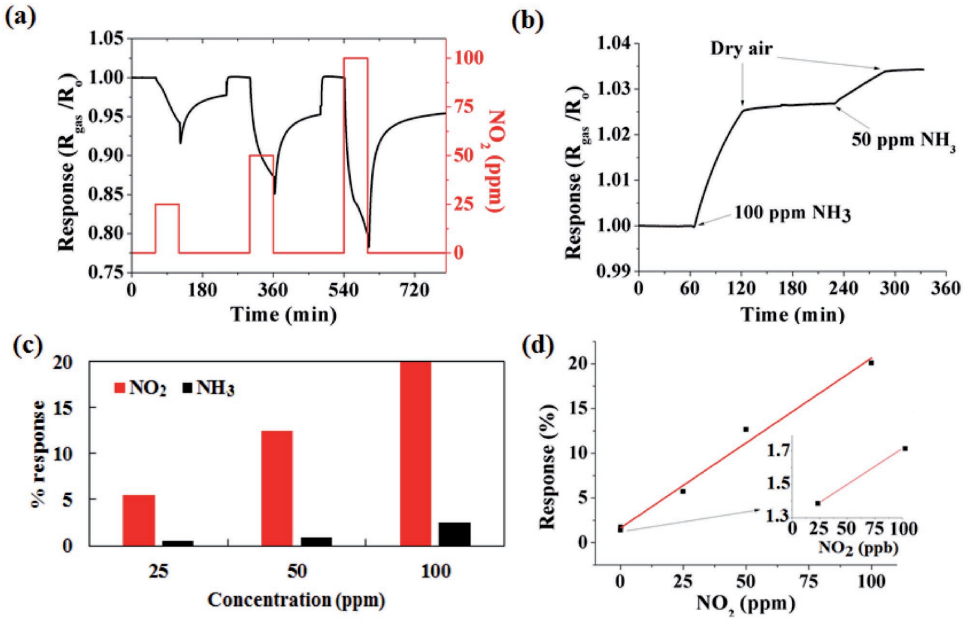


**Figure 6.** a) The $MoS_2$/CNT sensor response as a function of three nitrogen dioxide concentrations (25, 50, and 100 ppm) when operated at room temperature. Mild heating at 100 °C is applied at the beginning of the recovery phase to accelerate this process. b) Resistance change of $MoS_2$/CNT sensor when exposed to $NH_3$ vapors at 100 and 50 ppm. c) Comparison of the responsiveness toward $NO_2$ and $NH_3$ at 25, 50, and 100 ppm. d) Calibration curve for the response toward $NO_2$ the inset shows an enlargement of the low concentration area of the curve.

results for $MoS_2$ or carbon-based semiconducting materials (monolayer,[7] multilayer,[30] or vertically aligned[3] $MoS_2$ (0.3 to 0.8 ppm and 0.1 to 100 ppm, respectively), pristine and/or functionalized va-CNT (0.5 ppm),[31] and $MoS_2$ and graphene hybrid (50 ppb).[32] The most common gas-sensing principle relies on the adsorption and desorption of gas molecules on sensing materials. Therefore, it is quite understandable that by increasing the contact interfaces between the analysts and sensing materials, the sensitivity can be significantly enhanced. The extremely high surface-to-volume ratio and hollow structure of nanomaterials like our $MoS_2$/CNT hybrid system are ideal for the adsorption of gas molecules.

To reveal the $NO_2$ gas-sensing properties of our device DFT calculations were performed (see the Experimental Section). Since the pristine va-CNT system has lower sensitivity[31] (Figure S6, Supporting Information) compared to our $MoS_2$/CNT system and considering the gas-sensing measurement geometry (Figure 9) we focus on the effect of the $MoS_2$ HNPs with exposed edges (Figure 3b), which might play a dominant role in the sensing mechanism. For modeling the $MoS_2$ HNPs edge sites, we applied a $MoS_2$ multilayer ribbon geometry having an infinite length in the $x$ and $z$ directions by using periodic boundary conditions and finite width of six Mo atoms in the $y$ direction (**Figure 8**). Since the $MoS_2$ HNPs are much larger (200–300 nm) in the $y$ direction, we performed convergence test with respect to the ribbon width. We found that six Mo atoms width in the $y$ direction is sufficiently large to obtain converged values of the $NO_2$ adsorption energy. The experimentally observed 2H stacking of the $MoS_2$ causes that the edge type of the multilayer ribbon alternate in the $z$-direction between the so-called Mo edge and S edge on each side (Figure 8). In our calculations Mo edges are saturated with S dimers according to experimental and theoretical findings.[33,34] As a first step, we investigated the electronic properties of the system without

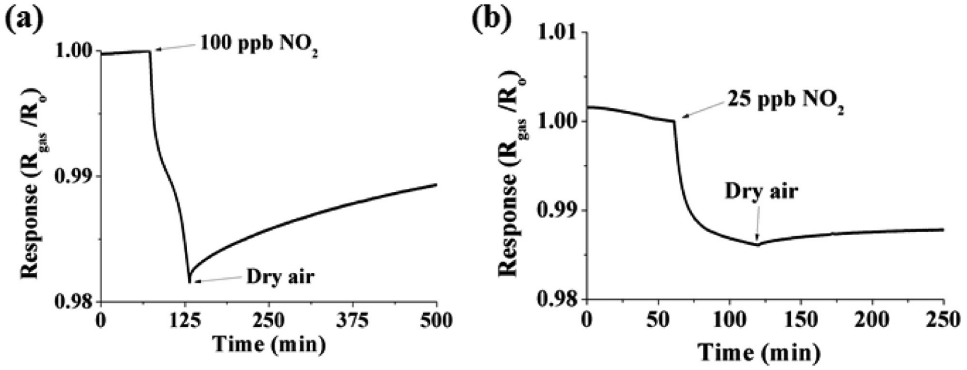


**Figure 7.** Responses at room temperature of $NO_2$ of $MoS_2$/CNT sensor. a) 100 ppb and b) 25 ppb.

 

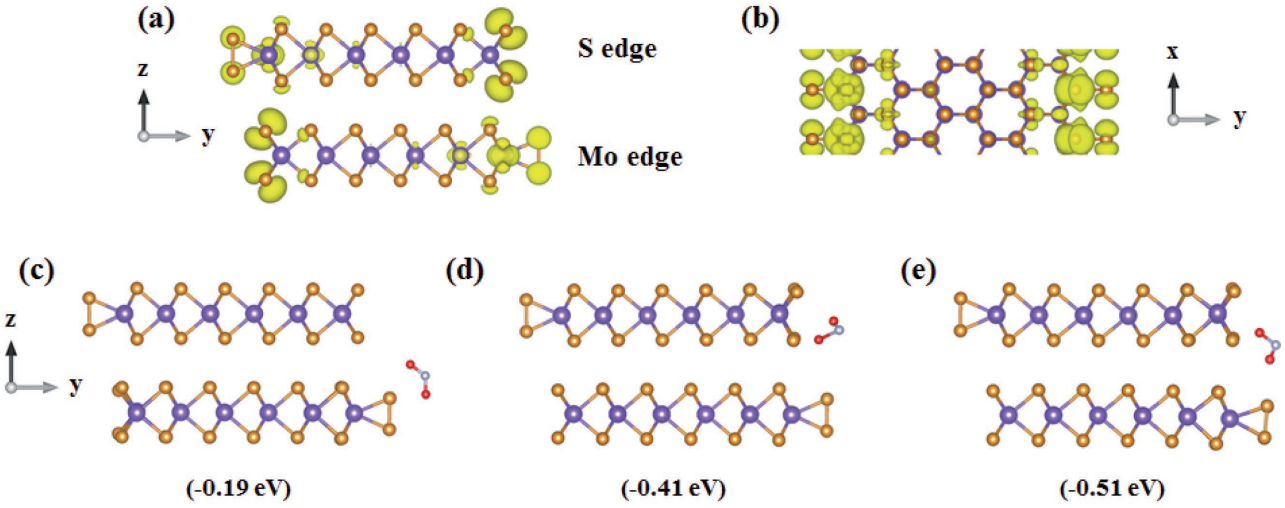


**Figure 8.** a–b) Charge density plots around the Fermi-level of the modeled $MoS_2$ HNP unit cell. The isovalue is set to be $10^{-3}e$ Å$^{-3}$ in both the *zy* and the *xy* planes. The metallic edge states localized at the Mo edges and S edges is clearly seen. c–e) Side views (*zy*) of the most favorable adsorption configurations for $NO_2$ at the edges. The low adsorption energy at the Mo edge (c) compared to the S edge configurations (d) and (e) is originated from the S dimer passivation of the Mo edge. Purple, red, orange, and white spheres represent molybdenum, oxygen, sulfur, and nitrogen, respectively.

gas molecules. Figure 8a,b shows the charge density distribution near the Fermi level where charge localization can be seen along the edges. These unusual metallic edge states were predicted earlier in $MoS_2$[33] and also measured both in single-layer[33] and multilayer[35] $MoS_2$ samples by using scanning tunneling microscopy. Because the states in the inner part of the multilayer ribbon are essentially bulk-like with a finite band gap, we assume that the current mainly flows around the edges in the *x*,*y*- and *z*-directions for our $MoS_2$ HNPs.[33] We have experimentally observed relatively low sensor resistance (a few Ohms for $MoS_2$/CNT while a few hundreds of Ohms for pristine CNT samples), for a semiconductor $MoS_2$ material supports these arguments. Next, we computed the adsorption energies of the $NO_2$ molecule at the different edges (Mo edge and S edge). The relaxed geometries with one Mo edge and two S edge configurations are shown in Figure 8b–d. In the S edge case, we investigated two geometries where the $NO_2$ is situated in the *xy* (Figure 8c) and the *yz* (Figure 8d) plane. In the latter case, the interaction between the underlying $MoS_2$ layers is more significant. The adsorption energies of the different positions of the $NO_2$ gas molecule were evaluated using $E_a = E_{(MoS_2-NO_2)} - \left[E_{(MoS_2)} + E_{(NO_2)}\right]$, where $E_{(MoS_2-NO_2)}$ is the total energy of the optimized structure of $NO_2$ adsorbed on $MoS_2$, $E_{(MoS_2)}$ is the total energy of the pristine $MoS_2$, and $E_{(NO_2)}$ is the energy of the isolated gas molecule. In the Mo edge and two S edge configurations, the adsorption energies are –0.19, –0.41, and –0.51 eV, respectively. For comparison, we also calculated the adsorption energy when $NO_2$ is adsorbed onto the surface (basal plane) of a multilayer $MoS_2$ sample, which was found –0.13 eV similar to the case of the monolayer $MoS_2$.[10] We note that this tendency of the adsorption energies of $NO_2$ where the molecule adsorbed more likely at the edges, especially the S edge, was previously reported for monolayer $MoS_2$ edge calculations.[3] The moderate values of the adsorption

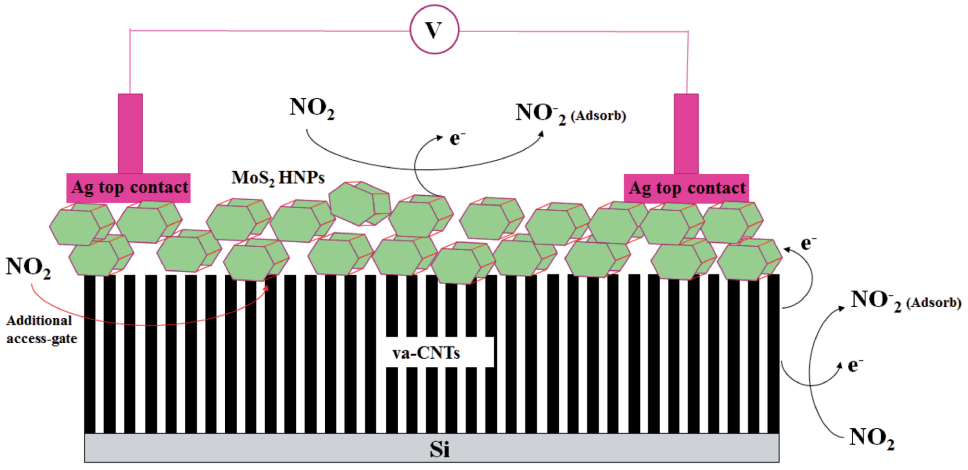


**Figure 9.** Pathways for gas-sensing mechanism. $NO_2$ adsorb on the edges of $MoS_2$ HNPs and the outer wall of CNTs increasing the p-doping of the hybrid film and lowering its resistance.

 

energies can be considered as physisorption rather than chemisorption, especially in the case of the saturated Mo edge.[4] Our experimental findings where the complete baseline recovery was achieved after just 100 °C annealing (Figure 6a) are in qualitative agreement with the DFT results. Finally, Bader analysis[36] is performed to predict the charge transfer between the $MoS_2$ and $NO_2$. It is found that in all geometries $NO_2$ behaves as an electron acceptor and the values of the charge transfer are 0.18*e*, 0.59*e*, and 0.48*e* for the different attachments. These values are larger compared to the case when $NO_2$ adsorbed on the basal plane (0.1*e*)[7,9] highlighting the increased p-doping when $NO_2$ adsorbed on the edges. Therefore, our DFT calculations revealed that the $NO_2$ molecules are not only likely to be adsorbed onto the edges of $MoS_2$ HNPs, but also increase the p-doping compared to the case of the $MoS_2$ basal plane adsorption. Because in our measurements, the gas sensing is based on the resistivity of the sample, the increased p-doping at the edges of the $MoS_2$ HNPs, where the current flows, explains the enhanced sensitivity of our $MoS_2$/CNT hybrid material.

### 2.3. Gas-Sensing Mechanism

It is well-known that $NO_2$ acts as an electron acceptor while $NH_3$ acts as an electron donor in the case of $MoS_2$ and CNT.[37] Our results show a clearly enhanced response of the $MoS_2$/CNT system to both $NO_2$ and $NH_3$ in which the resistance of the device decreases with $NO_2$ adsorption and increases with the adsorption of $NH_3$. Single-layer $MoS_2$ samples behave usually as n-type semiconductors.[38,39] However, the n-type or p-type character of $MoS_2$ depends on its morphology, the nanostructure alignment on the substrate.[3] It has been also reported,[40] that n-type and p-type regions can coexist on the same substrate. Furthermore, vertically aligned $MoS_2$ layers with exposed edges (a similar morphology as the one reported here) have been found to behave as p-type.[3] Also, $MoS_2$ thin films grown on graphene show p-type behavior.[15] Based on this, we consider our $MoS_2$/CNT hybrid structure as a p-type semiconductor material similar as previously reported for $MoS_2$/graphene hybrid systems[15,32] and in agreement with our experimental findings.

The mechanism of gas sensing in $MoS_2$/CNT is twofold (**Figure 9**). $NO_2$ molecules can adsorb on the edges and on the surface of $MoS_2$ HNPs where electronic charge transfer occurs from the $MoS_2$ HNP toward the molecule. This mechanism creates an accumulation region of holes and a consequent resistance decrease in the hybrid film. In Figure 6a slow and fast response (recovery) can be seen, which might correspond to the adsorption on the edge sites and on the surface, respectively.[28] According to the response signal, we suppose that the edges play a major role, however surface adsorption also helps to achieve the outstanding sensitivity. Additionally, $NO_2$ molecules can also interact and adsorb onto the CNT outer wall resulting in further increasing the p-doping of the hybrid film.[37,41] This translates again in the $MoS_2$/CNT hybrid film lowering its resistance. Nevertheless, future study to understand the detailed adsorption mechanism(s) is necessary.

A way often employed for ameliorating CNT gas sensors performance consists of functionalizing CNTs with metal clusters.[6,31,42] It is well known that CNTs decorated with gold nanoparticles improve their response toward $NO_2$.[31] The CNTs decoration with Au nanoparticles results in the p-doping of CNT films showing a response of 2% to 500 ppb of $NO_2$.[41] As discussed above, similarly to the Au functionalization yet achieving a significantly higher response, the $MoS_2$ layer on top of va-CNTs has also a strong p-doping effect on the hybrid CNT film (e.g., the response is 1.4% to a much lower $NO_2$ concentration of 25 ppb).

According to the theoretical and experimental findings, both the $MoS_2$ HNPs with exposed edges and the va-CNT layer play an important role in the observed sensitivity. Since the $MoS_2$ HNPs are on top of the va-CNT forest, the accessibility for the gas molecules to the exposed HNP edges is significantly increased (Figure 9). In our $MoS_2$/CNT hybrid material, $NO_2$ molecules can attach to the $MoS_2$ edges from all directions compared to the case where the sensing material ($MoS_2$) is grown on a flat substrate. In addition, the va-CNTs not only act as a support for the $MoS_2$ HNPs, but they are also sensitive to adsorption of gas molecules. Therefore, the enhanced $NO_2$ sensitivity of our device over pristine CNTs is assigned to the $MoS_2$/CNT hybrid system.

## 3. Conclusions

Abundant $MoS_2$ HNPs were grown on the va-CNT template layer by using a simple CVD technique. The CNT template layer plays an important role in the growth of hexagonal $MoS_2$. The high quality and crystallinity $MoS_2$ of HNPs were confirmed by using Raman, XPS, NEXAFS, and TEM characterization techniques. The HNPs with a thickness about 20 nm and a length of several hundreds of nanometers with highly exposed edges were produced by controlling the initial Mo film thickness. The $MoS_2$/CNT shows an enhanced room temperature gas-sensing performance as compared to monolayer $MoS_2$ or pristine CNTs. It also shows gas-sensing properties to both low and high (a few ppb to a few hundreds of ppm) concentrations of $NO_2$. Mild heating is necessary for desorbing $NO_2$ from the surface and completely recovering baseline resistance in a few minutes. The excellent $NO_2$ sensing response of the $MoS_2$/CNT hybrid system comes from the large affinity of $NO_2$ for $MoS_2$ HNPs edges and the more significant charge transfer at the edges, as revealed by DFT calculations. For gas-sensing application, it provides an enhanced surface area for the gas-adsorption and additional access-gate for the $NO_2$ to reach the HNPs provided by the underneath CNT forest. The current result could be beneficial for future gas-sensing studies to improve further the response and detection limit.

## 4. Experimental Section

*Material Growth*: A two-step strategy: (1) growth of va-CNTs and (2) sulfurization of Mo film deposited on it was used to produce $MoS_2$ HNPs on CNT ($MoS_2$/CNT) hybrid material. The growth of va-CNTs (with a typical height of 350 µm) on an Si substrate (with 10 nm Fe catalyst layer on it) was carried out as explained in detail elsewhere.[31] The as-synthesized va-CNTs[31] were used as a template substrate for hexagonal $MoS_2$ nanoplates growth. A sputter-coated Mo film

 

(10–50 nm) deposited using Quorum system on the CNT samples was used as a starting material. The S powder (99.5%), purchased from Alfa Aesar was used without any further purification. The Mo film samples were set downstream to the Ar (purity 99.9995%) flow at a distance of about 2 cm from the S source. The quartz tube was first flushed for 1 h to remove oxygen using a 0.725 L $min^{-1}$ Ar flow. Subsequently, the Mo/CNT samples were subjected to double sulfurization at 850 °C for 30 min each, under constant Ar flow (0.725 L $min^{-1}$) at atmospheric pressure. Afterward, the furnace was cooled down naturally to room temperature. The HNP growth parameters such as substrate temperature (850 °C), Ar gas flow (0.725 L $min^{-1}$), S powder quantity (210 mg for each sulfurization), and synthesis duration (60 min) were adapted from the previously reported $MoS_2$ nanosheet growth technique.[20]

*Material Characterization Techniques*: The sulfurized Mo films on va-CNTs samples morphology was characterized using a field-emission scanning electron microscope Hitachi 2000 and FEI Helios NanoLab 650 were used. The structural characterization was performed by employing an aberration-corrected TEM (FEI Titan Low-Base), working at 200 kV equipped with a Cs probe corrector, a high angle annular dark field imaging detector for imaging and energy dispersive spectroscopy (EDS) spectrometer. The specimens for TEM observations were prepared by spreading a few drops of a solution (some material removed from the sample and dissolved in isopropyl alcohol) on a lacey-carbon-coated copper grid. Raman spectroscopy was performed using a Horiba micro-Raman confocal microscopic system (Lab-RAM) with 483 nm laser. NEXAFS and XPS measurements were performed using synchrotron radiation from Russian–German Beamline at BESSY II, Helmholtz-Zentrum Berlin, Germany. The C K-edge spectra were obtained using the sample drain current mode. Photoemission spectra were acquired with a hemispherical Phoibos 150 electron energy analyzer (SPECS GmbH) for high-energy-resolution photoemission experiments. XPS measurements were carried out in the normal emission geometry. All the measurements were carried out at room temperature. Photoemission spectra obtained were fitted using Gaussian–Lorentzian convolution functions with a simultaneous background optimization.

*Sensor Device Fabrication and Characterizations*: To fabricate the sensor device, the $MoS_2$/CNT hybrid samples were processed as follows. Two-wire contacts were made on the surface (on $MoS_2$ HNP) of samples by employing a silver paste (Ag component metallization, Heraeus) and Pt wires. Samples were glued with a thermally conductive epoxy to an alumina heating plate and wire-bonded to a printed circuit board (Figure S5b,c, Supporting Information), which can be connected inside a 35 mL test chamber (Figure S5d, Supporting Information). This chamber was connected to a fully automated, continuous flow measurement set-up in which reproducible concentrations of dry or humidified gas mixtures could be delivered by mass-flow controllers.

The $MoS_2$/CNT sensors were tested with different gases at room temperature (20 °C). In a typical measurement process, the total flow was adjusted to 100 mL $min^{-1}$. Initially, samples were in a dry air flow for 1 h to stabilize their baseline resistance. Then, the samples were exposed to a given concentration of $NO_2$ or $NH_3$ diluted in the air for 1 h (in Figure S5a of the Supporting Information, a table for typical sensing experimental conditions are provided), and the evolution of their room-temperature resistance was monitored employing an Agilent 34972A multimeter. These measurements were spanned for over one month without noticeable changes in response and sensitivity. Some of the sensing measurements were also repeated after keeping the sample in air for one month and reproducible results were observed. Calibrated gas cylinders in which either nitrogen dioxide (at 1 or 100 ppm) or ammonia (at 100 ppm) balanced in the dry synthetic air. During the ppb range measurements, one of these cylinders was connected to an automated gas dilution system that comprised a cylinder of a dry synthetic air and two mass-flow controllers. Employing this system, the original concentration in the calibrated cylinders could be further reduced by a factor of up to 50. For example, by adjusting the dilution factor to 40, one could deliver 25 ppb of $NO_2$ when the 1 ppm $NO_2$ bottle was used. Finally, the samples were cleaned in a dry air. In some cases, the process of cleaning comprised two steps. In the first step, the samples were heated to 100 °C for 2 h by using the heating plate. In the second step, the heating was switched off and samples were flown with dry air for 1 h at room temperature. After this cycle, the samples were ready for another measurement cycle.

For the effect of humidity measurements in gas sensing was investigated, the baseline resistance of the samples was stabilized at a given level of humidity (e.g., 30% RH at 20 °C). This humidity level was kept constant during the exposure to $NO_2$ or $NH_3$.

*Computational Details*: All calculations were performed in the framework of spin-polarized DFT theory by using the Vienna ab initio simulation package.[43] Exchange–correlation effects were taken into account in the framework of the generalized gradient approximation by the Perdew–Burke–Ernzerhof functional.[44] Projector augmented wave pseudopotentials[45] were used, and the kinetic energy cut-off for the plane wave expansion was 400 eV. The geometry of the atomic positions was relaxed using the conjugate-gradient method until the forces of the atoms were reduced to 0.02 eV $Å^{-1}$, and the Brillouin-zone was sampled using a $6 \times 1 \times 4$ Monkhorst–Pack mesh. Large vacuum distance in the y direction (i.e., more than 13 Å) was imposed in the model to avoid unwanted interactions between the edges. The dimensions of the rectangular supercell were 6.36, 30.2, and 12.4 Å in the *x*, *y*, and *z* direction, respectively.

## Supporting Information

Supporting Information is available from the Wiley Online Library or from the author.

## Acknowledgements

This research used resources of the Electron Microscopy facilities of Masdar Institute and University of Mons. This research leading to these results received funding in part from European Union Seventh Framework H2020 Program under Grant Agreement No. 696656 Graphene Flagship. J.-F.C. is Senior Research Associate of FRS-FNRS. R.A. gratefully acknowledges the support from the Spanish Ministerio de Economia y Competitividad (MAT2016-79776-P), from the Government of Aragon and the European Social Fund under the project "Construyendo Europa desde Aragon" 2014–2020 (Grant No. E/26), and from the European Union H2020 program ETN project "Enabling Excellence" Grant Agreement No. 642742. E.L. was supported by the Catalan Institution for Research and Advanced Studies via the ICREA Academia Award and MINECO-FEDER (grant no. TEC2015-71663-R) and J.C.-C. was supported by Universitat Rovira i Virgili via a Martí i Franquès predoctoral fellowship. This research used resources of the "Plateforme Technologique de Calcul Intensif (PTCI)," which was supported by the F.R.S.-FNRS under Convention No. 2.5020.11. This work was supported by the Helmholtz-Zentrum Berlin für Materialien und Energie within a bilateral Russian–German Laboratory program. A.A.M. acknowledges support from DFG, Grant No. LA655/13-2. D.V.V. acknowledges Saint Petersburg State University (SPbU) for research Grant No. 15.61.202.2015.

## Conflict of Interest

The authors declare no conflict of interest.

## Keywords

CNT, DFT calculations, gas sensor, $MoS_2$, nanoplates

Received: July 6, 2017
Revised: August 10, 2017
Published online:

 

[1] G. Korotcenkov, *Mater. Sci. Eng. B* **2007**, *139*, 1.
[2] T. Zhang, S. Mubeen, N. V. Myung, M. A. Deshusses, *Nanotechnology* **2008**, *19*, 332001.
[3] S. Y. Cho, S. J. Kim, Y. Lee, J. S. Kim, W. B. Jung, H. W. Yoo, J. Kim, H. T. Jung, *ACS Nano* **2015**, *9*, 9314.
[4] S. J. Ray, *Sens. Actuators, B* **2016**, *222*, 492.
[5] J. Kong, N. R. Franklin, C. Zhou, M. G. Chapline, S. Peng, K. Cho, H. Dai, *Science* **2000**, *287*, 622.
[6] P. Young, Y. Lu, R. Terrill, J. Li, *J. Nanosci. Nanotechnol.* **2005**, *5*, 1509.
[7] D. J. Late, Y. K. Huang, B. Liu, J. Acharya, S. N. Shirodkar, J. Luo, A. Yan, D. Charles, U. V. Waghmare, V. P. Dravid, C. N. Rao, *ACS Nano* **2013**, *7*, 4879.
[8] B. Cho, M. G. Hahm, M. Choi, J. Yoon, A. R. Kim, Y.-J. Lee, S.-G. Park, J.-D. Kwon, C. S. Kim, M. Song, Y. Jeong, K.-S. Nam, S. Lee, T. J. Yoo, C. G. Kang, B. H. Lee, H. C. Ko, P. M. Ajayan, D.-H. Kim, *Sci. Rep.* **2015**, *5*, 8052.
[9] Q. Yue, Z. Shao, S. Chang, J. Li, *Nanoscale Res. Lett.* **2013**, *8*, 425.
[10] S. Zhao, J. Xue, W. Kang, *Chem. Phys. Lett.* **2014**, *595*, 35.
[11] S. Tongay, J. Suh, C. Ataca, W. Fan, A. Luce, J. S. Kang, J. Liu, C. Ko, R. Raghunathanan, J. Zhou, F. Ogletree, J. Li, J. C. Grossman, J. Wu, *Sci. Rep.* **2013**, *3*, 2657.
[12] H. Nan, Z. Wang, W. Wang, Z. Liang, Y. Lu, Q. Chen, D. He, P. Tan, F. Miao, X. Wang, J. Wang, Z. Ni, *ACS Nano* **2014**, *8*, 5738.
[13] Y. H. Kim, K. Y. Kim, Y. R. Choi, Y.-S. Shim, J.-M. Jeon, J.-H. Lee, S. Y. Kim, S. Han, H. W. Jang, *J. Mater. Chem. A* **2016**, *4*, 6070.
[14] S. J. Ray, M. V. Kamalakar, R. Chowdhury, *J. Phys.: Condens. Matter* **2016**, *28*, 195302.
[15] Q. He, Z. Zeng, Z. Yin, H. Li, S. Wu, X. Huang, H. Zhang, *Small* **2012**, *8*, 2994.
[16] Y. Shi, H. Li, L. J. Li, *Chem. Soc. Rev.* **2014**, *44*, 2744.
[17] G. Deokar, D. Vignaud, R. Arenal, P. Louette, J. F. Colomer, *Nanotechnology* **2016**, *27*, 075604.
[18] H. Dong, C. Liu, H. Ye, L. Hu, B. Fugetsu, W. Dai, Y. Cao, X. Qi, H. Lu, X. Zhang, *Sci. Rep.* **2015**, *5*, 17542.
[19] H. Yoo, A. P. Tiwari, J. Lee, D. Kim, J. H. Park, H. Lee, *Nanoscale* **2015**, *7*, 3404.
[20] G. Deokar, N. S. Rajput, P. Vancso, F. Ravaux, M. Jouiad, D. Vignaud, F. Cecchet, J. F. Colomer, *Nanoscale* **2017**, *9*, 277.
[21] S. Han, C. Yuan, X. Luo, Y. Cao, T. Yu, Y. Yang, Q. Li, S. Ye, *RSC Adv.* **2015**, *5*, 68283.
[22] M. Remskar, A. Mrzel, Z. Skraba, A. Jesih, M. Ceh, J. Demsar, P. Stadelmann, F. Levy, D. Mihailovic, *Science* **2001**, *292*, 479.
[23] Z. Wu, D. Wang, X. Liang, A. Sun, *J. Cryst. Growth* **2010**, *312*, 1973.
[24] Y. Shi, W. Zhou, A.-Y. Lu, W. Fang, Y.-H. Lee, A. L. Hsu, S. M. Kim, K. K. Kim, H. Y. Yang, L.-J. Li, J.-C. Idrobo, J. Kong, *Nano Lett.* **2012**, *12*, 2784.
[25] L. Cai, J. He, Q. Liu, T. Yao, L. Chen, W. Yan, F. Hu, Y. Jiang, Y. Zhao, T. Hu, Z. Sun, S. Wei, *J. Am. Chem. Soc.* **2015**, *137*, 2622.
[26] G. Pagona, C. Bittencourt, R. Arenal, N. Tagmatarchis, *Chem. Commun.* **2015**, *51*, 12950.
[27] C. Lee, H. Yan, L. E. Brus, T. F. Heinz, J. Hone, S. Ryu, *ACS Nano* **2010**, *4*, 2695.
[28] A. L. Friedman, F. K. Perkins, A. T. Hanbicki, J. C. Culbertson, P. M. Campbell, *Nanoscale* **2016**, *8*, 11445.
[29] A. L. Friedman, F. Keith Perkins, E. Cobas, G. G. Jernigan, P. M. Campbell, A. T. Hanbicki, B. T. Jonker, *Solid-State Electron.* **2014**, *101*, 2.
[30] H. Long, L. Chan, A. Harley-Trochimczyk, L. E. Luna, Z. Tang, T. Shi, A. Zettl, C. Carraro, M. A. Worsley, R. Maboudian, *Adv. Mater. Interfaces* **2017**, *4*, 1700217.
[31] P. R. Mudimela, M. Scardamaglia, O. Gonzalez-Leon, N. Reckinger, R. Snyders, E. Llobet, C. Bittencourt, J. F. Colomer, *Beilstein J. Nanotechnol.* **2014**, *5*, 910.
[32] H. Long, A. Harley-Trochimczyk, T. Pham, Z. Tang, T. Shi, A. Zettl, C. Carraro, M. A. Worsley, R. Maboudian, *Adv. Funct. Mater.* **2016**, *26*, 5158.
[33] M. V. Bollinger, J. V. Lauritsen, K. W. Jacobsen, J. K. Norskov, S. Helveg, F. Besenbacher, *Phys. Rev. Lett.* **2001**, *87*, 196803.
[34] J. V. Lauritsen, J. Kibsgaard, S. Helveg, H. Topsoe, B. S. Clausen, E. Laegsgaard, F. Besenbacher, *Nat. Nanotechnol.* **2007**, *2*, 53.
[35] A. A. Koós, P. Vancsó, G. Z. Magda, Z. Osváth, K. Kertész, G. Dobrik, C. Hwang, L. Tapasztó, L. P. Biró, *Carbon* **2016**, *105*, 408.
[36] G. Henkelman, A. Arnaldsson, H. Jónsson, *Comput. Mater. Sci.* **2006**, *36*, 354.
[37] R. Ionescu, E. H. Espinosa, E. Sotter, E. Llobet, X. Vilanova, X. Correig, A. Felten, C. Bittencourt, G. V. Lier, J. C. Charlier, J. J. Pireaux, *Sens. Actuators, B* **2006**, *113*, 36.
[38] B. Radisavljevic, A. Radenovic, J. Brivio, V. Giacometti, A. Kis, *Nat. Nanotechnol.* **2011**, *6*, 147.
[39] K. S. Novoselov, D. Jiang, F. Schedin, T. J. Booth, V. V. Khotkevich, S. V. Morozov, A. K. Geim, *Proc. Natl. Acad. Sci. USA* **2005**, *102*, 10451.
[40] S. McDonnell, R. Addou, C. Buie, R. M. Wallace, C. L. Hinkle, *ACS Nano* **2014**, *8*, 2880.
[41] Z. Zanolli, R. Leghrib, A. Felten, J. J. Pireaux, E. Llobet, J. C. Charlier, *ACS Nano* **2011**, *5*, 4592.
[42] A. Star, V. Joshi, S. Skarupo, D. Thomas, J.-C. P. Gabriel, *J. Phys. Chem. B* **2006**, *110*, 21014.
[43] G. Kresse, J. Hafner, *Phys. Rev. B* **1994**, *49*, 14251.
[44] J. P. Perdew, K. Burke, M. Ernzerhof, *Phys. Rev. Lett.* **1996**, *77*, 3865.
[45] P. E. Blöchl, *Phys. Rev. B* **1994**, *50*, 17953.

 

# Chapter 3

## Graphene

*This chapter provides the articles related to graphene included in the thesis*

UNIVERSITAT ROVIRA I VIRGILI
GAS SENSING WITH MODIFIED CARBON NANOTUBES, GRAPHENE AND DIAMONDOIDS
Juan Casanova Cháfer

# Section 3.1

## Gas Sensing Properties of Perovskite Decorated Graphene at Room Temperature

Juan Casanova-Cháfer, Rocío García-Aboal, Pedro Atienzar, Eduard Llobet

*Sensors, 19 (2019) 4563*

DOI:10.3390/s19204563

UNIVERSITAT ROVIRA I VIRGILI
GAS SENSING WITH MODIFIED CARBON NANOTUBES, GRAPHENE AND DIAMONDOIDS
Juan Casanova Cháfer

sensors

MDPI

*Article*

# Gas Sensing Properties of Perovskite Decorated Graphene at Room Temperature

**Juan Casanova-Cháfer [1], Rocío García-Aboal [2], Pedro Atienzar [2,*] and Eduard Llobet [1,*]**

[1] MINOS-EMaS, Universitat Rovira i Virgili, 43007 Tarragona, Spain; juan.casanova@urv.cat
[2] Instituto de Tecnología Química, CSIC-UPV, Universitat Politècnica de València, 46022 Valencia, Spain; rogarab@itq.upv.es
* Correspondence: pedatcor@itq.upv.es (P.A.); eduard.llobet@urv.cat (E.L.); Tel.: +34-963-877-805 (P.A.); +34-997-558-502 (E.L.)

Received: 27 September 2019; Accepted: 18 October 2019; Published: 20 October 2019


**Abstract:** This paper explores the gas sensing properties of graphene nanolayers decorated with lead halide perovskite ($CH_3NH_3PbBr_3$) nanocrystals to detect toxic gases such as ammonia ($NH_3$) and nitrogen dioxide ($NO_2$). A chemical-sensitive semiconductor film based on graphene has been achieved, being decorated with $CH_3NH_3PbBr_3$ perovskite ($MAPbBr_3$) nanocrystals (NCs) synthesized, and characterized by several techniques, such as field emission scanning electron microscopy, transmission electron microscopy and X-ray photoelectron spectroscopy. Reversible responses were obtained towards $NO_2$ and $NH_3$ at room temperature, demonstrating an enhanced sensitivity when the graphene is decorated by $MAPbBr_3$ NCs. Furthermore, the effect of ambient moisture was extensively studied, showing that the use of perovskite NCs in gas sensors can become a promising alternative to other gas sensitive materials, due to the protective character of graphene, resulting from its high hydrophobicity. Besides, a gas sensing mechanism is proposed to understand the effects of $MAPbBr_3$ sensing properties.

**Keywords:** lead halide perovskite; graphene; gas sensing; $NO_2$ detection; $NH_3$ detection; room temperature sensor

## 1. Introduction

Atmospheric contamination is one of the most important environmental issues in current societies. According to the World Health Organization (WHO), air pollution is linked to 7 million premature deaths in 2012 [1]. The most common anthropogenic pollution sources are coming from industrial processes, automotive and energy production [2]. The gases emitted can produce an important greenhouse effect such as carbon dioxide ($CO_2$), methane ($CH_4$), and ozone ($O_3$), or can be dangerous for human health above very low levels of exposure. Nitrogen dioxide ($NO_2$) and ammonia ($NH_3$) are two examples of these harmful species. For these reasons, the in-field monitoring of harmful gases is a mandatory goal to control dangerous levels of contaminants. Above the threshold limits, when human health is at risk, gas sensors can be the last wall to start actions like reducing the access of cars to city centers, to mitigate the impact on the public health.

Among the different types of gas sensors, chemoresistive sensors have been attracting great interest due to their high sensitivity, low cost, reproducibility and simplicity [3]. Other techniques, like gas chromatography, electrochemical, and optical sensors, present some drawbacks, because they are more expensive, require trained personnel and still present some problems to miniaturize and export the measurement systems out of the laboratory [4,5]. However, chemoresistive sensors can be easily adapted to in-field measurements with low power consumption, especially when these sensors work at room temperature [6], reducing the complexity of the sensor driving circuitry. Nevertheless,

selectivity is still an unsolved issue, especially regarding metal oxides [7]. Some approaches used arrays of sensors to mitigate this problem, but usually this alternative is more expensive and increases the complexity of sensor design and data treatment [8].

Many authors have developed chemoresistive gas sensors employing graphene semiconductors, however the use of pristine graphene for developing gas sensors still presents many intrinsic problems, including low gas sensitivity and complicated processability into devices [9]. On the one hand, the pre-processing and exfoliation of pristine graphene is complicated, for that reason oxidizing treatments (that ease the suspension of the nanomaterial in aqueous solutions)are employed [10], which are sometimes followed by reducing treatments [11]. These have opened the possibility of developing graphene oxide or reduced graphene oxide-based sensors, respectively. On the other hand, the interaction of gas molecules with pristine graphene is characterized by low adsorption energies and small charge transfer, especially when pristine graphene is operated at room temperature [12]. In consequence, different strategies have been developed, such as decorating graphene with metal or metal oxide nanoparticles [13,14] creating hybrid nanomaterials employing graphene and polymers [15] or via grafting organic molecules [16]. These modifications of graphene have been shown as good options to improve some sensing properties of graphene such as gas sensitivity, selectivity or response and recovery times.

Unlike metal oxides based sensors, which usually require high working temperatures to activate the oxidation-reduction processes and achieve the required electron mobility involved in gas sensing [17], graphene has been proved as a great option to develop room temperature based sensors [18], thanks to its extraordinary high carrier density and mobility even in the absence of heating [19]. This characteristic makes graphene an ideal candidate to be loaded with perovskite nanocrystals, another promising nanomaterial with exceptional properties such as large absorption coefficient, long carrier lifetime and high carrier mobility [20,21]. Perovskites require low operating temperatures to avoid degradation [22]. Some works reported the use of perovskite films as gas sensors [23,24], showing interesting results in the detection of $NH_3$ [25], acetone [26], oxygen [27], and $NO_2$ [28]. However, there are still some issues related to their fast degradation, high humidity, cross-sensitivity, and moderate gas sensitivity obtained [25].

Recently, graphene was successfully implemented in perovskite solar cells, improving these devices due to the high conductivity, enhanced charge carrier mobility and material stability conferred by graphene in electronic devices [29]. The stability is the main drawback of organolead perovskites due to their high sensitivity to atmospheric conditions. For instance, $CH_3NH_3PbI_3$ ($MAPbI_3$) usually shows a fast degradation, in most cases attributed to their hygroscopic properties [30], which result in the formation of their hydrates. This degradation is partially reversible upon removal of humidity [31]. However, the hydrophobic properties of graphene-based devices should mitigate one of the main problems using perovskites, which is the degradation in humid atmospheres [32]. In this paper, we evaluate, for the first time, the improvements in gas sensing performance achieved by decorating graphene with perovskites, showing high potential of the resulting hybrid nanomaterial for enhancing the sensitivity and selectivity to pollutant gases, and for blocking the perovskite degradation under the presence of ambient moisture. Here we employ a bromide perovskite ($MAPbBr_3$), which has been proved to be more resilient to the presence of ambient moisture [33]. Then, this work tries to open a new approach to employ perovskite gas sensorss in real applications by enhancing the $MAPbBr_3$ stability and increasing the sensor time-life, via limiting perovskite degradation. Moreover, the nanocomposite was characterized by several techniques, such as X-Ray photoelectron spectroscopy (XPS), high-resolution transmission electron microscopy (HRTEM), Field Emission Scanning Electron Microscope (FESEM), and Raman spectroscopy. In consequence, this paper shows the results with graphene decorated by $MAPbBr_3$ NCs, registering higher sensitivities and detecting lower concentrations than other gas sensors based on perovskite thin films or similar approaches (see Table 1).

**Table 1.** Comparison of the sensitivity for different chemoresistive sensors that employ perovskites. NT = not tested. $NO_2$ and $NH_3$ sensitivities expressed as $10^{-3}$% $ppb^{-1}$ and $10^{-3}$% $ppm^{-1}$, respectively. Relative humidity (R.H.) effect expressed as the variation of the sensitivity. Degradation information about the stability of the perovskite during a few days or weeks. EDPIC = ethylenediamine lead iodide chloride.

| | $NO_2$ | $NH_3$ | R.H. Effect | Degradation | Ref |
|---|---|---|---|---|---|
| **Graphene- $MAPbBr_3$ NCs** | 14.5 | 3.8 | ↓ 5% | No | This work |
| **$MAPbI_3$ film- $SCN^-$ ions** | 0.53 | 3.9 | ↓ 11% | No | [26] |
| **$MAPbBr_3$ film** | 0.13 | NT | NT | Yes | [28] |
| **NCNT- $MAPbBr_3$** | 0.88 | NT | NT | NT | [34] |
| **$MAPbI_3$ film** | 0.62 | 11 | ↓ 16% | NT | [35] |
| **EDPIC *** | NT | 4.3 | NT | NT | [36] |

Threshold limit values (TLV) to 1-h exposure to $NO_2$ are established at 200 ppb and 100 ppb, by the European Union [37] and the Environmental Protection Agency of the US [38], respectively. Furthermore, the average yearly limit mean for $NO_2$ exposure is set at 40 ppb in the EU and at 53 ppb in the US. Maximum exposure values for $NH_3$ are defined as the ST (short-term) and TWA (Time-Weighted Average) by the European Agency for Safety and Health at Work (EU-OSHA) [39] and by the National Institute for Occupational Safety and Health (NIOSH) in the US [40]. These data are summarized in Table 2. TWA means the average exposure of 8 h/day and ST is referred to short exposures of 15 min. Both institutions define similar ST and TWA values for $NH_3$ limits. Thus, the development of sensor networks able to detect these trace concentration levels in a wide range of locations would be highly advisable. In consequence, sensors should offer reversible interaction with gas molecules for allowing the continuous monitoring of these species at an affordable cost.

**Table 2.** TLV for $NO_2$ and $NH_3$ exposure correlated with their averaging time. ST = short-time. TWA = Time-Weighted Average).

| | Averaging Time | European Union | United States |
|---|---|---|---|
| **$NO_2$** | 1 h | 200 ppb | 100 ppb |
| | 1 year | 40 ppb | 53 ppb |
| **$NH_3$** | ST | 50 ppm | 35 ppm |
| | TWA | 20 ppm | 25 ppm |

## 2. Materials and Methods

### *2.1. Perovskite Synthesis and Graphene Preparation*

To synthesize lead halide perovskite ($MAPbBr_3$) nanocrystals, the method proposed by Schmidt, et al. [41] was followed, in which a 2 mL solution of 1-octadecene (ODE) was prepared and 85 mg of oleic acid (OLA) were added. Then, the solution was stirred and heated up to 80 °C in a hotplate and 33.5 mg of octylammonium bromide (OABr) were added. Continuously, both, a solution of methyl-ammonium bromide (MABr) in dimethylformamide (DMF) and another with lead (II) bromide ($PbBr_2$) were mixed in the same solvent. Subsequently, these two solutions were added to the main solution and was cooled to 60 °C. Finally, 5 mL of acetone was added to the final solution to create precipitates of perovskite nanocrystals, which were separated from the unreactive solution by using a centrifugation technique at 6000 rpm during 10 min. Afterwards, the nanocrystals obtained were suspended in toluene.

A graphene solution was prepared using 1 mg of graphene nanoplatelets from Strem Chemicals, Inc. (USA) dispersed in 1 mL of toluene. Then, graphene nanoplatelets were sonicated employing a Sonic Tip (FisherbrandTM Model 705) at 40% of 700W for 1 h and 30 min using a 1 s on −2 s off pulsed sonication.

### *2.2. Material Characterization*

The exfoliated graphene and the lead halide perovskite were characterized by several techniques such as XPS, HRTEM, FESEM and Raman spectroscopy.

The chemical composition of the nanomaterials obtained was studied via XPS, using a SPECS spectrometer (Berlin, Germany) equipped with a Phoibos 150 MCD detector, using a non-monochromatic X-ray source (Al) operating at 200 W. The intensity ratios of the different components were calculated from the area peak after a correction by the transition function of the spectrometer and a non-linear Shirley-type background subtraction. Additionally, graphene crystallinity was evaluated employing a Raman spectrometer from Renishaw, plc. (Wotton-under-Edge, UK), coupled to a confocal Leica DM2500 microscope. The laser used had a wavelength of 514 nm.

The morphology was studied employing a JEOL JEM 2100F (Tokio, Japan) HRTEM, at an operating voltage of 200 kV. Nanomaterials were ultrasonically dispersed in toluene and a drop of dispersion was deposited onto a carbon-coated copper grid, drying it at room temperature. Graphene porosity and perovskites NCs distribution were analyzed by Carl Zeiss AG - ULTRA 55 (Oberkochen, Germany) Field Emission Scanning Electron Microscope.

### *2.3. Sensor Fabrication*

The materials obtained were deposited onto 1.5 $cm^2$ quartz substrates previously cleaned in an ultrasonic bath, using an anionic detergent (Alconox) and miliQ water. Afterwards, a 1M solution of hydrochloric acid was employed in order to increase the surface hydrophilicity. Finally, the substrates were cleaned and dried several times with ethanol. Then, a film of graphene nanoplatelets was deposited onto quartz substrates by drop casting method, and subsequently, perovskite nanocrystals (5% wt solution) were deposited by spin coating at 1000 rpm for 120 s.

Once the hybrid material film was deposited onto quartz substrate, its backside was glued with a thermally conducting epoxy from Heraeus, Inc. (Hanau, Germany) to an alumina hotplate that comprised a screen-printed platinum heater. Then, the samples were placed on a 20 × 30 mm printed circuit board (PCB) to be connected to an airtight test chamber. Finally, two-wire contacts were made on the sensor surface employing a conductive silver paste and platinum wires (a picture of a typical sensor is shown in the supporting information, see Figure S1).

### *2.4. Gas sensing Measurements*

The resistance changes under different gases and experimental conditions were monitored using an Agilent HP 34972A multimeter connected to the gas sensing chamber. Additionally, calibrated gas cylinders were employed to apply synthetic air (Air Premier Purity: 99,995%) and different dilutions of gases tested to achieve the target concentration. In order to reproduce real atmospheric conditions, $NO_2$ and $NH_3$ gases were balanced in synthetic air as well. The total flow was adjusted to 100 mL/min using a set of Bronkhorst High-Tech B.V. (Ruurlo, The Netherlands) mass-flows controllers. The sensors were stabilized under synthetic dry air for 60 min before the application of the desired gas concentration during 30 min of exposure. Besides, a controller evaporator mixer (CEM) from Bronkhorst High-Tech B.V. (Ruurlo, The Netherlands) was used to humidify the gas mixture and thus, analyze the effect of ambient moisture on the sensing properties (see Figure S2). The relative humidity level was monitored by using a SHT51 humidity sensor from Sensirion AG (Stäfa, Switzerland) placed in a 35 $cm^3$ airtight chamber. The ambient temperature inside the test chamber throughout the measurement process was 23 °C ± 1 °C.

## 3. Results

### *3.1. Material Characterization*

A high-resolution transmission electron microscopy (HR-TEM) analysis was conducted to characterize graphene and perovskite nanocrystals independently. Figure 1a shows graphene layers

with diameters near hundreds of nanometers. The interplanar distance obtained was 2.4 Angstrom (Figure 1b), showing a suitable graphene crystallinity. The perovskite synthesis method produces small nanocrystals, these lead halide perovskite nanocrystals to appear as dark spots (Figure 1c) with an average size of 7.1 ± 2.2 nm (see Figure S3 in the Supplementary Materials). Figure 1d shows the high crystallinity of the perovskites synthesized (Figure 2b), with a calculated interplanar distance of 2.8 Angstrom.

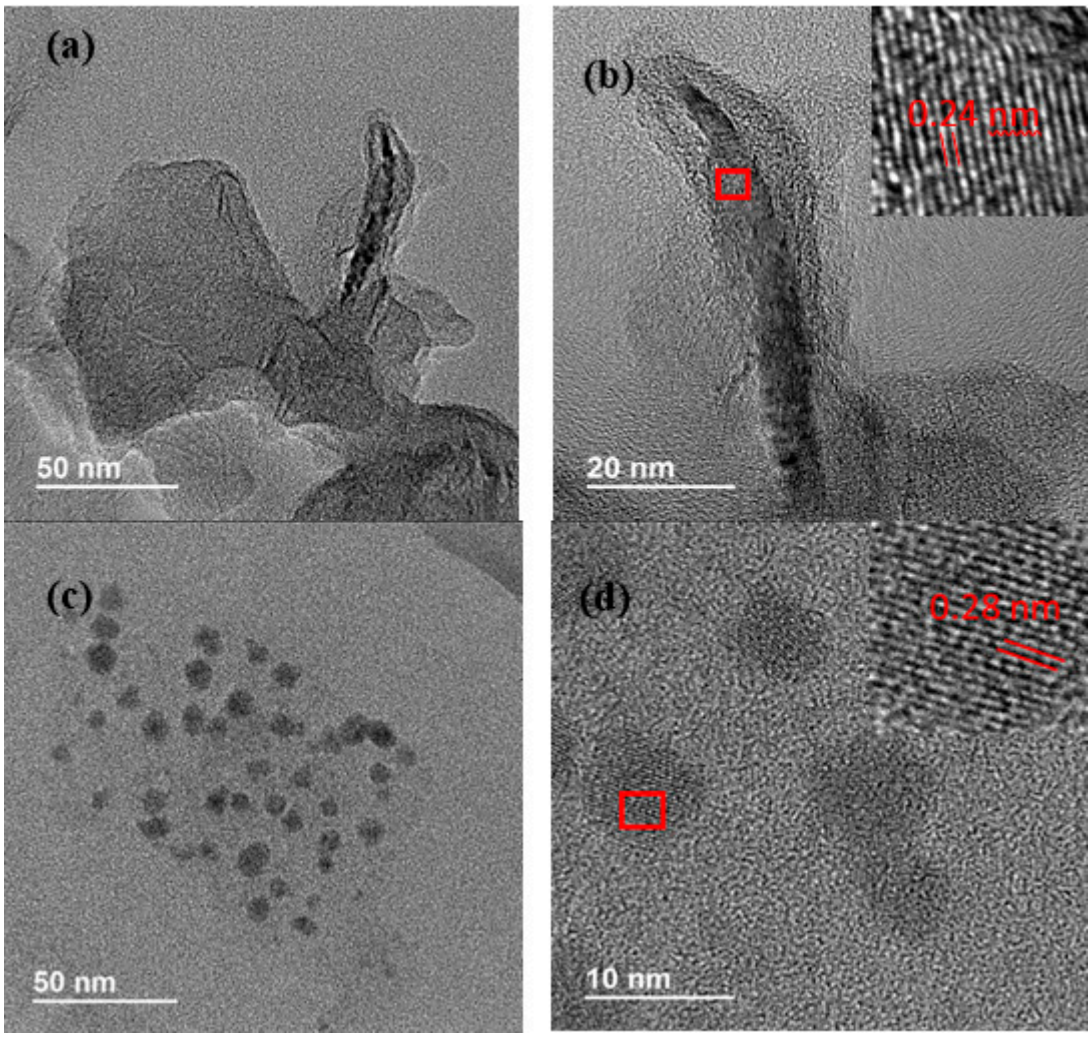


**Figure 1.** (**a**) HR-TEM image showing an example of the graphene layers size used. (**b**) HR-TEM image showing the graphene crystallinity. (**c**) Lead halide perovskites ($MAPbBr3_3$) nanocrystals. (**d**) HR-TEM image showing the $MAPbBr_3$ NCs crystallinity.

Additionally, FESEM images were obtained for both, bare and graphene decorated with $MAPbBr_3$ NCs. Figure 2a shows the graphene once it was deposited onto the quartz substrates to be employed as a gas sensor, presenting a porous surface, which is interesting for gas sensing. Besides, in Figure 2b, the graphene decorated with perovskites nanocrystals can be observed, corresponding to the bright spots. To obtain this image, a Back-Scattered Electron detector (BSE) was used, revealing a quite homogeneous distribution of the nanocrystals on the surface of graphene.

According to the XPS elemental quantification, the graphene used presents a 7.8% content of oxygen and 92.2% of carbon. The results of the XPS fitting analysis are represented in Figure 3. The C1s spectrum, centered at 284.35 eV, is deconvoluted in seven peaks (Figure 3a). The component at 284.2 eV is characteristic of photoelectrons emitted from carbon atoms, associated with $sp^2$ carbon

systems in the "graphite-like" [42]. The peak reproduced at 290.5 eV is also characteristic of $sp^2$ carbon systems, but in this case due to the $\pi$-$\pi^*$ interactions and $\pi$ plasmon, which is derived from the energy loss due to the excitation of $\pi$ electrons [43]. Components associated with carbon in amorphous or $sp^3$ configuration appear at 285.0 eV [44], and defects associated with carbon vacancies appear at 282.9eV [45]. Meanwhile, associated to carbon-oxygen bonds, three peaks can be observed at 286.5 eV, 288.1 eV and 289.0 eV, which correspond to C-O, C=O and carboxylic groups, respectively [46]. Peak quantification is summarized in Tables S1 and S2 (see the supporting information).

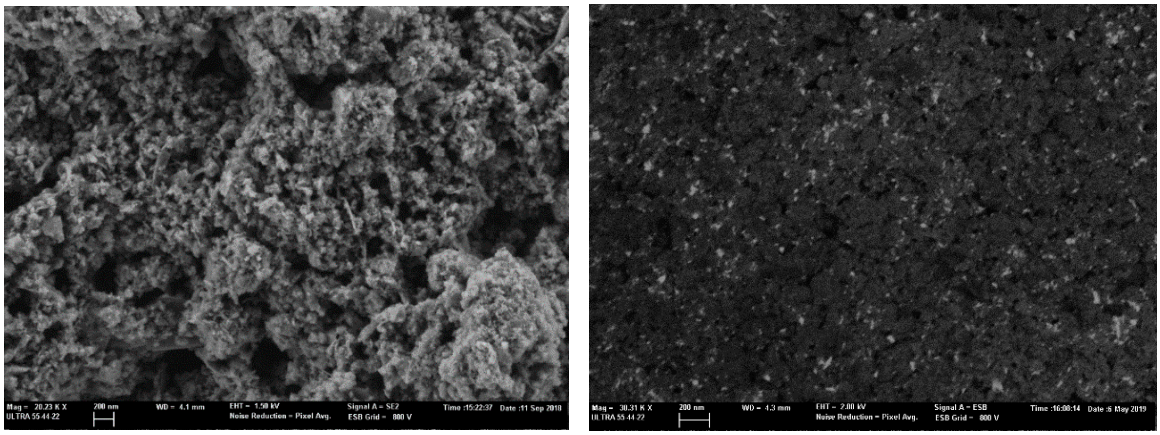

(**a**) (**b**)

**Figure 2.** (**a**) FESEM image showing the sensor surface composed only by graphene. (**b**) FESEM image recorded with Back-Scattered Electron (BSE) detector, showing the graphene (black background) decorated with perovskite nanocrystals (bright spots).

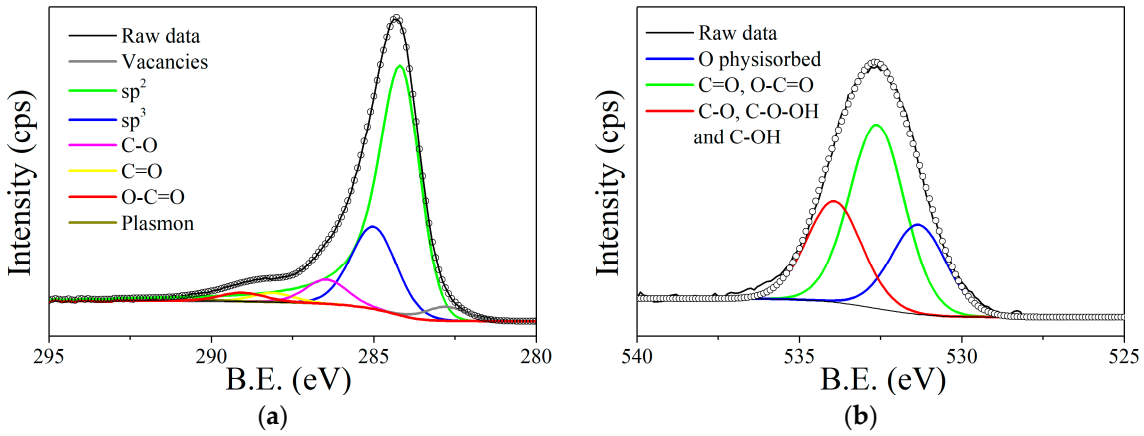


**Figure 3.** Deconvolution of the C 1s (**a**) and O 1s (**b**) core level peak for graphene.

The O 1s spectrum is reproduced employing three components centered at different binding energies, which are 531.3 eV, 532.6 eV and 533.9 eV (Figure 3b). The first one at 531.3 eV is attributed to oxygen physically absorbed, meanwhile the two peaks centered at 532.3 eV is associated to C=O, O-C=O and isolated OH, the peaks at 533.9 eV should correspond to C-O, C-O-OH and C-OH groups [47]. These oxygenated species will help to anchor and stabilize the perovskites in the graphene layers, similarly to the typical decoration of carbon nanomaterials with nanoparticles of different nature. Additional Raman Spectroscopy analysis was conducted to confirm the crystallinity reported before and after loading graphene with the perovskite (see Figure S4 Supplementary Materials).

### 3.2. Gas Sensing Results

Two different gases, nitrogen dioxide and ammonia, with high interest to be monitored due to the danger to human health derived from their exposure at certain levels were measured. Several dilutions were performed in order to apply different concentrations, especially under the threshold limits. Due to the different baseline levels of the two films studied, normalized responses are show for better comparison in Figure 4. Also, it can be expected that a slight baseline drift appears, given the difficulty to completely clean the surface from adsorbed gas molecules due to the room temperature working conditions. However, a temperature treatment was performed on a weekly basis, to counteract drift, in which the sensors are heated up to 80 °C during 1 h to desorb the gas molecules at the surface and regain the original baseline.

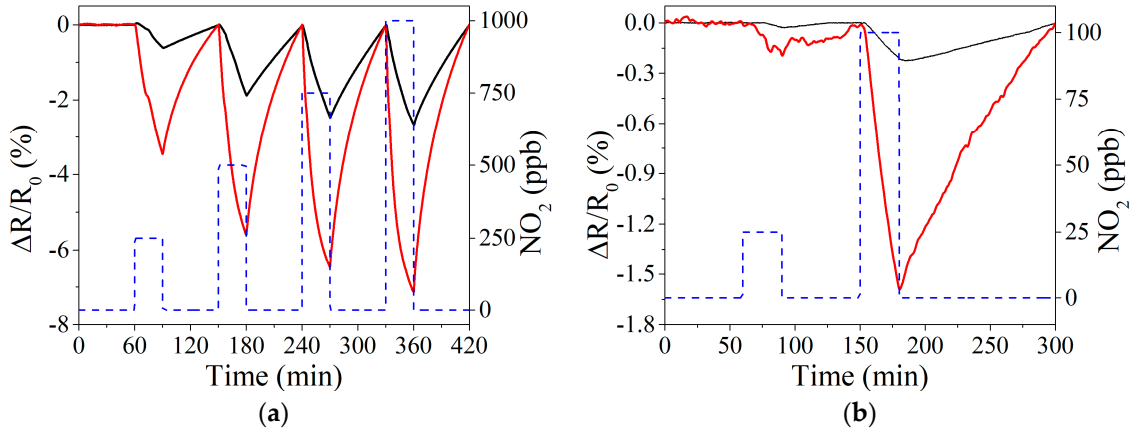


**Figure 4.** Example of resistance response when detecting $NO_2$ at room temperature in the range of 250–1000 ppb (**a**) and 25–100 ppb (**b**). In both figures, black and red line corresponds to bare graphene and perovskite doped graphene, respectively. The concentration of $NO_2$ applied is shown in right-Y, represented by a blue dashed line.

Nitrogen dioxide detection was performed by applying repeated exposure and recovery cycles to increasing concentrations of the analyte considered. Figure 4a shows the response to 250, 500, 750, and 1000 ppb, in which graphene loaded with perovskite nanocrystals obtained higher responses compared to bare graphene. Due to the high responses obtained in this range of concentrations, especially for perovskite-loaded graphene, the concentrations measured were decreased in order to analyze the sensitivity under a few ppb of $NO_2$. Figure 4b shows the responses obtained at 25 and 100 ppb, under room temperature conditions.

Figure 4 shows that response dynamics are slow and the saturation of the response is not achieved during the 30-min gas exposure. This drawback is often experienced with carbon nanomaterial chemoresistors, especially for room-temperature operated sensors. Slow response dynamics can be ameliorated by reducing the dead volume of the test chamber or by increasing the gas flow. Sensor response was computed as $R(\%) = 100*(R-R_0)/R_0$, Where $R_0$ is the resistance value immediately before gas exposure (i.e., under dry air), and R is the resistance immediately before the start of a new cleaning step (in other words, the last resistance value acquired while under exposure to $NO_2$ or $NH_3$). Figure 5 shows the calibration curves obtained for the whole range of $NO_2$ concentrations measured. Graphene doped with perovskite nanocrystals presents a higher response (up to 3-fold) than bare graphene, even under a hundred ppb of $NO_2$ exposure. Additionally, bare graphene presents a slight saturation above 500 ppb, decreasing the slope obtained and, in consequence, reducing sensitivity.

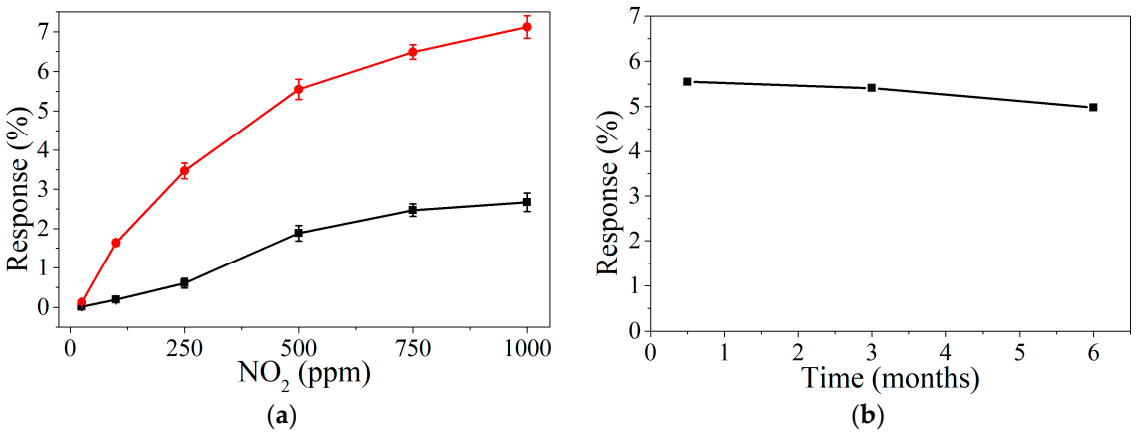


**Figure 5.** Calibration curves obtained for bare graphene (black) and perovskite doped graphene (red) detecting $NO_2$ at ppb range (**a**). Stability study of the sensor based on graphene loaded with perovskite nanocrystals, 500 ppb of $NO_2$ are measured over a 6-month period (**b**).

A stability study of graphene loaded with perovskite nanocrystals was conducted (Figure 5b), revealing a slight decrease in the response towards 500 ppb of $NO_2$ after six months of sensor operation. This result confirms the high stability of $MAPbBr_3$ under ambient moisture and reactive gases, probably due to the nanocrystal structure of the perovskite. Zhu et al. [28] report the high stability of perovskites in nanocrystal structure over other alternatives. Besides, in our work, the perovskites are probably protected by the hydrophobic properties of graphene.

The process and experimental conditions followed for $NO_2$ detection, were applied as well for $NH_3$ detection at ppm range (Figure 6a). Similarly, to the detection of nitrogen dioxide, ammonia measurements reveal a higher sensitivity for graphene decorated with perovskite nanocrystals (Figure 6b). Besides, meanwhile bare graphene presents a saturated response, decorated graphene shows a high potential to enhance the response under longer exposures to the analytes. However, an analysis of the steady-state reveals that several hours were not enough to get the saturation of the perovskite decorated graphene (Figure S5) at room temperature.

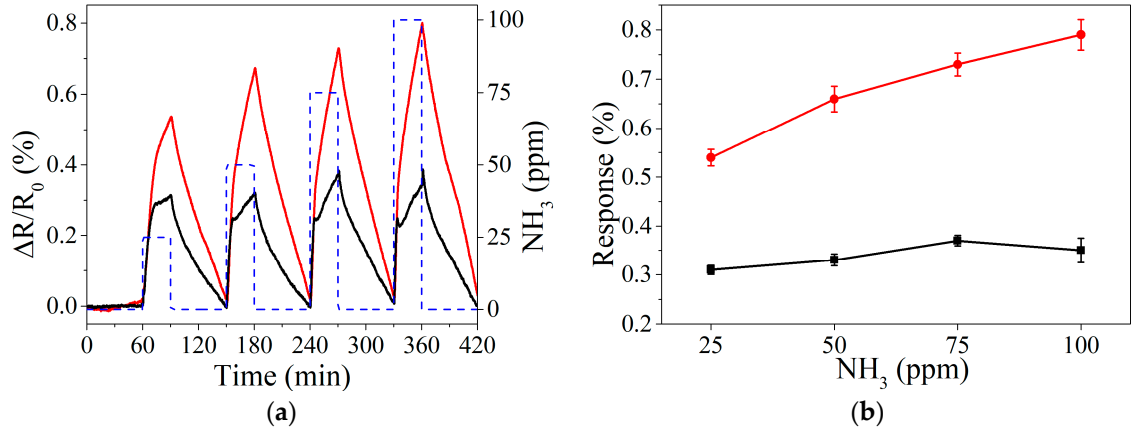


**Figure 6.** Example of resistance response when detecting $NH_3$ at room temperature in ppm range (**a**). Calibration curves obtained for bare graphene and perovskite doped graphene, black and red lines, respectively (**b**).

Additionally, the sensitivity under dry and humid conditions was evaluated to both, bare and perovskite loaded graphene. Figure 7 shows an increase in the response for graphene to 500 ppb of $NO_2$ (about 30%) when moisture is present. However, graphene decorated with perovskite nanocrystals shows a very stable response with only a slight decrease (about 5%) when under humid conditions.

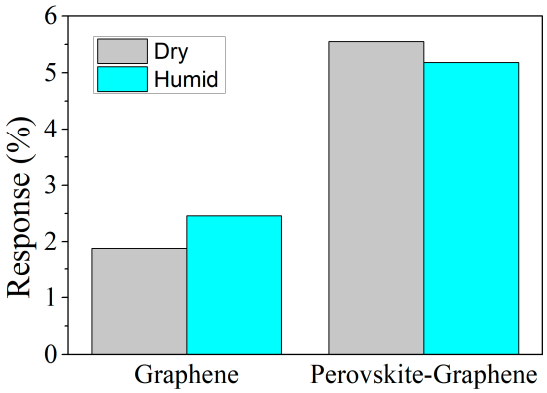


**Figure 7.** Comparison of the response for 500 ppb of $NO_2$ under dry and humid (50% of relative humidity) conditions for bare and perovskite-decorated graphene.

## 4. Discussion

Graphene with oxygen-containing functional groups such as carbonyl, hydroxyl, epoxy, and ether groups exhibited enhanced hole transport characteristics due to its suitable work function [48,49]. In addition, it is well known that molecules adsorbed on the surface of graphene can change the local carrier concentration [50]. In this regard, exposure to an electron-withdrawing gas, like $NO_2$ leads to a lower sensor resistance. Conversely, an electron-donating gas, such as $NH_3$, decreases the hole concentration resulting in a higher sensor resistance. In films decorated with perovskite nanocrystals, the p-type behavior of the sensor is defined as well by the graphene nanolayers (these are the dominant carrier transport material), meanwhile the $MAPbBr_3$ NCs are ambipolar charge transporters [23]. In other words, perovskites can act as a p- or n-type semiconductor depending on the interaction between the sensor surface and the nature of the gas (electron-donating or electron-withdrawing).

Bare graphene samples offer a response to both, $NO_2$ and $NH_3$, due to the interaction of these gases with the oxygenated defects and functional groups located on the graphene nanosheets. However, all the measurements were done at room temperature, obtaining limited sensitivity derived from the small transfer of electronic charge between graphene and adsorbed gas molecules. Nevertheless, from the gas sensing tests, it was derived that the presence of $MAPbBr_3$ NCs decorating the graphene nanolayers was advantageous for detecting $NO_2$ and $NH_3$ at room temperature. In addition, surface trap sites at the perovskite have been demonstrated to act as active sites for the gas sensing process. It is reported that a net positive charge is formed at the surface of the perovskite due to the loss of bromine and undercoordination of the Pb atom, favouring the perovskite to be sensitive to the environmental gases [23]. Regarding the baseline level in dry air, bare graphene shows a lower resistance baseline (3-fold) than the decorated one with $MAPbBr_3$ NCs. Upon the formation of the hybrid perovskite the overall resistance of hybrid films is higher than that of bare graphene due to the intrinsic electrical properties of the perovskite nanocrystals.

This enhancement in the response when graphene is decorated with $MAPbBr_3$ NCs is associated to the creation of electron-hole pairs by the perovskites, once these are exposed to the gases (Figure 8). On the one hand, nitrogen dioxide is getting adsorbed on the graphene due to the interaction between the gas and the oxygen defects and functional groups of graphene. As a consequence, the hole concentration is increasing, resulting in a decrease in the resistance. Additionally, the perovskite NCs have a crucial role in the improvement of the sensitivity towards $NO_2$, because the electron-hole pairs are separated, creating an interface between the graphene and the $MAPbBr_3$. As a result, the excess of positive charges (holes) generated at perovskite NCs are transferred from the perovskite to the graphene sheet [51]. Therefore, the graphene film will suffer a large increase in the number of holes (and associated decrease in resistivity) when exposed to nitrogen dioxide, thanks to the presence of perovskite NCs. Inversely, when perovskite NCs initiate the creation of electron-hole pairs by the interaction with an electron-donating gas, in our case $NH_3$, an excess of negative charges (electrons)

are generated. As a consequence, perovskite NCs transfer electrons to graphene (and this is associated to an increase in resistivity), enhancing the response of the film to $NH_3$ due to the higher concentration of electrons.

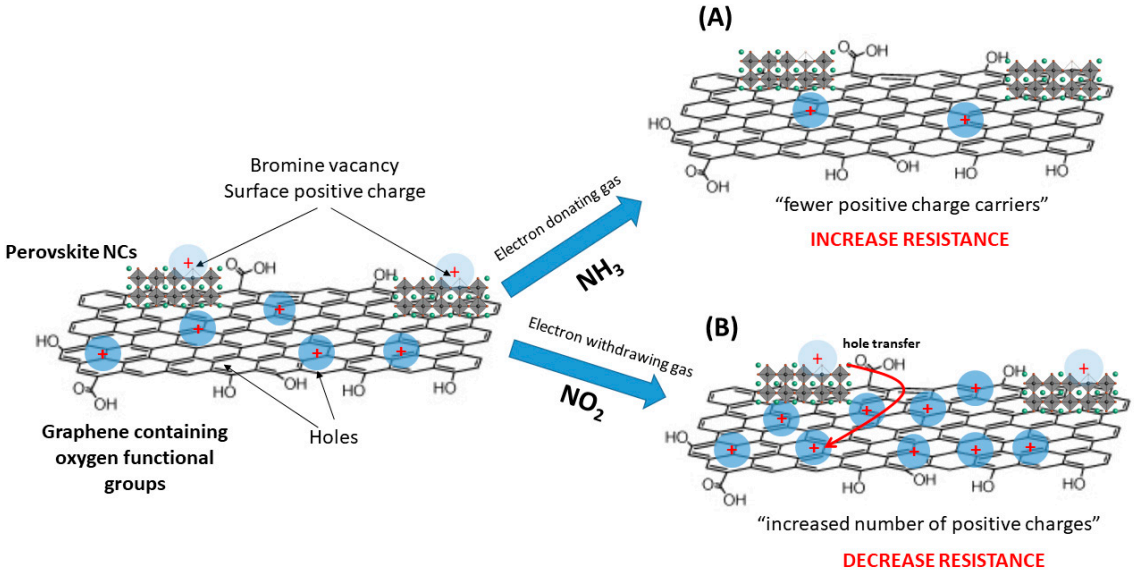


**Figure 8.** Schematic illustration of perovskite decorated graphene sensor showing the mechanism proposed after interaction with different gases. Two adsorption processes are proposed, one at the graphene surface and another at the perovskite NCs. (**A**) During the exposure to an electron-donating gas, an excess of positive charges is neutralized at the defective perovskite surface and the local hole concentration of the p-type graphene is decreased, which results in an increase in film resistance. (**B**) During the exposure to an electron-withdrawing gas, positive charges (holes) in the NCs are formed, which are transferred to the graphene layers from the NCs, decreasing the overall resistance of the hybrid film.

One of the main drawbacks of the sensors based on perovskites films is the fast degradation derived from the exposure to ambient moisture. For that reason, a lead halide perovskite with bromide was chosen, due to the well-known stability over other perovskites based in halides like iodine [33]. Additionally, this paper reports perovskites in nanocrystal form, in front of the most usual approximation, based on films. With NCs, more stable perovskites can be obtained [28], enhancing the lifetime and durability of the sensor. Besides, the high hydrophobicity of the graphene can protect the $MAPbBr_3$ NCs and slow down their degradation, due to the limited interaction with ambient moisture [30].

Considering the effect of ambient moisture in the sensing mechanism, higher sensitivity under humid conditions can be observed for bare graphene. This is in agreement with other works that report the use of graphene as humidity sensors [52]. Normally, water molecules act as electron-withdrawing, interacting with the oxygen functional groups grafted in the graphene. Besides, the detection of $NO_2$ in humid conditions can be favored by a water-mediated adsorption, as reported in chemoresistive sensors [53].

Nevertheless, the detection of $NO_2$ in the presence of ambient moisture for $MAPbBr_3$ decorated graphene shows interesting characteristics. Figure 7 shows that a very similar response to 500 ppb of $NO_2$ is achieved for hybrid sensors under dry and humid conditions. The response is only slightly lower in the presence of ambient moisture. Probably water molecules partly passivate the charge transport and the creation of electron-hole pairs of perovskite nanocrystals [54], slightly decreasing the improvement in the response registered by the presence of $MAPbBr_3$ under dry conditions. The hydrophilic properties of perovskite decorated graphene were further studied by contact angle measurements (see Figure S6 in the Supplementary Materials).

The gas-sensitive layer developed shows its potential for detecting concentrations of nitrogen dioxide and ammonia at trace levels, even below their threshold limit values. These results are a promising beginning for the use of perovskite nanocrystal decorated graphene in gas sensing applications. However, selectivity should be further studied before their use under real conditions. One reasonable approach could be the development of multi-sensor arrays employing decorated graphene with different types of perovskite nanocrystals.

## 5. Conclusions

This work reports the first use of graphene loaded with perovskite nanocrystals as a chemoresistive sensor. This nanocomposite material has been shown to be a good option to obtain gas sensors with high stability over time, avoiding the main problem associated with perovskites, which is their degradation in contact with ambient moisture. Decorated graphene nanolayers show enhanced nitrogen dioxide and ammonia sensitivity in comparison to their bare graphene counterparts and much reduced cross-sensitivity to the ambient moisture. Furthermore, a reversible response to $NO_2$ and $NH_3$ was achieved at room temperature, enabling the integration of these hybrid films in low-power gas sensing devices. In summary, perovskites can constitute an alternative to metals, metal oxides, polymers or other molecules commonly used in the modification of the surface of carbon nanomaterials such as graphene in view of tuning sensitivity and selectivity.

**Supplementary Materials:** The following are available online at http://www.mdpi.com/1424-8220/19/20/4563/s1, Figure S1: sensor device images, Figure S2: schematic diagram of the gas sensing system set up, Figure S3: histogram based on the diameter of $MAPbBr_3$ NCs, Figure S4: Raman spectra for graphene, Table S1: Graphene peak quantification of C 1s core level, Table S2: Graphene peak quantification of O 1s core level, Figure S5: Steady-state analysis, Figure S6: contact angle measurements.

**Author Contributions:** J.C.-C. performed the sensor fabrication, the gas sensing studies and material characterization. R.G.-A. synthesized the lead halide perovskite and performed the material characterization. P.A. and E.L. supervised the work. All authors contributed to the writing and discussion of results.

**Funding:** This work was funded in part by MINECO, MICINN and FEDER via grants no. RTI2018-101580-B-I00, by AGAUR under grant. 2017SGR 418 J.C.C gratefully acknowledges a doctoral fellowship from URV under the Martí i Franquès fellowship program. E.L. is supported by the Catalan institution for Research and Advanced Studies via the 2012 and 2018 Editions of the ICREA Academia Award. P.A. acknowledges the financial support from the Spanish Government through 'Severo Ochoa" (SEV-2016-0683, MINECO) and PGC2018-099744-B-I00 (MCIU/AEI/FEDER, UE), and R.G.A. acknowledges FPI scholarship the Spanish Government-MINECO for a (TEC2015-74405-JIN), MAT2015-69669-P.

**Acknowledgments:** The Electron Microscopy Service of the UPV is acknowledged for their help in sample characterization.

**Conflicts of Interest:** The authors declare no conflict of interest

## References

1. World Health Organization. 7 Million Premature Deaths Annually Linked to Air Pollution. Available online: https://www.who.int/mediacentre/news/releases/2014/air-pollution/en/ (accessed on 12 March 2019).
2. Hansen, J.; Sato, M.; Ruedy, R.; Lacis, A.; Oinas, V. Global warming in the Twenty-First century: An alternative scenario. *Proc. Natl. Acad. Sci. USA* **2000**, *97*, 9875–9880. [CrossRef] [PubMed]
3. Ibañez, F.J.; Zamborini, F.P. Chemiresistive Sensing with Chemically Modified Metal and Alloy Nanoparticles. *Small* **2012**, *8*, 174–202. [CrossRef] [PubMed]
4. Mirzaei, A.; Leonardi, S.G.; Neri, G. Detection of hazardous volatile organic compounds (VOCs) by metal oxide nanostructures-based gas sensors: A review. *Ceram. Int.* **2016**, *42*, 15119–15141. [CrossRef]
5. Zaidi, N.A.; Tahir, M.W.; Vellekoop, M.J.; Lang, W.; Zaidi, N.A.; Tahir, M.W.; Vellekoop, M.J.; Lang, W. A Gas Chromatographic System for the Detection of Ethylene Gas Using Ambient Air as a Carrier Gas. *Sensors* **2017**, *17*, 2283. [CrossRef]
6. Meng, F.-L.; Guo, Z.; Huang, X.-J. Graphene-Based hybrids for chemiresistive gas sensors. *TrAC Trends Anal. Chem.* **2015**, *68*, 37–47. [CrossRef]

7. Miller, D.R.; Akbar, S.A.; Morris, P.A. Nanoscale metal Oxide-Based heterojunctions for gas sensing: A review. *Sens. Actuators B Chem.* **2014**, *204*, 250–272. [CrossRef]
8. Scott, S.M.; James, D.; Ali, Z. Data analysis for electronic nose systems. *Microchim. Acta* **2006**, *156*, 183–207. [CrossRef]
9. Rodríguez-Pérez, L.; Herranz, M.Á.; Martín, N. The chemistry of pristine graphene. *Chem. Commun.* **2013**, *49*, 3721–3735. [CrossRef]
10. Prezioso, S.; Perrozzi, F.; Giancaterini, L.; Cantalini, C.; Treossi, E.; Palermo, V.; Nardone, M.; Santucci, S.; Ottaviano, L. Graphene Oxide as a Practical Solution to High Sensitivity Gas Sensing. *J. Phys. Chem. C* **2013**, *117*, 10683–10690. [CrossRef]
11. Lipatov, A.; Varezhnikov, A.; Wilson, P.; Sysoev, V.; Kolmakov, A.; Sinitskii, A. Highly selective gas sensor arrays based on thermally reduced graphene oxide. *Nanoscale* **2013**, *5*, 5426–5434. [CrossRef]
12. Varghese, S.S.; Lonkar, S.; Singh, K.K.; Swaminathan, S.; Abdala, A. Recent advances in graphene based gas sensors. *Sens. Actuators B Chem.* **2015**, *218*, 160–183. [CrossRef]
13. Rodner, M.; Puglisi, D.; Ekeroth, S.; Helmersson, U.; Shtepliuk, I.; Yakimova, R.; Skallberg, A.; Uvdal, K.; Schütze, A.; Eriksson, J.; et al. Graphene Decorated with Iron Oxide Nanoparticles for Highly Sensitive Interaction with Volatile Organic Compounds. *Sensors* **2019**, *19*, 918. [CrossRef] [PubMed]
14. Kaniyoor, A.; Jafri, R.I.; Arockiadoss, T.; Ramaprabhu, S. Nanostructured Pt decorated graphene and multi walled carbon nanotube based room temperature hydrogen gas sensor. *Nanoscale* **2009**, *1*, 382–386. [CrossRef] [PubMed]
15. Seekaew, Y.; Lokavee, S.; Phokharatkul, D.; Wisitsoraat, A.; Kerdcharoen, T.; Wongchoosuk, C. Low-Cost and flexible printed graphene–PEDOT: PSS gas sensor for ammonia detection. *Org. Electron.* **2014**, *15*, 2971–2981. [CrossRef]
16. Kang, M.-A.; Ji, S.; Kim, S.; Park, C.-Y.; Myung, S.; Song, W.; Lee, S.S.; Lim, J.; An, K.-S. Highly sensitive and wearable gas sensors consisting of chemically functionalized graphene oxide assembled on cotton yarn. *RSC Adv.* **2018**, *8*, 11991–11996. [CrossRef]
17. Fine, G.F.; Cavanagh, L.M.; Afonja, A.; Binions, R. Metal oxide Semi-Conductor gas sensors in environmental monitoring. *Sensors* **2010**, *10*, 5469–5502. [CrossRef]
18. Sun, D.; Luo, Y.; Debliquy, M.; Zhang, C. Graphene-Enhanced metal oxide gas sensors at room temperature: A review. *Beilstein J. Nanotechnol.* **2018**, *9*, 2832–2844. [CrossRef]
19. Llobet, E. Gas sensors using carbon nanomaterials: A review. *Sens. Actuators B* **2013**, *179*, 32–45. [CrossRef]
20. Correa-Baena, J.P.; Abate, A.; Saliba, M.; Tress, W.; Jesper Jacobsson, T.; Grätzel, M.; Hagfeldt, A. The rapid evolution of highly efficient perovskite solar cells. *Energy Environ. Sci.* **2017**, *10*, 710–727. [CrossRef]
21. Sun, S.; Salim, T.; Mathews, N.; Duchamp, M.; Boothroyd, C.; Xing, G.; Sum, T.C.; Lam, Y.M. The origin of high efficiency in Low-Temperature Solution-Processable bilayer organometal halide hybrid solar cells. *Energy Environ. Sci.* **2014**, *7*, 399–407. [CrossRef]
22. Juarez-Perez, E.J.; Ono, L.K.; Maeda, M.; Jiang, Y.; Hawash, Z.; Qi, Y. Photodecomposition and thermal decomposition in methylammonium halide lead perovskites and inferred design principles to increase photovoltaic device stability. *J. Mater. Chem. A* **2018**, *6*, 9604–9612. [CrossRef]
23. Chen, H.; Zhang, M.; Bo, R.; Barugkin, C.; Zheng, J.; Ma, Q.; Huang, S.; Ho-Baillie, A.W.Y.; Catchpole, K.R.; Tricoli, A. Superior Self-Powered Room-Temperature Chemical Sensing with Light-Activated Inorganic Halides Perovskites. *Small* **2018**, *14*, 1702571. [CrossRef] [PubMed]
24. Kakavelakis, G.; Gagaoudakis, E.; Petridis, K.; Petromichelaki, V.; Binas, V.; Kiriakidis, G.; Kymakis, E. Solution Processed CH3NH3PbI3-xClx Perovskite Based Self-Powered Ozone Sensing Element Operated at Room Temperature. *ACS Sens.* **2018**, *3*, 135–142. [CrossRef] [PubMed]
25. Bao, C.; Yang, J.; Zhu, W.; Zhou, X.; Gao, H.; Li, F.; Fu, G.; Yu, T.; Zou, Z. A resistance change effect in perovskite CH3NH3PbI3 films induced by ammonia. *Chem. Commun.* **2015**, *51*, 15426–15429. [CrossRef]
26. Zhuang, Y.; Yuan, W.; Qian, L.; Chen, S.; Shi, G. High-Performance gas sensors based on a thiocyanate ion-doped organometal halide perovskite. *Phys. Chem. Chem. Phys.* **2017**, *19*, 12876–12881. [CrossRef]
27. Samorì, P.; Orgiu, E.; Liscio, F.; Gobbi, M.; Stoeckel, M.-A.; Ferlauto, L.; Bonacchi, S. Reversible, Fast, and Wide-Range Oxygen Sensor Based on Nanostructured Organometal Halide Perovskite. *Adv. Mater.* **2017**, *29*, 1702469.

28. Zhu, R.; Zhang, Y.; Zhong, H.; Wang, X.; Xiao, H.; Chen, Y.; Li, X. High-Performance Room-Temperature NO2 sensors based on CH3NH3PbBr3 semiconducting films: Effect of surface capping by alkyl chain on sensor performance. *J. Phys. Chem. Solids* **2019**, *129*, 270–276. [CrossRef]
29. Acik, M.; Darling, S.B. Graphene in perovskite solar cells: Device design, characterization and implementation. *J. Mater. Chem. A* **2016**, *4*, 6185–6235. [CrossRef]
30. Christians, J.A.; Miranda Herrera, P.A.; Kamat, P.V. Transformation of the excited state and photovoltaic efficiency of CH3NH3PbI3 perovskite upon controlled exposure to humidified air. *J. Am. Chem. Soc.* **2015**, *137*, 1530–1538. [CrossRef]
31. Leguy, A.M.A.; Hu, Y.; Campoy-Quiles, M.; Alonso, M.I.; Weber, O.J.; Azarhoosh, P.; van Schilfgaarde, M.; Weller, M.T.; Bein, T.; Nelson, J.; et al. Reversible Hydration of CH3NH3PbI3 in Films, Single Crystals, and Solar Cells. *Chem. Mater.* **2015**, *27*, 3397–3407. [CrossRef]
32. O'keeffe, P.; Catone, D.; Paladini, A.; Toschi, F.; Turchini, S.; Avaldi, L.; Martelli, F.; Agresti, A.; Pescetelli, S.; Del, A.E.; et al. Graphene-Induced Improvements of Perovskite Solar Cell Stability: Effects on Hot-Carriers. *Nano Lett.* **2019**, *19*, 684–691. [CrossRef] [PubMed]
33. Berhe, T.A.; Su, W.N.; Chen, C.H.; Pan, C.J.; Cheng, J.H.; Chen, H.M.; Tsai, M.C.; Chen, L.Y.; Dubale, A.A.; Hwang, B.J. Organometal halide perovskite solar cells: Degradation and stability. *Energy Environ. Sci.* **2016**, *9*, 323–356. [CrossRef]
34. Lee, G.Y.; Yang, M.Y.; Kim, D.; Lim, J.; Byun, J.; Choi, D.S.; Lee, H.J.; Nam, Y.S.; Kim, I.; Kim, S.O. Nitrogen-Dopant-Induced Organic–Inorganic Hybrid Perovskite Crystal Growth on Carbon Nanotubes. *Adv. Funct. Mater.* **2019**, *29*, 1902489. [CrossRef]
35. Fu, X.; Jiao, S.; Dong, N.; Lian, G.; Zhao, T.; Lv, S.; Wang, Q.; Cui, D. A CH3NH3PbI3 film for a Room-Temperature NO2 gas sensor with quick response and high selectivity. *RSC Adv.* **2018**, *8*, 390–395. [CrossRef]
36. Gupta, N.; Nanda, O.; Grover, R.; Saxena, K. A new inorganic-organic hybrid halide perovskite thin film based ammonia sensor. *Org. Electron.* **2018**, *58*, 202–206. [CrossRef]
37. European Union. Air Quality Standards. Available online: https://ec.europa.eu/environment/air/quality/standards.htm (accessed on 12 October 2019).
38. Environmental Protection Agency. NAAQS Table. Available online: https://www.epa.gov/criteria-air-pollutants/naaqs-table (accessed on 12 October 2019).
39. European Union. Commission Directive 2000/39/EC. Available online: https://eur-lex.europa.eu/legal-content/EN/TXT/HTML/?uri=CELEX:02000L0039-20100108&from=EN (accessed on 12 October 2019).
40. Centers for Disease Control and Prevention. Ammonia. Available online: https://www.cdc.gov/niosh/npg/npgd0028.html (accessed on 12 October 2019).
41. Schmidt, L.C.; Pertegás, A.; González-Carrero, S.; Malinkiewicz, O.; Agouram, S.; Mínguez Espallargas, G.; Bolink, H.J.; Galian, R.E.; Pérez-Prieto, J. Nontemplate Synthesis of CH3NH3PbBr3 Perovskite Nanoparticles. *J. Am. Chem. Soc.* **2014**, *136*, 850–853. [CrossRef]
42. Yang, G.; Kim, B.-J.; Kim, K.; Woo Han, J.; Kim, J. Energy and dose dependence of Proton-Irradiation damage in graphene. *RSC Adv.* **2015**, *5*, 31861–31865. [CrossRef]
43. D'Acunto, G.; Ripanti, F.; Postorino, P.; Betti, M.G.; Scardamaglia, M.; Bittencourt, C.; Mariani, C. Channelling and induced defects at ion-bombarded aligned multiwall carbon nanotubes. *Carbon* **2018**, *139*, 768–775. [CrossRef]
44. Johra, F.T.; Lee, J.-W.; Jung, W.-G. Facile and safe graphene preparation on solution based platform. *J. Ind. Eng. Chem.* **2014**, *20*, 2883–2887. [CrossRef]
45. Ganesan, K.; Ghosh, S.; Krishna, N.G.; Ilango, S.; Kamruddin, M.; Tyagi, A.K. A comparative study on defect estimation using XPS and Raman spectroscopy in few layer nanographitic structures. *Phys. Chem. Chem. Phys.* **2016**, *18*, 22160. [CrossRef]
46. Roy, S.; Das, T.; Ming, Y.; Chen, X.; Yue, C.Y.; Hu, X. Specific functionalization and polymer grafting on multiwalled carbon nanotubes to fabricate advanced nylon 12 composites. *J. Mater. Chem. A* **2014**, *2*, 3961–3970. [CrossRef]
47. Datsyuk, V.; Kalyva, M.; Papagelis, K.; Parthenios, J.; Tasis, D.; Siokou, A.; Kallitsis, I.; Galiotis, C. Chemical oxidation of multiwalled carbon nanotubes. *Carbon* **2008**, *46*, 833–840. [CrossRef]
48. Kumar, P.V.; Bernardi, M.; Grossman, J.C. The Impact of Functionalization on the Stability, Work Function, and Photoluminescence of Reduced Graphene Oxide. *ACS Nano* **2013**, *7*, 1638–1645. [CrossRef] [PubMed]

49. Liu, J.; Durstock, M.; Dai, L. Graphene oxide derivatives as Hole- and Electron-Extraction layers for High-Performance polymer solar cells. *Energy Environ. Sci.* **2014**, *7*, 1297–1306. [CrossRef]
50. Georgakilas, V.; Otyepka, M.; Bourlinos, A.B.; Chandra, V.; Kim, N.; Kemp, K.C.; Hobza, P.; Zboril, R.; Kim, K.S. Functionalization of Graphene: Covalent and Non-Covalent Approaches, Derivatives and Applications. *Chem. Rev.* **2012**, *112*, 6156–6214. [CrossRef] [PubMed]
51. Wang, Y.; Zhang, Y.; Lu, Y.; Xu, W.; Mu, H.; Chen, C.; Qiao, H.; Song, J.; Li, S.; Sun, B.; et al. Hybrid Graphene-Perovskite Phototransistors with Ultrahigh Responsivity and Gain. *Adv. Opt. Mater.* **2015**, *3*, 1389–1396. [CrossRef]
52. Lv, C.; Hu, C.; Luo, J.; Liu, S.; Qiao, Y.; Zhang, Z.; Song, J.; Shi, Y.; Cai, J.; Watanabe, A. Recent Advances in Graphene-Based Humidity Sensors. *Nanomater* **2019**, *9*, 422. [CrossRef]
53. Casanova-Cháfer, J.; Navarrete, E.; Noirfalise, X.; Umek, P.; Bittencourt, C.; Llobet, E. Gas Sensing with Iridium Oxide Nanoparticle Decorated Carbon Nanotubes. *Sensors* **2019**, *19*, 113. [CrossRef]
54. Fang, H.H.; Adjokatse, S.; Wei, H.; Yang, J.; Blake, G.R.; Huang, J.; Even, J.; Loi, M.A. Ultrahigh sensitivity of methylammonium lead tribromide perovskite single crystals to environmental gases. *Sci. Adv.* **2016**, *2*, e1600534. [CrossRef]

# Section 3.2

## Wafer-Scale Few Layer Graphene Growth on Cu/Ni Films for Gas Sensing Applications

Geetanjali Deokar, Juan Casanova-Chafer, Nitul S. Rajput, Cyril Aubry, Eduard Llobet, Mustapha Jouiad, Pedro M. F. J. Costa

*Sensors & Actuators: B. Chemical 2019 (in press)*

DOI: in process

UNIVERSITAT ROVIRA I VIRGILI
GAS SENSING WITH MODIFIED CARBON NANOTUBES, GRAPHENE AND DIAMONDOIDS
Juan Casanova Cháfer

# Wafer-scale few-layer graphene growth on Cu/Ni films for gas sensing applications

Geetanjali Deokar [1, 2*], Juan Casanova-Cháfer [3], Nitul S. Rajput [2], Cyril Aubry [2], Eduard Llobet [3], Mustapha Jouiad [4*], Pedro M. F. J. Costa[1]

[1]Physical Science and Engineering Division, King Abdullah University of Science and Technology, Thuwal 23955-6900, Saudi Arabia
[2] Department of Materials & Engineering, Masdar Institute of Science and Technology-Khalifa University, Abu-Dhabi
[3] MINOS-EMaS, Universitat Rovira i Virgili, Tarragona, Spain
[4]LPMC-EA2081, University of Picardie Jules Vernes, Amiens, France

## Abstract

Pristine, few-layer graphene (FLG)/Si nanopillar assemblies are introduced as gas sensitive chemiresistors showing unprecedented sensitivity towards $NO_2$ when operated at room temperature (25ºC) and in humid air. To achieve this, we first developed wafer-scale (~50 $cm^2$) FLG growth using sub-micrometer thick films of thermally evaporated Cu/Ni on a $SiO_2$/Si substrate. The Ni film was deposited and annealed to induce the formation of a Cu-rich binary alloy. This alloy formation limited the inter-diffusion of Cu and $SiO_2$, a phenomenon known to take place during the CVD growth of graphene on Cu/$SiO_2$/Si. The as-grown high structural quality FLG was transferred, using a conventional wet chemical method, to lithographically patterned arrays of Si nanopillars (non-flat substrate). Testing of the FLG/Si assembly revealed a $NO_2$ sensitivity that outperforms what is reported in the literature for pristine graphene. Overall, our growth and device fabrication work-flow demonstrate a way to design graphene-based gas sensing systems without incurring inconvenient processing steps such as metal foil etching, surface functionalization or particle loading.

**Keywords:** Graphene, CuNi alloy, Chemical Vapor Deposition, Patterned Substrates, Gas Sensing

**Corresponding authors:** geetanjali.deokar@kaust.edu.sa, mustapha.jouiad@u-picardie.fr

## 1. Introduction

Graphene has a string of superlative qualities such as an extremely high charge carrier mobility, high thermal conductivity, extraordinary electrical and optical properties, etc.. [1, 2]. In a case, for decades, graphene would become proponent in a wide range of applications such as electronics [1, 3], optoelectronics [4], supercapacitors [5], solar cells [6, 7], electrochemical sensing [8], and gas sensing [9-12]. Considering the latter, it has been repeatedly shown that graphene is uniquely suited because of its high surface area [13, 14]. However, the scale-up of the graphene-based sensors is constrained by the synthesis limitation of the active material [13]. It is currently consensual that to produce large-area graphene with controlled structural quality, the chemical vapor deposition (CVD) technique is the most appropriate choice [15]. In this respect, the most popular catalytic CVD substrate for single-layer graphene growth is the Cu metal foil. This is explained by the extremely low solubility of C in Cu at the temperature of the reaction, i.e., close to the melting point of Cu (1085ºC) [16, 17]. To progress beyond the lab-scale several bottlenecks remain in this approach. Furthermore, during the growth process, some of the Cu evaporates and gets deposited on the walls of the reactor. Therefore, the reaction chamber has to undergo periodic cleaning steps. In addition, the Cu foil is delicate to handle. At post-growth, a minor mishap can cause it to bend and, ultimately, compromise the structural quality of the graphene on it. Besides, the financial and environmental challenges using metal foils are also notable. At the industrial scale, the waste would be considerable because the sacrificial catalytic metal sheets are used in the range of 25 to 50 μm in thickness [17, 18]. In view of this, alternative processes to grow graphene by CVD include the use of thermally-deposited Cu films on $SiO_2$/Si or sapphire substrates [19, 20]. This approach is promising for electronic and gas-sensing device applications as these devices fabrication require straightforward transfer and large-area of the active materials [13, 21]. However, due to the high-temperature instability at of the deposited Cu films (resulting from the inter-diffusion of Cu and $SiO_2$), the growth of uniform, continuous, and large area graphene continues to be elusive. Recently, Howsare et al. proposed that a 50 nm Ni film could act as a barrier layer to minimize the inter-diffusion of Cu and $SiO_2$ [19]. This research could be an essential step towards producing tens of $cm^2$ graphene films required for scaling of gas sensing.

Highly hazardous gases such as $NO_2$ and $NH_3$ are produced daily by various industries. This situation demands fast, reliable, and low-cost gas sensing solutions. The gas-sensing properties of

graphene were first investigated by Novoselov *et al.* [22]. They demonstrated that a graphene-based sensor (prepared using micromechanical cleavage of graphite) was able to detect adsorbed individual molecules of $NO_2$ and $NH_3$. Interestingly, these authors relied on a Hall geometry, gas sensing device. To this day, challenges persist in reaching a sensitivity of that level when using graphene produced by other synthesis techniques and/or chemiresistor type devices (i.e., the most straightforward working design). Accordingly, efforts have included the use of chemically exfoliated graphene by tailoring the degree of oxidation, by decorating with inorganic nanoparticles, or by functionalizing with diverse organic moieties, polymers, etc. [9, 11, 23-27]. These approaches suffer from various drawbacks; for instance, it is difficult to reliably reproduce the oxidation degree for powdered graphene material [23, 28-30]. Also, chemical exfoliation and/or decoration of graphene include cumbersome surface modification and coating steps. As concerns, CVD grown graphene was used by several research groups to achieve a $NO_2$ sensitivity in the range of few parts per million to parts per billion (ppm to ppb). However, these films and devices required specific treatments such as metal oxide Schottky junctions [31], $O_3$ treatment [32], S doping [33], high operating/recovery temperatures (80 - 250°C) [33-36], etc.. In summary, structural and chemical tailoring of the graphene surface provides additional sensitivity, it also brings in additional costs and fabrication complexity [9, 11, 23-27, 31-33].

Here, we report a simple and less expensive workflow for FLG production and its device integration than other proposed methods for graphene-based gas sensing systems. We developed a wafer-scale growth of FLG on Cu/Ni films with high structural quality and purity. To demonstrate its direct application, the as-produced FLG was transferred onto a patterned array of Si nanopillars and used as active gas-sensing material. The unique FLG/Si nanopillar device showed excellent $NO_2$ detection results in ppm to ppb range.

## 2. Experimental details

### Materials:

### 2.1 Growth

A 6” Si (001) wafer (test grade, University Wafer Inc.) was cleaned, with successive rinses of acetone and ethanol, in an ultrasonic bath. Following this, a 300 nm layer of silica ($SiO_2$) was

deposited using inductively coupled plasma chemical vapor deposition (PlasmaLab 100, Oxford Instruments). Immediately after, the $SiO_2$/Si wafer was loaded into a thermal evaporation chamber (PVD 75, Kurt J. Lesker) for Cu or Ni film deposition. The deposition was performed after pumping down the chamber to a base pressure below $10^{-6}$ mbar. Five wafers were prepared with different thickness of Cu and Ni films, as listed in **Table 1**. The processed wafers (hereafter, CNS = Cu/Ni/$SiO_2$/Si) were cut into sample-pieces of 1 to 50 $cm^2$. The samples were then placed in a thermal CVD system (BM Pro 4", Aixtron GmbH) and annealed for 10 to 30 min (at 900°C and using an $H_2/N_2$ atmosphere with flows of 1000/250 sccm, respectively). To promote the growth of graphene, a mixture of $H_2$ (100 to 1000 sccm) and $CH_4$ (5 to 100 sccm) was used at 930 to 950°C. The reaction times were varied from 2 to 10 min. The chamber pressure was maintained at 10 mbar throughout the process. Finally, the samples were cooled down under a mixed flow of $H_2$ and $N_2$, at 1000 sccm each. For reference, a cut piece of an as-received 25 μm thick Cu foil (99.95% purity, Alfa Aesar) was placed in the reaction chamber, next to the CNS samples, during initial annealing/growth runs.

### 2.2 Characterization

Pictures of the graphene samples were taken with a standard digital optical camera. To measure the surface root mean square (RMS) roughness of the Cu/Ni films, atomic force microscopy, AFM (Dimension Icon, Bruker) was used in intermittent contact mode. The morphological analysis was performed using scanning electron microscopy, SEM (Nova Nano, Thermo Fisher Scientific). The microstructure and elemental analysis of the Cu/Ni films were examined using transmission electron microscopy, TEM (Titan, Thermo Fisher Scientific, operated at 300 kV), and energy dispersive X-ray spectroscopy, EDX. To prepare the cross-sectional TEM lamella, SEM with a focused ion beam (FIB) source was employed (dual-beam Helios 650, Thermo Fisher Scientific) and followed a standard *in-situ* lift-out method [37]. The grain orientation distribution was studied using electron backscatter diffraction, EBSD (Quanta 3D, Thermo Fisher Scientific). The structural analysis of the as-deposited samples was carried out with powder X-ray diffraction, XRD (D8 Advance DaVinci, Bruker, with a Cu Kα source, 1.5418 Å). To identify and characterize the graphene films, Raman spectra were collected at 1 mW power (Alpha 300 RA, WITeC, 532 nm laser).

### 2.3 Graphene transfer

The as-grown FLG was transferred using a classical polymethyl methacrylate (PMMA)-assisted method [17]. Firstly, the graphene/CNS sample was spin-coated with ~200 nm PMMA and, then, floated on a buffered oxy-etchant solution (6:1 volume ratio of 40% $NH_4F$ in water to 49% HF in water). This overnight etching step was done to remove the $SiO_2$ layer, thereby detaching the Si substrate from the heterostructure composed by the stacked layers of graphene and catalyst. Following this, the CuNi alloy was dissolved (also overnight) by keeping it in a solution of $H_2O$ (250 ml), HCl (2.5 ml), and $H_2O_2$ (2.5 ml). Afterward, the remaining PMMA/graphene film was transferred onto different substrates, namely alumina, $SiO_2$/Si, and for the gas sensing experiments, patterned arrays of Si nanopillars (with native oxide layer on top). The nanopillars were fabricated on a highly-resistive Si wafer, as described elsewhere [38]. Finally, the PMMA was removed using a combination of UV-exposure, methyl isobutyl ketone (MIBK), and warm acetone [17].

### 2.4 Device fabrication and testing

First, the as-grown FLG was transferred onto a patterned array of Si nanopillars, as per the procedure explained above. Then, an alumina substrate (which included a screen-printed heating resistor) was glued, with a thermally conductive and electrically insulating epoxy resin, to the backside of the patterned $SiO_2$/Si die. This set-up was used to control the operating temperature of the device. The assembly was wire-bonded to a 2 × 3 $cm^2$ printed circuit board (PCB). Then, a silver epoxy paste (Heraeus) was employed to attach two platinum wire contacts on the graphene surface. The resulting planar electrode configuration enables the monitoring of the electrical resistance of the nanopillar-supported graphene assembly. This process was selected to avoid contamination or damage to the graphene during the patterning of electrodes. Finally, the assembled and wire-bonded device was connected to a Teflon airtight chamber, linked to a mass-flow controller system (Bronkhorst, High-Tech B.V., Netherlands) and a multimeter (HP 34972A, Agilent), to record the changes in film resistance upon exposure to gas flow. Calibrated gas cylinders of $NO_2$, $NH_3$, and synthetic dry air (purity: 99,995%) were used during the gas detection experiments. Well-controlled $NO_2$ and $NH_3$ flows of 25 ppb to a hundred parts per million (ppm) were employed [39]. Due to limitations in our experimental setup, it was not possible to go below 25 ppb. The response and recovery dynamics of sensors were studied (see **Figure SI1** and description), and it was found that reaching a steady-state response to a stepwise change in gas

concentration would take about 180 min. To speed-up the gas sensing characterization process, the measurement strategy was implemented as follows. The sensor baseline resistance was stabilized in dry air for 1 hour to test different concentrations of a given gas. Then, a selected gas concentration (obtained via dilution and employing the mass-flow controller system) was delivered to the test chamber for 30 minutes. Meanwhile, the resistance changes were monitored at room temperature (RT = 25ºC, measured and monitored constant throughout the measurements). The response was recorded as $\Delta R/R_0$, where $\Delta R$ is the resistance variation experienced by the film during the 30 min exposure to a given gas concentration, and $R_0$ is the baseline resistance in dry air. After this measurement, a 1 hour cleaning cycle in dry air was applied. This was done before performing measurements with a different gas concentration. The power source (E3648A, Agilent) was connected to the screen printed heater to raise the operating temperature of the sample. This air cleaning allowed us to heat-up the sample to 100ºC while maintaining the overall chamber temperature at RT. Besides this, an evaporator and mixer (Bronkhorst, High-Tech B.V., Netherlands) were employed to adjust the humidity during some of the gas detection tests. The relative humidity (RH) level achieved inside the test chamber was verified employing a commercially available humidity sensor (E+E Electronics, Austria) placed in the vicinity of the device.

## 3. Results

### 3.1 Graphene growth optimization

Here, we expanded on Howsare *et al.* work [19], and evaluated the effect of the Cu and Ni films thickness in achieving wafer-scale growth of graphene by CVD. **Figure 1** shows representative SEM micrographs of the samples obtained via the following growth steps: 1) sample annealing at 900°C, for 10 min, 2) graphene growth at 940°C and using a $H_2$:$CH_4$ ratio of 1.5, for 10 min. To compare our graphene synthesis technique with the standard CVD graphene grown on Cu foil, a piece of a 25 µm thick Cu foil was placed beside the CNS samples. **Figure 1a** shows the presence of a significant number of spherical nanoparticles on the Cu foil surface after the growth step. This observation indicates that the Cu foil needs a pre-cleaning step, as explained elsewhere [17]. By contrast, there was no particle formation on the CNS samples (**Figures 1b to f**). For the N2S sample (**Figure 1b**), the formation of Ni grains with few tens of nm was observed. On the sample

surface, different image contrast was observed. Raman spectroscopy confirmed that the darkest area (marked with a red arrow) in **Figure 1b** corresponds to multi-layer graphene (not shown). The fainter area (top-left corner of **Figure 1b**) was identified as FLG, whereas the lighter area did not show the presence of graphene. This results agrees with previous reports confirming that it is rather challenging to control the number of graphene layers on a Ni substrate [40]. On the other hand, looking at the CNS, the surface texture is fairly uniform. For the C2N1S sample, no grain formation was noticed. However, the surface looks damaged (**Figure 1c**). For the other three samples, µm-sized grains were observed (**Figures 1d, e, f**) as well as holes that appeared in the thicker Cu films (500 nm) with a Ni barrier layer (100 or 200 nm) (**Figures 1e, f)**. Interestingly, for the C2N2S, these holes were rarely observed (**Figure 1d**). No full coverage of graphene was observed, except black patches were present in some areas. Using Raman spectroscopy, graphene was detected only in those areas of the C2N2S.

From above, the C2N2S-type samples were considered the most stable at the graphene growth conditions employed. Therefore, these samples were used to optimize large-area with full sample coverage graphene growth. Different reaction parameters were explored, as detailed in **Figure SI2** and the corresponding description. Briefly, the growth conditions were improved by introducing $CH_4$ (at 930°C) after the annealing step (at 900°C) for 30 min and ramping the temperature (to 950°C) for a graphene growth time of 10 min (**Figure 2a**). The results are presented in **Figures 2b to d**. SEM and Raman spectroscopy analyses were performed at different locations over a quarter of a 6" Si wafer (~50 $cm^2$), as shown in the inset of **Figure 2b**. The low magnification SEM image (**Figure 2b**) provides an overview of the sample, revealing no surface defects or damage. The corresponding high-resolution image (**Figure 2c**), showed the presence of 1 - 3 µm grains on the surface. Optical microscopy (**Figure 2d**) carried out on an identical sample showed areas with three different shades (dark, faint, and light). Typical Raman spectra recorded at these areas are presented in **Figure 2e**. As expected, the two main characteristic peaks of graphene were observed: the 2D band, located at ~2700 $cm^{-1}$, and the G band, centered at ~1580 $cm^{-1}$. Thus, with a 2D to G peak intensity ratio of 1 and 0.6, the light and faint areas correspond to bi-layer and tri-layer graphene (BLG and TLG), respectively. The dark regions correspond to multi-layer graphene (MLG). The lack of a D peak confirms the growth of graphene with high structural quality. In fact, only two dark patches (with a few $\mu m^2$) are visible over a 252 $\mu m^2$ area (**Figure 2d**). This indicates the dominance of FLG over the entire sample surface. The effect of the annealing step on the

topography and surface microstructure of the CNS samples was studied using AFM and EBSD, respectively (refer to **Figures SI3, SI4 SI5,** and corresponding descriptions). The majority of the *fcc*-Cu grains with large size (1- 3 μm) had the (111) planes parallel to the surface (**Figure SI5**), an orientation known to be favorable for SLG growth [41]. In these circumstances, we achieved uniform FLG on the C2N2S samples, i. e. without surface structural defects such as particle formation and/or agglomeration, holes, etc.. (**Figure 2**). Henceforth, the growth conditions in **Figure 2a** will be considered as the optimized conditions to grow high-quality FLG.

### 3.3 Structural characterization of the optimal C2N2S samples

The XRD, presented in **Figure 3** shows diffraction peaks at 2θ = 44.1º, 51.6º, and 75.2º, which match closely to the (111), (200) and (220) planes, respectively, of the $Cu_{2.7}$ $Ni_{1.8}$ $Si_{0.4}$ alloy (JCPDS data PDF 65-7517). However, and as discussed later, the localized EDX analyses on the cross-sectional TEM lamella (**Figures 4** and **SI6**), did not show the presence of Si in the Cu/Ni film region. Therefore, rather than the $Cu_{2.7}$ $Ni_{1.8}$ $Si_{0.4}$ phase, we refer to the formation of a Cu-rich CuNi alloy instead. The sharp (111) peak agrees well with the EBSD results (**Figure SI5**). Two other peaks, at 2θ = 33º and 69.5º, correspond to the $SiO_2$/Si substrate [42]. Thus, the Ni barrier layer prevents inter-diffusion of Cu and $SiO_2$ by the formation of a Cu-rich Cu-Ni alloy.

To understand the microstructural evolution of the Cu and Ni films, cross-sectional TEM imaging (**Figure 4**) was performed on the as-deposited and graphene grown C2N2S samples. **Figure 4a** is a low magnification image of the as-deposited C2N2S, where the presence of a boundary between the Cu and Ni layers is clearly visible (also confirmed with EDX mapping in this region, not shown). The TEM analysis (**Figure 4b)** of the C2N2S sample after the graphene growth suggests that during the annealing and growth steps, the Ni and Cu film underwent mixing and formed a solid solution (refer to **Figures SI6f-k**). This process occurrence is in agreement with the change in the sample color (top layer of the graphene/C2N2S sample) observed with naked-eye: from a Cu-like brown to a grey hue (see sample photo, inset of **Figure 2b**). From **Figure 4b**, the Cu-Ni film appears crystalline in the vicinity of the surface. Fast Fourier Transform (FFT) of the Cu-Ni portion (marked with a dotted red square) is shown in the inset of **Figure 4b**. From this, the measured interplanar distance (d) is found to be 0.21 nm. The (111) interplanar distance is close to that of a $Cu_{3.8}Ni$ alloy, $d_{(111)}$ = 0.208 nm [43]. This result agrees with the XRD and indicates the formation of a Cu-rich Cu-Ni alloy (**Figure 3**). The slight difference in the exact CuNi alloy phase

determination can be explained by the fact that the XRD detection occurs over a few microns of depth (averaged signal over $\mu m^3$) while TEM characterization is more localized (few $nm^2$).

The EDX mapping of the FLG/C2N2S (**Figure SI6g-k**) shows a homogeneous distribution of Cu and Ni over the 400 nm film thickness. It supports the formation of a Cu-Ni solid solution during the annealing and growth steps. The formation of voids in the Cu and Ni film was not observed in the cross-sectional TEM images, confirming the absence of holes in the catalyst film (**Figure 2**). This result is attributed to the strengthening of the Cu film, provided by alloying. The EDS mapping suggests that diffusion of Cu and Ni in $SiO_2$ did not occur. This result agrees with the results of Howsare et al., who claimed that a 5 - 50 nm Ni film reduces the inter-diffusion of Cu and $SiO_2$ [19]. We, therefore, confirm that the main cause of the Cu film instability on $SiO_2$/Si is overcome by the addition of a Ni film that acts as a barrier buffer. It should be noted that the inter-diffusion phenomenon explained here is growth specific and bears no direct effect on the gas-sensing influence of FLG, explained next.

### 3.4. Characterization of transferred FLG

For most applications, the graphene grown by CVD usually needs to be transferred from the catalytic metal sheet/film to the desired substrate. A digital picture of the transferred FLG (with PMMA layer and Cu grids trapped underneath) onto an alumina substrate is shown in **Figure 5a**. After the removal of PMMA, the Cu grids were detached from the FLG layer **(Figure 5b)**. Except for the area that was covered with the grids, the presence of a continuous FLG film is obvious. A piece of about 2 $cm^2$ was extracted from a second FLG sample and transferred to the array of Si nanopillars. The homogeneity of this layer was assessed using SEM, AFM, and Raman spectroscopy. The SEM images, displayed in **Figures 5c** and **d**, indicate that the graphene is present over a large extension of the Si nanopillars array. In **Figures 5d and e**, it is possible to distinguish the edge of the FLG and the nanopillars underneath it, revealing that the transferred layer is thin and transparent to the electron beam. Considering that the substrate had a 3D morphology, the absence of cracks in the graphene is remarkable and attests its mechanical resilience. Raman spectra characteristic of BLG and TLG were obtained when analyzing this layer (**Figure 5f**). The negligible D peak confirms the presence of a clean and high structural quality FLG film. Alongside, the substrate peaks - of Si (520 $cm^{-1}$) and $SiO_2$ (hump at ~950 $cm^{-1}$) - were

also seen. Overall, it was possible to mount a $cm^2$ FLG film on a three-dimensional substrate without compromising its structural integrity.

### 3.4 Gas sensing studies

Afterward, the FLG/Si nanopillar sensor was exposed to repeated response and recovery cycles of $NO_2$ at 250, 500, 750, and 1000 ppb. The values of the sensor baseline resistance under dry or humid conditions either at room temperature or when operated at 100ºC are summarized in **Table S1** (supporting information). Overall, the device response increased with increments in gas concentration (**Figure 6**). The augmented response correlates with a better charge transport by the film, implying a measurable interaction with the gas. In fact, in the absence of moisture and at RT, it is known that $NO_2$ molecules can be physisorbed on graphene (with an energy of 67 meV) besides acting as electron acceptors [44]. The transfer of electronic charges will increase the concentration of holes in shifting its behavior to a mild p-type semiconductor, i.e., with its Dirac point below the Fermi level [45]. When the operating temperature was increased from RT to 100ºC, a slight improvement in the response ($\Delta R/R_0$) to $NO_2$ was obtained (**Figure 6b**). Likely, the adsorption/desorption interaction is more intense, which leads to more pronounced charge transfer between the gas molecules and the FLG [46]. Our results match well with those of Xie et al., who reported that the best working temperature for monolayer graphene is near 100ºC [46]. According to these authors, when the operating temperature is raised to 200ºC (or more), the response decreases because the desorption process dominates over the adsorption one. The detection of $NO_2$ in the presence of moisture was also studied, and the response to $NO_2$ was always higher than under dry conditions (**Figure 6b**). The well-structured lattice of the FLG could account for this. When moisture is adsorbed, charge transfer from graphene to the $H_2O$ molecule is expected [44] [22]. Accordingly, the simultaneous presence of $NO_2$ and $H_2O$ increases the conductivity of the film, via an additive effect, since both molecules behave as electron acceptors over a p-type material. Further to this, it is interesting to notice that the best response occurs at RT. Possibly, and at 100ºC, the additive effect is weaker because the water molecules are more mobile and less likely to adsorb onto the graphene (i.e., they are in a higher vibrational energy state, hence with lower surface residency time)., Additional measurements down to ultra-low concentrations were performed (**Figure SI7**), considering the good reproducibility and stability of the $NO_2$ response in the 250 to 1000 ppb range. The device could reliably detect this gas at 25 ppb, a remarkable figure

for a pristine graphene layer. Taken together, and at the optimum working conditions (RT and 50% RH), the $NO_2$ sensitivity of the chemiresistive FLG-based device was $1.5\times10^{-2}$ % per ppb. The FLG sensor showed high reproducibility and stability over time, obtaining repeatable responses after several weeks of use. We observed a slight baseline drift during the repeated measurements. However, the relative resistance changes upon specific gas concentrations remain stable.

To better understand the sensing mechanism, the detection of $NH_3$ was also evaluated. The typical resistance changes experienced by our FLG sensor, under repeated cycles of $NH_3$ exposure and varied conditions, are shown in **Figure 7**. Repeated baseline recovery cycles were performed before each set of measurements. At 100ºC and dry conditions, the response pattern is highly reproducible and stable over long periods of time (**Figure 7a**). When compared to $NO_2$, a relatively lower response was observed. This lower response is explained by the $NH_3$ molecules acting as electron donors and having lower physisorption energy on graphene (31 meV) [47] [44]. In the presence of moisture, the $NH_3$ response was lower. It is worth noting that $H_2O$ molecules can act as electron-acceptor or electron-donors, depending on the experimental conditions and the nature of the sensing film [48]. Although a donor behavior cannot be completely discarded, Hall measurements reveal that water molecules act as electron-acceptors in graphene gas sensors at room or moderate temperature [22, 49]. This is logical: since the $H_2O$ molecules act as electron acceptors (while $NH_3$ acts as an electron donor). Hence, there is an opposite effect that will cancel out major changes to the FLG conductivity. On the whole, the ammonia-to-graphene charge transfers are more pronounced at 100ºC and in the absence of moisture (**Figure 7b**). In the 25 to 100 ppm range, and at these optimum working conditions, the $NH_3$ sensitivity is 5.3 x $10^{-2}$ % per ppm. This sensitivity is roughly three orders of magnitude lower than the $NO_2$.

Taking into consideration the sensitivities obtained for $NO_2$ and $NH_3$, the limits of detection (LOD) and quantification (LOQ) were estimated. The LOD is the lowest concentration that can be surely registered; in other words, the minimum change in the signal that can be clearly distinguished from noise. As for the LOQ, it represents the lowest concentration that can be quantified. A factor of 3 and 10 was applied for the LOD and the LOQ, respectively, establishing a noise level of 150 mΩ and employing the slope obtained in the linear regression for the optimum working conditions for $NO_2$ and $NH_3$ [50]. For $NO_2$, a LOD of 5 ppb and a LOQ of 16.7 ppb were calculated. For $NH_3$,

these values were higher, at 1 ppm and 3.4 ppm, respectively. In both cases, the estimated limits are below the gas exposure thresholds advised by the World Health Organization [51], making our FLG-based sensor a promising alternative to more expensive and cumbersome devices.

### 3.5 Discussion

Commonly, the high-temperature exposure of Cu films deposited on $SiO_2$/Si substrates leads to a damaged surface due to the inter-diffusion of Cu and $SiO_2$ [19]. Our results show that this phenomenon is suppressed using a 200 nm barrier layer of Ni, which upon the annealing and growth steps, bonds with Cu. Besides eliminating inter-diffusion, the presence of Ni also increases the solubility of C in the catalytic layer. For this reason, the production of FLG took place rather than the self-limited monolayer growth usually observed on Cu [16].

Pristine graphene is often reported to possess limited responsiveness to gas molecules [52], as summarized in **Tables 2** and **3**. For our FLG layers, X-ray photoelectron (XPS, not shown) and Raman spectroscopies revealed that there were no oxygenated chemical groups or a high density of other carbon lattice defects. Still, the $NO_2$ sensitivity reported here is higher than that claimed for CVD graphene [34, 53] or highly defective graphene materials such as graphene oxide [54] [55] or reduced graphene oxide [56, 57], even when functionalized with chemical moieties or nanoparticles [25, 32, 58]. In fact, it is well-known that the presence of defects and functional groups in carbon nanomaterials represent additional sites for adsorption of $NO_2$ molecules [59]. Generally, these lattice imperfections correlate with higher gas adsorption energies, in which case it will be more difficult to recover the sensor baseline [59]. While our FLG layer did not have oxygenated groups or defects, it was made of BLG, TLG, and MLG domains (**Figure 5f**). In these circumstances, we propose that the surface steps derived from the presence of these domains contributed to the notable gas response observed. These steps would not alter considerably the Raman and XPS spectral signatures but would be preferred adsorption sites for the gas molecules [60-63]. At RT, the sensing mechanism is dominated by charge transfer through physisorption of $NO_2$ and $NH_3$, because, if there was chemisorption of $NO_2$, we would not observe significant baseline recovery.

Here, it should be steered that unlike previous reports (**Tables 2 and 3**), the gas-sensing studies were carried out using low gas flows (100 sccm) and long reaction times (30 min), close to the practical conditions of environmental monitoring sensors. The response/recovery is slow, which could be further improved by decreasing the dead volume in the airtight chamber or device miniaturization [64]. Therefore, considering the high sensitivity obtained for low concentration of pollutants (**Table 2**), the as-produced FLG shows a high potential to be further optimized towards a commercial $NO_2$ gas-sensor for continuous environmental monitoring [13].

Finally, one other factor at the origin of the excellent sensitivity and reproducibility of the $NO_2$ detection is the unique device configuration used. When compared to flat substrates [65], an array of nanopillars bears the advantage of providing access to the backside surface of the graphene layer, thereby increasing the exposed surface area of sensing material [39]. In this respect, the available active area is almost doubled. Suspending the graphene could also assist in obtaining an excellent baseline recovery, even at moderate temperatures. Such a configuration prevents trapping of gas molecules underneath the sensing layer and allows for a faster evacuation ahead of the next detection cycle.

## 4. Conclusions

The growth of wafer-scale (~50 $cm^2$) FLG with high structural quality was successfully achieved using Cu films deposited on $SiO_2$/Si and an optimized Ni barrier layer. The formation of a Cu-rich Cu-Ni alloy, during the annealing and growth steps, is crucial to minimize the Cu and $SiO_2$ inter-diffusion and controllably obtain FLG. We demonstrated the applicability of the as-produced graphene for $NO_2$ and $NH_3$ gas sensing, after transferring it onto an array of Si nanopillars. A remarkable response was observed for both gases. At RT and in the presence of moisture, $NO_2$ could be detected over a wide concentration range, with a calculated LOD of 5 ppb. Under similar conditions, a relatively lower sensitivity was observed for $NH_3$ (LOD of 1 ppm) but this low sensitivity was explained by the type of gas interrogated.

The CVD growth of the FLG and its device integration, as described, represent a more viable work-flow than previous approaches for the fabrication of graphene-based gas-sensing systems. Besides minimizing the financial and environmental costs, this work-flow does not compromise

critical properties such as sensitivity (for electron acceptor gases, e.g., $NO_2$) and avoids cumbersome steps such as graphene surface functionalization and particle loading.

**Acknowledgements**

This work was funded by the Masdar Institute (contract EX2016-000026) and KAUST (BAS/1/1346-01-01). We are thankful to Dr. Sozaraj Rasappa (Tampere University, Finland) for the patterned Si nanopillar substrate. GD is thankful to Leslie George (Khalifa University, Abu Dhabi) for technical support. E.L. is supported by the Catalan Institution for research and Advanced Studies via the 2018 ICREA Academia Award, by MINECO and FEDER under grant no. TEC2015- 71663R and by AGAUR under grant no. 2017 SGR 418.

**References**

[1] K.S. Novoselov, V.I. Fal'ko, L. Colombo, P.R. Gellert, M.G. Schwab, K. Kim, A roadmap for graphene, Nature 490 (2012) 192-200.
[2] A.C. Ferrari, F. Bonaccorso, V. Fal'ko, K.S. Novoselov, S. Roche, P. Boggild, et al., Science and technology roadmap for graphene, related two-dimensional crystals, and hybrid systems, Nanoscale 7(2015) 4598-4810.
[3] W. Wei, X. Zhou, G. Deokar, H. Kim, M.M. Belhaj, E. Galopin, et al., Graphene FETs With Aluminum Bottom-Gate Electrodes and Its Natural Oxide as Dielectrics, Ieee T Electron Dev 62(2015) 2769-2773.
[4] F. Bonaccorso, Z. Sun, T. Hasan, A.C. Ferrari, Graphene photonics and optoelectronics, Nat Photonics 4(2010) 611-622.
[5] X.H. Cao, Y.M. Shi, W.H. Shi, G. Lu, X. Huang, Q.Y. Yan, et al., Preparation of Novel 3D Graphene Networks for Supercapacitor Applications, Small 7(2011) 3163-3168.
[6] F. Lang, M.A. Gluba, S. Albrecht, J. Rappich, L. Korte, B. Rech, et al., Perovskite Solar Cells with Large-Area CVD-Graphene for Tandem Solar Cells, J Phys Chem Lett 6 (2015) 2745-2750.
[7] Z.Y. Yin, J.X. Zhu, Q.Y. He, X.H. Cao, C.L. Tan, H.Y. Chen, et al., Graphene-Based Materials for Solar Cell Applications, Adv Energy Mater 4(2014).
[8] X.D. Wang, D.L. Gao, M.J. Li, H.J. Li, C.P. Li, X.G. Wu, et al., CVD graphene as an electrochemical sensing platform for simultaneous detection of biomolecules, Scientific reports 7 (2017).
[9] S.X. Yang, C.B. Jiang, S.H. Wei, Gas sensing in 2D materials, Appl Phys Rev 4(2) (2017).
[10] F. Yavari, N. Koratkar, Graphene-Based Chemical Sensors, J Phys Chem Lett 3(2012) 1746-1753.
[11] W.J. Yuan, G.Q. Shi, Graphene-based gas sensors, J Mater Chem A 1(2013) 10078-10091.

[12] F. Yavari, E. Castillo, H. Gullapalli, P.M. Ajayan, N. Koratkar, High sensitivity detection of $NO_2$ and $NH_3$ in air using chemical vapor deposition grown graphene, Applied Physics Letters 100(20) (2012).
[13] W.C. Tian, X.H. Liu, W.B. Yu, Research Progress of Gas Sensor Based on Graphene and Its Derivatives: A Review, Applied Sciences-Basel 8(7) (2018).
[14] Q.Y. He, S.X. Wu, Z.Y. Yin, H. Zhang, Graphene-based electronic sensors, Chemical Science 3(2012) 1764-1772.
[15] S. Bae, H. Kim, Y. Lee, X.F. Xu, J.S. Park, Y. Zheng, et al., Roll-to-roll production of 30-inch graphene films for transparent electrodes, Nature Nanotechnology 5(2010) 574-578.
[16] X. Li, W. Cai, J. An, S. Kim, J. Nah, D. Yang, et al., Large-area synthesis of high-quality and uniform graphene films on copper foils, Science 324(2009) 1312-4.
[17] G. Deokar, J. Avila, I. Razado-Colambo, J.L. Codron, C. Boyaval, E. Galopin, et al., Towards high quality CVD graphene growth and transfer, Carbon 89(2015) 82-92.
[18] D.R. Cooper, B. D'Anjou, N. Ghattamaneni, B. Harack, M. Hilke, A. Horth, et al., Experimental Review of Graphene, ISRN Condensed Matter Physics 2012 (2012) 56.
[19] C.A. Howsare, X.J. Weng, V. Bojan, D. Snyder, J.A. Robinson, Substrate considerations for graphene synthesis on thin copper films, Nanotechnology 23(13) (2012).
[20] K. Hayashi, S. Sato, N. Yokoyama, Anisotropic graphene growth accompanied by step bunching on a dynamic copper surface, Nanotechnology 24(2013) 025603.
[21] M.P. Levendorf, C.S. Ruiz-Vargas, S. Garg, J. Park, Transfer-Free Batch Fabrication of Single Layer Graphene Transistors, Nano letters 9(2009) 4479-4483.
[22] F. Schedin, A.K. Geim, S.V. Morozov, E.W. Hill, P. Blake, M.I. Katsnelson, et al., Detection of individual gas molecules adsorbed on graphene, Nature Materials 6(2007) 652-655.
[23] J.D. Fowler, M.J. Allen, V.C. Tung, Y. Yang, R.B. Kaner, B.H. Weiller, Practical Chemical Sensors from Chemically Derived Graphene, Acs Nano 3(2009) 301-306.
[24] T.T. Tung, N.V. Chien, N. Van Duy, N. Van Hieu, M.J. Nine, C.J. Coghlan, et al, Magnetic iron oxide nanoparticles decorated graphene for chemoresistive gas sensing: The particle size effects, J Colloid Interface Sci 539 (2019) 315-325.
[25] M. Zhao, F.L. Dong, L.Q. Yan, L.H. Xu, X.F. Zhang, P.P. Chen, et al., High efficiency room temperature detection of NO2 gas based on ultrathin metal/graphene devices, Rsc Advances 6(2016) 84082-84089.
[26] S.L. Zhang, N.T. Hang, Z.J. Zhang, H.Y. Yue, W. Yang, Preparation of g-$C_3N_4$/Graphene Composite for Detecting $NO_2$ at Room Temperature, Nanomaterials-Basel 7(1) (2017).
[27] B. Zhang, G.N. Liu, M. Cheng, Y. Gao, L.J. Zhao, S. Li, F.M. Liu, et al., The preparation of reduced graphene oxide-encapsulated alpha-$Fe_2O_3$ hybrid and its outstanding $NO_2$ gas sensing properties at room temperature, Sensor Actuat B-Chem 261(2018) 252-263.
[28] T.T. Wang, J.Y. Hao, S.L. Zheng, Q. Sun, D. Zhang, Y. Wang, Highly sensitive and rapidly responding room-temperature $NO_2$ gas sensors based on $WO_3$ nanorods/sulfonated graphene nanocomposites, Nano Res 11(2018) 791-803.
[29] A. Alazmi, S. Rasul, S.P. Patole, P.M.F.J. Costa, Comparative study of synthesis and reduction methods for graphene oxide, Polyhedron 116 (2016) 153-161.
[30] Z.F. Liu, Z.H. Chen, F. Yu, Microencapsulated phase change material modified by graphene oxide with different degrees of oxidation for solar energy storage, Solar Energy Materials and Solar Cells 174 (2018) 453-459.

[31] V.V. Quang, N.V. Dung, N.S. Trong, N.D. Hoa, N.V. Duy, N.V. Hieu, Outstanding gas-sensing performance of graphene/$SnO_2$ nanowire Schottky junctions, Applied Physics Letters 105(2014).
[32] M.G. Chung, D.H. Kim, H.M. Lee, T. Kim, J.H. Choi, D.K. Seo, et al., Highly sensitive $NO_2$ gas sensor based on ozone treated graphene, Sensor Actuat B-Chem 166 (2012) 172-176.
[33] L.F. Guo, T. Li, Sub-ppb and ultra selective nitrogen dioxide sensor based on sulfur doped graphene, Sensor Actuat B-Chem 255 (2018) 2258-2263.
[34] H. Choi, J.S. Choi, J.S. Kim, J.H. Choe, K.H. Chung, J.W. Shin, et al., Flexible and Transparent Gas Molecule Sensor Integrated with Sensing and Heating Graphene Layers, Small 10(18) (2014) 3685-3691.
[35] Y.H. Kim, S.J. Kim, Y.J. Kim, Y.S. Shim, S.Y. Kim, B.H. Hong, et al., Self-Activated Transparent All-Graphene Gas Sensor with Endurance to Humidity and Mechanical Bending, ACS nano 9 (2015) 10453-10460.
[36] S. Novikov, N. Lebedeva, A. Satrapinski, Ultrasensitive $NO_2$ Gas Sensor Based on Epitaxial Graphene, Journal of Sensors (2015).
[37] N.S. Rajput, S.-G. Kim, J.B. Chou, J. Abed, J. Viegas, M. Jouiad, Electron beam induced rapid crystallization of water splitting nanostructures, MRS Advances 1(2016) 825-830.
[38] S. Rasappa, D. Borah, R. Senthamaraikannan, C.C. Faulkner, M.T. Shaw, P. Gleeson, et al., Block copolymer lithography: Feature size control and extension by an over-etch technique, Thin Solid Films 522 (2012) 318-323.
[39] G. Deokar, P. Vancso, R. Arenal, F. Ravaux, J. Casanova-Chafer, E. Llobet, et al., $MoS_2$-Carbon Nanotube Hybrid Material Growth and Gas Sensing, Adv Mater Interfaces 4(2017).
[40] A. Dahal, M. Batzill, Graphene-nickel interfaces: a review, Nanoscale 6(2014) 2548-62.
[41] J.D. Wood, S.W. Schmucker, A.S. Lyons, E. Pop, J.W. Lyding, Effects of Polycrystalline Cu Substrate on Graphene Growth by Chemical Vapor Deposition, Nano letters 11(2011) 4547-4554.
[42] P.S. Lee, D. Mangelinck, K.L. Pey, Z.X. Shen, J. Ding, T. Osipowicz, A. See, Micro-Raman spectroscopy investigation of nickel silicides and nickel (platinum) silicides, Electrochem Solid St 3(2000) 153-155.
[43] N. Rajasekaran, S. Mohan, Structure, microstructure and corrosion properties of brush-plated Cu-Ni alloy, J Appl Electrochem 39(2009) 1911-1916.
[44] O. Leenaerts, B. Partoens, F.M. Peeters, Adsorption of $H_2O$, $NH_3$, CO, $NO_2$, and NO on graphene: A first-principles study, Physical Review B 77(12) (2008).
[45] W. Zhang, L. Wu, Z. Li, Y. Liu, Doped graphene: synthesis, properties and bioanalysis, Rsc Adv 5(2015) 49521-49533.
[46] H.F. Xie, K.K. Wang, Z.Q. Zhang, X.J. Zhao, F. Liu, H.C. Mu, Temperature and thickness dependence of the sensitivity of nitrogen dioxide graphene gas sensors modified by atomic layer deposited zinc oxide films, Rsc Advances 5(2015) 28030-28037.
[47] G. Lee, G. Yang, A. Cho, J.W. Han, J. Kim, Defect-engineered graphene chemical sensors with ultrahigh sensitivity, Physical Chemistry Chemical Physics 18(2016) 14198-14204.
[48] G. Korotcenkov, Handbook of Humidity Measurement, 1st Edition ed., CRC Press, Boca Raton, 2019.
[49] S. Knight, T. Hofmann, C. Bouhafs, N. Armakavicius, P. Kuhne, V. Stanishev, et al., In-situ terahertz optical Hall effect measurements of ambient effects on free charge carrier properties of epitaxial graphene, Scientific Reports 7(2017) 5151.
[50] A. Shrivastava;, V.B. Gupta, Methods for the determination of limit of detection and limit of quantitation of the analytical methods, Chron. Young. Sci. 2(2011) 5.

[51] https://www.who.int/en/news-room/fact-sheets/detail/ambient-(outdoor)-air-quality-and-health.
[52] F.L. Meng, Z. Guo, X.J. Huang, Graphene-based hybrids for chemiresistive gas sensors, Trac-Trend Anal Chem 68 (2015) 37-47.
[53] C. Lee, J. Ahn, K.B. Lee, D. Kim, J. Kim, Graphene-based flexible $NO_2$ chemical sensors, Thin Solid Films 520(2012) 5459-5462.
[54] C. Piloto, M. Notarianni, M. Shafiei, E. Taran, D. Galpaya, C. Yan, et al., Highly NO2 sensitive caesium doped graphene oxide conductometric sensors, Beilstein J Nanotech 5 (2014) 1073-1081.
[55] L. Guo, Y.W. Hao, P.L. Li, J.F. Song, R.Z. Yang, X.Y. Fu, et al., Improved $NO_2$ Gas Sensing Properties of Graphene Oxide Reduced by Two-beam-laser Interference, Scientific reports 8 (2018).
[56] H. Zhang, Q. Li, J.Y. Huang, Y. Du, S.C. Ruan, Reduced Graphene Oxide/Au Nanocomposite for $NO_2$ Sensing at Low Operating Temperature, Sensors 16(7) (2016).
[57] P.G. Su, H.C. Shieh, Flexible $NO_2$ sensors fabricated by layer-by-layer covalent anchoring and in situ reduction of graphene oxide, Sensor Actuat B-Chem 190 (2014) 865-872.
[58] L. Li, S.J. He, M.M. Liu, C.M. Zhang, W. Chen, Three-Dimensional Mesoporous Graphene Aerogel-Supported SnO2 Nanocrystals for High-Performance $NO_2$ Gas Sensing at Low Temperature, Anal Chem 87(2015) 1638-1645.
[59] Y. You, J. Deng, X. Tan, N. Gorjizadeh, M. Yoshimura, S.C. Smith, et al., On the mechanism of gas adsorption for pristine, defective and functionalized graphene, Physical Chemistry Chemical Physics 19(8) (2017) 6051-6056.
[60] A. Salehi-Khojin, D. Estrada, K.Y. Lin, M.H. Bae, F. Xiong, E. Pop, R.I. Masel, Polycrystalline Graphene Ribbons as Chemiresistors, Adv Mater 24(2012) 53-57.
[61] R.K. Paul, S. Badhulika, N.M. Saucedo, A. Mulchandani, Graphene Nanomesh as Highly Sensitive Chemiresistor Gas Sensor, Anal Chem 84(2012) 8171-8178.
[62] M.M. Pour, A. Lashkov, A. Radocea, X.M. Liu, T. Sun, A. Lipatov, et al., A. Sinitskii, Laterally extended atomically precise graphene nanoribbons with improved electrical conductivity for efficient gas sensing, Nature communications 8(2017).
[63] A. N. Abbas, B. Liu, L. Chen, Y. Ma, S, Cong, N. Aroonyadet et. al., ACS Nano., Black Phosphorus Gas Sensors, 9 (2015) 5618-5624.
[64] O. Moncea, J. Casanova-Chafer, D. Poinsot, L. Ochmann, C.D. Mboyi, H.O. Nasrallah, et. al, J.C. Hierso, Diamondoid Nanostructures as sp3- Carbon- Based Gas Sensors, Angewandte Chemie-International Edition 58(2019) 9933-9938.
[65] S.W. Lee, W. Lee, Y. Hong, G. Lee, D.S. Yoon, Recent advances in carbon material-based $NO_2$ gas sensors, Sensor Actuat B-Chem 255 (2018) 1788-1804

**Figures**

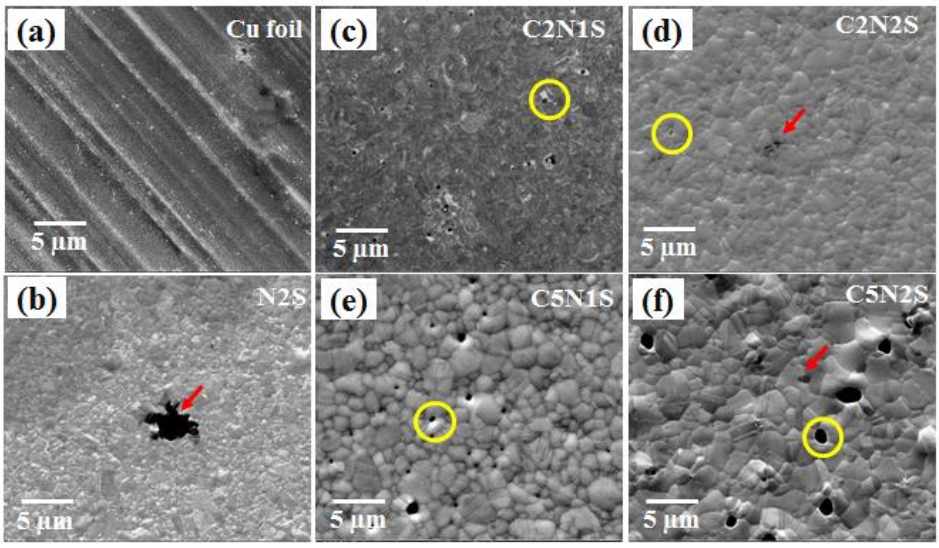


**Figure 1.** Graphene growth carried out on different samples (refer Table 1) with varied Ni and Cu thickness and 25 µm Cu foil with pre-annealing at 900°C for 10 min and growth temperature 940°C, with $H_2$ to $CH_4$ flow ratio of 1.5 for 10 min. Typical dark patches of graphene are marked by red arrow. Typical holes in the CNS films are marked by yellow circle. Scale bar is same for all images as that of panel (a)

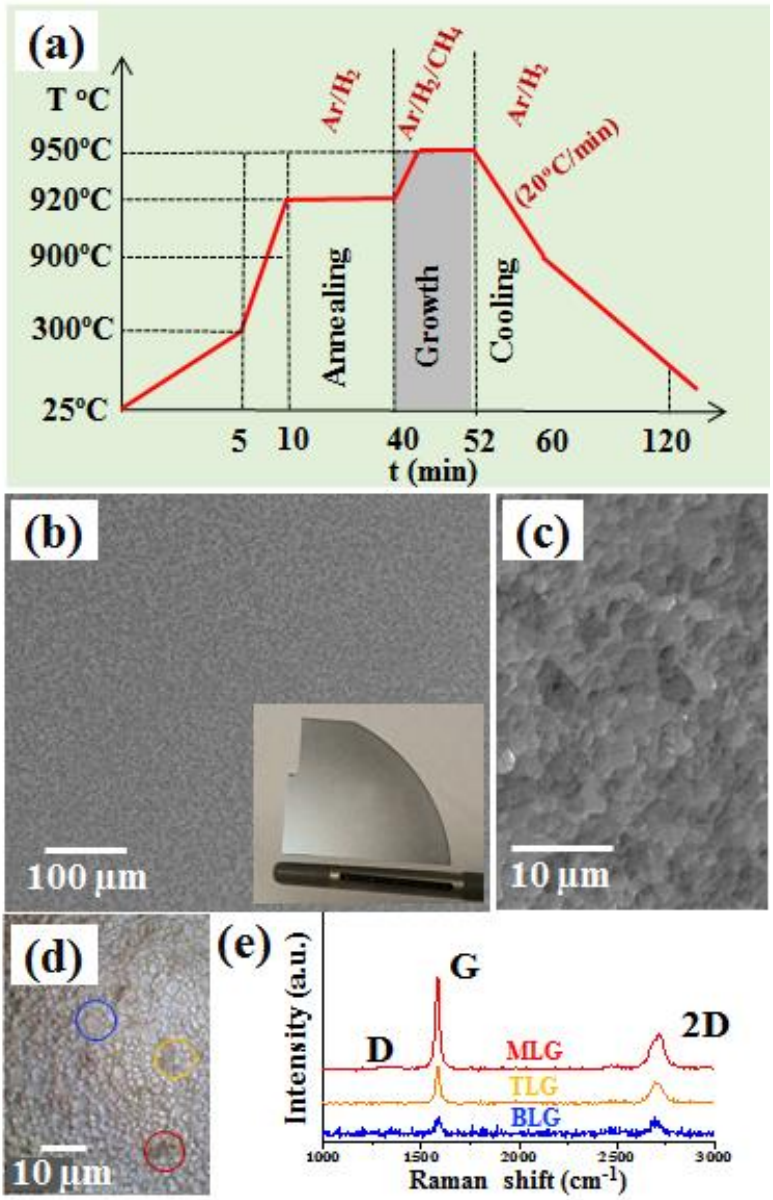


**Figure 2**. (a) Schematic of optimized growth recipe. SEM images of graphene grown on C2N2S at optimized growth conditions: (b) Low magnification image graphene growth with a photo of sample in the inset (quarter of 6" Si wafer), (c) High resolution image. (d) Optical microscopy image. (e) Raman spectra recorded at different positions on the image in panel (d) marked by red, orange and blue circles.

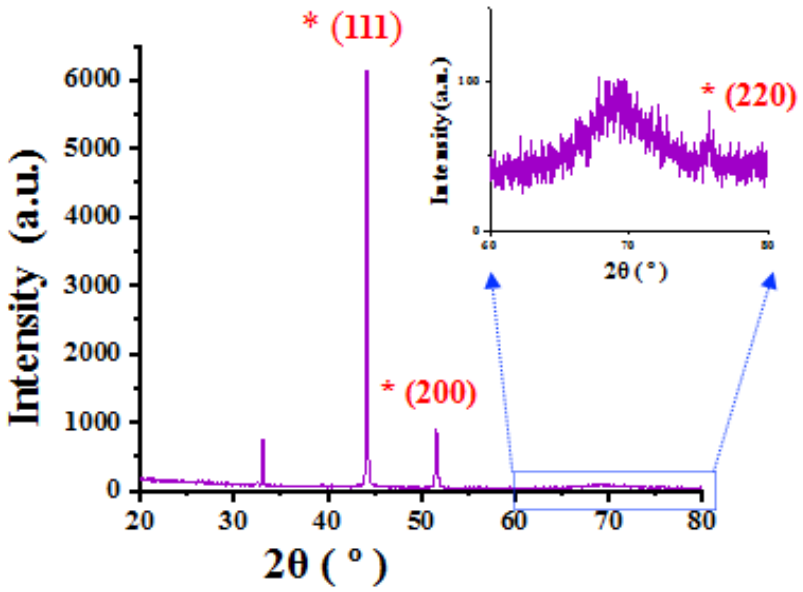


**Figure 3.** XRD spectra for C2N2S sample grown at optimized condition. Peaks marked with ' * ' corresponds to $Cu_{2.7}$ $Ni_{1.84}Si_{0.4}$ phase.

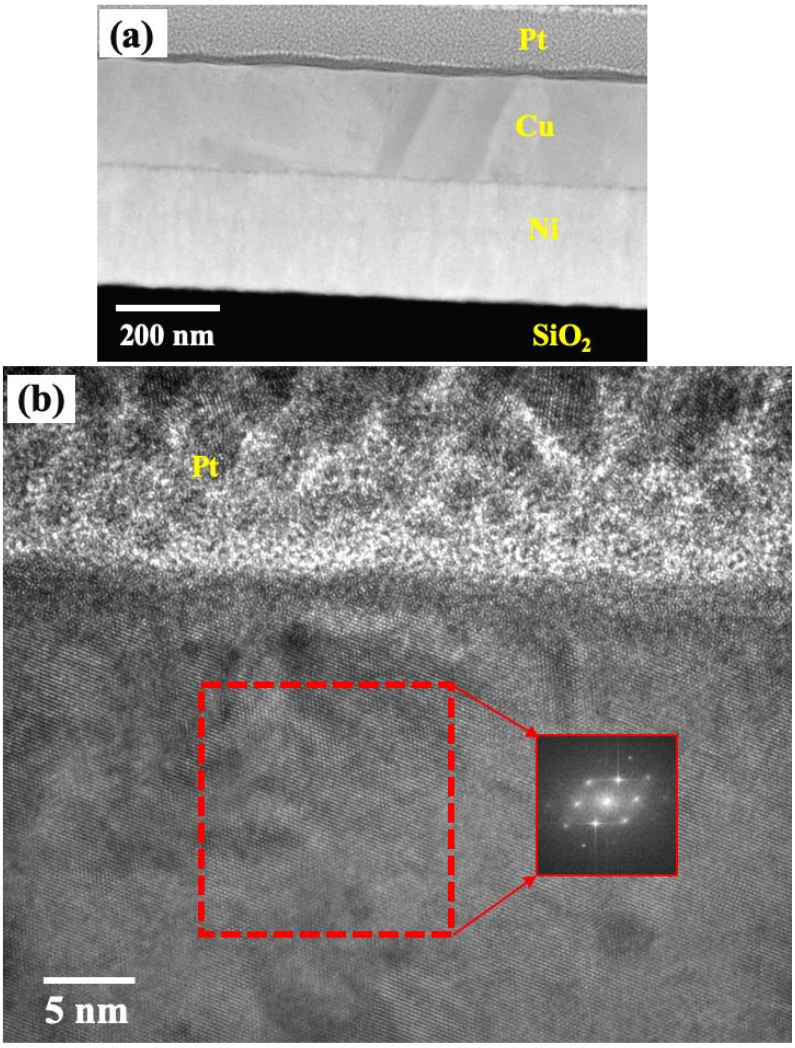


**Figure 4**. Cross-section TEM images for C2N2S sample: (a) Un-annealed film, (b) After FLG growth at optimized conditions with low resolution TEM image and FFT pattern for red dotted square in the inset.

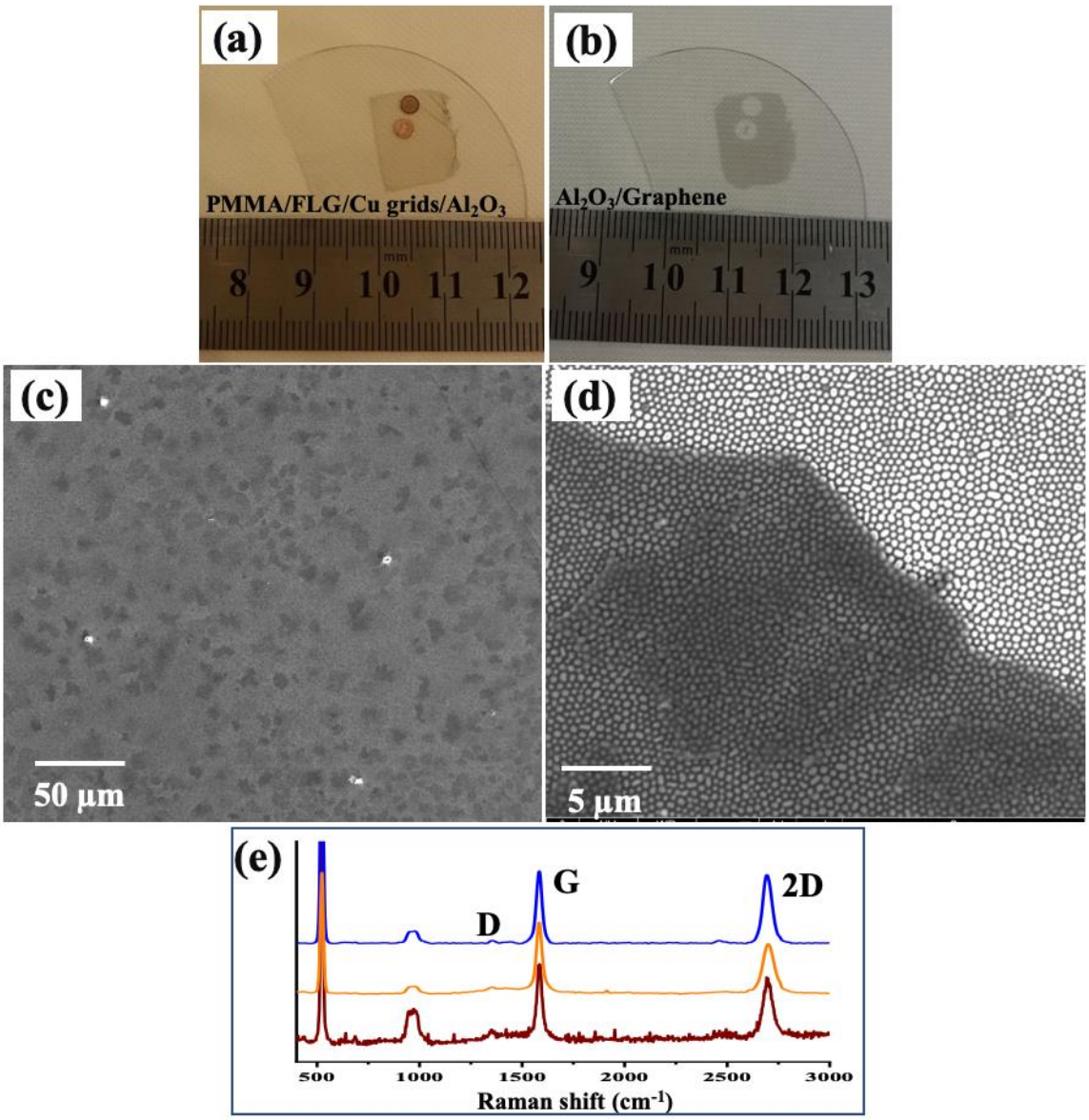


**Figure 5**. Digital photographs of FLG transferred on alumina: (a) PMMA/FLG with Cu grids underneath, (b) after PMMA and Cu grids removal. SEM images of FLG transferred on patterned $SiO_2$/Si nanopillar substrates: (c) Low resolution SEM image, (d) and (e) High resolution SEM images around the graphene edge. (f) Typical Raman spectra at different positions.

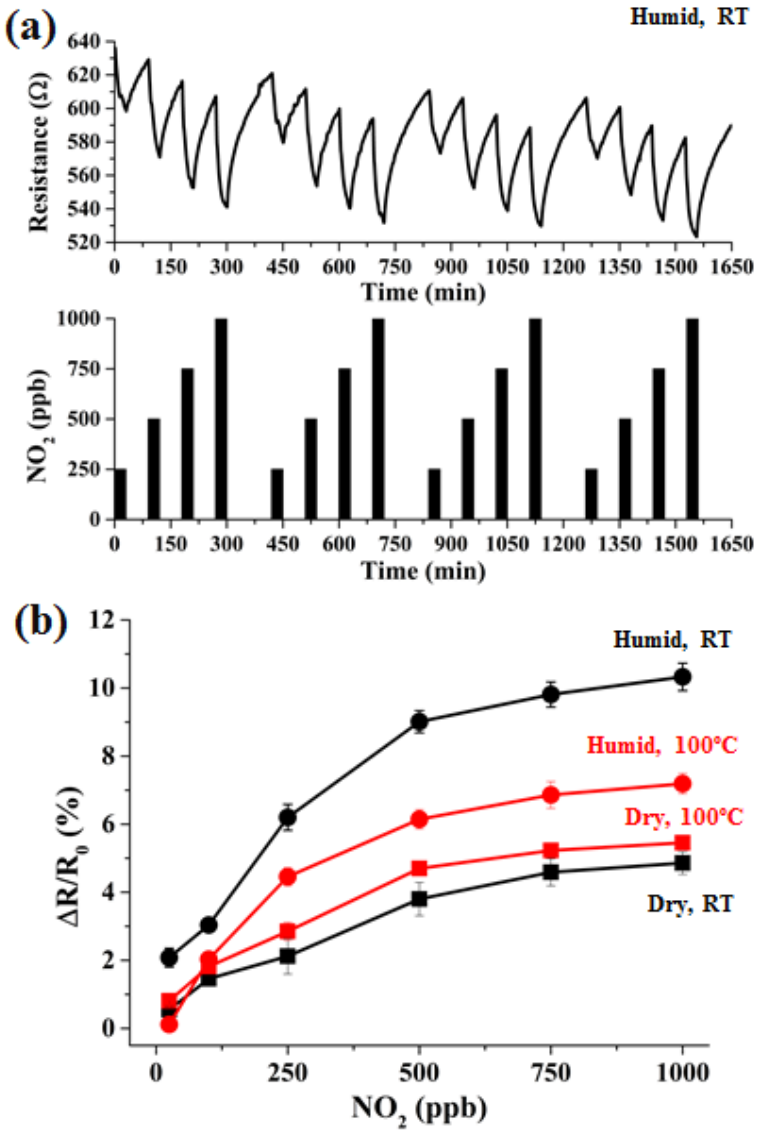


**Figure 6.** (a) Example of $NO_2$ detection at RT and under a RH of 50%. (b) Calibration curves obtained for $NO_2$ detection (black line: RT; red line: 100ºC; square symbol: dry conditions; circle symbol: 50% of RH).

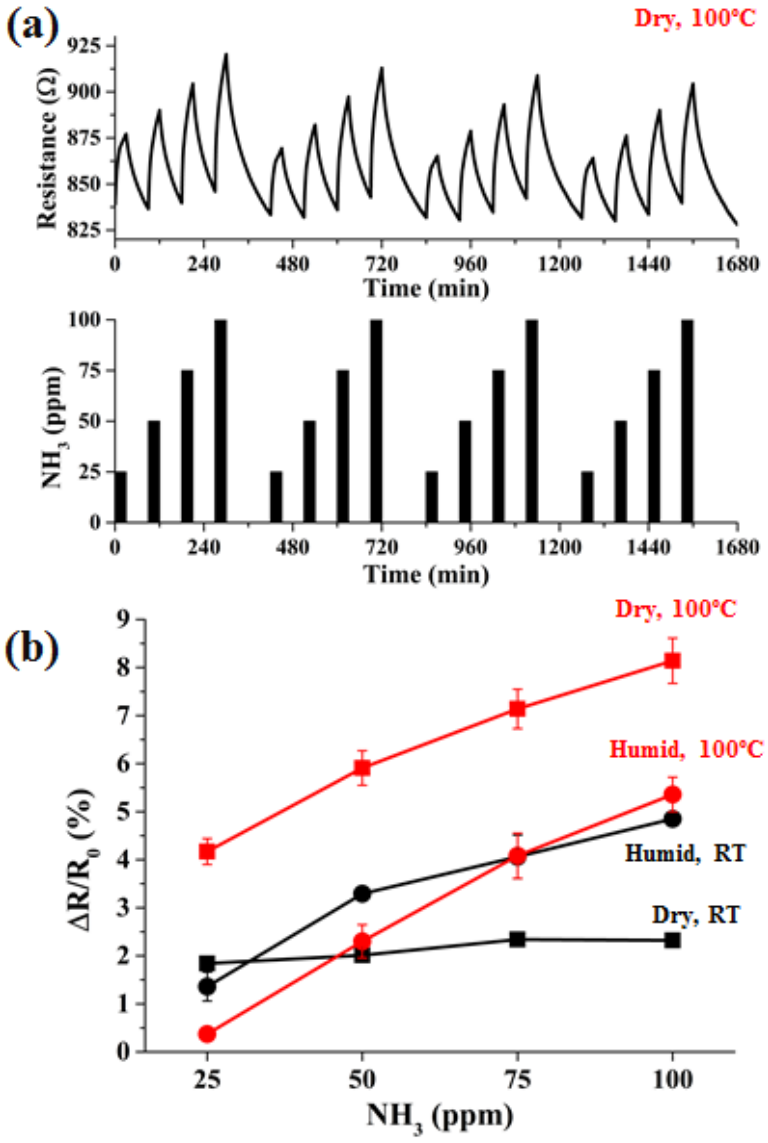


**Figure 7.** (a) Example of $NH_3$ detection at 100ºC in dry conditions. (b) Calibration curves obtained for $NH_3$ detection (black line: RT; red line: 100ºC; square symbol: dry conditions; circle symbol: 50% RH).

**Tables:**

**Table 1.** Different samples were used for graphene growth. 300 nm $SiO_2$ on Si substrate was deposited with 100 or 200 nm Ni films. Afterwards, on the Ni films 200 nm or 500 nm Cu films were deposited. The short-forms for given Ni and Cu films decided as listed below.

| Sample Short-form | Cu film | Ni film | Substrate |
|---|---|---|---|
| C2N1S | 200 | 100 | $SiO_2$ (300nm) /Si |
| C5N1S | 500 | 100 | |
| C2N2S | 200 | 200 | |
| C5N2S | 500 | 200 | |
| N2S | 0 | 200 | |

**Table 2.** Comparison of sensitivities to $NO_2$ expressed as $10^{-2}$ % / ppb in chemo-resistive sensors with dry air as a carrier gas. LCA: lowest concentration applied. R.H: study of relative humidity effect on gas sensing. NA: not available

| Material | Synthesis technique | Additional preparation | T (°C) | Substrate | LCA (ppb) | LOD (ppb) | Sensitivity | RH | Reaction time (min) | Flow rate (sccm) | Reference (Year) |
|---|---|---|---|---|---|---|---|---|---|---|---|
| FLG | CVD | NA | RT | $SiO_2$ nano-pillars | 25 | 5 | 1.5 | Yes | 30 | 100 | This work |
| Graphene | CVD | S doping at 500°C | RT | Micro-hotplate form | 1000 | NA | 0.07 | No | 10 | 1000 | [33] (2018) |
| Graphene | CVD | Electron beam lithography - plasma dry etching | RT | $SiO_2$ | 200 | NA | 0.25 | No | 3 | 500 | [25] (2016) |
| Graphene | CVD | Photo-lithography and $O_2$ treatment | 180 | Polyimide | 5000 | 7 | - | Yes | NA | 1000 | [35] (2015) |
| Graphene | CVD | Graphene heater, Laser patterning | 250 | Polyethersulfone | 500 | NA | 0.07 | No | 5 | NA | [34] (2014) |
| Graphene | CVD | $SnO_2$ nanowire Schottky contact, 1V bias | 120 | $SiO_2$ | 10 | 0.024 ppt | 0.09 | No | <5 | 200 | [31] (2014) |
| Graphene | CVD | Ozone treatment | RT | $SiO_2$ | 200000 | 1.3 | 0.0055 | No | 15 | 500 | [32] (2012) |
| Graphene | CVD | Photo-lithography | RT | $SiO_2$ | 100000 | NA | 0.01 | Yes | 50 | NA | [12] (2012) |
| Graphene | CVD | Lithography-RIE | RT | $SiO_2$ | 1000 | 15 | 0.43 | No | 15 | 200 | [61] (2012) |
| Graphene | CVD | NA | - | PET | 200000 | NA | 0.01 | No | <5 | NA | [53] (2012) |
| Graphene | Commercial graphite | Acid treatment enhanced liquid-phase exfoliation | RT | Alumina | 5000 | NA | 0.22 | No | NA | 250 | [26] (2017) |
| Graphene | Epitaxial graphene | Laser Photolithography | 120 | 4H-SiC | | 0.06 ppt | 1 | Yes | 60 | NA | [36] (2015) |
| GO | Hummers method | Two-beam-laser interference | RT | Ceramic | 4000 | NA | 0.15 | No | <2 | 1000 | [55] (2018) |
| GO | Commercial graphite | Graphene oxidation | RT | Alumina | 3 ppm | 90 ppb | 0.51 | No | 4 | 200 | [54] (2014) |
| rGO | Hummers method | rGo-$Fe_2O_3$ hybrid preparation | RT | | 5 ppm | NA | 0.05 | Yes | 10 | NA | [27] (2018) |
| rGO | Hummers method | Two-beam-laser interference | RT | Ceramic | 4 ppm | NA | 0.5 | No | <1 | NA | [55] (2018) |
| rGO | Commercial GO | Reduction of GO | RT | PET | 1 ppm | NA | 0.23 | No | 20 | NA | [56] (2014) |

**Table 3.** Comparison of sensitivities to $NH_3$ expressed as $10^{-2}$% / ppm in chemo-resistive sensors with dry air as a carrier gas. LCA: lowest concentration applied. R.H: study of relative humidity effect on gas sensing. NA: not available.

| Material | Synthesis technique | Additional preparation | T (°C) | LCA (ppm) | LOD (ppm) | Sensitivity | RH | Reaction time (min) | Flow rate (sccm) | Reference (Year) |
|---|---|---|---|---|---|---|---|---|---|---|
| **Graphene** | CVD | NA | 100 | 25 | 1 | 5.3 | Yes | 30 | 100 | This work |
| **Graphene** | CVD | Photo-lithography and $O_2$ treatment | 180 | 50 | NA | 5.4 | Yes | NA | 1000 | [35] (2015) |
| **Graphene** | CVD | Electron beam lithography - plasma dry etching | RT | 1 | 0.16 | 71 | No | 15 | 200 | [61] (2012) |
| **Graphene** | CVD | Photo-lithography | RT | 0.5 | NA | 83 | Yes | 50 | NA | [12] (2012) |
| **rGO** | Commercial GO | Reduction of GO | RT | 0.2 | NA | 5.5 | No | 20 | NA | [57] (2014) |

# Chapter 4

## Diamondoids

*This chapter provides the article related to diamondoids included in the thesis*

UNIVERSITAT ROVIRA I VIRGILI
GAS SENSING WITH MODIFIED CARBON NANOTUBES, GRAPHENE AND DIAMONDOIDS
Juan Casanova Cháfer

# Section 4.1

# Diamondoid Nanostructures as $sp^3$-Carbon-Based Gas Sensors

Oana Moncea*, Juan Casanova-Chafer*, Didier Poinsot*, Lukas Ochmann, Clève D. Mboyi, Houssein O. Nasrallah, Eduard Llobet, Imen Makni, Molka El Atrous, Stéphane Brandès, Yoann Rousselin, Bruno Domenichini, Nicolas Nuns, Andrey A. Fokin, Peter R. Schreiner, Jean Cyrille Hierso.

*Angewandte Chemie - International Edition, 58 (2019) 9933-9938*

DOI:10.1002/anie.201903089

* Authors that contributed equally to the work

UNIVERSITAT ROVIRA I VIRGILI
GAS SENSING WITH MODIFIED CARBON NANOTUBES, GRAPHENE AND DIAMONDOIDS
Juan Casanova Cháfer

Diamondoids Hot Paper

International Edition: DOI: 10.1002/anie.201903089
German Edition: DOI: 10.1002/ange.201903089

# Diamondoid Nanostructures as $sp^3$-Carbon-Based Gas Sensors

*Oana Moncea, Juan Casanova-Chafer, Didier Poinsot, Lukas Ochmann, Clève D. Mboyi, Houssein O. Nasrallah, Eduard Llobet,* Imen Makni, Molka El Atrous, Stéphane Brandès, Yoann Rousselin, Bruno Domenichini, Nicolas Nuns, Andrey A. Fokin, Peter R. Schreiner,* and Jean-Cyrille Hierso**

***Abstract:*** *Diamondoids, $sp^3$-hybridized nanometer-sized diamond-like hydrocarbons (nanodiamonds), difunctionalized with hydroxy and primary phosphine oxide groups, enable the assembly of the first $sp^3$-C-based chemical sensors by vapor deposition. Both pristine nanodiamonds and palladium nanolayered composites can be used to detect toxic $NO_2$ and $NH_3$ gases. This carbon-based gas sensor technology allows reversible $NO_2$ detection down to 50 ppb and $NH_3$ detection at 25–100 ppm concentration with fast response and recovery processes at 100 °C. Reversible gas adsorption and detection is compatible with 50 % humidity conditions. Semiconducting p-type sensing properties are achieved from devices based on primary phosphine–diamantanol, in which high specific area (ca. 140 $m^2 g^{-1}$) and channel nanoporosity derive from H-bonding.*

Outdoor air pollution, associated with global climate change, causes several million deaths per year.[1] Many toxic gases are produced through combustion processes from vehicles as well as industrial plants. Nitrogen dioxide ($NO_2$) is the most hazardous gas with a 3 ppm threshold limit value (TLV, human level of exposure to be strictly controlled).[2] $NO_2$ plays a role in atmospheric reactions causing acid rain, and contributes to ozone formation, which is the major cause of photochemically produced smog.[1,2] Detection and emission control of nitrogen oxides are thus essential objectives to reduce their hazardous effects on environment and mankind.[1–3]

Metal oxide semiconductors are low-cost, robust sensors most frequently used for the $NO_2$ detection.[4,5] These usually operate at temperatures of a few hundred degrees Celsius, which is costly and reduces sensor lifetime. Other significant limitations are cross-sensitivities with other gases, and detrimental interference from relative humidity. Because of the emergence of nanotechnology, a shift in sensor materials occurred toward more sensitive recognition layers,[6] increasingly elaborate architectures,[7,8] and reduced dimensionality.[2,9] Research addresses low-power devices from sensitive and stable sensors usable at moderate temperatures, and thus suited for trace detection for a wide spectrum of applications ranging from lab-on-a-chip and in vivo biosensors to environmental monitoring and warfare agent detection.[10] In 2000, the Dai group demonstrated the potential of carbon nanotube (CNT)-based gas sensors.[3] The role of graphene in fabricating gas sensors for the detection of various hazardous gases, including $NO_2$, rapidly emerged.[11,12] Thus, sensor development experienced a remarkable rise in attention focusing on $sp^2$-hybridized carbon structures.[13] There is, however, a large group of $sp^3$-hydridized carbon semiconductor materials, the so-called diamondoids, which essentially are hydrogen-terminated diamond nanoparticles (that is, pristine nanodiamonds).[14] These mechanically rigid and thermodynamically extremely stable structures[15] are available in large quantities from fossil resources and in part through chemical synthesis.[16] Diamondoids are promising for nanoelectronics,[17] since they exhibit unique effects such as quantum confinement, hence offering possibilities for band gap tuning.[18,19] Diamondoid derivatives serve as building blocks in "bottom-up" strategies to build unique $sp^3$-carbon-based nanocomposites.[20,21]

[*] Dr. O. Moncea, D. Poinsot, Dr. C. D. Mboyi, Dr. H. O. Nasrallah, I. Makni, M. El Atrous, Dr. S. Brandès, Dr. Y. Rousselin, Prof. Dr. J.-C. Hierso
Institut de Chimie Moléculaire de l'Université de Bourgogne (ICMUB) UMR-CNRS 6302, Université de Bourgogne Franche-Comté (UBFC)
9 avenue Alain Savary, 21078 Dijon (France)
E-mail: jean-cyrille.hierso@u-bourgogne.fr

Dr. O. Moncea, L. Ochmann, Prof. Dr. A. A. Fokin, Prof. Dr. P. R. Schreiner
Institute of Organic Chemistry, Justus Liebig University
Heinrich-Buff-Ring 17, 35392 Giessen (Germany)
and
and Center for Materials Research (LaMa), Justus Liebig University
Heinrich-Buff-Ring 16, 35392 Giessen (Germany)
E-mail: prs@uni-giessen.de

J. Casanova-Chafer, Prof. Dr. E. Llobet
MINOS-EMaS, University Rovira i Virgili
Avda. Països Catalans, 26, 43007 Tarragona (Spain)
E-mail: eduard.llobet@urv.cat

Prof. Dr. B. Domenichini
Laboratoire Interdisciplinaire Carnot de Bourgogne (ICB), UMR-CNRS 6303, Université de Bourgogne Franche-Comté (UBFC)
9 avenue Alain Savary, 21078 Dijon (France)

Dr. N. Nuns
Unité de Catalyse et de Chimie du Solide, UMR 8181, Université Lille1 Sciences et Technologies
Cité Scientifique, bâtiment C3, 59655 Villeneuve d'Ascq (France)

Prof. Dr. A. A. Fokin
Department of Organic Chemistry, Kiev Polytechnic Institute
Pr. Pobedy 37, 03056 Kiev (Ukraine)

Prof. Dr. J.-C. Hierso
Institut Universitaire de France (IUF)
103 Bd. Saint Michel, 75005 Paris Cedex 5 (France)

Supporting information and the ORCID identification number(s) for the author(s) of this article can be found under: https://doi.org/10.1002/anie.201903089.

Surfaces of CNT-based $NO_2$ sensor materials react with the detected gas in mechanisms involving charge-transfer or Schottky-barrier modification,[2,22] which results in a measurable change in resistance. In semiconducting p-type sensors, electron donation into the valence band results in charge-carrier recombination causing an increase in resistance. Conversely, electron-withdrawing effects increase the hole concentration in the material, leading to lower resistance.[2] Additionally, $NO_2$ adsorption is more favorable on CNTs with high metallic character than on semiconducting nanotubes.[23] We thus envisioned that nanocomposites combining $sp^3$-carbon 3D diamondoids coated with thin metal nanolayers would yield hybrid materials with electronically modified surfaces. These materials would then be potential catalysts or sensors. This band-structure doping inspired approach would combine $sp^3$-C nanodiamond semiconductors with transition metals. Accordingly, we recently reported robust self-assemblies of volatile P-functionalized diamondoids into nanocrystals by mild vapor deposition,[20] followed by Pd nanolayer coating under mild CVD conditions.[21]

Herein we present the first use of $sp^3$-C-based nanostructures as high sensitivity gas sensors for the reversible detection of $NO_2$, $NH_3$, and $H_2$. These new materials were structurally characterized at different scales (single-crystal X-ray diffraction, powder X-ray diffraction, porosity measurements, time-of-flight secondary ion mass spectrometry, ToF-SIMS). The materials proved gas responsive both in pristine form and used as metal composite with a thin Pd nanolayer on the surface. These chemical p-type sensors promote reversible $NO_2$ detection at 50 ppb to 100 ppm concentration with fast response and recovery processes at 100 °C; $NO_2$ detection was even possible in 50 % relative humidity. $NH_3$ detection at 25–100 ppm was also found to be highly efficient.

The primary phosphine 9-(hydroxydiamant-4-yl)phosphine ($H_2$P-DiamOH, **1**) and its oxide ($H_2$(O)P-DiamOH, **2**) were synthesized from diamantane (Figure 1; Supporting Information, Figure S1,S2). These diamondoid derivatives were used in powder form, first for their vapor-phase self-assembly, then for generating the metal composites Pd@$PH_2$-DiamOH (**3**) and Pd@P(O)$H_2$-DiamOH (**4**), respectively.[21] This was achieved by low-temperature chemical vapor deposition of a Pd nanolayer over the crystal self-assembly.[24] We elucidated the structure of **1** by growing single crystals in the vapor phase since all our attempts in solution failed. We found for **1** tetragonal symmetry (space group $I\bar{4}$, with $a = b =$ 17.8965(4) Å, $c = 8.1224(2)$ Å, $V = 2601.48(13)$ Å$^3$, Supporting Information, Tables S1–S4). There is a single molecule in the asymmetric unit with strong H-bonding that leads to tetrameric arrangement (Figure 1).[25] We observed a large-scale arrangement of the crystalline structure in which significant nanoporosity appears. Channel voids with a total volume of 168 Å$^3$ (ca. 6.4 % of the unit cell, Figure 2) is accessible to small molecules or solvent. We examined voids within related diamondoid structures to establish that cavities in **1** are larger (or exist) than observed for related crystalline diamantane derivatives (see details in the Supporting Information, Figure S3).

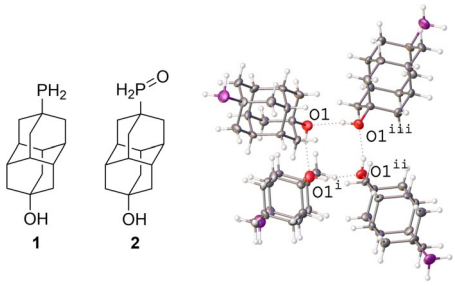


***Figure 1.*** 9-(Hydroxydiamant-4-yl)phosphine 1 and its oxide 2 (left). Tetramer arrangement for 1 with O1–H1···O1$^{i}$ = 2.737(4) Å and O1-H-O1$^{i}$ = 164.8° (right). ORTEP ellipsoids are set at 50% probability.

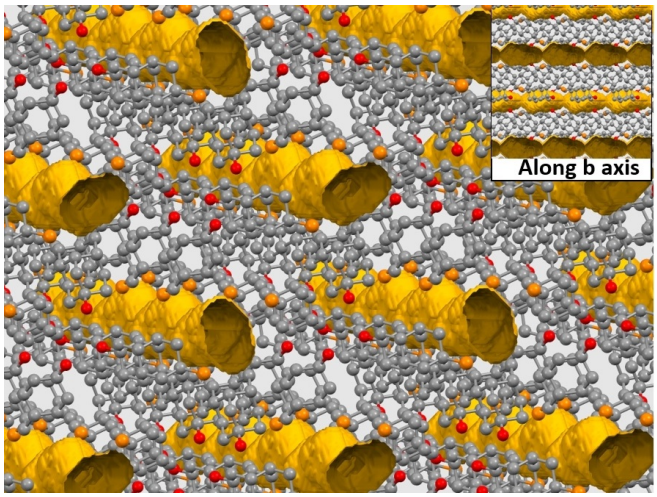


***Figure 2.*** View of accessible channel voids in diamondoid **1** (Platon program crystallographic tool; probe 1.2 Å, grid 0.2 Å).

The powder X-ray diffraction (PXRD) confirmed that this crystalline arrangement is conserved in the granular materials arising from diamantane functionalization, which was used for vapor-phase self-assembly of **1** and **2**. We found excellent agreement between the experimental (Supporting Information, Figure S4) and simulated PXRD patterns that were obtained from the single-crystal unit cell by Le Bail refinement. Two major peaks at 2$\theta$ 15.2° and 15.8°, completed with smaller peaks at 6.9, 9.8, 13.9, and 18.2°, were observed and calculated. In relation with the XRD channel voids and the highly textured surface observed from SEM (Figure 3, top left), we measured the surface area of **1** from the crystalline powder following the Langmuir method using $CO_2$ absorption at 198 K (Supporting Information, Figure S5a–c). We surprisingly found for this purely organic phosphine a $S_{BET} =$ 138 m$^2$ g$^{-1}$, which is significantly higher than several reported porous composite materials.[26] Accordingly, we measured the surface area of (9-hydroxydiamant-4-yl)phosphonic dichloride[15a] (**5**, named $Cl_2$(O)P-DiamOH) and its chlorinated analogue (9-chlorodiamant-4-yl)phosphonic dichloride (**6**, $Cl_2$(O)P-Diam-Cl) to found much lower values $S_{BET} = 40$ and 25 m$^2$ g$^{-1}$, respectively (Supporting Information, Figure S5d). While single crystals of **5** could not be obtained, the XRD structure of $Cl_2$(O)P–DiamCl,[15a] clearly reveals no

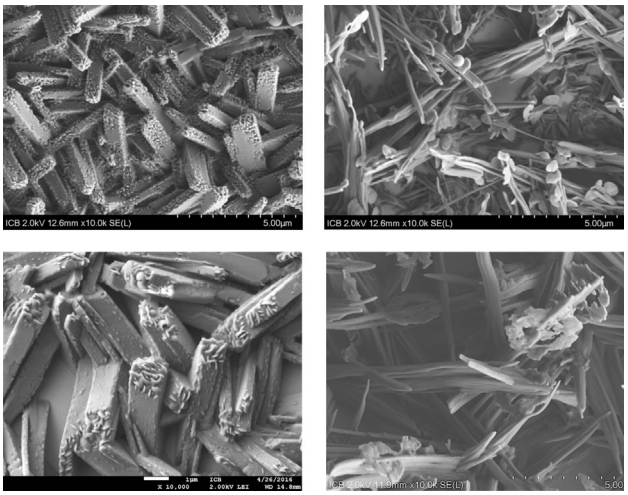

*Figure 3.* Scanning electron microscopy (SEM) of **1** (top left) and **2** (top right), and metal nanocomposites Pd@$PH_2$-DiamOH, **3** (bottom left) and Pd@P(O)$H_2$-DiamOH **4** (bottom right).

voids. A $S_{BET} = 54\ m^2\,g^{-1}$ was found for the oxide $H_2$(O)P–DiamOH, **2**.

The nanolayering of palladium over self-assembled **1** and **2** led to nanocomposites **3** and **4**, respectively, for which scanning electron microscopy views are given in Figure 3. The self-assemblies of **1**–**4** were produced with high structural uniformity and reproducibility.[21] The surfaces composition of these materials has been characterized by XPS, showing covalently built robust Pd@diamondoid hybrids that incorporate Pd–O–P(H)$_n$–diamantane binding motifs. Our initial studies had been limited to a low surface depth below 10 nm, and we thus achieved bulk characterization of these materials in view of gas sensing.

ToF-SIMS analyses (Supporting Information, Table S5, Figures S6–S9) from self-assembly of **1** indicated that the surface of primary diamantanol phosphines is mostly in the oxidized form. Additionally, in composite **3** the palladium interactions with oxygen are prevalent, with the palladium isotopic distribution visible in many mass fragments attributable to palladium phosphorus oxides (Supporting Information, Table S5, Figures S6–S9). This is in full agreement with a Pd–O–P bonding suggested by XPS. The ToF-SIMS technique also allowed monitoring and quantifying the different elements of our materials in-depth (bulk) owing to dual beam sputtering and analysis. Figure 4 represents the profile of the elements of interest (Pd, P, C, Si) as a function of sputter time for nanocomposite Pd@$PH_2$-DiamOH **3**. The clearly distinguishable areas correspond to the palladium layer (I), diamondoid phosphine deposit (II), and silicon support (III). The steep decrease of curve I from an initially dominant detection attested the Pd present as a thin nanolayer on the surface. The monitoring of phosphorus and carbon from the diamondoid cages (curves II) was achieved through the detection of characteristic fragments (Supporting Information, Figures S6–S9). P and C content detection follow first an increase, while the Pd trace diminishes (the lines cross at 70 s), then they decrease with the emergence of signals from the silicon wafer (curve III, line crossing at 4000 s). The profiles

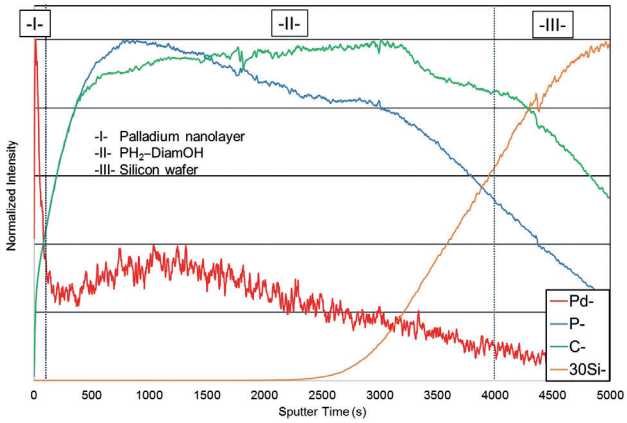


*Figure 4.* ToF-SIMS depth profile of nanocomposite Pd@$PH_2$-DiamOH, **3**.

for P- and C-containing fragments follow a remarkable parallel evolution that attests to excellent homogeneity of the diamondoid phosphine deposit. According to Yamamura's sputter yield calculation as a function of the sputter type and energy,[27] it is possible to estimate sputter rate for Pd nanolayer ($\leq 0.07\ nm\,s^{-1}$). ToF-SIMS depth profiling indicates thus a Pd nanolayer thinner than 5 nm. From SEM the diamondoid deposit thickness was estimated above 175 nm.

$NO_2$ gas sensing experiments were conducted with Pd nanocomposites **3** and **4**, but for comparison also with crystal self-assemblies of **1** and **2**. We conducted our experiments in a 35 $cm^3$ airtight test chamber, with pieces of silicon wafers glued to a miniaturized ceramic hotplate and connected to a printed circuit board (Supporting Information, Figures S10 and S11). The exposure to $NO_2$ was 10 min with a recovery process of 30 min at 100 $mL\,min^{-1}$ flow of dry air. Nanocomposites operated at 100 °C and their electrical resistance was monitored within repeated response–recovery cycles. The materials were all found responsive (Figure 5). The self-assembly of diamondoid phosphine $H_2P$–DiamOH **1** showed an $NO_2$ response (3.0 % at 100 ppm, cycling time-resolved detection in Figure 6a) slightly superior to its oxide $H_2$(O)P–DiamOH **2** (1.5 % at 100 ppm) and its Pd nanocomposite Pd@$PH_2$–DiamOH **3** (2.1 % at 100 ppm). A significant $NO_2$ response was achieved with metal nanocomposite Pd@P-

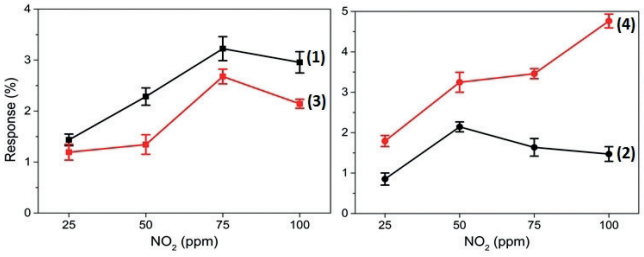


*Figure 5.* $NO_2$ response with chemical sensors **1**–**4** at increasing 25 to 100 ppm concentration: black $\nu = H_2P$–DiamOH (**1**), black $\lambda = H_2$-(O)P–DiamOH (**2**), red $\nu$ = Pd@$PH_2$–DiamOH (**3**), red $\lambda$ = Pd@P-(O)$H_2$-DiamOH (**4**). Response is defined as the relative $(R_{air} - R_{gas})/R_{air}$ after 10 min exposure to $NO_2$. See also the Supporting Information, Figure S11.

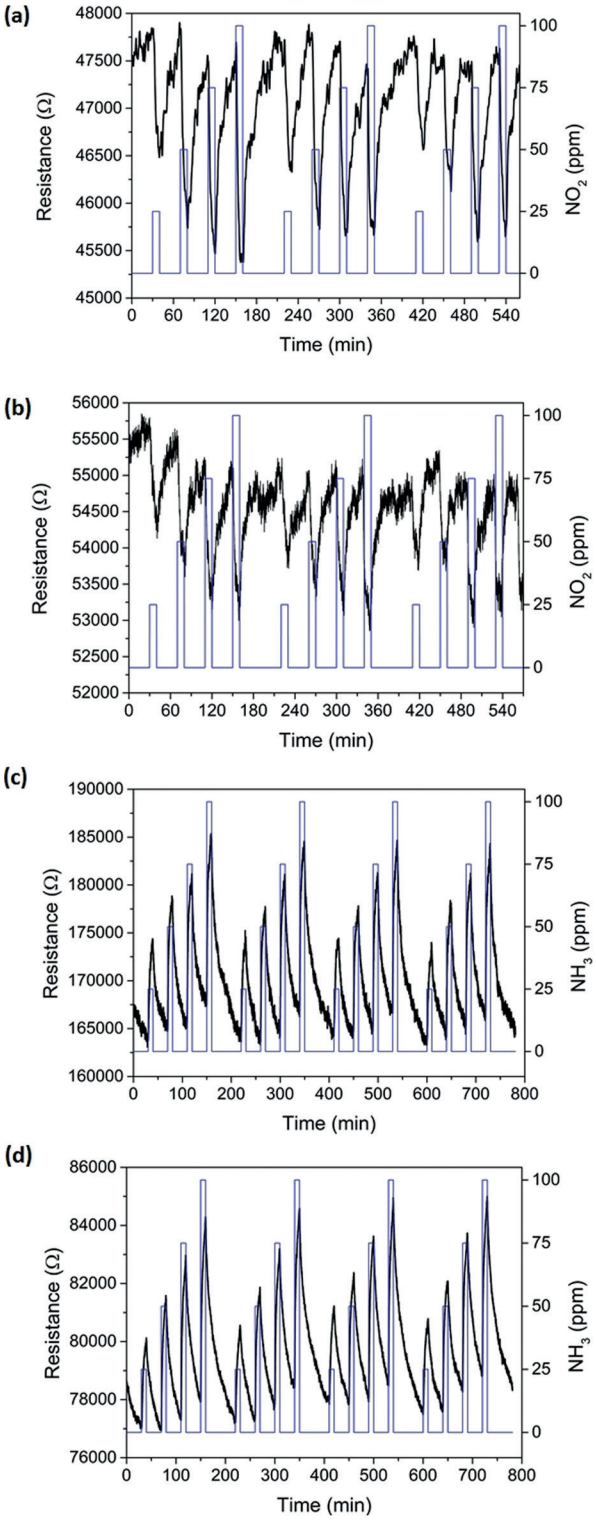


***Figure 6.*** a),b) Reversible $NO_2$ detection for sensors of higher sensitivity at 25, 50, 75, and 100 ppm: $H_2$P–DiamOH **1** (a), Pd@P(O)$H_2$-DiamOH **4** (b). Signals are smoothed using the Savitzky–Golay method. c),d) Reversible $NH_3$ detection for sensors of higher sensitivity at 25, 50, 75, and 100 ppm: $H_2$P–DiamOH **1** (c) and Pd@$PH_2$-DiamOH **3** (d). Signals smoothed using the Savitzky–Golay method.

(O)$H_2$–DiamOH **4** with fast response and recovery processes (4.8% at 100 ppm, cycling detection in Figure 6b).

The same samples were used for $NH_3$ detection in the 25–100 ppm concentration range under the same conditions (air flow 100 mL $min^{-1}$, 100 °C, 35 $cm^3$ chamber) showing an even higher sensitivity for the $NH_3$ response (> 10.0% for $H_2$P–DiamOH **1** and > 7.0% for Pd@$PH_2$–DiamOH **3** at 100 ppm $NH_3$, see cycling time-resolved detection in Figure 6c and d, respectively, and Figure 7a). Exposure to $NH_3$ (as an electron-donating species) resulted in a resistance increase while the presence of $NO_2$ (electron-withdrawing) resulted in resistance decrease, which corresponds to typical semiconducting p-type behavior for all samples. Consistently, we found that uptake of $H_2$ was also possible with nanomaterials **1**–**4**, inducing resistance increase (Supporting Information, Figure S12) that confirms the p-type character of these gas sensors. Using the diamondoid phosphine **5** $Cl_2$(O)P–DiamOH,[21] we checked that efficient gas sensing properties were related to the primary phosphine-based diamantanol compounds. We observed for $Cl_2$(O)P–DiamOH-based materials much lower $H_2$ uptake (if any) compared to **1** (Supporting Information, Figure S12a). This is visibly consistent with the high surface area for gas adsorption in **1**, which is found 3.5 time higher than in **5** (138 vs. 40 $m^2 g^{-1}$).

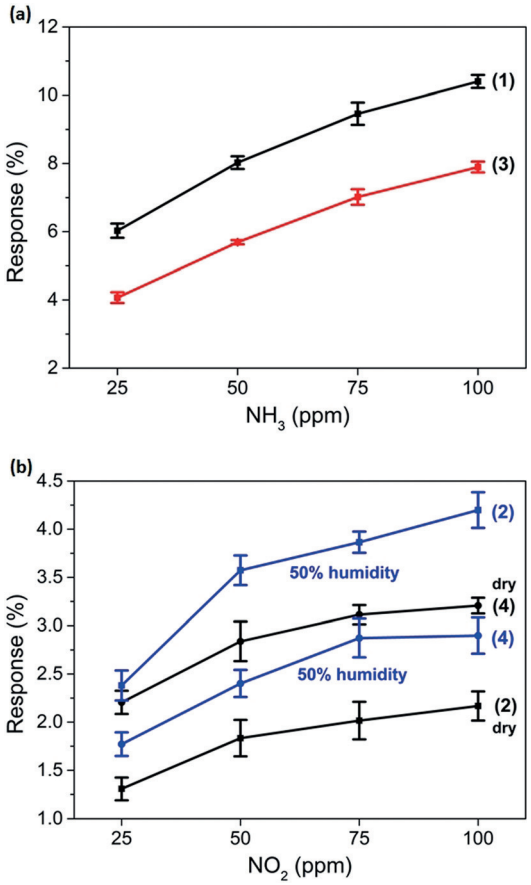


***Figure 7.*** a) $NH_3$ response of **1** and **3** at increasing 25–100 ppm concentrations (after 10 months storing); b) $NO_2$ response with sensors **2** and **4** in dry or humid conditions (after six months storing): black $\nu$ = $H_2$P(O)–DiamOH (**2**), black $\lambda$ = Pd@P(O)$H_2$–DiamOH (**4**) in dry conditions; blue $\nu$ = $H_2$P(O)–DiamOH (**2**), blue $\lambda$ = Pd@P(O)$H_2$–DiamOH (**4**) in humid conditions (50% relative humidity).

An issue of low-temperature sensing is the potential interference of relative humidity and the sensitivity to water is a factor to consider for practical devices.[2,10] For $NO_2$ detection we compared the performances of nanomaterials **1**–**4** under dry and humid atmospheres (50% relative humidity) as illustrated in Figure 7b with **4** and **2** (**1** and **3** in the Supporting Information, Figure S11.5). The detection of $NO_2$ was effective under either set of conditions, with different behavior still to rationalize, since **2** (and **3**) increases the sensitivity in humid atmosphere compared to dry conditions, while **4** (and **1**) performed better under dry conditions. In any case the responses were kept detectable in the same range (1–4%). Remarkably, uptake experiments reported in Figure 7 were achieved six months ($NO_2$ sensing) to ten months ($NH_3$ sensing) after device preparation, attesting their robustness upon storing.

Operational devices for toxic gas request a TLV at low levels of 25 ppm for $NH_3$ and 3 ppm for $NO_2$.[2] While our $sp^3$-C-based diamondoid sensors efficiently detected $NH_3$ at this environmental level requirement (Figure 6 and Figure 7b), we further explored the detection limit of our systems for $NO_2$ in a 13 $cm^3$ airtight test chamber, reducing the dead volume with unchanged operating temperature (100 °C) and exposure/recovery times. Under these conditions, the detection of $NO_2$ concentrations from 50 to 1000 ppb was successfully achieved, and confirmed the suitability of $sp^3$-carbon-based sensors for detecting few ten ppb of nitrogen dioxide (Figure 8).

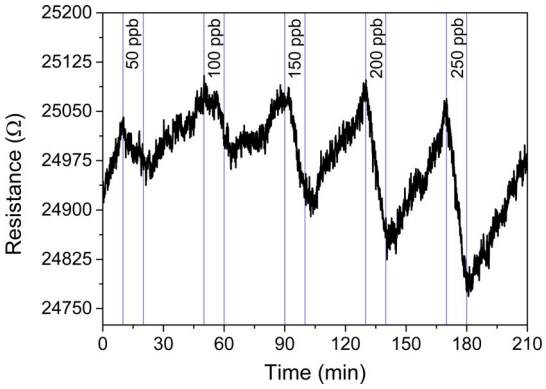


***Figure 8.*** Reversible $NO_2$ detection at 50–250 ppb level for high-sensitivity hybrid nanostructure sensor Pd@PH2–DiamOH **3**.

In summary, we report the first application of $sp^3$-C-based gas sensors ($NO_2$, $NH_3$, and $H_2$). Remarkably, they tolerate humid conditions and achieve sensing of $NO_2$ at ppb levels at 100 °C. Pristine and metal-nanolayered diamondoids can both be gas responsive. Such gas sensing properties are related to primary phosphine–diamantanol based compounds for which channel nanoporosity (and $S_{Bet}$ ca. 140 $m^2 g^{-1}$) derives from H-bonding in the solid state. We aim at extending our new approach to other metals and nanoobjects built on suitably functionalized diamondoid $sp^3$-carbon-based nanostructures.

## Acknowledgements

This work was supported by the ANR-DFG program HYBRIDIAMS (ANR-16-CE92-0037-01 and Schr 597/31-1). In Dijon, it was partly supported by the Université de Bourgogne (CoMUE BFC and ISITE-BFC), CNRS, and Conseil Régional de Bourgogne through the plan d'actions régional pour l'innovation (PARI) and the European Union through the PO FEDER-FSE Bourgogne 2014/2020 (via CoMICS program, Chemistry of Molecular Interactions: Catalysis & Sensors). In Tarragona it was supported by MINECO, FEDER (TEC 2015–71663-R) and AGAUR (2017SGR418). E.L. was supported by the ICREA Academia Award 2018. The work in Giessen was supported in part by the U.S. Department of Energy (Contract No. DE-AC02-76SF00515). Mobility was supported by the Université Franco-Allemande/Deutsch-Französische Hochschule. O.M., J.C.C., and D.P. contributed equally to the work. We thank J.-F. Lamonier, O. Heintz, F. Herbst, and R. Chassagnon for their help in the materials characterization.

## Conflict of interest

The authors declare no conflict of interest.

**Keywords:** gas sensing · hybrid materials · nanodiamonds · palladium · phosphine

**How to cite:** *Angew. Chem. Int. Ed.* **2019**, *58*, 9933–9938
*Angew. Chem.* **2019**, *131*, 10038–10043

[1] A. C. Rai, P. Kumar, F. Pilla, A. N. Skouloudis, S. Di Sabatino, C. Ratti, A. Yasar, D. Rickerby, *Sci. Total Environ.* **2017**, *508*, 383 and related World Health Organization (WHO) annual reports cited therein.
[2] D. R. Kauffman, A. Star, *Angew. Chem. Int. Ed.* **2008**, *47*, 6550; *Angew. Chem.* **2008**, *120*, 6652.
[3] J. Kong, N. R. Franklin, C. Zhou, M. G. Chapline, S. Peng, K. Cho, H. Dai, *Science* **2000**, *287*, 622.
[4] K. Wetchakun, T. Samerjai, N. Tamaekong, C. Liewhiran, C. Siriwong, V. Kruefu, A. Wisitsoraat, A. Tuantranont, S. Phanichphant, *Sens. Actuators B* **2011**, *160*, 580.
[5] S. S. Shendage, V. L. Patil, S. A. Vanalakar, S. P. Patil, N. S. Harale, J. L. Bhosale, J. H. Kim, P. S. Patil, *Sens. Actuators B* **2017**, *240*, 426.
[6] M. Schulz, A. Gehl, J. Schlenkrich, H. A. Schulze, S. Zimmermann, A. Schaate, *Angew. Chem. Int. Ed.* **2018**, *57*, 12961; *Angew. Chem.* **2018**, *130*, 13143.
[7] M.-S. Yao, X.-J. Lv, Z.-H. Fu, W.-H. Li, W.-H. Deng, G.-D. Wu, G. Xu, *Angew. Chem. Int. Ed.* **2017**, *56*, 16510; *Angew. Chem.* **2017**, *129*, 16737.
[8] J. Z. Ou, W. Ge, B. Carey, T. Daeneke, A. Rotbart, W. Shan, Y. Wang, Z. Fu, A. F. Chrimes, W. Wlodarski, S. P. Russo, Y. X. Li, K. Kalantar-zadeh, *ACS Nano* **2015**, *9*, 10313.
[9] a) T. M. Swager, *Angew. Chem. Int. Ed.* **2018**, *57*, 4248; *Angew. Chem.* **2018**, *130*, 4325; b) G. Cao, *Nanostructures and Nanomaterials*, Imperial College Press, London, **2004**; c) Z. Chen, J. Appenzeller, J. Knoch, Y. M. Lin, P. Avouris, *Nano Lett.* **2005**, *5*, 1497.
[10] E. Llobet, *Sens. Actuators B* **2013**, *179*, 32.
[11] E. Singh, M. Meyyappan, H. S. Nalwa, *ACS Appl. Mater. Interfaces* **2017**, *9*, 34544.

[12] F. Yavari, Z. Chen, A. V. Thomas, W. Ren, H.-M. Cheng, N. Koratkar, *Sci. Rep.* **2011**, *1*, 166 – 161.
[13] V. Schroeder, S. Savagatrup, M. He, S. Lin, T. M. Swager, *Chem. Rev.* **2019**, *119*, 599.
[14] a) J. E. Dahl, S. G. Liu, R. M. K. Carlson, *Science* **2003**, *299*, 96; b) H. Schwertfeger, A. A. Fokin, P. R. Schreiner, *Angew. Chem. Int. Ed.* **2008**, *47*, 1022; *Angew. Chem.* **2008**, *120*, 1038; c) M. A. Gunawan, J.-C. Hierso, D. Poinsot, A. A. Fokin, N. A. Fokina, B. A. Tkachenko, P. R. Schreiner, *New J. Chem.* **2014**, *38*, 28.
[15] a) O. Moncea, M. A. Gunawan, D. Poinsot, H. Cattey, J. Becker, R. I. Yurchenko, E. D. Butova, H. Hausmann, M. Šekutor, A. A. Fokin, J.-C. Hierso, P. R. Schreiner, *J. Org. Chem.* **2016**, *81*, 8759; b) N. A. Fokina, B. A. Tkachenko, A. Merz, M. Serafin, J. E. P. Dahl, R. M. K. Carlson, A. A. Fokin, P. R. Schreiner, *Eur. J. Org. Chem.* **2007**, 4738; c) P.-L. E. Chu, L.-Y. Wang, S. Khatua, A. B. Kolomeisky, S. Link, J. M. Tour, *ACS Nano* **2013**, *7*, 35.
[16] a) J. E. Dahl, J. M. Moldowan, K. E. Peters, G. E. Claypool, M. A. Rooney, G. E. Michael, M. R. Mello, M. L. Kohnen, *Nature* **1999**, *399*, 54; b) J. E. P. Dahl, J. M. Moldowan, T. M. Peakman, J. C. Clardy, E. Lobkovsky, M. M. Olmstead, P. W. May, T. J. Davis, J. W. Steeds, K. E. Peters, A. Pepper, A. Ekuan, R. M. K. Carlson, *Angew. Chem. Int. Ed.* **2003**, *42*, 2040; *Angew. Chem.* **2003**, *115*, 2086.
[17] a) W. L. Yang, J. D. Fabbri, T. M. Willey, J. R. I. Lee, J. E. Dahl, R. M. K. Carlson, P. R. Schreiner, A. A. Fokin, B. A. Tkachenko, N. A. Fokina, W. Meevasana, N. Mannella, K. Tanaka, X. J. Zhou, T. van Buuren, M. A. Kelly, Z. Hussain, N. A. Melosh, Z.-X. Shen, *Science* **2007**, *316*, 1460; b) W. A. Clay, Z. Liu, W. Yang, J. D. Fabbri, J. E. Dahl, R. M. K. Carlson, Y. Sun, P. R. Schreiner, A. A. Fokin, B. A. Tkachenko, N. A. Fokina, P. A. Pianetta, N. Melosh, Z.-X. Shen, *Nano Lett.* **2009**, *9*, 57; c) Y. Nakanishi, H. Omachi, N. A. Fokina, P. R. Schreiner, R. Kitaura, J. E. P. Dahl, R. M. K. Carlson, H. Shinohara, *Angew. Chem. Int. Ed.* **2015**, *54*, 10802; *Angew. Chem.* **2015**, *127*, 10952.
[18] a) G. C. McIntosh, M. Yoon, S. Berber, D. Tománek, *Phys. Rev. B* **2004**, *70*, 045401; b) A. A. Fokin, P. R. Schreiner, *Mol. Phys.* **2009**, *107*, 823.
[19] L. Landt, K. Klünder, J. E. Dahl, R. M. K. Carlson, T. Möller, C. Bostedt, *Phys. Rev. Lett.* **2009**, *103*, 047402.
[20] M. A. Gunawan, D. Poinsot, B. Domenichini, C. Dirand, S. Chevalier, A. A. Fokin, P. R. Schreiner, J.-C. Hierso, *Nanoscale* **2015**, *7*, 1956.
[21] M. A. Gunawan, O. Moncea, D. Poinsot, M. Keskes, B. Domenichini, O. Heintz, R. Chassagnon, F. Herbst, J. E. P. Dahl, A. A. Fokin, P. R. Schreiner, J.-C. Hierso, *Adv. Funct. Mater.* **2018**, *28*, 1705786.
[22] Controversy exists over $NO_2$ uptake mechanisms, especially concerning related CNT-based sensors; for a thorough discussion, see Ref. [2].
[23] a) K. Seo, K. A. Park, C. Kim, S. Han, B. Kim, Y. H. Lee, *J. Am. Chem. Soc.* **2005**, *127*, 15724; b) G. Ruiz-Soria, A. Pérez Paz, M. Sauer, D. J. Mowbray, P. Lacovig, M. Dalmiglio, S. Lizzit, K. Yanagi, A. Rubio, A. Goldoni, P. Ayala, T. Pichler, *ACS Nano* **2014**, *8*, 1375.
[24] a) J.-C. Hierso, C. Satto, R. Feurer, P. Kalck, *Chem. Mater.* **1996**, *8*, 2481; b) J.-C. Hierso, R. Feurer, P. Kalck, *Chem. Mater.* **2000**, *12*, 390.
[25] For 1D H-bonding network between hydroxylated diamantanes, see: Y. Nakanishi, H. Omachi, N. A. Fokina, P. R. Schreiner, J. Becker, J. E. P. Dahl, R. M. K. Carlson, H. Shinohara, *Chem. Commun.* **2018**, *54*, 3823.
[26] H. Nasrallah, J.-C. Hierso, *Chem. Mater.* **2019**, *31*, 619.
[27] Y. Yamamura, H. Tawara, *At. Data Nucl. Data Tables* **1996**, *62*, 149.

Manuscript received: March 12, 2019
Revised manuscript received: April 29, 2019
Accepted manuscript online: May 14, 2019
Version of record online: June 11, 2019

  

# Chapter 5

# Conclusions and Future Perspectives

*This chapter summarizes the conclusions followed by the future perspectives in this field*

UNIVERSITAT ROVIRA I VIRGILI
GAS SENSING WITH MODIFIED CARBON NANOTUBES, GRAPHENE AND DIAMONDOIDS
Juan Casanova Cháfer

## 5.1. Conclusions

After more than two decades of carbon nanomaterial research for gas sensing, there is still a need for essential breakthroughs before their industrial production and commercialisation. Thus, the release of inexpensive, reproducible, sensitive and selective carbon-based gas sensors to the market remains some way off. In this thesis, we reported some works demonstrating that carbon nanomaterials gather the properties required for the next generation of sensors. For instance, their high versatility to modify or functionalize them, being adapted to different sensing strategies; their capability to work at room temperature, fulfilling a claim of current societies, which is the low power consumption devices to reduce the ecological footprint; and the possibility to develop devices at nanoscale, with the consequent reduction of the amount of the material needed (and lower quantity of waste material generated), leading to a lower cost of manufacturing.

Gas sensors based on carbon nanomaterials have been demonstrated as suitable candidates to detect concentrations below the TLV in short time analysis. However, despite the fact that many works report the development of outstanding carbon nanomaterial for gas detection, more efforts are needed towards the device-to-device reproducibility in industrial scale and cost-effective production methods. Some techniques, such as CVD, have shown the possibility of growing ultrapure and highly crystalline carbon nanostructures, but significant breakthroughs are needed to achieve an effective control of chirality and diameter during their growth. With that, predictable metallic or semiconductor properties can be obtained, and would surely pave the way for highly reproducible devices. Nevertheless, high-quality carbon nanomaterials usually do not provide the characteristics needed for gas detection at trace levels, such as high sensitivity, selectivity, stability, low noise level and fast response/recovery times. In consequence, further modifications or functionalization of these carbon nanomaterials are required to obtain ameliorated properties. Accordingly, several strategies to enhance the sensing properties were developed during this thesis.

On the mere fact that inducing the presence of impurities and defects on the carbon lattice, has been proved as a straightforward approach to ameliorate the sensitivity. However, this simple strategy does not boost the enhancement of other crucial properties, such as selectivity or fast detection. An easy alternative is the functionalization of the carbon nanomaterial surface by their decoration with metal or metal oxide nanoparticle. This approach is a practical way to increase the sensitivity, reduce unwanted effects (e.g. ambient moisture interference) and sometimes the selectivity can be tuned. As negative features, metallic NPs require moderate or high operating temperatures, increasing the device power-consumption and reducing the shell-life of the sensor.

Conversely, grafting functional groups or molecules to the carbon nanomaterial surface is a good strategy to preserve the room temperature working conditions. Additionally, these compounds grafted on the outer walls via covalent or non-covalent interactions can act as specific receptors towards gases or vapours, increasing the selectivity. In such an approach, the excellent electronic properties of carbon nanomaterials are preserved because they act as support and charge transport transducing elements, while grafted molecules show the receptor or recognition functions. However, operate at room temperature usually compromises the stability and induce drift problems, due to the low desorption rate of gases. Thus, further modifications should be considered in order to enhance the reversibility of the gas adsorption. Against this problem, the use of ultraviolet (UV) light has been proved as an

easy and effective approach. Continuous or pulsed UV light exposure is a fast and clean method to regenerate the sensor surface by favouring the desorption of analytes. Also, the use of UV light can be engineered to protect the carbon nanomaterial surface area from the impurities adsorption or to reduce the cross-sensitivity by reaching the energy binding between the sensor surface and some interfering species.

Other advanced techniques to modify the carbon nanomaterial are the use of reactive plasma and ion implantation. These single-step approaches are an advantageous way to create defects and functionalise the surface in a controlled, reproducible and clean conditions. As a consequence, the use of reactive plasma and ion implantation techniques lead to environmentally friendly routes against other ways such as wet chemistry. Also, the use of nanocrystals (in our case lead halide perovskites) to decorate carbon nanomaterials, or diamondoids-based gas sensors (in our research we explore the $sp^3$ configuration), would surely attract considerable interest in the next years due to their outstanding and promising electronic properties.

Since the enhancement of sensing properties is essential, a well-designed functionalization of carbon nanomaterial should be balanced. For instance, the strengthening of analyte adsorption is required for higher sensitivity, but an excessive adsorption strength during the detection step could compromise the reversibility of the reaction. Thus, in this example, a high irreversible gas sensor response will limit the realization of continuous measurements. Or at least, baseline correction will require more strategies to counteract the drift.

In summary, carbon nanomaterials show the ideal electronic properties to be employed in gas sensors, and as well as high versatility for its modification, being adapted to different measurement strategies. It is still challenging to determine which carbon nanomaterial or type of functionalization hold more promise for reaching the gas sensor market. Probably, the best material and its modification will depend on the desired target properties of the sensors (superior selectivity, shell-life, power consumption…), or the measurement set up needed. The standard solution is the development of sensor arrays, combining different approaches with partially overlapping sensitivity and selectivity. Followed by advanced data treatment. Moreover, for mass-market applications, probably lower quality carbon nanomaterials are more interesting than their high-quality counterparts. Because the decrease in the sensing properties (e.g. sensitivity, stability, etc.) can be compensated by their reduced cost. Anyway, more research in carbon nanomaterial gas sensors is required to overtake the properties of the metal oxide based gas sensors, and consequently open new possibilities for these to be commercialised.

## 5.2. Future Perspectives

After presenting this thesis, several issues remain open. Possibly, the main one is the improvement towards the realization of successful commercial applications. In other words, since carbon nanomaterials have been proved as good candidates to be employed in gas sensors, further optimizations are needed to make them suitable for air quality monitoring under real conditions and for long periods of time.

The modifications of carbon nanomaterials developed in this thesis constitute new approaches to detect trace levels of pollutants, and the creation of sensor arrays by combining different modification strategies will allow sensitive and selective detection of gas molecules. The main discussion about this work is probably the relatively long exposure times (about a few minutes) applied. The sensing measurements performed indicate that our materials are still not suitable for detecting pollutant concentrations in a few seconds. However, there are many other gas-sensing applications with less stringent response and recovery time requirements, more adapted to the current performance of our sensors. For instance, air quality monitoring in working environments (TWA values) or air pollution in urban areas from automotive sources, usually consider an average hourly concentration. Thus, just in the situation that pollutant concentrations are above the TLV during several consecutive hours, the public institutions or companies start to apply protective and corrective actions.

In consequence, the sensing set up employed in this thesis could be engaged in such sort of sensor network. Nevertheless, the work developed is not able to detect an ultra-high concentration of gases, high enough to be dangerous or lethal after a few seconds or minutes of exposure. In this case, further optimizations are needed. For instance, reducing the volume of the test chamber and increasing the flow rate are straightforward actions to minimize the reaction/recovery times considerably.

To obtain a selective detection of gas molecules, we proposed the development of sensor arrays. However, more work is needed to further sensor device miniaturization, and advanced data treatment analysis should be extensively studied. Additional research that could be performed in parallel would consist of mixing several pollutants at different relative concentrations and then, detect them by using a sensor array in order to create complex models that allow better pollutant discrimination.

UNIVERSITAT ROVIRA I VIRGILI
GAS SENSING WITH MODIFIED CARBON NANOTUBES, GRAPHENE AND DIAMONDOIDS
Juan Casanova Cháfer

# Annex I

**Publications directly related with the thesis**

1) Casanova-Cháfer, J.; Navarrete, E.; Noirfalise, X.; Umek, P.; Bittencourt, C.; Llobet, E. *Gas Sensing with Iridium Oxide Nanoparticle Decorated Carbon Nanotubes*. Sensors **2019**, *19*, 113.

2) Elnabawy, H.M.; Casanova-Chafer, J.; Anis, B.; Fedawy, M.; Scardamaglia, M.; Bittencourt, C.; Khalil, A.S.G.; Llobet, E.; Vilanova, X. *Wet chemistry route for the decoration of carbon nanotubes with iron oxide nanoparticles for gas sensing*. Beilstein J. Nanotechnol. **2019**, *10*, 105–118

3) Casanova-Cháfer, J.; Bittencourt, C.; Llobet, E. *Hydrophilicity and carbon chain length effects on the gas sensing properties of chemoresistive, self-assembled monolayer carbon nanotube sensors*. Beilstein J. Nanotechnol. **2019**, *10*, 565–577.

4) Bohli, N.; Belkilani, M.; Behi, S.; Casanova-Chafer, J.; Llobet, E.; Abdelghani, A. *Multiwalled Carbon Nanotubes Based Aromatic VOCs Sensor: Sensitivity Enhancement Through 1-Hexadecanethiol Functionalization.* Beilstein J. Nanotechnol 2019 (in press).

5) Struzzi, C.; Scardamaglia, M.; Casanova-Chafer, J.; Calavia, R.; Colomer, J.-F.; Kondyurin, A.; Bilek, M.; Britun, N.; Snyders, R.; Llobet, E.; et al. *Exploiting sensor geometry for enhanced gas sensing properties of fluorinated carbon nanotubes under humid environment.* Sensors Actuators B Chem. **2019**, *281*, 945–952.

6) Acosta, S.; Casanova-Chafer, J.; Sierra-Castillo, A.; Llobet, E.; Snyders, R. Colomer, J.F.; Quintana, M.; Ewels, C.; Bittencourt, C. *Low kinetic energy oxygen ion irradiation in vertically aligned carbon nanotubes*. Submitted to Applied Sciences.

7) Deokar, G.; Vancsó, P.; Arenal, R.; Ravaux, F.; Casanova-Cháfer, J.; Llobet, E.; Makarova, A.; Vyalikh, D.; Struzzi, C.; Lambin, P.; et al. *$MoS_2$-Carbon Nanotube Hybrid Material Growth and Gas Sensing.* Adv. Mater. Interfaces **2017**, *4*, 1700801.

8) Casanova-Cháfer, J.; García-Aboal, R.; Atienzar, P.; Llobet, E. *Gas Sensing Properties of Perovskite Decorated Graphene at Room Temperature.* Sensors **2019**, *19*, 4563.

9) Deokar, G.; Casanova-Chafer, J.; Rajput, N.S.; Aubry, C.; Llobet, E.; Jouiad, M.; Costa, P. *Wafer-scale few layer graphene growth on Cu/Ni films for gas sensing applications*. Sensors and Actuators B 2019 (in press).

10) Moncea, O.*; Casanova-Chafer, J.*; Poinsot, D.*; Ochmann, L.; Mboyi, C.D.; Nasrallah, H.O.; Llobet, E.; Makni, I.; El Atrous, M.; Brandès, S.; et al. *Diamondoid Nanostructures as sp3-Carbon-Based Gas Sensors*. Angew. Chemie - Int. Ed. **2019**, 58, 9933-9938.

** Contributed equally to the work*

## Publications not included in the thesis

1) Casanova-Chafer, J.; Llobet, E. *Carbon Nanomaterials Integrated in Rugged and Inexpensive Sensing Platforms for the In-Field Detection of Chemical Warfare Agents.* In Nanoscale Materials for Warfare Agent Detection: Nanoscience for Security; **2019**; pp. 13–32. (Book chapter)

2) Casanova-Cháfer, J.; Navarrete, È.; Llobet, E. *Gas Sensing Properties of Carbon Nanotubes Decorated with Iridium Oxide Nanoparticles*. Proceedings **2018,** 2, 874.

# Annex II

## Contributions to Conferences

- **ISOCS/IEEE**, Montreal, Canada (2017).
  - Oral contribution: *Sniffest, the machine olfaction competition.*

- **IBERNAM**, Tordesillas, Spain (2017).
  - Poster presentation: *Gas sensor based on $MoS_2$-carbon nanotube hybrid material.*

- **Cátedra Nanotecnología**, Zaragoza, Spain (2018)
  - Oral contribution: *Los cinco sentidos y la Nanotecnología: el olfato.*

- **Eurosensors**, Graz, Austria (2018).
  - Oral contribution: *Gas sensing properties of CNT decorated with $IrO_2$ nanoparticles.*

- **IBERNAM-CMC2**, Tarragona, Spain (2018).
  - Poster presentation: *Carbon nanotubes decorated with iridium oxide nanoparticles.*

- **Mardi des Chercheurs**, Mons, Belgium (2019).
  - Poster presentation: *Hydrophilicity and carbon chain length effects on the gas sensing properties in SAM-CNT sensors.*

- **Multicomp**, Aveiro, Portugal (2019).
  - Oral presentation: *Hydrophilicity and carbon length chain effect on gas sensing mechanism for thiol SAM/CNT sensor.*

- **CMC2**, Toulouse, France (2019)
  - Poster presentation: *Pulsed UV light on Au-decorated carbon nanotubes gas sensor to determine the $NO_2$ concentration.*

- **IBERNAM**, San Sebastian, Spain (2019).
  - Oral presentation: *Graphene decorated with perovskite nanocrystals for gas sensing at room temperature.*

UNIVERSITAT ROVIRA I VIRGILI
GAS SENSING WITH MODIFIED CARBON NANOTUBES, GRAPHENE AND DIAMONDOIDS
Juan Casanova Cháfer

UNIVERSITAT ROVIRA I VIRGILI
GAS SENSING WITH MODIFIED CARBON NANOTUBES, GRAPHENE AND DIAMONDOIDS
Juan Casanova Cháfer

UNIVERSITAT ROVIRA I VIRGILI
GAS SENSING WITH MODIFIED CARBON NANOTUBES, GRAPHENE AND DIAMONDOIDS
Juan Casanova Cháfer